Unsteady pressure measurement around aerodynamic bodies: Development of a calibration apparatus and wind tunnel testing

Master thesis realized with the aim of obtaining the degree of Master in Aerospace Engineering

François Rigo

Supervisors:
T. Andrianne
G. Dimitriadis

Jury members:
V. Denoël
A. Philippart

University of Liège
Faculty of Applied Sciences

Academic year 2016 - 2017

To the optimist, the glass is half full. To the pessimist, the glass is half empty. To the engineer, the glass is twice as big as it needs to be.

Anonymous

Unsteady pressure measurement around aerodynamic bodies: Development of a calibration apparatus and wind tunnel testing

François Rigo

Supervisors: T. Andrianne, G. Dimitriadis
Master in Aerospace Engineering, University of Liège
Academic year 2016-2017

Abstract

Separated flows are complex but interesting to study because they are variable and unsteady. They are present for every bluff bodies and stalled streamlined bodies (at high angle of attack). Experimental aerodynamics is able to study these types of flow, using pressure sensors. Due to sensor size, pressure tubes are used to connect the pressure scanner to the tap (where the pressure is effectively measured). Statically, nothing is changed, but when an unsteady flow is studied, the signal measured by the sensor is perturbed by the tube. The Transfer Function of the tube has to be computed, to correct for the pressure measure using an inverse Fourier Transform and to obtain the pressure effectively present at the tap. The correction is made on the fluctuation amplitudes (around the mean) and the phase of the signal. The synchronization is important when vortex shedding is studied. This Transfer Function is computed by comparing the pressure measured at the begin and at the end of the tube. For that purpose, pressure with a frequency content has been applied on the tube entry (periodic for KTH calibrator and aperiodic for ULg calibrator). The ratio between these pressures gave the desired correction, showing resonance peaks for some frequencies. When a simple tube is used, theoretical models from fluid equations give very similar results to experimental ones. A parallel with electricity has also been made, replacing the pressure tube by an RLC circuit or a transmission line. The longer and the narrower the tube, the higher the signal distortion.

3D printed models are nowadays commonly used in experimental aerodynamics, allowing not only to build complex shaped models easily, but also pressure taps directly on the model and pressure channels into the structure. These more complex measurement systems have also to be experimentally calibrated. Indeed, diameter restriction on tap or shrinks in tube channels highly distorts the signal. We used this calibration to correct the pressure on a stalled wind turbine wing (at high incidence). The stall is linked to viscous effects, the flow becoming separated and turbulent. The fluctuations and phase of pressure taps signal have been studied to understand the Reynolds effect on a stalled wind turbine wing. Experiments were compared with CFD and theoretical models to validate the results.

Another application of unsteady pressure that we have studied the vortex shedding process, occurring around bluff bodies (in particular for rectangular cylinders). The synchronization and amplitude fluctuations of these vortices have been corrected using the dynamic calibration device. Fluid-structure interaction (vortex induced vibration) has then been studied: when vortices were ejected at the resonance frequency of the cylinder, the structure entered auto-excitation and vibrated a lot. When the cylinders were closely spaced in the flow (assembled into a grid), they interfered with each other and the vortex shedding process was changed compared to a single cylinder. To understand deeply this grid, theoretical and numerical models have been used (FEM and CFD) in parallel with experimental sensors: accelerometers (for vibration), pressure sensors connected on taps by tubes, Cobra Probe (velocity in the wake of cylinders), Hot Wire (free stream velocity). The study of this process in function of the incidence and the cylinder spacing allowed us to predict airspeed that induces instability. This is crucial in order to find parameters that minimize vibrations occurring on a real grid, with undesirable noise. In conclusion, this work can be used to take into account unsteady effects when pressure is measured around streamlined and bluff bodies.

Unsteady pressure measurement around aerodynamic bodies: Development of a calibration apparatus and wind tunnel testing

François Rigo

Promoteurs: T. Andrianne, G. Dimitriadis
Master en ingénieur civil en aérospatiale, à finalité approfondie, Université de Liège
Année académique 2016-2017

Résumé

Les écoulements décrochés sont complexes mais intéressants à étudier car variables (instationnaires). Ils sont présents pour tous les corps non profilés. Les corps profilés sont aussi sujet à ce décrochage à grand angle d'attaque. L'aérodynamique expérimentale permet d'étudier ces types d'écoulement avec des capteurs de pression. L'encombrement dû à la taille de ces capteurs rend difficile la mesure directe à la surface des modèles. Des tubes de pression sont donc utilisés pour connecter le capeur (loin du modèle pour ne pas perturber l'écoulement) à l'endroit où la pression veut être connue. Cela ne pose pas de problème pour la mesure de quantité moyenne (ou statique). Lorsque l'écoulement est instationnaire, le signal mesuré par le capteur est perturbé par le tube. La fonction de transfert du tube doit donc être calculée, pour corriger la pression à l'aide d'une transformée de Fourrier inverse et obtenir la pression effectivement présente sur le modèle. La correction est réalisée sur l'amplitude des fluctuations (autour de la moyenne) et la phase du signal, très important lorque la synchronisation est étudiée (éjection de vortex). Cette fonction de transfert est calculée en comparant la pression mesurée au début et à la fin du tube. Une pression avec du contenu fréquentiel est donc apliquée au tube (périodique pour le calibrateur de KTH et apériodique pour celui de l'ULg). Le rapport entre ces pressions donne la correction à appiquer, charactérisée par des pics de résonance à certaines fréquences. Lorsqu'un simple tube est utilisé, les modèles théoriques basés sur les équations des fluides donnent les mêmes résultats que l'expérience. Un parallèle peut même être fait entre un tube de pression, un circuit RLC et une ligne de transmission. Plus le tube est long et fin, plus le signal est déformé.

Les modèles imprimés en 3D sont de plus en plus utilisés en aérodynamique expérimentale, de manière à imprimer directement des cannaux de pression, des formes plus complexes. La forme de ces cannaux étant plus complexe, une calibration experimentale est nécessaire. En effet, une restriction de diamètre à la prise de pression ou dans le coude d'un cannal pertube beaucoup le signal. Nous avons utilisé cette calibration est très utile pour corriger la pression sur une pale d'éolienne décrochée (à grande incidence). Le décrochage est lié aux effets visqueux et à la séparation de l'écoulement. L'effet Reynolds peut être étudié à l'aide des fluctuations de pression, charactéristique de la turbulence. L'expérience est comparée avec des modèles CFD et théoriques pour en valider les résultats.

L'éjection de vortex, autour de corps peu profilés (cylindre rectangulaire par exemple) constitue un autre exemple de pression instationnaire que nous avons étudié. La calibration a été utilisée pour corriger les fluctuations et la phase du signal de pression. L'interaction fluide-structure a pu alors être étudiée: lorsque les tourbillons ont été éjectés à la fréquence propre de la structure, le cylindre s'est auto excité et a beaucoup vibré. Lorsque des cylindres ont été placés proche les un des autres (dans une grille), ils ont interféré les uns avec les autres et le processus était différent de celui d'un cylindre seul. Pour comprendre en détail le phénomène de grille, des modèles théoriques et numériques (FEM et CFD) ont été utilisés en parallèle avec des capteurs expérimentaux: accéléromètres (vibration), capteur de pression à la surface des cylindres, sonde Cobra (vitesse dans le sillage), fil chaud (vitesse incidente). L'étude de ce processus en fonction de l'incidence et de l'espacement a permis de prédire la vitesse qui produisait l'instabilité. Ceci fut crucial pour trouver les paramètres qui minimisent les vibrations apparaissant sur la grille réelle (produisant un bruit indésirable). En conclusion, ce travail peut être utilisé pour tenir compte et étudier les effets instationnaires, lorsque la pression est measurée autour de corps aérodynamiques ainsi que pour éviter les instabilités fluide-structure, pour des grilles ou des constructions du génie civil.

Acknowledgements

This thesis is the final project that ends my five-year Master in Aerospace Engineering in University of Liège (ULg). Several persons have helped me during this work.

First, I would like to express my special thanks of gratitude to my supervisors, Dr. Thomas Andrianne and Prof. Greg Dimitriadis thanks to whom I had the opportunity to work on this exciting work. Especially Dr. Thomas Andrianne has provided great support, many wise advices and interesting conversations. I would also thank him for giving me the opportunity to realize observations and experiments at Kungliga Tekniska Högskolan (KTH) in Stockholm. I would like to thank V2i company in Liège, who lent me devices highly necessary for my work.

I wish to emphasize my gratefulness to Edouard Verstraelen from ULg, for his availability, technical support and advice. Thank also to Vincent Denoël from ULg for his interesting remarks during discussions. I would also like to thank Giulio Vita from Birmingham University and Amandine Guissart from ULg. Many thanks for their precious advice and collaboration on experiments. I would like to thank Nenad Glodic and Johan Dahlqvist from KTH for their welcome, availability and support during my visit.

I am thankful to Arnaud Fabbri from Sirris and technicians of the mechanical department of ULg for their technical support and provided stuff, necessary to build my models and devices. A special thank for Jeroen van Beeck and Fabrizio Fontaneto from Von Karman Institute for their welcome and advices during my visit.

I also thank my family and friends, who supported me during this work and throughout my studies.

Finally, I express my thanks to all those who helped me during the achievement of this work, in one way or another, and who are not mentioned here, especially assistants and professors of the faculty, from also other department.

Liège, June 8^{th}, 2017

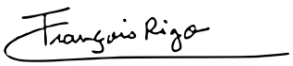

François Rigo

Contents

List of Figures

List of Tables

List of Abbreviations

(U)RANS (Unsteady) Reynolds Averaged Navier-Stokes Equations.

2D Two Dimensional.

3D Three Dimensional.

BL Boundary layer.

CFD Computational Fluid Dynamics.

DNS Direct Numerical Simulation.

FEM Finite Element Method.

FFT Fast Fourier Transform.

FRF Frequency Response Function.

IFFT Inverse Fast Fourier Transform.

LE Leading edge.

NS Navier-Stokes.

RFP Rational Function Polynomial.

RMS Root Mean Square.

TE Trailing edge.

TF Transfer Function.

TFI Turbulent Flow Instrumentation.

VIV Vortex Induced Vibration.

WT Wind Tunnel.

List of Symbols

Quantity	Unit	Description
E	[MPa]	Young Modulus
I	[m^4]	Cross Section Inertia
$\mathcal{F}_t[\cdot](f)$	[.s]	Fourier Transform (in frequency)
$(\cdot)'$	[-]	Fluctuations
B	[m]	Cylinder chord
B/D	[-]	Cylinder aspect ratio
$C_{Di}/C_D^p/C_D^v$	[-]	Drag coefficient (induced/pressure/viscous)
D	[mm] or [m]	Tube diameter (Chapters 2 and 3) or cylinder cross flow dimension (Chapter 4)
J_ν	[-]	Bessel function of the first kind of order ν
L	[m]	Tube length
N	[-]	Number of tubes, modes
Pr	[-]	Prandtl number
R_0	[J/(kg·°K)]	Gas constant
Re	[-]	Reynolds number
SG	[-]	Skop-Griffin number
Sc	[-]	Scruton number
St	[-]	Strouhal number based on D
St'	[-]	Strouhal number based on D'
T	[°C] or [°K]	Temperature
T/D	[-]	Cylinder spacing
T_s	[s]	Vortex shedding period
U_∞	[m/s]	Free stream velocity
U_r	[-]	Reduced velocity
V or Vol	[m^3]	Transducer volume
V_t	[m^3]	Tube volume
Δt	[s]	Time step
Δx	[m]	Mesh size
α, α_∞	[∘]	Angle of attack
$\gamma = C_p/C_v$	[-]	Specific heat ratio (at constant pressure/at constant volume)
γ_1	[-]	Skweness
λ	[W/(m°K)]	Thermal conductivity
μ	[kg/(m·s)]	Absolute fluid (dynamic) viscosity
ν	[m^2/s]	Kinematic fluid viscosity
$\omega = 2\pi f$	[rad/s]	Pulsation
$\overline{(\cdot)}$ or $(\cdot)_s$	[-]	Mean operator
ϕ	[rad]	Phase angle
ρ	[kg/m^3]	Density
$\rho\overline{u'v'}$	[Pa]	Reynolds stress component
σ	[-] or standard deviation	Fractional increase in transducer volume due to diaphragm deflection

Quantity	Unit	Description
τ_w	[Pa]	Wall shear stress
ε	[J/(kg·s)]	Rate of dissipation of turbulent kinetic energy
ζ, η_S	[-]	Damping ratio
a_0	[m/s]	Speed of sound
$c_d/C_D/C'_D$	[-]	Drag coefficient (2D/3D/3D at mid-span
$c_l/C_L/C'_L$	[-]	Lift coefficient (2D/3D/3D at mid-span)
c_p	[-]	Pressure coefficient
f	[Hz]	Frequency
f_c	[Hz]	Cut-off frequency
f_s	[Hz]	Free motion frequency
f_s^0	[Hz]	Free motion frequency (still fluid)
f_{samp}	[Hz]	Sampling frequency
f_{vs}	[Hz]	Vortex shedding frequency
g	[m/s^2]	Gravity constant
$j = \sqrt{-1}$	[-]	Imaginary unit
k	[-], [J] or [-]	Polytropic constant for the volumes, turbulent kinematic energy or Kurtosis
m	[kg/m]	Mass per unit length
m_r	[-]	Mass ratio
p	[Pa]	Pressure
p_∞	[Pa]	Free stream (static) pressure
q	[Pa]	Dynamic pressure
s/D	[-]	Dimensionless curvilign coordinate along cylinder contour
t	[s]	Time
u or v	[m/s]	Local velocity
u^+	[-]	Dimensionless velocity
y^+	[-]	Dimensionless distance from the wall
$\|(\cdot)\|$	[-]	Amplitude, absolute value

Chapter 1

Introduction

1.1 Motivations

Experimental Aerodynamics is one of the ways to study the flow around a body, others are analytical and numerical methods. Experiment allows to make the link between theoretical predictions and their application in real conditions. Despite the increased importance of numerical methods in the study of models and phenomena, an experimental validation is always necessary, to make the link with physical events and find new opportunities.

In aerodynamics, a lot of interesting phenomena can be studied, among those, some are difficult to predict: unsteady flows, *i.e.* when quantities (velocity, pressure) change over time. This work will focus more precisely on the description and understanding of separated flows. For a simple attached flow, a steady state is reached. However, under certain conditions, vortices, turbulence can be created. This leads to a complex flow, necessary to be studied experimentally. For example, wings at a high angle of attack show a detached flow due to viscous effects. Vortices and turbulence induce chaotic and time varying flow on the upper side (Figure 1.1).

Stall occurs for wings, *i.e.* streamlined bodies. Non profiled shapes are called "bluff bodies" and are present in a lot of civil engineering applications. They are characterized by a detached flow, with vortices ejection, called "vortex shedding". Because of sharp corners, a large front surface, the flow around cylinders (particularly rectangular) is separated. Vortices are ejected and produce an unsteady flow, at each scales (Figures 1.2 with clouds drawing the vortex shedding process).

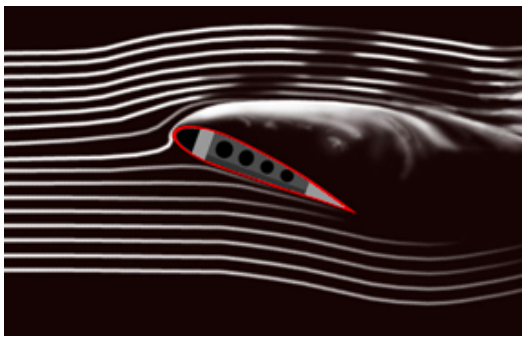

Figure 1.1 – Airflow separation of an airfoil at a high angle of attack (stall) [1]

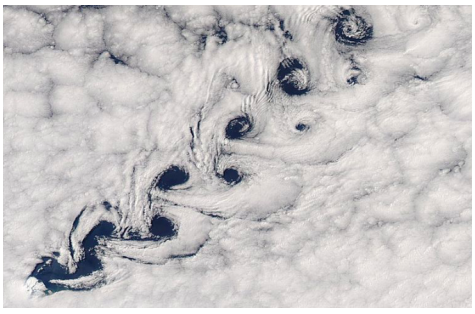

Figure 1.2 – Vortex shedding as winds pass Heard Island (bottom left) in the southern Indian Ocean resulted in this Karman vortex street in the clouds [2]

When this process interacts with the structural motion, some instability can happens. For example, the Tacoma collapsed due to a complex interaction of vortex induced vibration and galloping (fluid-structure interaction).

Figure 1.3 – Tacoma bridge collapse (1940), from Vortex Induced Vibration/Galloping combination [3]

To study such unsteady phenomena, three different approaches will be used: experiment, numerical and theoretical models. First of all, sensors are required for the experimental study. They allow the collection of data and have to be chosen according to the scope of the phenomena to be studied. Pressure is one of the quantity that gives the most information about the aerodynamics around a body. Indeed, by measuring it on several locations of the model surface, the flow can be known: where peak pressure occur, where the flow is separated, from where vortices are ejected. Global quantities (aerodynamical *pressure* forces (but not viscous ones)) can be directly deduced from the pressure by integration along the whole body surface.

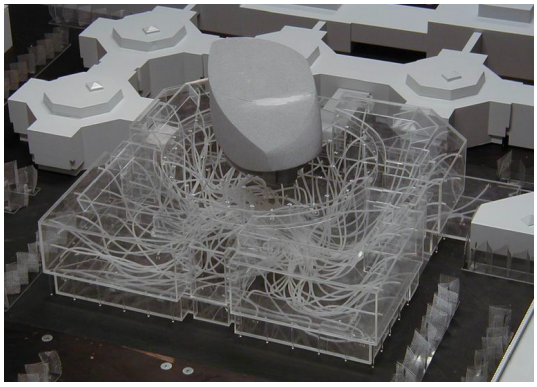

Figure 1.4 – Subscale model of buildings for pressure measurement in the test section of the wind tunnel in TU Munich [4]

With the objective to study unsteady aerodynamic loading, the objective is to characterize the time varying pressure at several (tenth or hundreds of pressure taps, as in Figure 1.4). Some pressure sensors can be miniaturized and putted on model surface, they are so called "flush-mounted transducers". The problem is their very high individual cost. When tenths or hundreds of pressure location are required, it becomes priceless and useless to use them. Larger pressure scanner can be used but pressure tube are required to connect this scanner to the pressure tap (to not perturb the flow).

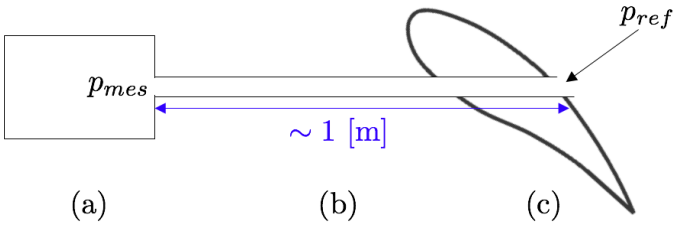

Figure 1.5 – Simple WT pressure set-up: (a) pressure scanner (outside the flow, measuring p_{mes}), (b) pressure tube, (c) model (subjected to p_{ref} at the tap))

A simple WT pressure measurement set-up is shown in Figure 1.5, using typically vinyl pressure tubes of 1 [m] (order of magnitude), the pressure scanner is a box placed next to the model (spacing constraints). Because of this tube need, the dynamic effect of the tube (measured pressure p_{mes}) must

be first measured and then removed from the measurement on the body surface. This important step corresponds to the dynamic pressure calibration (to obtain the true pressure p_{ref}). Because of taps density, a lot of pressure tubes have to be used; they can overlap, bend, fold,... (Figure 1.4). A very important question is the effect of these tubes on the measured signal. How is the signal perturbed by tubes? What are the parameters influencing this? How to correct and predict it ? All these questions will be studied in the first part of this work, the dynamic calibration.

Additionally, numerical models can be used to study unsteady flows, using CFD. This will not be the principal scope of this work but an supplementary way to understand and compare these phenomena. Analytical and theoretical models will also be used, knowing that they are valid only for particular (simpler) assumptions. For example, viscous effects at stall cannot be analytically computed.

During this work, comparison of experiment, numerical and theoretical methods will highlight conclusions on unsteady (detached) flows. More precisely, two kinds of fields linked to unsteadiness will be studied. Firstly, in Wing Engineering,Wing Turbine Wing performances during stall (at high angle of attack, Figure 1.6) will be examined. Secondly, aeroelastic properties will be investigated, for a grid composed of rectangular cylinders (Figure 1.7). Experimental study of these two applications will be done thanks to the dynamic calibration of their pressure measurement system. Theoretical context and simplifications will be introduced as well. Numerical tools (Finite Element Method (FEM) and CFD) will complete the study.

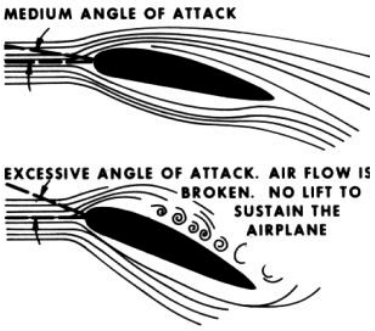

Figure 1.6 – Flow around an aircraft foil, increasing angle of attack to stall point, airflow is separated [5]

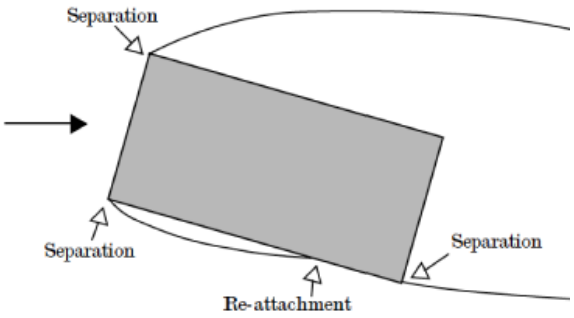

Figure 1.7 – Flow around a rectangle, separation point and separated region [66]

1.2 Structure

Chapter 2 defines and studies dynamic pressure calibration, starting with some theoretical models. A review and sate-of-the-art about calibration devices is done. Then, two types of experimental devices are used to compare and characterize the dynamic response of different pressure tubes commonly used for WT applications.

Chapter 3 uses the dynamic calibration performed in Chapter 2, for the pressure tube used in WT measurement on a Wind Turbine Wing profile at high angle of attack. Theoretical and numerical models are used to compare experimental results and understand the stall phenomenon.

Chapter 4 studies a real problematic of a grid composed of rectangular cylinders, subjected to aeroelastic phenomenon. The characterization of the structure is done, with a reproduction of the real grid in the WT. Experimental measures use the calibration of Chapter 2 to correct pressure signals around the cylinders. The theoretical context is posed and numerical models (FEM and CFD) are used to support experiments.

Finally, some conclusions on the unsteady measurement principle and the two applications will be drawn, to open some perspectives.

Chapter 2

Pressure calibration

2.1 Concept

Over the past decades, the importance of numerical methods to solve flow around bodies increased a lot. Use of Computational Fluid Dynamics for steady flows is simple and the solution can be trusted rapidly. Unsteady flows, *i.e.* when the pressure varies with time, are not so obvious. They can happen for streamlined bodies at very high angle of attack, when the lift drops (called *stall*, because of a separated flow, Figure 1.6) or for bluff bodies, composed of sharp angles and non-smooth geometry (Figure 1.7). In these cases, streamlines are not smooth and steady, they vary with time because of turbulence, separated regions,... . Numerical model of such phenomena is more complex and experimental tests are required to know physically what happens. Then, numerical models can be constructed to represent the reality but experimental investigations are mandatory for such complex flows.

A simple way to know experimentally the flow around a model is to measure the pressure. Several taps are build on the model and by measuring the pressure on these locations, the flow (pressure, velocity) around the body is known. Global quantities can also be deduced from pressure (lift and pressure drag). Practically, this is not possible to place pressure sensors on taps. Indeed, because of their size and connection (electric cable), they would perturb the flow. Sometimes, there is also not enough place in the model to place these sensors. This is solved by connecting PVC tubes from taps (on model surface) to pressure sensors (outside of the model neighbor). There is a tube for each tap so a lot of tubes are often next to each other. Pressure is thus measured *at the end* at the pressure tube end, not on the pressure tap (Figure 1.5 in Chapter 1). Nevertheless, the pressure has to be known on the model surface. Intuitively, the pressure tube (more generally called the pressure measurement system) will have an influence on this value, depending on his shape, diameter, length,... . The purpose of this chapter is to quantify this influence, thanks to theoretical and experimental investigations, for given pressure tubes.

The principle of dynamic calibration is to construct the FRF of the tube (Figure 2.1). As mentioned, the tube changes the frequency response of the pressure measured by the sensor at the tube end (p_{mes}). It is possible to correct this measured signal to obtain the true pressure (p_{ref}) using the FRF ($\mathcal{F}_t^{corr}$): the ratio between FFT of measured and reference signals.

$$\mathcal{F}_t^{corr} = FRF = \frac{\mathcal{F}_t[p_{mes}(t)](f)}{\mathcal{F}_t[p_{ref}(t)](f)} \tag{2.1}$$

To reconstruct the reference signal p_{ref} from the measured one p_{mes}, the procedure is to compute the inverse FFT of the ratio between FFT of p_{mes} and Transfer Function (experimental tube correction),

$$p_{ref}(t) = \mathcal{F}_f^{-1}\left[\frac{\mathcal{F}_t[p_{mes}(t)](f)}{\mathcal{F}_t^{corr}}\right] \tag{2.2}$$

The FRF is the particular case of Transfer Function (TF) when the variable is the frequency f. It consists of a complex number, with amplitude and phase. The FRF is always decomposed in this way,

it has an influence of fluctuations amplitude around the mean and also on the phase shift of the signal.

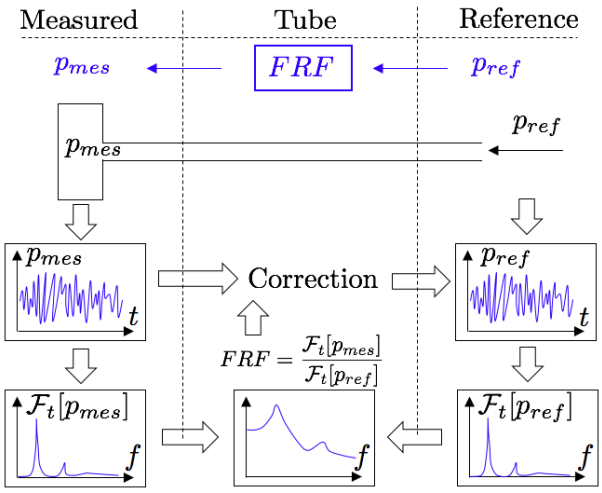

Figure 2.1 – Principle of the dynamic calibration, construction of the FRF

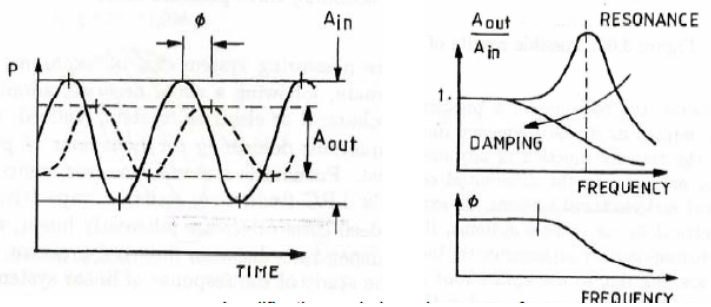

Figure 2.2 – Principle of dynamic response comparison, from time to frequency domain [25]

2.2 Theoretical models

The dynamic response of a pressure measurement system will be first studied with theoretical models, based on strong assumptions and simplifications. The physical behavior inside pressure lines will then be described and discussed to understand the phenomenon. Some firsts theoretical results will be discussed before comparing them with experimental measurements. The three modelisations are:

- One-dimensional fluid model based on Navier-Stokes (NS) equations
- RLC circuit analogy
- Impedance analogy

2.2.1 Fluid model

General solution To start efficiently the study of the dynamic response of measuring systems, a theoretical investigation is performed, taken from the work of H. Bergh and H. Tijdeman [35]. To be consistent, their results will be presented, using same notations. H. Bergh and H. Tijdeman [35] based their study in the same way as Iberall [18], which gives a complete study of the dynamic response of a single constant diameter tube and volume. They extend the work of [18] to a series of connected tubes and volumes. They consider a general series of N thin tubes separated by N volumes. This is a general representation of a pressure measuring system. The simplest one is obviously a single tube with no volume ($N = 1, L_j = L_1 = L, V_j = V_1 = 0$) but their purpose was to stay as more general as possible.

The aim of this study is to derive in an analytical way a recursion formula to link the sinusoidal pressure disturbances in the volume i with those of volumes $i-1$ and $i+1$. For each i^{th} tube/volume, a complex ratio (because of the oscillating pressure behavior) of p_i over p_{i-1} can be found. By applying this formula recursively (product), the pressure is any volume p_i can be calculated, knowing the input one p_0. These formulae involve a lot of parameters such as the length, the diameter discontinuity, etc. Only the most interesting ones will be experimentally studied. All used notations are found in the list of Symbols, and those who have a particular fixed value for this study are on Table 2.1.

Notation	Quantity	Value (if fixed)	Unit
a_0	Mean velocity of sound	$\sqrt{\frac{\gamma p_s}{\rho_s}}$	[m/s]
C_p	Specific heat at constant pressure	1005	[J/(kg°K)]
C_v	Specific heat at constant volume	718	[J/(kg°K)]
γ	Specific heat ratio	$\frac{C_p}{C_v} = 1.4$	[-]
i	Subscript referred to tube i		[-]
g	Gravity constant	9.81	[m/s^2]
j	Imaginary number	$\sqrt{-1}$	[-]
λ	Thermal conductivity	0.0257	[W/(m°K)]
μ	Absolute fluid (dynamic) viscosity	$1.846{\cdot}10^{-5}$	[kg/(m·s)]]
Pr	Prandtl number	$\frac{\mu g C_p}{\lambda} = 0.713$	[-]
R_0	gas constant	287	[J/(kg°K)]
ρ_s	Mean density	1.204	[kg/m^3]
T_s	Mean temperature	300	[° K]
V_e	Additional volume due to diaphragm flexibility	$k\sigma V$	[m^3]
V_t	Tube volume	$\pi \left(\frac{D}{2}\right)^2 L$	[m^3]

Table 2.1 – Notations and values used in the theoretical pressure response, at $T_\infty = 300$ [° K]

The fluid motion inside a circular tube can be computed using Navier-Stokes equations, *i.e.*, continuity (conservation of mass), conservation of momentum (axial and radial), conservation of energy and state equation. With sinusoidal oscillations in the fluid, it can be assumed that the total pressure, density, temperature are,

$$\bar{p} = p_s + pe^{j\omega t},\ \bar{\rho} = \rho_s + \rho e^{j\omega t},\ \bar{T} = T_s + Te^{j\omega t} \tag{2.3}$$

With $\omega = 2\pi f$. The velocities in axial and radial direction are: $\bar{u} = ue^{j\omega t}$ and $\bar{v} = ve^{j\omega t}$. The model proposed by Bergh and Tijdeman [35] is based on several assumptions[1]:

1. Small disturbances (in pressure, density, temperature and velocity) compared to mean values
2. Small internal diameter of the tube compared to its length (to neglect ends effect)
3. Laminar flow throughout the system (low Reynolds number)
4. Large thermal conductivity of the tube walls compared to the one of air so that there is no temperature variation at the wall (no conductive heat exchange between the fluid within the tube, the tube wall and the environment).
5. Pressure expansions in the tubes and volumes follow the polytropic law
6. The reduced frequency $\frac{\omega D}{a_0}$ is mush less than 1

Boundary conditions have to be chosen, to solve linearized flow equations for p, ρ, T, u and v. At the wall of the tube ($r = R = \frac{D}{2}$): impermeability, zero axial and radial velocity, *i.e.* $u = v = 0$ and thanks to (4), $\Delta T = 0$. At the center of the tube ($r = 0$): $v = 0$ due to axial symmetry of the problem and u, p, ρ, T remain finite. Tubes connection impose also boundary conditions. At the tube entrance i: pressure disturbance p_i is equal to the given pressure disturbance $p_{i-1}e^{i\omega t}$ At the tube end, where volume V_i is connected: increase of mass of the pressure transducer is equal to the mass flow difference between tube i and $i+1$. The total transducer volume i is[2] Vol_i in Figure 2.3.

[1] Iberall [18] has given 1^{st} order corrections to solve equations when assumptions 1, 2 and 6 are not verified.

[2] Valid if the diaphragm resonance frequency is much larger than the frequency f of the pressure fluctuation.

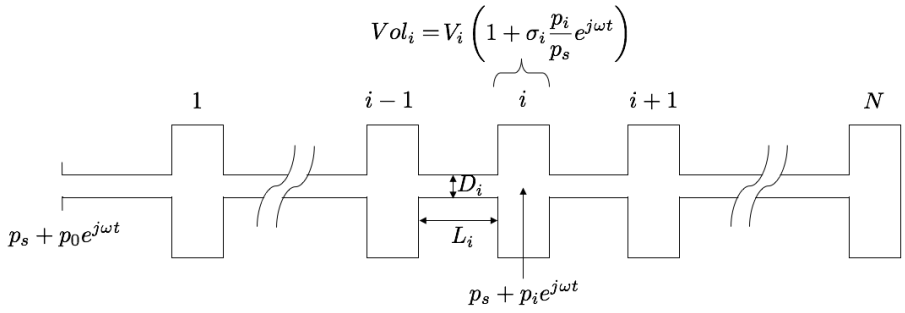

Figure 2.3 – Series connection of lubes and transducers

Assuming a reference pressure $p_{ref} = p_0 e^{i\omega t}$, the ratio of transmitted pressure is (shear wave number α_i, measuring the wall shear effects, and the polytropic factor),

$$\frac{p_{mes}}{p_{ref}} = Ae^{\phi x} + Be^{-\phi x} \text{ with } \phi_i = \frac{\omega}{a_{0_i}}\sqrt{\frac{J_0\left\langle\alpha_i\right\rangle}{J_2\left\langle\alpha_i\right\rangle}}\ ,\ \alpha_i = j^{\frac{3}{2}}\frac{D_i}{2}\sqrt{\frac{\rho_{s_i}\omega}{\mu_i}} \text{ and } n_i = \left[1+\frac{\gamma-1}{\gamma}\frac{J_0\left\langle\alpha_i\sqrt{Pr}\right\rangle}{J_2\left\langle\alpha_i\sqrt{Pr}\right\rangle}\right]^{-1} \tag{2.4}$$

Computing coefficients A and B with boundary conditions, the recursion formula is,

$$\frac{p_i}{p_{i-1}} = \left[\cosh(\phi_i L_i) + \frac{V_i}{V_{t_i}}\left(\sigma_i + \frac{1}{k_i}\right) n_i\phi_i L_i \sinh(\phi_i L_i) + \frac{V_{t_{i+1}}\phi_{i+1}L_i J_0\left\langle\alpha_i\right\rangle J_2\left\langle\alpha_{i+1}\right\rangle}{V_{t_i}\phi_i L_{i+1} J_0\left\langle\alpha_{i+1}\right\rangle J_2\left\langle\alpha_i\right\rangle}\frac{\sinh(\phi_i L_i)}{\sinh(\phi_{i+1}L_{i+1})}\right.$$
$$\left.\left\{\cosh(\phi_{i+1}L_{i+1}) - \frac{p_{i+1}}{p_i}\right\}\right]^{-1} \tag{2.5}$$

The evolution of n_i as a function of $\alpha_i\sqrt{Pr}$ is associated to asymptotic values: isothermal when $\lim_{\alpha_i\to 0} n_i = 1$ and isentropic when $\lim_{\alpha_i\to\infty} n_i = \gamma = 1.4$. The recursion formula can be applied to have the ratio of end pressure p_N (where the test transducer is placed, for N tubes) over the entry pressure p_0 (at the tap, where the reference transducer is), and noting that the 3^{rd} term in equation 2.5 disappears for $i = N$, so

$$\frac{p_N}{p_0} = \frac{p_N}{p_{N-1}}\frac{p_{N-1}}{p_{N-2}}...\frac{p_1}{p_0} \tag{2.6}$$

$$\frac{p_N}{p_{N-1}} = \left[\cosh(\phi_N L_N) + \frac{V_N}{V_{t_N}}\left(\sigma_N + \frac{1}{k_N}\right) n_i N\phi_N L_N \sinh(\phi_i N L_N)\right]^{-1} \tag{2.7}$$

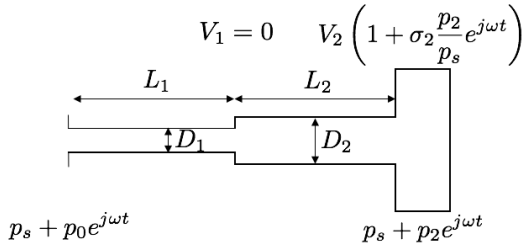

Figure 2.4 – Tube with discontinuity in tube diameter

By inspecting equation 2.5, some (geometric) parameters can be studied, with $i = 1$ (simplest case) consisting of a measurement system composed of only one tube of length L, diameter D and transducer volume V. A discontinuity in tube diameter can be studied using 2 tubes and $V_1 = 0$, a diameter discontinuity is represented, *i.e.* change of tube, discontinuity in 3D printed channel,... with the representation in Figure 2.4. Other parameters are physical, and will be studied only in theory but not experimentally (Table 2.2).

Theoretical results Using equation 2.5, the influence of geometrical and physical parameters on the dynamic response can be highlighted. The following figures will plot the amplitude and the phase of the TF in equation 2.5. The phase is shown in absolute values (from 0 to $\pi, 2\pi...$), not conventional ($-\pi$ to π). It corresponds to the ratio of FFT of pressure signals (measured p_N and reference p_0):

$$\left|\frac{\mathcal{F}_t(p_N)(f)}{\mathcal{F}_t(p_0)(f)}\right| \text{ and } \phi\left(\frac{\mathcal{F}_t(p_N)(f)}{\mathcal{F}_t(p_0)(f)}\right) \tag{2.8}$$

Physical		Geometrical	
Quantity	Value	Quantity	Value
Fluid	air	L	1 [m]
Tube	PVC	D	2 [mm]
k	1.4 [-]	V	300 [mm^3]
T_s	300 [°K]	σ	0 [-]
p_s	10^5 [Pa]	N	1 (one tube)

Table 2.2 – Parameters used in theoretical results

In Figures 2.7 to 2.12, all parameters (except the one studied in the figure, with various values in legend) are fixed to values in Table 2.2. Lengthening the tube decreases the resonance peak, at a smaller resonance frequency. This is easily understandable by comparing with the simple organ pipe theory: standing sound waves are responsible for the tones from organs (Figure 2.5). The air inside the tube travels at the speed of sound a_0 and vibrates at certain *odd* harmonics. If a sinusoidal pressure is given at the inlet $p_0 \sin(\omega t)$, the pressure measured at the outlet will be $p_1 \sin(\omega t)$ with

$$p_1 = p_0 \sec\left(\frac{\pi}{2}\frac{\omega}{\omega_0}\right) \to \pm\infty \text{ when } \frac{\omega}{\omega_0} \to 1, 3... \text{ or } \omega \to \frac{a_0}{4L}, 3\frac{a_0}{4L} \tag{2.9}$$

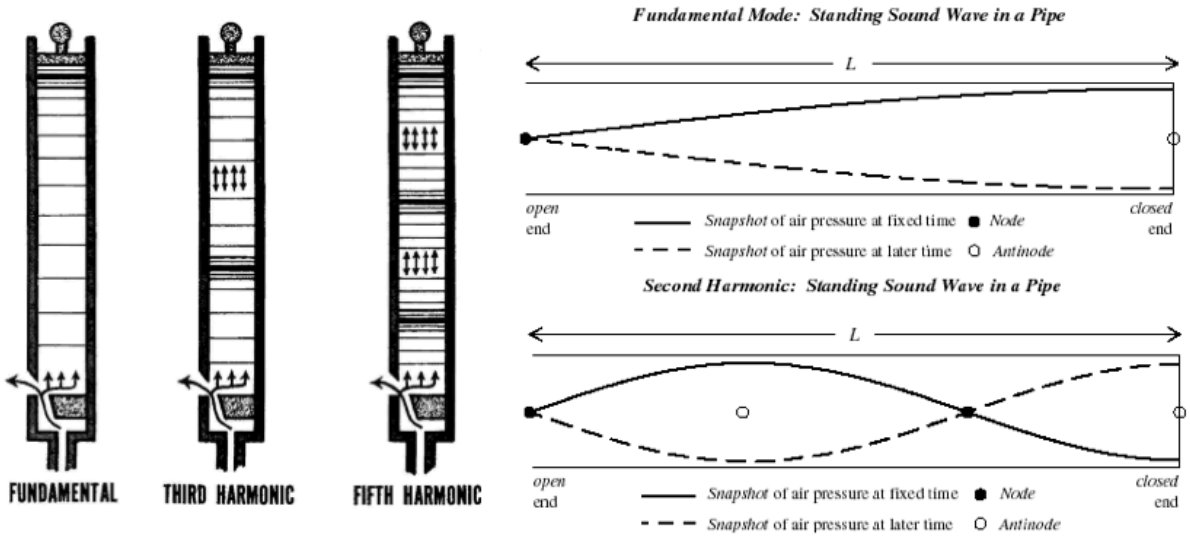

Figure 2.5 – Simple organ pipe theory: real view of waves and standing waves [6]

Increasing the length decreases the resonance frequency, which corresponds theoretically to infinite amplitude (Figure 2.6 right, peaks at $\omega/\omega_0 = 1, 3, ...$ and steps at $\phi = 0, \pi, ...$). This distortion is undesirable and "safety" zone can be drawn between $0.95 < |p_1/p_0| < 1.05$. For $a_0 = 340$ [m/s] in the region of interest $f \in [0, 100]$ [Hz], this requires a length $L < 0.17$ [m]. Nevertheless, this is too small for experimental applications, often requiring $L = 0.5 - 1$ [m] for practical reasons. This theory is however too simple because of strong assumptions: no viscosity, no conductivity, no volume. In reality, the transducer is composed of a small cavity, which damps the resonance pressure peaks. In Figure 2.6, results from [35] show an attenuation of pressure and phase shift (distortion of the signal between

p_1 and p_0) when L increases, because of viscous and conductive effects. For long and thin tubes, these effects eliminate completely the peaks and the pressure signal is attenuated for all frequencies ($L = 1$ [m], $D = 0.5$ [mm] in Figure 2.7). By adimensionalizing the frequency ω/ω_0, all peaks are aligned, close to 1,3,... but not exactly because of viscous and conductive effects (even more when L increases, also visible for the phase, with a lower slope when L increases). Figure 2.7 shows that the narrower the tube, the more attenuated the amplitude and the higher the phase lag. A wider tube perturbs less the fluctuations. Increasing the length or decreasing the diameter has thus a similar effect. Thus, for a same tube volume ($V_{tube} = \pi(D/2)^2 L$), the response will be totally different if a long and narrow tube ($L >>, D <<$) is used instead of a short and wide one ($L <<, D >>$), with different L and D producing the same V_{tube}. Figure 2.8 shows that the higher the transducer volume, the higher the attenuation and the phase lag (more dissipation inside the volume).

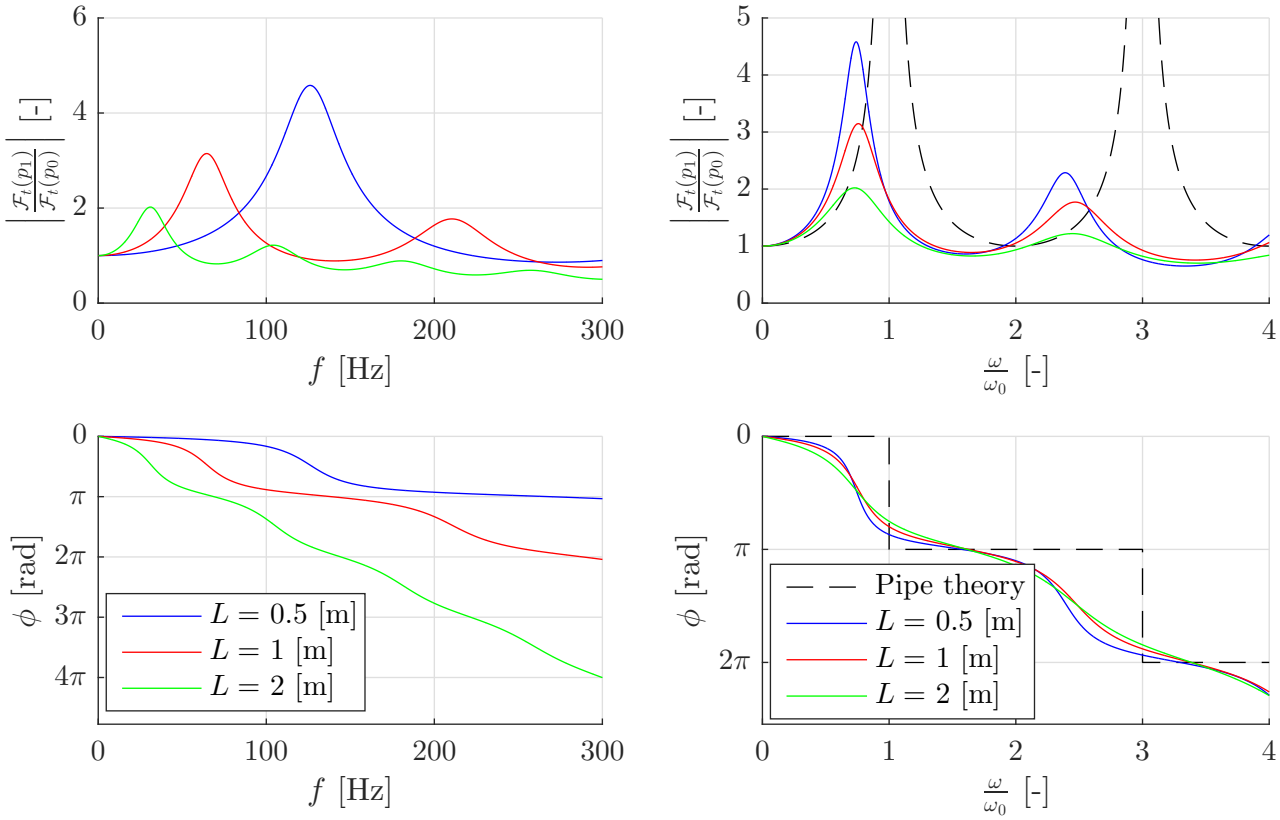

Figure 2.6 – Influence of L on the dynamic response as a function of frequency f [Hz] and adimensional frequency $\frac{\omega}{\omega_0}$ [-], comparison with simple organ pipe theory

Figure 2.9 shows the two extreme cases for polytropic constant k, which gives almost no influence of the dynamic response. The additional volume due to transducer diaphragm deflection σ has only a small influence on the response (Figure 2.10). The product $\left(\sigma + \frac{1}{k}\right)$ has to be huge to see an influence. Even for $\sigma = 1 = 100\%$ (so a doubled volume), the response is not so much affected. Figure 2.11 shows that the higher the mean pressure p_s, the higher the peak amplitude and the lower the phase lag, in a strong way. However, relative pressure in a wind tunnel measurement is expected to be very low compared to atmospheric pressure ($p_0 = 10^5$ [Pa]). Indeed, sensors used in experimental setup work only in a range of pressures just above the atmospheric pressure (with an overpressure of several [kPa] for Kulite©XCQ060 in KTH and Endevco©8515 flush-mounted transducer in ULg, see sections 2.3.3 and 2.3.4). The absolute pressure will thus be only slightly higher than 10^5 [Pa] and the first peak will not vary so much. Indeed, the range $f \in [0, 200]$ [Hz] is of interest for pressure measurement applications (vortex shedding, separated flow,...). The temperature has a negligible effect on the dynamic response: it changes the values of physical parameters μ, λ, c_p but the amplitude and the phase do not change so much. Because a_0 is a function of T, adimensional resonance frequencies ω/ω_0 are the same (Figure 2.12). A value of T very high or low can change more the response but because of the expected range for pressure measurement conditions, this will not happen.

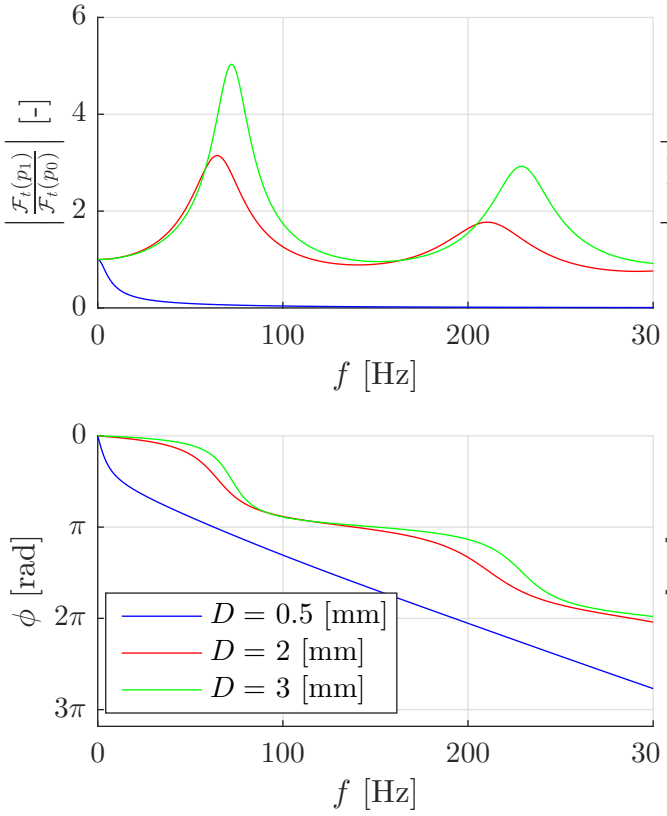

Figure 2.7 – Influence of D on the dynamic response

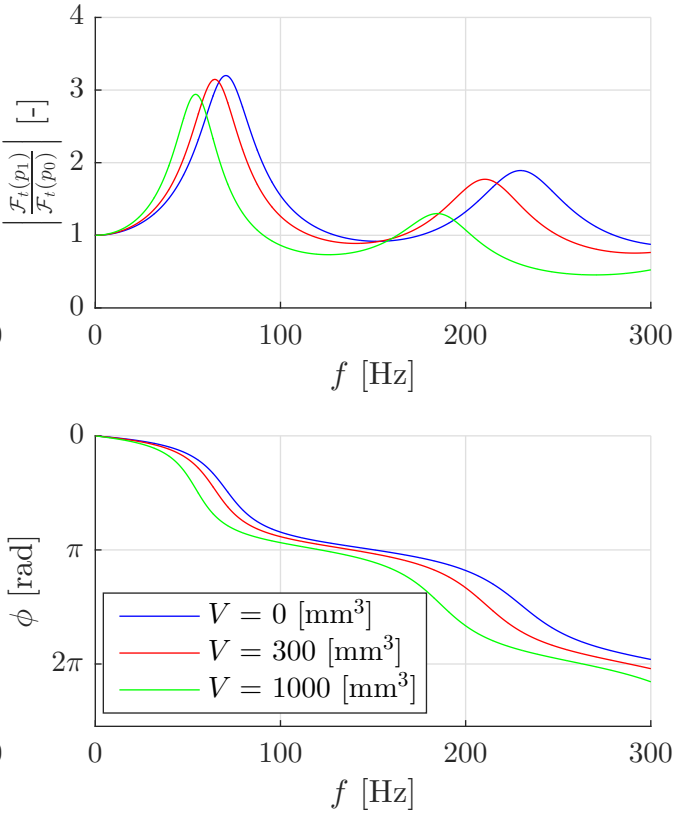

Figure 2.8 – Influence of V on the dynamic response

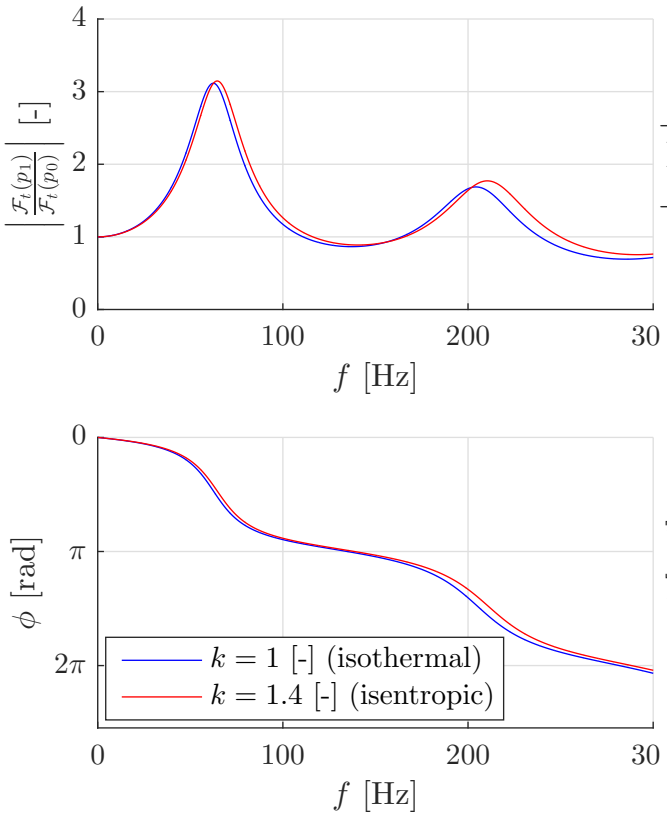

Figure 2.9 – Influence of k on the dynamic response

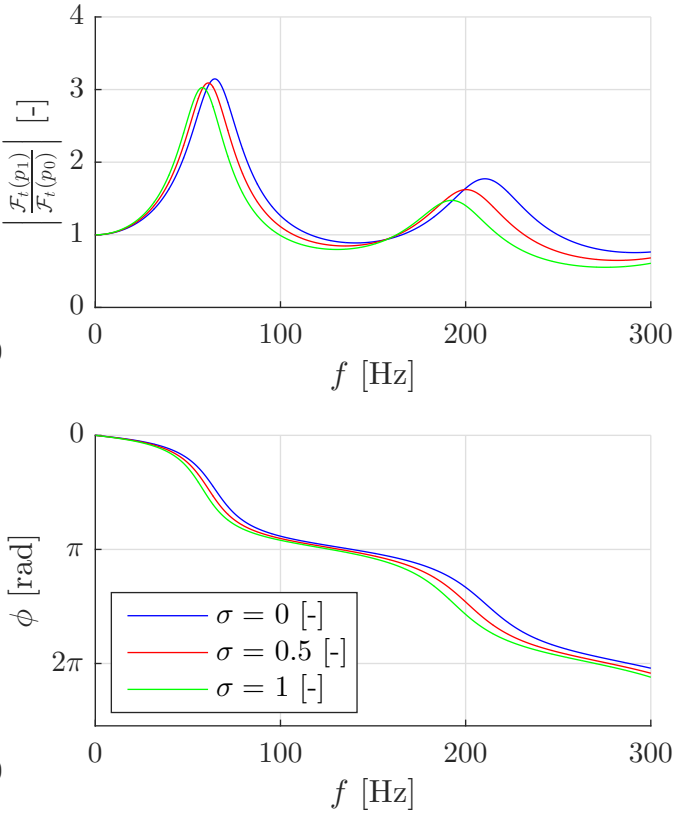

Figure 2.10 – Influence of σ on the dynamic response

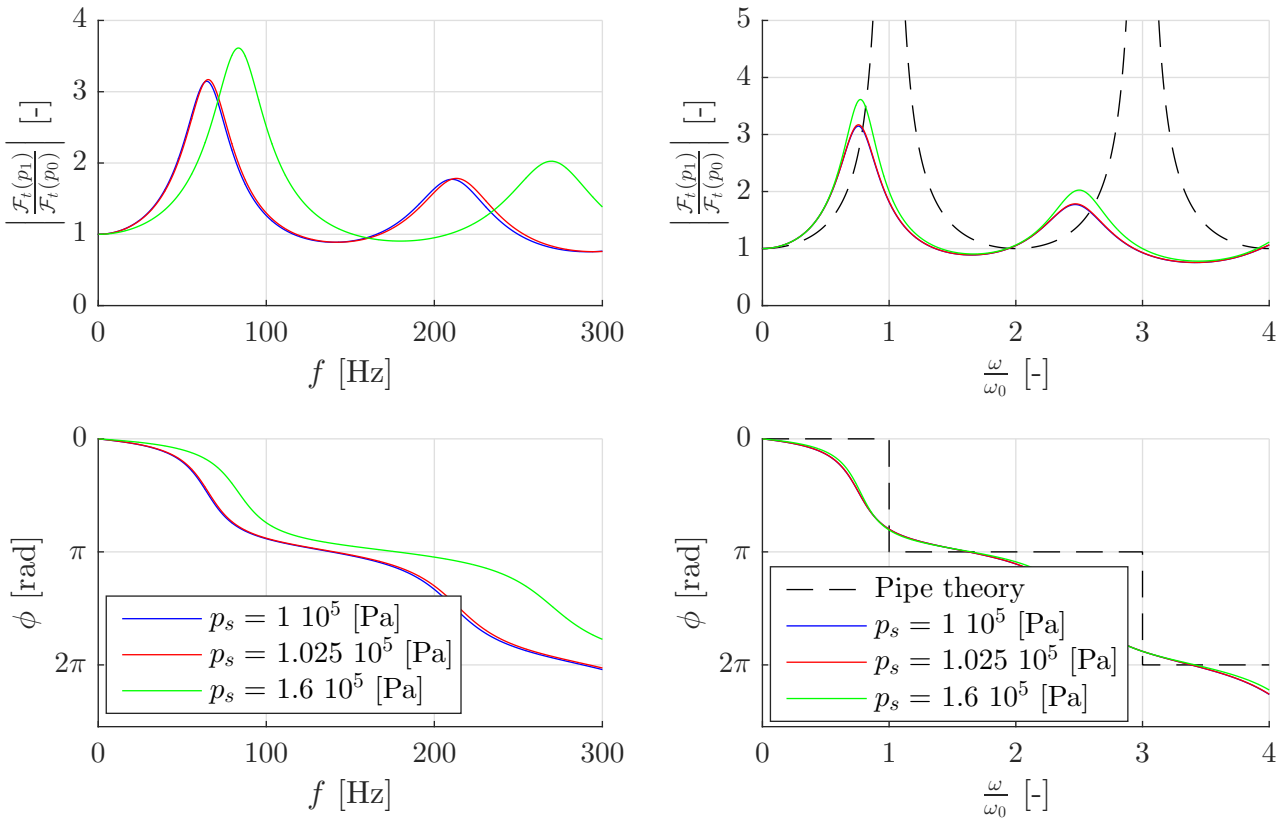

Figure 2.11 – Influence of p_s on the dynamic response as a function of frequency f [Hz] and adimensional frequency $\frac{\omega}{\omega_0}$ [-], comparison with simple organ pipe theory

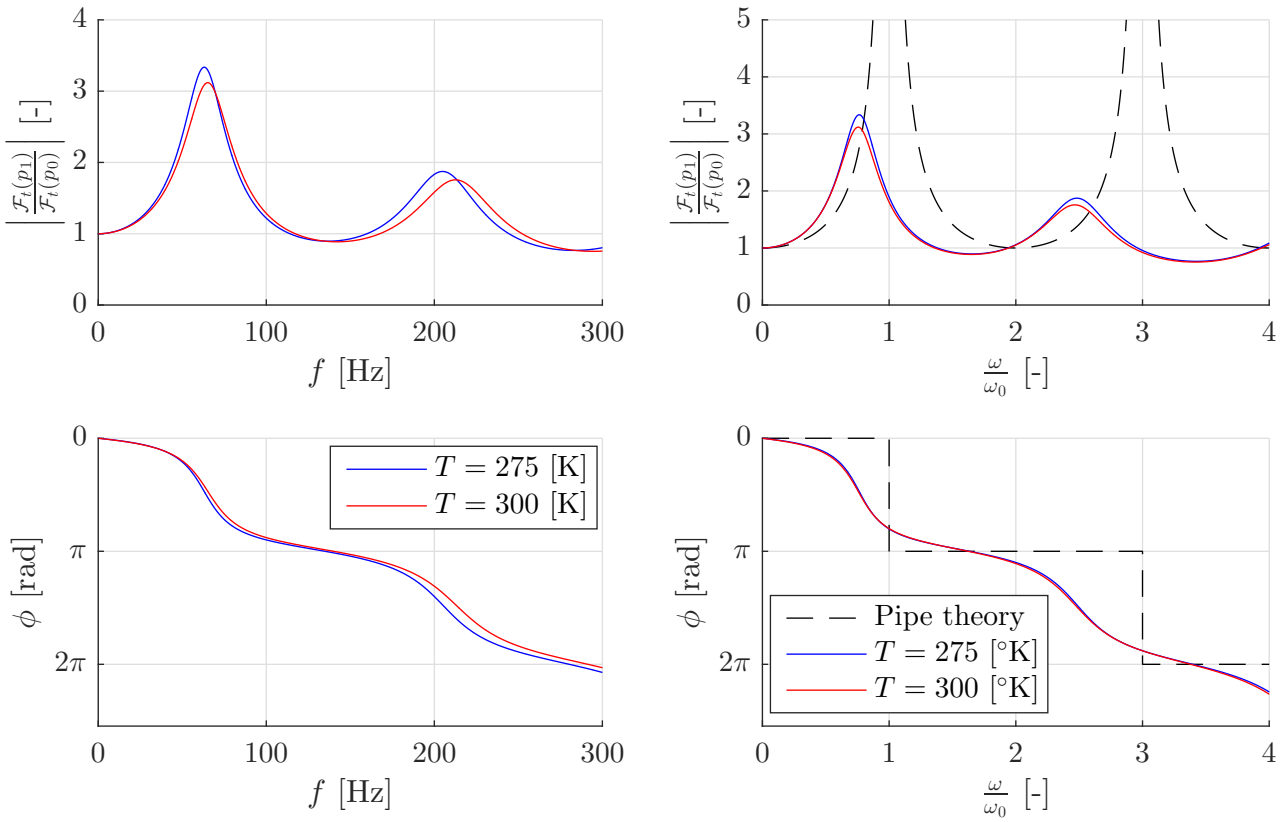

Figure 2.12 – Influence of T on the dynamic response as a function of frequency f [Hz] and adimensional frequency $\frac{\omega}{\omega_0}$ [-], comparison with simple organ pipe theory

Figures 2.13 and 2.14 show the influence of D_1 and L_1 on the dynamic response. This is the case of Figure 2.4 with 2 tubes. The second one has fixed characteristics (same as previous Figures: $L_2 = 1$ [m], $D_2 = 2$ [mm],...). Tube 1 also, except the parameter discussed in Figures above. Note that to represent the diameter discontinuity, $V_1 = 0$. Figure 2.13 shows 3 configurations: tube of constant diameter $D = 2$ [mm], smaller tube followed by a wider one and wider tube followed by a smaller one. For a wider first tube, the amplitude is higher than for a constant and smaller one. The phase lag around the first peak ($f \in [0, 100[$ Hz]) is lower for a wider tube. The friction is lower in the first tube. There is thus less attenuation so an amplification compared to a higher volume. Therefore, the combination of both gives an amplification (a smaller first tube gives higher friction so attenuation). The shape of the response for a wider first tube shows a superposition of the 2 first peaks, linked to some pressure fluctuation reflection because of the restriction of the tube. Figure 2.14 shows that the length of the first (smaller, $D_1 = 1.5 < D_2$) tube has an influence on the dynamic response. This length has however to be comparable to L_2, if L_1 is a few [cm], the response is almost the same as if there was no discontinuity. This is good to know for further applications: a diameter restriction along a small tube length does not distort the signal in a strong way.

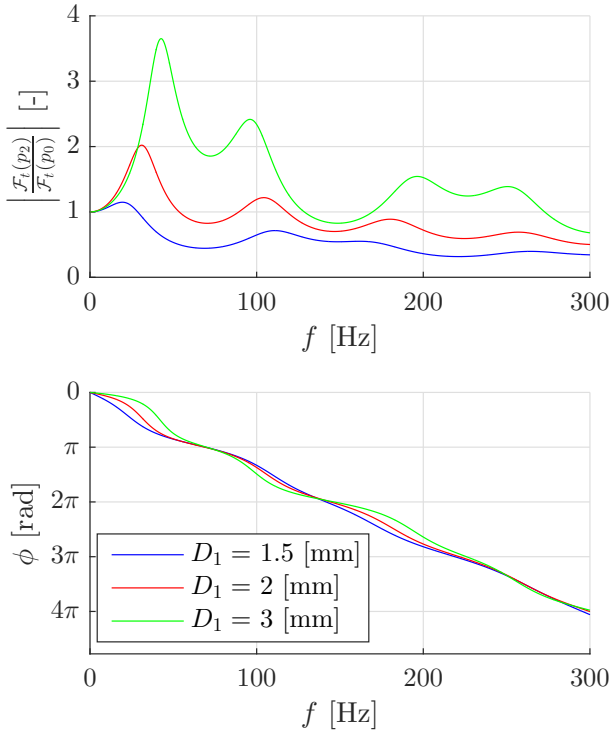

Figure 2.13 – Influence of D_1 on the dynamic response, $D_2 = 2$ [mm], $L_1 = L_2 = 1$ [m]

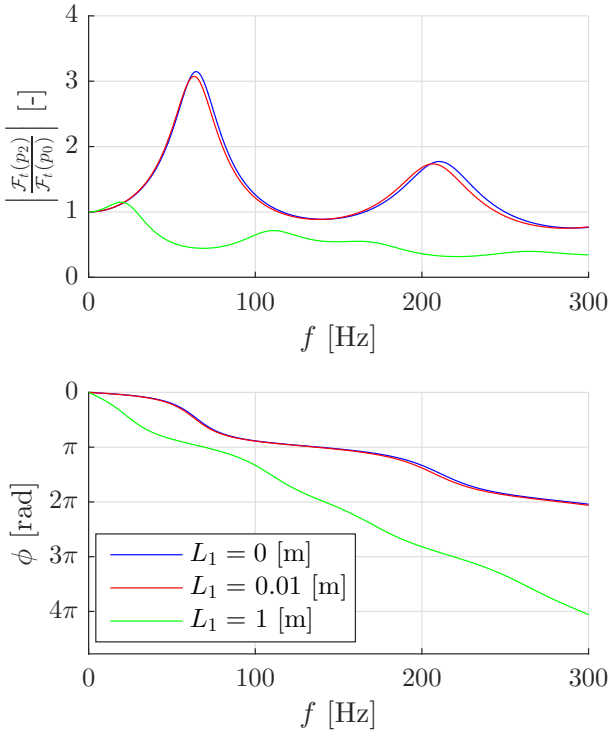

Figure 2.14 – Influence of L_1 on the dynamic response, $D_1 = 1.5$, $D_2 = 2$ [mm], $L_2 = 1$ [m]

From Figures 2.15 to 2.18, interesting things happen. It can be interpreted that a second wider tube does not have always a favorable effect (*i.e.* some combinations of $D_{1,2}$ and $L_{1,2}$ leads to amplification (Figures 2.15 and 2.18) *or* attenuation (Figures 2.16 and 2.17). On the opposite, a smaller second tube does not have always an unfavorable effect (*i.e.* it does not amplify always the response in a strong way, for some $L_{1,2}$ the amplitude is closer to 1 for a smaller second tube (Figures 2.15 and 2.18)). This can be explained by 2 phenomena with opposite effects. For a wider second tube, there is less friction so less attenuation. Nevertheless, the higher diameter leads to a higher volume, thus dissipating more the signal (as shown in Figure 2.8). Depending on the relative importance of friction and additional volume, the response can be higher or lower. The same phenomenon in the reversed way can be explained for a smaller second tube. A constant behavior is observed for the phase lag. A wider second tube has always a lower phase lag (fewer reflections because of no restriction). Finally, combinations of $D_{1,2}$ and $L_{1,2}$ can be chosen in order to obtain a desired dynamic response, linked with a certain purpose or application. Nevertheless, discontinuities in the tube that are neglected in the theoretical assumptions can lead to non-linear effects, only visible with experimental tests.

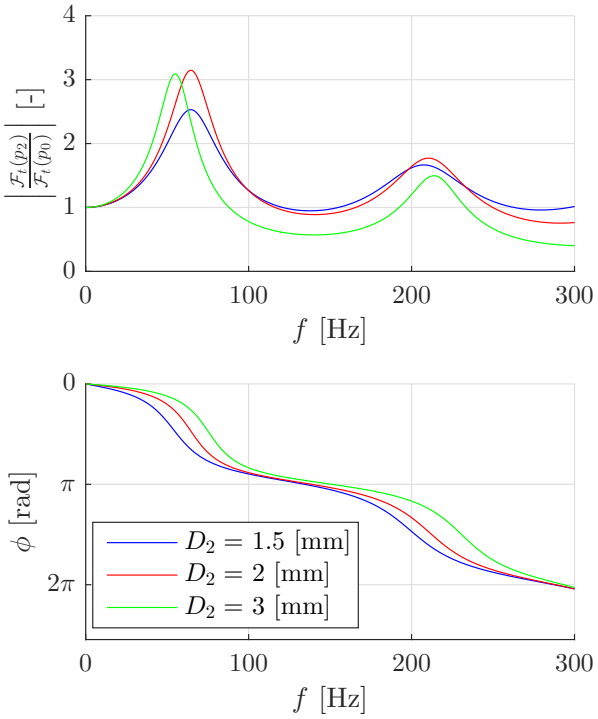

Figure 2.15 – Influence of D_2 on the response, with $D_1 = 2$ [mm], $L_1 = L_2 = 0.5$ [m]

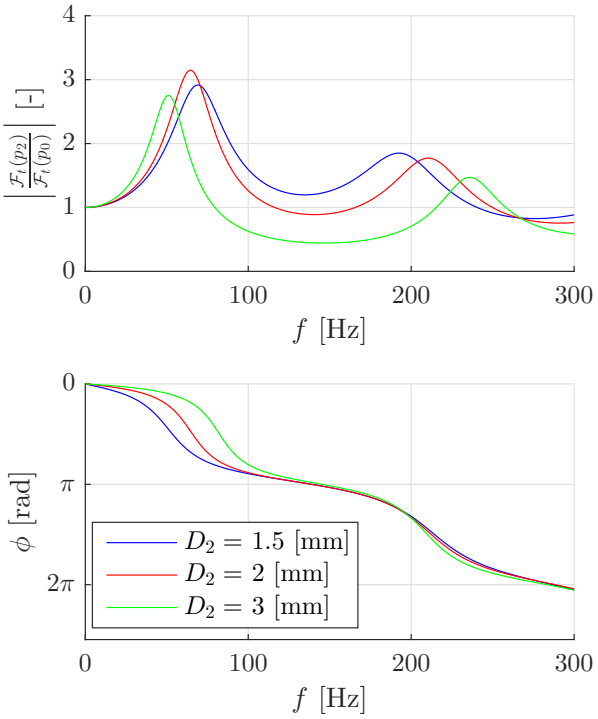

Figure 2.16 – Influence of L_2 on the response, with $D_1 = 2$ [mm], $L_1 = 0.4$ and $L_2 = 0.6$ [m]

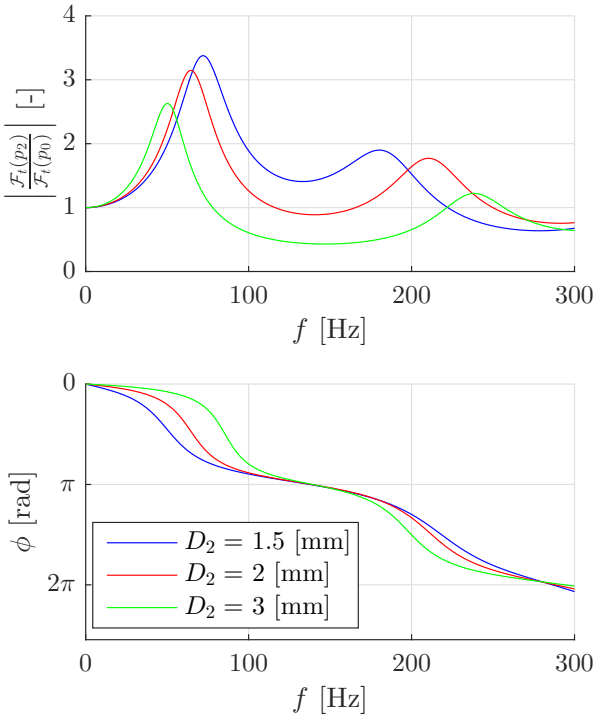

Figure 2.17 – Influence of D_2 on the response, with $D_1 = 2$ [mm], $L_1 = 0.6$ and $L_2 = 0.4$ [m]

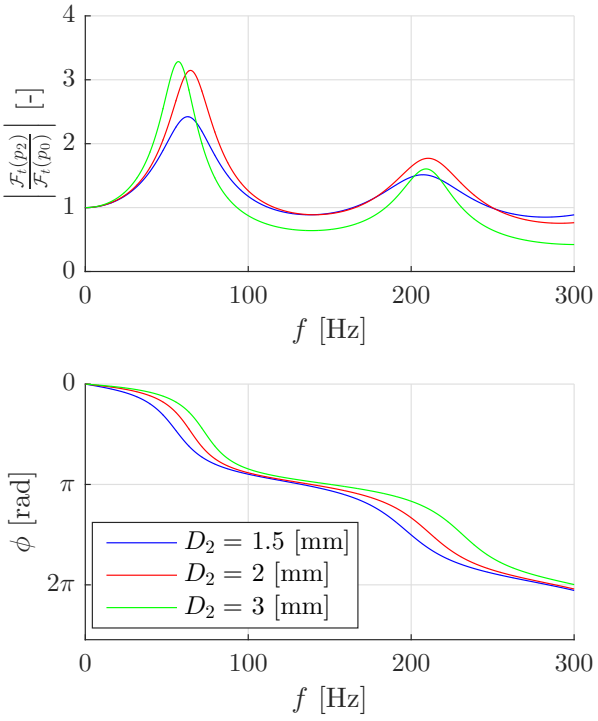

Figure 2.18 – Influence of D_2 on the response, with $D_1 = 2$ [mm], $L_1 = 0.2$ and $L_2 = 0.8$ [m]

Moreover, the dynamic response can be adjusted by a certain combination of D and L with multiple tubes. A good idea could be to choose parameters that give a response very close to an amplitude ratio of 1. By this way, the pressure line will in fact not distort the reference signal (at least in a given range of frequencies). So using a pressure tube to measure the signal at the end will give the same value as the reference one. The restrictor is a small piece added to decrease the diameter of the tube over a certain length. It can be modelled using the theory with $N = 3$ tubes, in Figure 2.19.

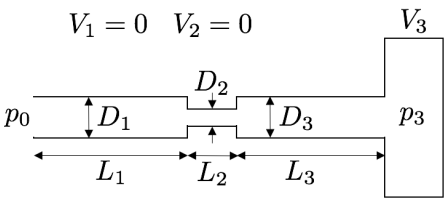

Figure 2.19 – Model of a restrictor inside the pressure line, $N = 3$

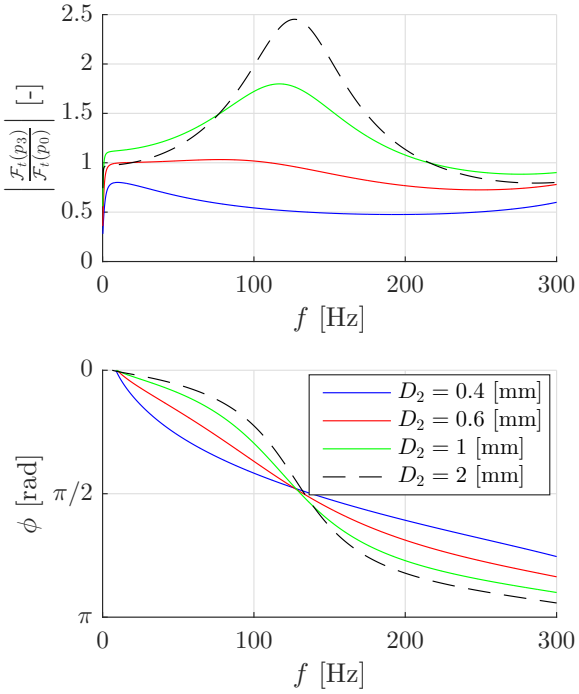

Figure 2.20 – Influence of a restrictor D_2 on the dynamic response $D_1 = D_3 = 2$ [mm], $L_2 = 0.01, L_1 = L_3 = 0.25$ [m]

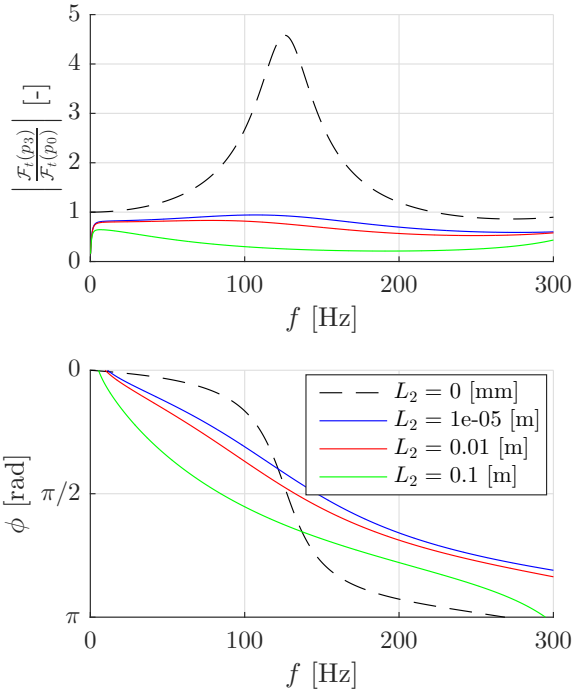

Figure 2.21 – Influence of a restrictor L_2 on the dynamic response $D_2 = 0.6, D_1 = D_3 = 2$ [mm], $L_1 = L_3 = 0.25$ [m]

Figure 2.20 shows the influence of the restrictor diameter on the response, with $D_1 = D_3 = 2$ [mm], $L_2 = 0.01, L_1 = L_3 = 0.25$ [m] so exactly if a pressure tube of total length $L = 0.51$ [m] was restricted at its middle length with a diameter D_2. The restrictor is characterized by D_2. For $D_2 = 0.4$ [mm]: excess restrictor, too high attenuation. For $D_2 = 1$ [mm]: insufficient restrictor, too low attenuation. For $D_2 = 2$ [mm]: no restrictor. For $D_2 = 0.6$ [mm]: optimum restrictor, amplitude ratio close to 1 in the range $f \in [0, 150]$ [Hz], satisfactory for applications of interest. No correction of the signal in *amplitude* at [0,100] [Hz]. Nevertheless, attention must pe paid for the phase lag. Even if the amplitude is the same, there is a phase lag (with a constant slope compared to frequency). The measured signal is thus delayed compared to the reference one. This will obviously have an influence when the purpose of an analysis is the synchronization study in vortex shedding process for example. This demonstrates that dynamic calibration is always necessary, even with a restrictor. Physically, this phase lag is easily understandable because the air has to "travel" the pressure line, at the speed of sound, so there is a small delay between the two measured pressure: $\Delta t = \frac{L}{a_0} = \frac{0.5}{340} = 1.47$ [ms]. The general expression of the signal is proportional to $\sin(\omega t + \phi) = \sin(\omega(t + \Delta t))$, thus proportional to the frequency $\phi = \omega \Delta t = 2\pi f \Delta t$. Thus, $\phi = \frac{\pi}{2}$ when $f \approx 150$ [Hz][3]. Figure 2.21 shows the same case as Figure 2.20 but with a varying L_2 and a fixed $D_2 = 0.6$ [mm]. The simple fact to add a restrictor decreases a lot the amplitude and there is no more peak. The length of this restrictor must be low to not attenuate too much the signal. There is only a slight difference in response comparing $L_2 = 10^{-5}$ and 0.02 [m]. This is always possible to control the response by carefully choosing the tubes geometry.

[3]Very close to the value in Figure 2.20 below when $D_2 = 0.6$ [mm]. Note that this analysis is based on a very simple case, assuming the signal as a sine and neglecting non-linear effects

2.2.2 RLC circuit analogy

Pressure measurement systems are mostly composed of a pressure tube of constant diameter and section connected to a pressure transducer by a volume cavity (Figure 2.22).

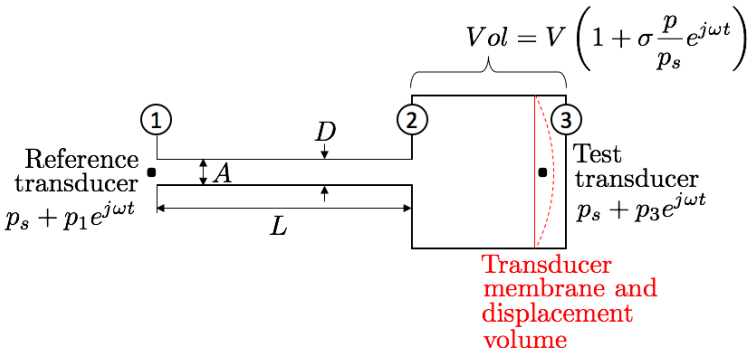

Figure 2.22 – Pressure measurement model: tube connected to cavity

Delio [31] described this lumped parameter model thanks to a second order differential equation and he proposed a model based on the RLC circuit analogy. By neglecting he pressure drop due to friction, he obtained,

$$\frac{\rho_s L}{A} \frac{Vol}{p_s} \frac{d^2 p_3}{dt^2} + \frac{32\mu L}{D^2 A} \frac{Vol}{\gamma p_s} \frac{dp_3}{dt} + p_3 = p_1 \tag{2.10}$$

With subscripts referring to locations in Figure 2.22. The derivation of equation 2.10 is done by Delio [31] and Kurtulus [25], summarized in Appendix A.1. Clearly, this equation is of the same form as an RLC (series) circuit, where the output voltage is across the capacitor (Figure 2.23). As done by Taback [39], an analogy can thus be made between fluid and electricity. Applying Kirchoff's law and constitutive equations,

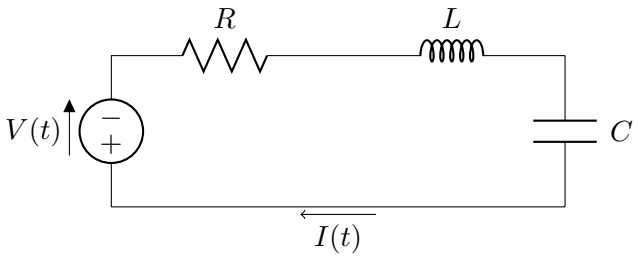

Figure 2.23 – Simple RLC series circuit

Fluid	Equivalence	Electricity
$L_{geom}\frac{d^2U}{dt^2} + (k_1 + k_2 U)\frac{dU}{dt} + \frac{A}{\rho C}U = 0$	$\Leftrightarrow$	$L\frac{d^2I(t)}{dt^2} + R\frac{dI(t)}{dt} + \frac{I(t)}{C} = \frac{dV(t)}{dt}$
$Q = UA$	$\Leftrightarrow$	$I(t)$
p	$\Leftrightarrow$	$V(t)$
Pressure drop (Poiseuille)	Resistor	Ohm's law for an electrical resistance
$\Delta p = 32\frac{\mu L_{geom}}{D^2}U = 32\frac{\mu L_{geom}}{AD^2}Q$	$R = 32\frac{\mu L_{geom}}{AD^2}$	$V(t) = RI(t)$
Dynamic balance of flow	Inductance	Voltage across and inductance
$\Delta p = \frac{force}{A} = \frac{\rho L_{geom} A}{A}\frac{dU}{dt} = \frac{\rho L_{geom}}{A}\frac{dQ}{dt}$	$L = \frac{\rho L_{geom}}{A}$	$V = L\frac{dI(t)}{dt}$
	Capacitor	
$p_3 = \frac{1}{\frac{Vol}{np_s}}\int Q dt$	$C = \frac{Vol}{np_s}$	$V(t) = \frac{1}{C}\int I(t)dt$

Table 2.3 – Anaolgy flui-electricity for line-cavity flow

$$RI(t) + L\frac{dI(t)}{dt} + \frac{1}{C}\int_{-\infty}^{t} I(\tau)d\tau = V(t) \tag{2.11}$$

Deriving and multiplying by C and making the analogy between fluid and electricity leads to Table 2.3 (according to Delio [31]). The resistor represent viscous pressure losses, the inductance the inertia of the fluid and the capacitor the behavior of the transducer volume. As $C = \frac{Vol}{np_s}$ it depends not only on the transducer volume but also on the pressure p_s and so on the dynamic response (as seen in Tijdeman results [35]).This simple (1D) system has 2 characteristics, natural frequency ω_0 and damping ratio ζ. For an RLC circuit,

$$\omega_0 = \sqrt{\frac{1}{LC}} \text{ and } \zeta = \frac{R}{2L\omega_0} \tag{2.12}$$

The Transfer Function associated with this system in frequency domain $\omega = 2\pi f$ (Laplace domain with $s = j\omega$) is

$$F(f) = \frac{\mathcal{F}_t[p_3(t))](f)}{\mathcal{F}_t[p_0(t)](f)} = \frac{1}{-\frac{\omega^2}{\omega_0^2} + \frac{2j\zeta\omega}{\omega_0} + 1} \tag{2.13}$$

These results state for one tube with one volume. To model a series of tubes (and discontinuity in diameter), RLC analogy can also be used but by assembling circuits, in Figure 2.24 (each R and L characterizes the tube length and diameter, each C the volume). The circuit in Figure 2.24 is represented by 6 first-order differential equations solved using an ordinary differential equation (numerical).

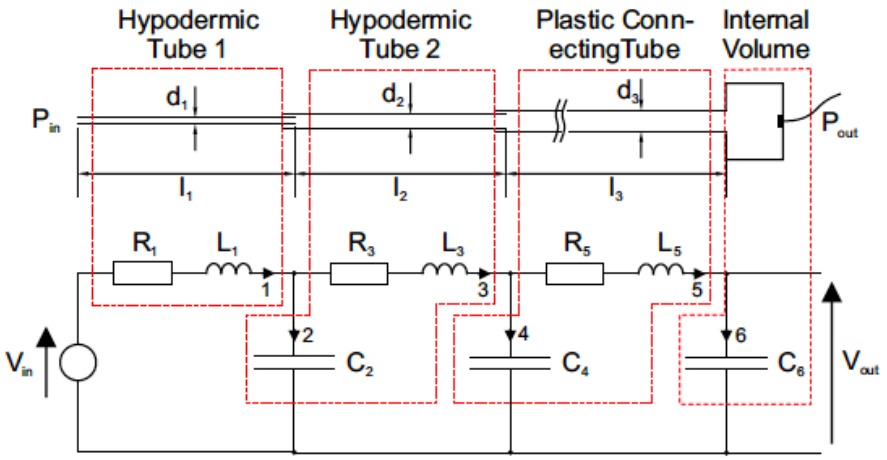

Figure 2.24 – Series of 3 tubes an analogous RLC circuit [53]

More generally, a series of N tubes can be modeled using a system $2N$ first order differential equations (equation 2.14). The transducer pressure p_N is related to the output voltage $V_{out} = \frac{q_{2N}}{C_{2N}}$.

$$\begin{bmatrix} \frac{d\phi_1}{dt} \\ \frac{d\phi_3}{dt} \\ \vdots \\ \frac{d\phi_{2n-1}}{dt} \\ \frac{dq_2}{dt} \\ \frac{dq_4}{dt} \\ \vdots \\ \frac{dq_{2n}}{dt} \end{bmatrix} = B \begin{bmatrix} \frac{\phi_1}{L_1} \\ \frac{\phi_3}{L_3} \\ \vdots \\ \frac{\phi_{2n-1}}{L_{2n-1}} \\ \frac{q_2}{C_2} \\ \frac{q_4}{C_4} \\ \vdots \\ \frac{q_{2n}}{C_{2n}} \end{bmatrix} + \begin{bmatrix} V_{in} \\ 0 \\ \vdots \\ 0 \\ 0 \\ 0 \\ \vdots \\ 0 \end{bmatrix} \quad \text{with} \quad B = \begin{bmatrix} \begin{bmatrix} R_1 & 0 & \dots & 0 \\ 0 & R_3 & \dots & 0 \\ \vdots & \vdots & \ddots & \vdots \\ 0 & 0 & \dots & R_{2n-1} \end{bmatrix} \begin{bmatrix} -1 & 0 & \dots & 0 \\ 1 & -1 & \dots & 0 \\ \vdots & \ddots & \ddots & \vdots \\ 0 & \dots & 1 & -1 \end{bmatrix} \\ \begin{bmatrix} 1 & -1 & \dots & 0 \\ 0 & 1 & \ddots & 0 \\ \vdots & \vdots & \ddots & -1 \\ 0 & 0 & \dots & 1 \end{bmatrix} \begin{bmatrix} 0 & 0 & \dots & 0 \\ 0 & 0 & \dots & 0 \\ \vdots & \vdots & \ddots & \vdots \\ 0 & 0 & \dots & 0 \end{bmatrix} \end{bmatrix} \tag{2.14}$$

2.2.3 Impedance analogy

Taback [39] used a similar analogy (same equivalent R, L, C values as the RLC analogy by using the general equations for a transmission line (real schematic in Figure 2.25). Air in a pressure line has inertia, viscous properties, elasticity so energy is dissipated during the motion: it can thus be described by a wave propagation just as in transmission lines. As seen during the bachelor course of "Electromagnetisme" [20], electromagnetic incoming wave travels a transmission line and is reflected by a load. Figure 2.25 is very similar to a line-cavity pressure measurement system, so the analogy is consistent. This line can be modelled using an equivalent circuit in Figure 2.26, with the impedance of the line Z and the load Y.

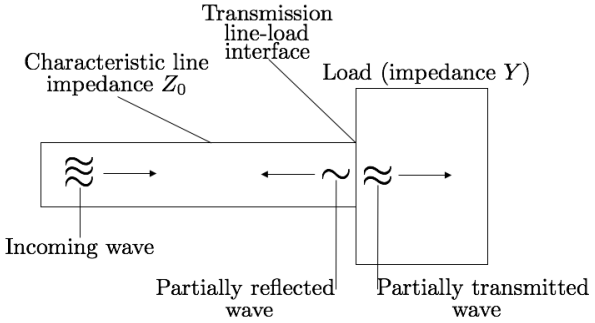

Figure 2.25 – Transmission line schematic with load and reflections [7]

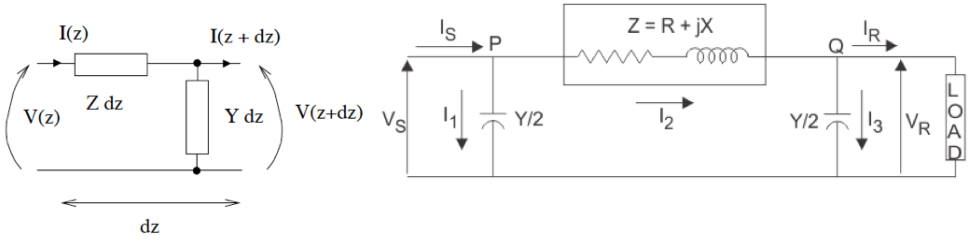

Figure 2.26 – Transmission line circuit [20]

Using "telegraphist's equations", Taback constructed the model of such a system, with equivalent R, L and C on Table 2.3.

$$V_S = V_r \cosh(\sqrt{ZY}L) + I_r Z_0 \sinh(\sqrt{ZY}L) \tag{2.15}$$

$$I_S = I_r \cosh(\sqrt{ZY}L) + \frac{V_r}{Z_0} \sinh(\sqrt{ZY}L) \tag{2.16}$$

With impedances Z, Y and characteristic line impedance Z_0,

$$Z = r + j\omega L \text{ and } Y = j\omega C \text{ so } \sqrt{ZY} = \alpha + j\beta \text{ and } Z_0 = \sqrt{\frac{Z}{Y}} = \frac{\sqrt{ZY}}{Y} = \frac{\alpha + j\beta}{Y} \tag{2.17}$$

Where α is an attenuation constant determined by the decrement in pressure amplitude per length of tube and $\beta = \frac{2\pi f}{a_0}$ is a propagation constant or phase-angle change per unit length of tube (with propagation velocity a_0). Equation 2.15 can be written as,

$$\frac{V_S}{V_r} = \sqrt{\sinh^2(\alpha L) + \cosh^2(\beta L)} e^{\arctan(\tan(\beta L)\tanh(\alpha L))} + \frac{Z_0}{Z_r} \sqrt{\sinh^2(\alpha L) + \sinh^2(\beta L)} e^{\arctan\left(\frac{\tan(\beta L)}{\tanh(\alpha L)}\right)} \tag{2.18}$$

Which defines the ratio of the voltage (or pressure) at the open end of the tube to the one at the cavity. The inverse of this ratio is the dynamic system response, with simple case,

- Pressure systems having transducer volume: $Z_r = \frac{1}{j\omega C_r}$ with $C_r = \frac{Vol}{np_s}$ as in RLC analogy and $Z_0 = \frac{(\alpha L + j\beta L)np_{av}}{j\omega V_t}$, with tube volume $V_t = \pi(D/2)^2 L$. The system response in term of pressure (measured P_S the mean pressure p_s in [35] is written p_{av}) and reference P_r)

$$\frac{P_r}{P_S} = \left[\sqrt{\sinh^2(\alpha L) + \cosh^2(\beta L)} e^{\arctan(\tan(\beta L)\tanh(\alpha L))} + \frac{Vol}{V_t} \sqrt{(\alpha L)^2 + (\beta L)^2} \sqrt{\sinh^2(\alpha L) + \sinh^2(\beta L)} e^{\arctan\left(\frac{\tan(\beta L)}{\tanh(\alpha L)}\right) + \arctan\left(\frac{\beta}{\alpha}\right)} \right]^{-1} \tag{2.19}$$

- System having an inlet restriction (diameter discontinuity): assuming a negligible volume now, $I_r \to 0$. A short restriction (compared to the wave length) can be modelled by an inertance (caused by the mass of air in the restriction)

$$Z_d = \frac{L_{restriction}}{\pi \left(\frac{D_{restriction}}{2}\right)^2} \left(\frac{8\mu}{\left(\frac{D_{restriction}}{2}\right)^2} + \frac{4}{3} j\omega\rho \right) \tag{2.20}$$

  Causing pressure loss $V_S - V'_S = I_S Z_d$ where V_S is the applied pressure and V'_S is the pressure applied to the tube past the restriction. So that,

$$\frac{P_r}{P_S} = \left[\left(1 + \frac{Z_d}{Z_0} \tanh(\alpha L + j\omega L) \right) \sqrt{\sinh^2(\alpha L) + \cosh^2(\beta L)} e^{\arctan(\tan(\beta L)\tanh(\alpha L))} \right]^{-1} \tag{2.21}$$

Figures 2.27 and 2.28 shows influence of D on dynamic response for RLC and impedance analogy models. Other parameters are fixed (same as for Tijdeman study: $L = 1$ [m], $V = 300$ [mm^3],...). The RLC circuit is characterized by one resonance and one damping, typical for a Bode diagram (Figure 2.27). All frequencies are amplified near the peak and attenuated after, typical for a 1D circuit in one direction. In fact, it does not allow to represent reflections that happen in reality in the tubes and lead to several resonance peaks instead of one. Such reflections can be represented with the impedance (transmission line) analogy and so the multiple peaks (Figure 2.28). Moreover, transmission line and Navier-Stokes equation show that decreasing the tube diameter D decreases the resonance frequency (more friction). Nevertheless, resonance frequency of Bode diagram (for RLC circuit) depends only on L and C, which are independent to D, so peaks in Figure 2.27 are aligned. Except for these differences (inherent to model assumptions), the shape of the response, the magnitude and the influence of D for both analogies are consistent with Tijdeman [35].

The RLC analogy uses directly the same parameters as Navier-Stokes (Tijdeman) so $D, V, ...$ to compute equivalent resistor, capacitor,... . Nevertheless, impedance analogy introduce new parameters,

$$\beta = \frac{2\pi f}{a_0} \tag{2.22}$$

With a_0 the propagation speed, fixed at the speed of sound 340 [m/s] for results. There is still one parameter α, the attenuation constant. Its value has been calculated experimentally for sound pressure amplitudes. Nevertheless, for large pressure amplitudes, it is more difficult to predict its value (because the flow is no more a laminar steady state). Binder [55] shows a semi-empirical equation indicating the variation of α as:

a) Directly as $\sqrt{f}$
b) Inversely with D
c) Inversely as $\sqrt{\rho_s}$
d) Directly as $\sqrt{\nu_{eff}}$ (effective viscosity[4]).

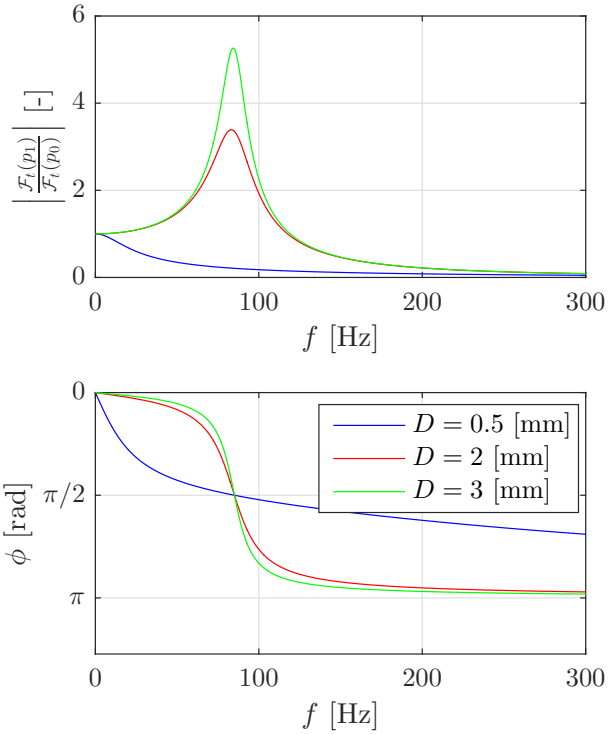

Figure 2.27 – Influence of D on the dynamic response, RLC analogy

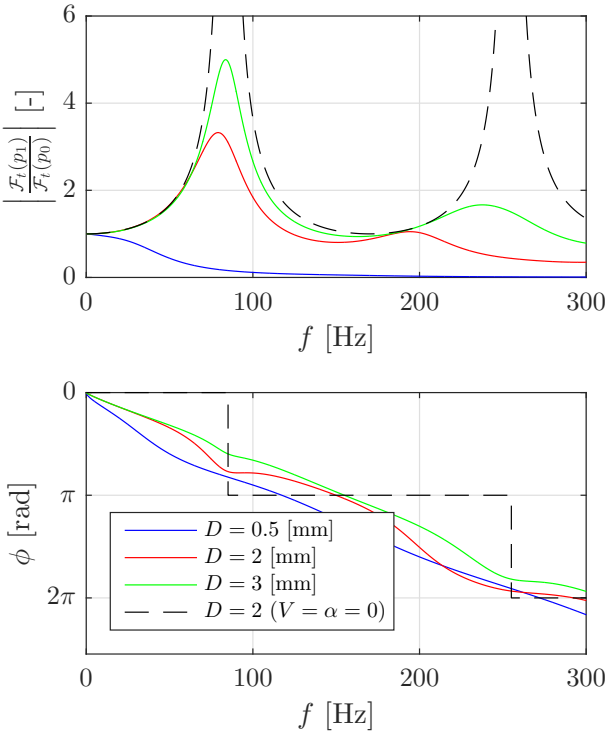

Figure 2.28 – Influence of D on the dynamic response, impedance analogy

Definitions (a) and (b) are easy to use experimentally, (c) and (d) are difficult to use in practice (lack of equipment to generate large pressure at different mean density). The common definition of the attenuation constant is thus,

$$\alpha = A\sqrt{f} \tag{2.23}$$

With A the attenuation factor. α cannot be determined automatically and experiments are necessary to compute it. This can be done for example using simple tubes (no restriction and negligible instrument volume, with only parameters L and D) to compute α and use it for more complicated systems. For example, Taback [39] used this method to compute attenuation factor A depending on the tube diameter and length (Figure 2.29). This parameter is thus a limitation of the impedance analogy, but A can be adjusted to match experiments.

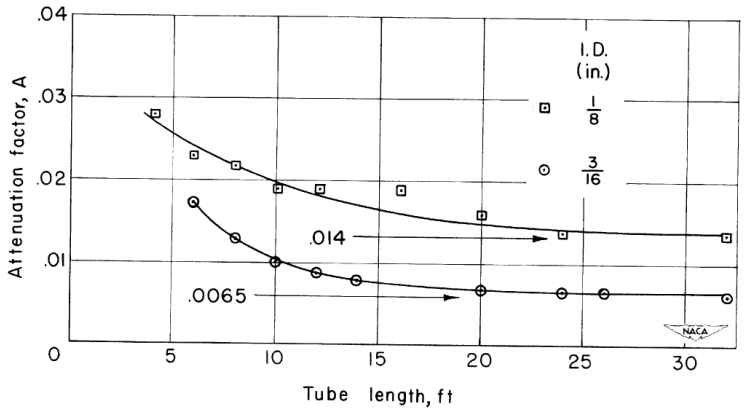

Figure 2.29 – Attenuation factor A as a function of tube diameter and length for a sinusoidal pressure amplitudes of ±10 [in] of water [39]

[4]It depends on the Reynolds number Re of the flow in the tube, dependent upon pressure amplitude and frequency

Hopefully, α does not have a strong influence, if the instrument volume V is not negligible. Indeed, the case $V = \alpha = 0$ in Figure 2.28 shows infinite amplitude at resonance and phase in sharp steps (undamped cases). Note that the other cases of Figure 2.28 are computed with $\alpha = 0$ but $V = 300$ [mm^3] . The volume and α attenuate the signal. In the comparison between theory and results, factor A will be adjusted to match well the wanted response. In conclusion, α control attenuation (so amplitude) and β the peak location (through a_0, as in Tijdeman, $\omega = a_0/4L$).

2.3 Experimental investigation

After a theoretical study of the dynamic pressure calibration phenomenon, an experimental study has been performed, to compare it afterwards with theoretical modelisation. After a small review of calibration techniques, the set-ups used and tested in KTH (Stockholm) and ULg (Liège) will be presented, and the recorded data will be compared and discussed.

2.3.1 Review

The term *calibration* refers to techniques that give a comparison between the output of a (pressure) measurement system and a reference pressure. The traceability is important for calibration, in order to re-use standards already defined and to be consistent when people talk together and exchange data. By this way, measurements done by different companies, at different times, can be compared. This is not obvious. On the one hand, dynamic calibration is still under experiment and no standard already exists, only France has developed dynamic pressure standards [40]. These standards are base on shock tubes and fast-opening devices. On the other hand, static calibration already exists. Nevertheless, as they correspond to different phenomena, there is a need of dynamic calibration traceability. To start this review, it is thus important to make a difference between *static* and *dynamic* calibration. The pressure sensors come already statically calibrated (like a balance) but this is not the purpose of this work.

As mentioned, not so much work has been done on dynamic calibration. Standards exist only for acoustic and sound pressure but people usually use the same static standards to start their own dynamic calibration and combine static calibration with dynamic checking of measurement chain transfer function. Dynamic effects involve unsteady and time-varying phenomena, the pressure changes in amplitude, by 2 ways:

- Periodic excitation (sine, combination of sine,...)
- Aperiodic excitation (impulse, step,...)

They have both advantages and drawbacks depending on their use: a dynamic calibration based on periodic excitation will be preferred if the transducer or scanner is used for periodic phenomena measurements, and conversely. Note that generating high amplitude static pressure is easy to do and control, but dynamically, the amplitude is less controllable.

As mentioned, the calibration consists in comparing the reference pressure measured at the tap by a reference transducer with the pressure measured at the end of the measurement chain (Figure 2.30). The reference transducer measures thus the pressure delivered by the pressure generator (periodic or aperiodic). Characteristics of transducers have to be well-known

- Sampling frequency f_{samp}
- Cut-off frequency[5]
- Same type of fluid (constant physical properties)

[5]Indeed, conventions [62] state that the maximum frequency of the pressure generator cannot exceed 1/5 of the natural frequency of the reference transducer

The advantage of aperiodic excitation is the wide range of frequencies covered in one time. Different kinds of periodic and aperiodic experimental setup will be presented hereafter.

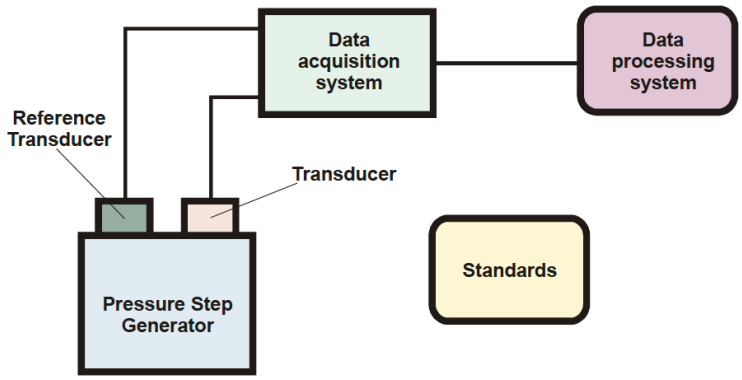

Figure 2.30 – Dynamic pressure calibration principle [59]

1. **Periodic excitation**: the pressure generator delivers a periodic pressure signal (harmonic, sinusoidal,...). To calibrate a transducer under test, knowing a reference transducer, it is important to locate them very close to each other, less than $1/10$ of the wavelength $\lambda = a/f$ with a the speed of sound and f the frequency [62]. To construct a graph showing the amplitude of the ratio between reference and tested transducer pressure as a function of the frequency necessitates to make measurement for each desired frequencies (because only one frequency is selected at each measurement test).

   (a) Acoustic shock generator: used to calibrate microphone and low-pressure scanner. Pressure pulses close to a sawtooth shape by using a piston, bursting an inflated paper bag, in a cyclic way (Figure 2.31)

   (b) Siren: also used for microphone and low-frequency calibration based on variable mass. At the inlet of a cylindrical chamber (under pressure), a rotating cylinder with equally spaced holes makes the pressure varying as a half-wave or a sine under particular fluid properties, frequencies,... (Figure 2.32).

   (c) Rotating valve: it uses a similar principle but with pressure directly injected inside a rotating valve to deliver a square wave pressure signal (Figure 2.33).

   (d) Loudspeaker: used for pressure up to 2000 [Pa] with frequencies between 280 and 3700 [Hz] (Figure 2.34). A loudspeaker of the same diameter as the tube is placed at one end. The other end consists of a piston, giving the desired standing wave. This set-up is noisy, and not adapted for low frequencies (the low speaker will be too big because its size is inversely proportional to the desired frequency).

   (e) Shaker-based inertial loading systems: it delivers a sinusoidal pressure signal with amplitudes up to 70 [kPa] and a maximum frequency of 100 [Hz]. A tube is filled with a liquid and is excited by an electrodynamic shaker (Figure 2.35).

   (f) Shaker-based direct force loading systems: it uses a shaker to vibrate a load cell. The complexity of contact area (actuator-sensor) modelisation makes this method not used in practice (Figure 2.36).

   (g) Pistonphone: it consists in a piston-in-cylinder steady-state generator. This is the simplest way to produce a sinusoidal pressure signal inside the cylinder. The piston could be driven by a shaker and it leads to signal at a given amplitude and frequency (Figure 2.37).

   Periodic generators have some drawbacks, such as the need of a reference transducer each time and a limitation in amplitude and frequency. This motivates the use of *aperiodic* generators.

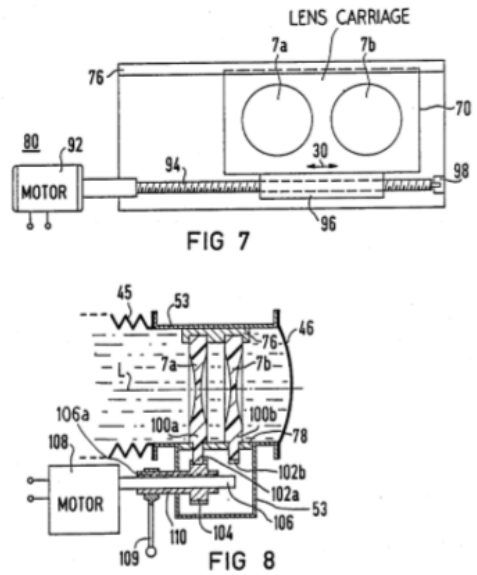

Figure 2.31 – Schematic of an acoustic shock generator, with motor giving a cyclic motion to a piston bursting a paper bag [37]

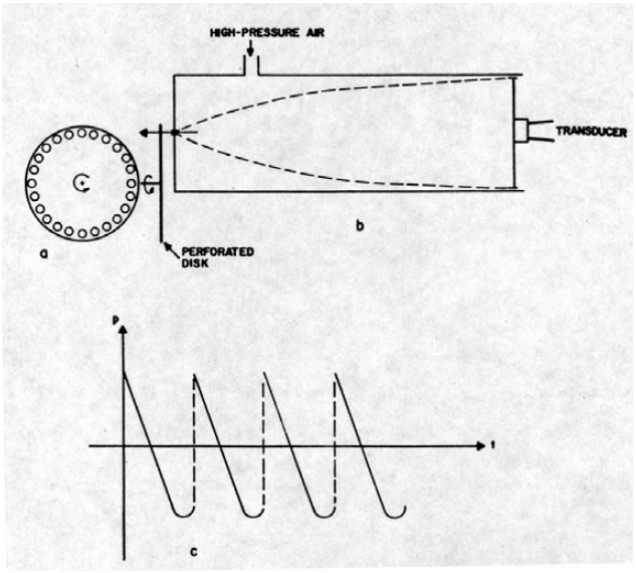

Figure 2.32 – Schematic of a siren generator, with (a) rotating disk, (b) tuned cavity and (c) typical generated non-sinusoidal pressure waveform [60]

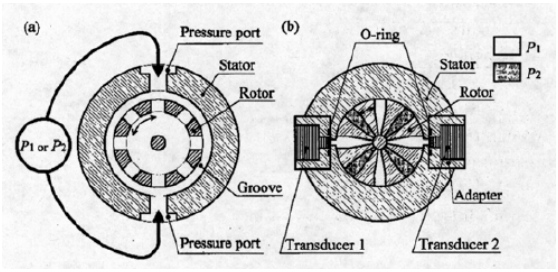

Figure 2.33 – Rotating valve for generating square-wave pressures with pressure input ports (a) and transducer ports (b) [67]

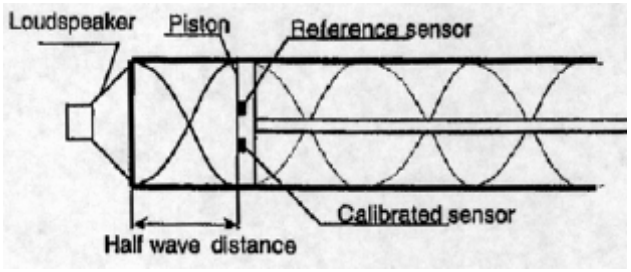

Figure 2.34 – Dynamic calibration of pressure transducer using standing waves obtained by use of loudspeaker and a moveable piston [79]

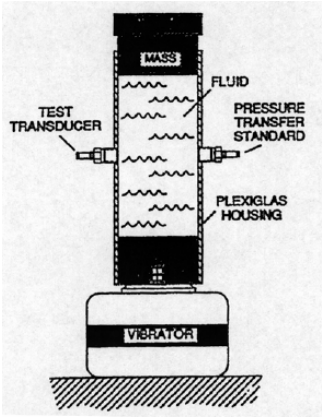

Figure 2.35 – Schematic set-up using a shaker and a liquid column to generate sinusoidal pressure. Note the additional seismic mass on top of the liquid column [41]

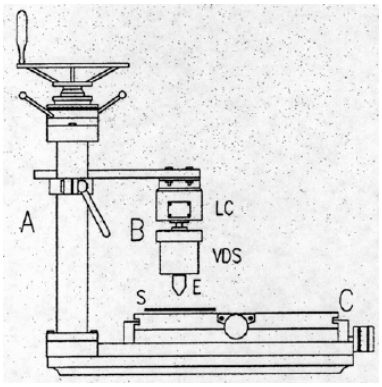

Figure 2.36 – Set-up for static and dynamic testing of pressure map sensors. Letters in the picture denote the frame (A), the operating head (B), the sensor bearing plate (C), the load cell (LC), the voltage driven shaker (VDS), the actuator (E) and the sensor (S). [27]

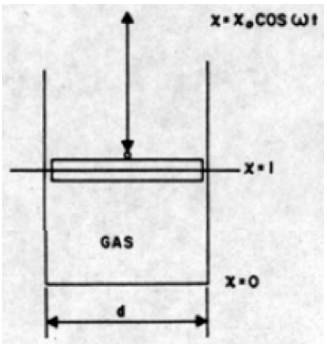

Figure 2.37 – Moveable piston in a cylinder to generate dynamic pressure. Sensor to be calibrated and optional reference transducers are not shown [60]

2. **Aperiodic excitation**: This type of signal generation creates a single event phenomenon (like step, impulse,...). By computing the Fourier Transform of the tested transducer $\mathcal{F}_t[S(t)](f)$ and the one of the reference transducer $\mathcal{F}_t[E(t)](f)$, one can construct the Transfer Function $H(f)$ of the measurement chain (Figure 2.38).

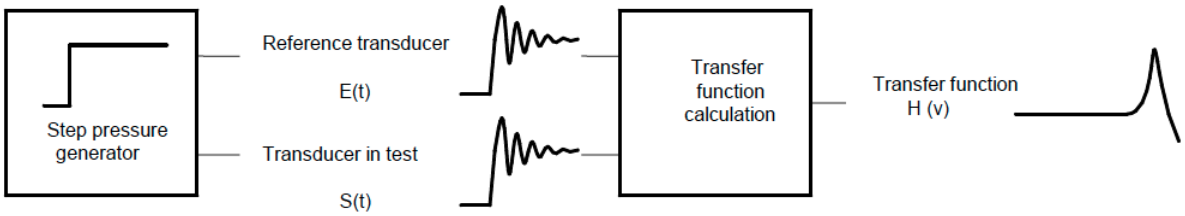

Figure 2.38 – Typical procedure to determine the Transfer Function of the measurement chain (tested transducer) [59]

$$H(f) = \frac{S(f)}{E(f)} = \frac{\mathcal{F}_t[S(t)](f)}{\mathcal{F}_t[E(t)](f)} = \frac{\int_0^\infty S(t)e^{-2\pi jft}dt}{\int_0^\infty E(t)e^{-2\pi jft}dt} \tag{2.24}$$

With t the time, f the frequency, $j = \sqrt{-1}$. This TF can thus be computed in "one time" (one measurement) whereas periodic pressure generator necessitate to test all particular frequencies of interest, select the amplitude at this particular frequency (test and reference transducers), make a division and report it on an amplitude (or phase) graph as a function of the frequency.

(a) Shock tube: This device is the best way to create a pressure step, almost perfect. Figure A.1 shows a shock tube facility at NASA ARC: it is composed of high and low-pressure tubes, separated by a diaphragm (Figure 2.39). Once the diaphragm bursts, the air (or fluid) moves from high-pressure to low-pressure tube with a shock wave (thus at the speed of sound). Its frequency content is clearly identifiable, with a pressure transducer (Figure 2.39 shows also the pressure step, in the time domain) or a spectrometer (Figure A.1).

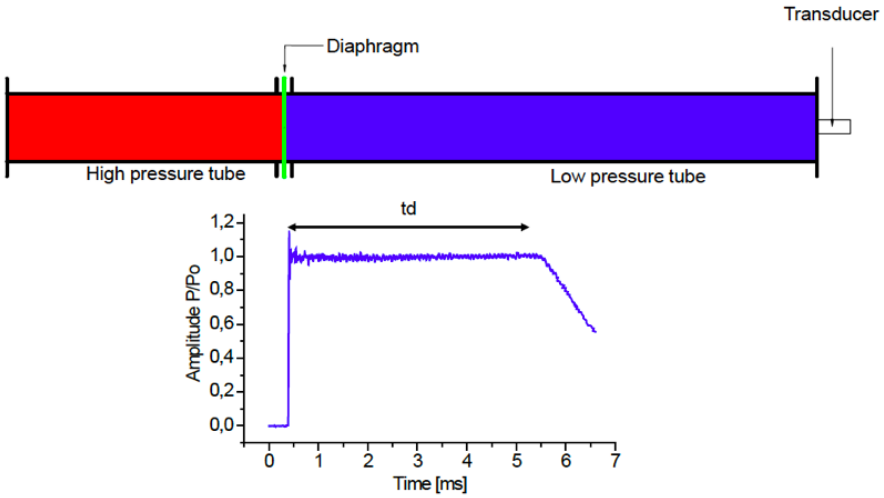

Figure 2.39 – Schematic of shock tube and time variation of pressure during a shock wave [59]

More precisely, Figure 2.40 shows the time evolution of pressure during the shock wave motion. In Figure 2.40a, the diaphragm bursts at time $t = 0$. The flow is at rest and gases at ambient temperature. The driver gas is at high pressure in region 4 and the driven one in region 1 ($p_1 << p_4$). The wave propagates at $t = t^* > 0$. There is an expansion wave in region $3 \rightarrow 4$, a contact discontinuity wave in region $3 \rightarrow 2$ and what is the most interesting here: a shock wave in region $2 \rightarrow 1$. The graph on below side of Figure 2.40a shows characteristic lines (expansion wave, discontinuity and shock wave) in space x and

time t. Figure 2.40c shows the pressure distribution in the whole tube during different time sequences, showing pressure step (shock wave) propagation and reflections on the 2 ends. As done in [40], it is possible to calculate the pressure step from gas dynamics with these assumptions, in Appendix A.2

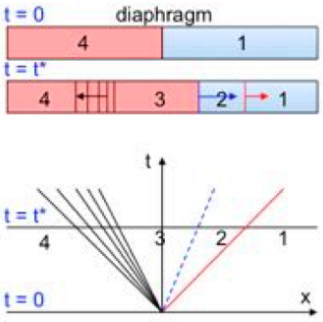

(a) Above: Schematic of the diaphragm bursting and wave propagation, below: characteristics graph [68]

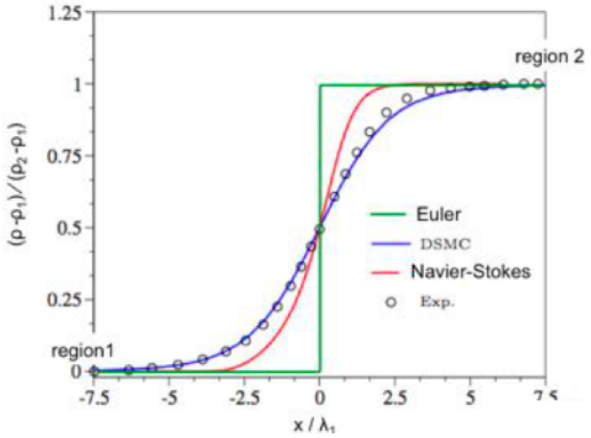

(b) Normalized density distribution across shock wave in Argon ($M_\infty = 9$), comparison of methods [68]

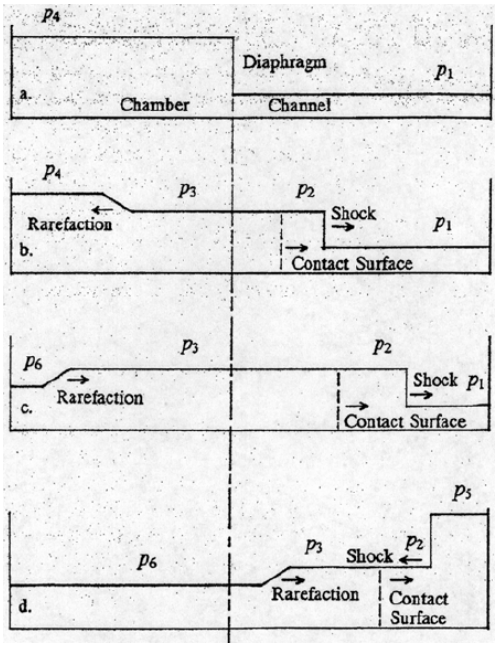

(c) Time sequence plots of pressure as a function of location within a shock tube. On the vertical axis is pressure and on the horizontal the location along the tube. In (a) is the condition before diaphragm rupture, in (b) pressures are given before any wave is reflected, in (c) the rarefaction wave has been reflected at the left end and in (d) also the shock wave has been reflected at the right end [21]

Figure 2.40 – Qualitative description of the shock wave created by shock tube (in time domain)

(b) Fast-opening device: as shock tube, this device is also used to generate a pressure step but associated with lower frequencies. As shown in Figure 2.41, a large cavity is pressurized at p_2. A small cavity on top of it is initially at pressure p_1 and connected to the large one by a communication device. Once it is opened, the pressure in the small cavity goes from p_1 to p_2. The pressure step is $p_2 - p_1$ positive or negative depending on p_2.

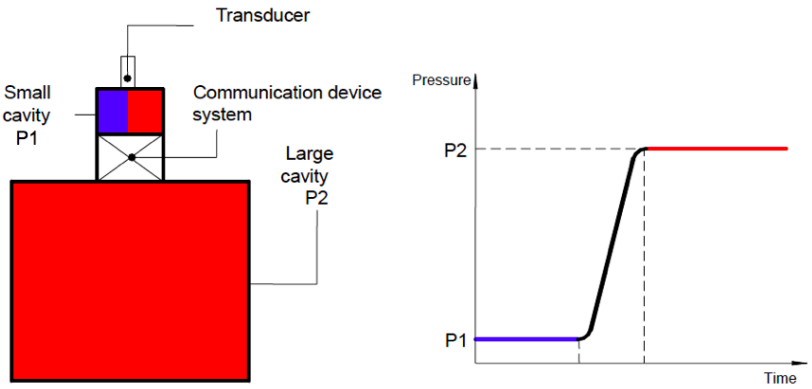

Figure 2.41 – Schematic of fast opening device and time variation of pressure inside the small cavity during the valve opening, from p_1 to p_2 [59]

This device is an extension of the shock tube but the main difference is the rising time in the pressure step, higher than the one of shock tube, leading to lower frequencies (advantage if the calibration target is low frequency but a drawback if very fast and high-frequency phenomena are studied). The ENSAM fast opening device [59] goes to 20 [MPa] with a rising time of a few [ms], leading to frequencies up to a few hundred [Hz]. Fast-opening devices and shock tubes are similar in term of amplitude (Figure 2.42), but the advantage of fast opening devices is that the pressure amplitude can be controlled during a chosen time. Conversely, these devices are very different in term of frequency range (Figure 2.42). Typically, aerodynamic phenomena studied in Chapters 3 and 4 are in the range [0,200] [Hz], with an amplitude of maximum thousands of [Pa] so [0.1-0.01] [bar]. Depending on the device, ranges of shock tube and fast opening device can vary but the range of interest in this work is related with fast opening tubes and balloon explosion setup (discussed in section 2.3.4).

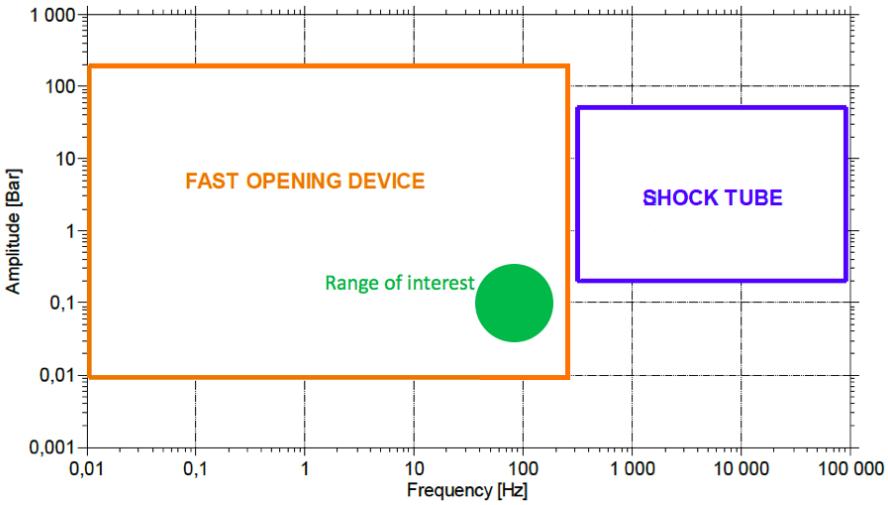

Figure 2.42 – Comparison of amplitude and frequency range of fact opening device and shock tube [59]

The true measured pressure during this process present 2 experimental characteristics (Figure 2.43):

- Internal leaks due to communication device system imperfections creating small oscillations before opening the valve
- Deformation of the seal at the opening, creating a small depression

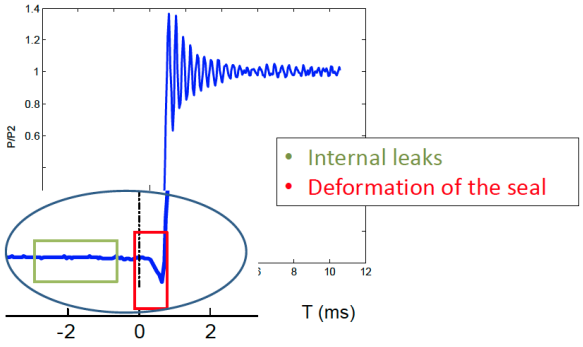

Figure 2.43 – Time variation of the normalized measured pressure in the small cavity p/p_2 [59]

(c) Aronson shockless pressure step generator: the goal of this device is to create pressure step with a rising time approaching the one of shock tube (according to the supplier PCB[14], this can reach less than 50 [μs] rising time). In Figure 2.44, pressures at A and E are controlled (reference). The pressure step is generated by the fast opening of the poppet valve, with an impact weight. The rising time depends on,

- Gas type inside the chamber (often Helium)
- Poppet valve diameter
- Initial pressure difference $p_A - p_E$
- Type of transducer (flush or recess mounted)

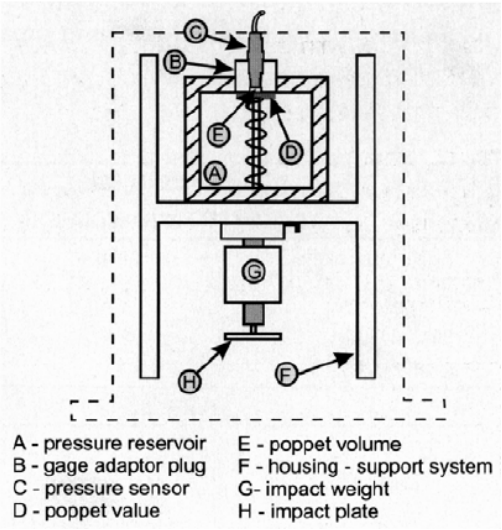

Figure 2.44 – Schematic picture of the Aronson shockless pressure step generator [41]

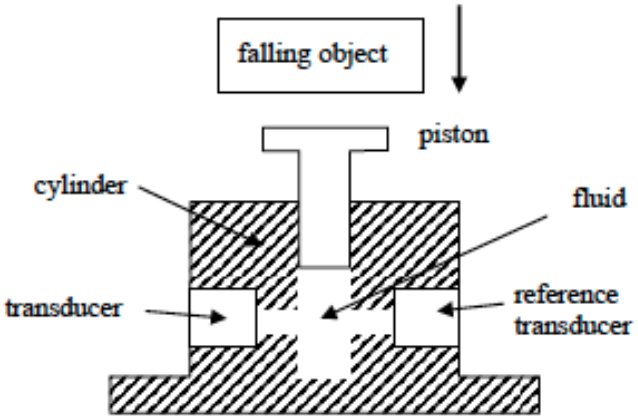

Figure 2.45 – Schematic picture of the method with a dropping weight to dynamically calibrate pressure transducers [60]

(d) Dropping weight: very simple way to obtain pressure step, to let falling an object on a piston on top of a fluid chamber (Figure 2.45). Momma and Lichtarowicz [69] presented a simple calibration: small steel balls (diameter $d = 4 - 7$ [mm]) dropped from several heights ($h = 10 - 50$ [mm]). The rebound height was measured. By conservation of linear momentum, averaged force on the transducer is: $F = \frac{m(v_1+v_2)}{\tau}$, with m the object mass, τ the contact time. v_i is the velocity before and after the impact, in free-falling (dropped = 1, rebounded = 2): $v_i = \sqrt{2gh_i}$, with g gravity acceleration, h_i the initial height. Assuming an homogeneously distributed force on the area, the pressure is deduced from $p = F/A$. The rising time is about 40-80 [μs]. Accuracy depends on how the steel ball drops onto the transducer cavity.

(e) Negative step with deadweight tester: the pressure inside the transducer cavity goes suddenly from a given pressure to the ambient pressure (like fast-opening device). The principle is the same but the added-value is another, more simple technique. Momma and Lichtarowicz [69] developed a calibration method based on a pencil lead, which consists of a weak link, burst, to recover the ambient pressure (Figure 2.46) with rising (decreasing here because of the negative step) time of 7-8 [μs]..

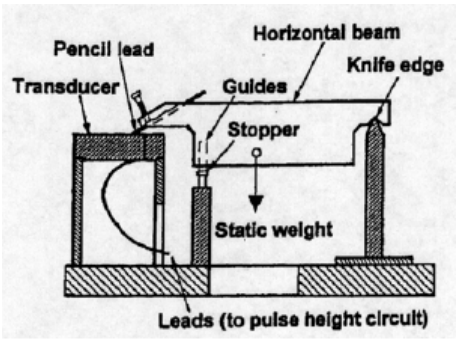

Figure 2.46 – Negative step load with static weight of a water volume and a breaking pencil lead [69]

2.3.2 Parameters

Chapin [76] shows that the tube material does not have effect on the dynamic response (Figure A.2). He studied also the effect of tube bending, that does not influence either the response (Figure A.3), if the tube is not submitted to shrinkage, due to folding (according to the work of Kurita [78] in Figures A.5 to A.7). From the theoretical investigation and review, interesting parameters to study are,

- Tube diameter D and length L
- Discontinuity in tube diameter and channel shape: using 2 tubes and $V_1 = 0$, a discontinuity in diameter can be represented, *i.e.* change of tube, discontinuity in 3D printed channel,...
- Partial shrink (inner diameter restriction ϕ) has to be avoided because it distorts completely the signal and attenuates too much the amplitude (Figure A.7). This shrink can happen when the tube is bent too much and becomes folded. To ensure that this does not happen, pressure tube manufacturer (Scanivalve©) provides data sheet with minimum bend radius (so maximum curvature, depending on the material, Urethane is less resistant than Vinyl) on Table 2.4[6].

Reference	Inner diameter D [mm]	Minimum Bend Radius [mm]
URTH-063	1.37	6.35
VINL-040	0.86	12.7
VINL-063	1.37	12.7

Table 2.4 – Tubing specifications for tubes used in experimental tests (Sections 2.3.3, 2.3.4)

- Transducer volume V and additional volume due to diaphragm deflection σ. Bergh and Tijdeman [35] suggests also to use a calibration apparatus to determine precisely the internal diameter of pressure tubes. Indeed, the dynamic pressure response is very sensitive to small variations in tube volume and diameter. This is simply done by measuring the external diameter and weighing the tube (empty) or filled with water, comparing it and deducing the internal diameter knowing the density of PVC and water. The set-up in Figure 2.47 can be used to determine the transducer volume V and additional volume due to diaphragm deformation σ as explained by [35]. The pressure p_2 and so the volume of the sensor (with known tube diameter) varies if p_1 varies. The value of σ can be determined thanks to the displacement of mercury drop 2. V can be computed with mercury displacement 1 using Boyle's law (pV = constant). This process will be used in experimental results to deduce the transducer volume V.

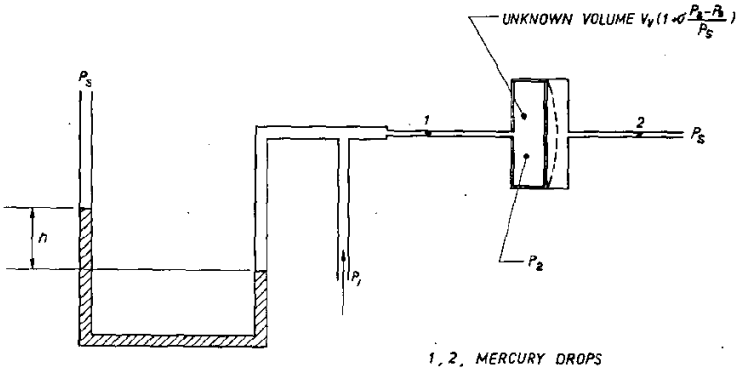

Figure 2.47 – Test set-up for the determination of V and σ [35]

- Everything will be done in a frequency range $f \in [0, 300]$ [Hz], because targeted unsteady phenomena (separated flows, stall, vortex shedding) have only an important response in this range.

[6] From Scanivalve Corp, January 18, 2012, Tubing Specifications

2.3.3 KTH calibrator

In this section, all tools and measurement techniques used during the visit to KTH University in Stockholm will be presented. This gave the opportunity to use the pressure calibrator developed by Damian Vogt, during a lab session with students of the THRUST program. Then, with the help of Johan Davquist and Nenad Glodic, this calibrator was used as well as the set-up to calibrate dynamically pressure tubes of several lengths and diameters (set-up in Figure 2.50). This calibration was also made for 3D printed wing profiles, but this will be the topic of the next chapter. As explained during the review on dynamic calibration, different ways to calibrate pressure measurement system can be used: here, a periodic excitation is used, to control precisely each frequency of interest.

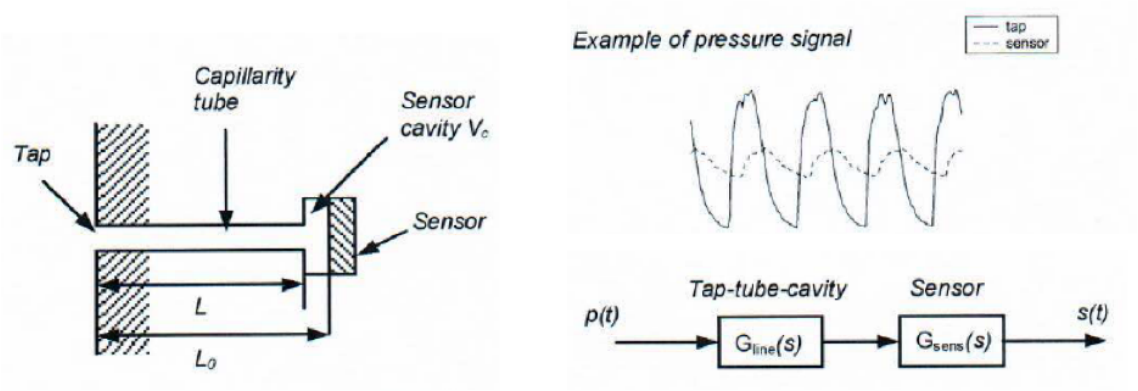

Figure 2.48 – Schematic of the pressure line, cavity and sensor (recessed-mounted sensor), example of pressure signals and its system representation [75]

Figure 2.48 shows the principle of a recessed mounted sensor, *i.e.* mounted on a sensor cavity at the end of a tube. The advantage of such a system is that the transducer can be mounted easily, on the most favorable location, or can be used to measure different locations at one time. The set-up tube, sensor cavity and sensor are characterized by resonant frequency limiting the operating range (measurable frequency range). Assuming the set-up as an organ pipe, the following resonance frequencies are (from the theoretical investigation),

$$f = k\frac{a}{4L} \tag{2.25}$$

Or assuming an Helmoltz resonator[7]

$$f = \frac{\pi}{2}a\sqrt{\frac{d^2\pi}{4LV_c}} \tag{2.26}$$

With a the speed of sound, d the tube diameter, L the tube length, V_c the cavity volume. This modelisation is too simple because pressure perturbation propagation, gas exchange, etc are complex phenomena that induce amplitude attenuation and phase shift (as shown in the theoretical investigation). The dynamic Transfer Function has thus to be experimentally studied, with the system representation in Figure 2.48),

$$G(j\omega) = G_{line}(j\omega) \cdot G_{sensor}(j\omega) \tag{2.27}$$

Experimentally, this Transfer Function is measured by,

$$G(j\omega) = \frac{\mathcal{F}_{\sqcup}[p_{sensor}(t)](f)}{\mathcal{F}_{\sqcup}[p_{ref}(t)](f)} \tag{2.28}$$

Where $\mathcal{F}_{\sqcup}[p_{sensor}(t)](f)$ is the Fourier Transform (frequency domain) of the time pressure signal of the sensor (ref states for the reference transducer at the tap). The tap pressure signal can thus be reconstructed by,

[7] resonance of air in a cavity

$$p_{tap}(t) = \mathcal{F}_t^{-1}[G^{-1}(j\omega)\mathcal{F}_{\sqcup}[p_{sensor}(t)](f)] \tag{2.29}$$

Different types of tubes will be tested (different L, d, L-shaped (bending), diameter discontinuity) to compare with theoretical expectations and other references (Figure 2.49).

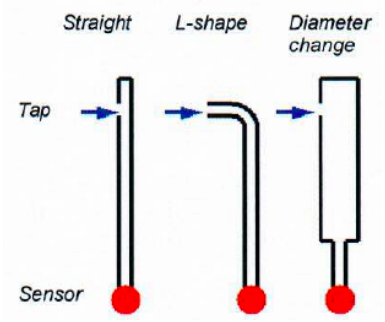

Figure 2.49 – Test tube shapes [75]

The set-up is shown in Figure 2.50 and all tools are described below. A sinusoidal pressure signal is delivered (at a given frequency) by a pressure generator (Figure 2.51) to a reference transducer and a pressure line to be characterized (transducer at the end of the line). As said before, the range of amplitude and frequency is limited with this method but this is not a problem because knowing the theoretical predictions, the frequency range of interest[8] for typical pressure tubes (length around 1 [m] and diameter of around 1 [mm]) is around 0-300 [Hz]. This method is thus very precise but requires to select each frequency one at a time and to make as many tests as the desired number of frequencies.

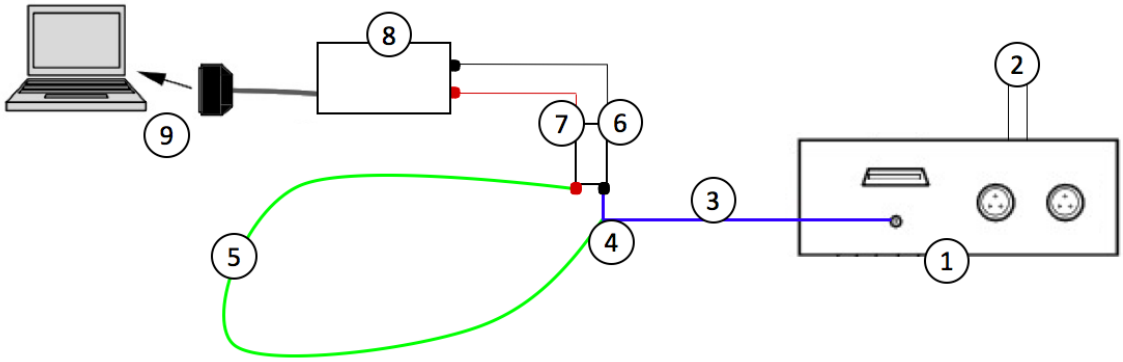

Figure 2.50 – Schematic of the set-up used in KTH to calibrate dynamically pressure tubes

1. **Dyncal - Pressure pulse generator**: it uses the principle of siren pulse generator presented in the review (square wave, sine function). This device is developed in KTH by Damian Vogt that generates a pressure signal with a chosen frequency (screen in red on the left of Figure 2.51, from 1 to 300 [Hz] for these measurements) and the amplitude of fluctuations (right picture in Figure 2.51, fixed at $p' = 0.6$ [bar] $= 0.6 \cdot 10^5$ [Pa] for all measurements[9]).

   Inside the device of Figure 2.51, there is a rotating disk with equally spaced holes and the rotating speed is adjusted to respect the chosen frequency (Figure 2.52). This disk is installed in a pressure chamber This device gives several different harmonics but only the base one (the most dominant) is selected as the resonance frequency.

[8] *i.e.* the range of frequency where the Transfer Function varies the most, also associated to the physical phenomenon measured, *i.e.* stall of a wing (Chapter 3) and Vortex Induced Vibration grid (Chapter 4), typically between 0 and 300 [Hz]

[9] Note that the amplitude of the initial signal is not particularly important, as the purpose to compute the TF of the measurement system, ratio of FFT of reference signal on the measured one, thus only a relative importance

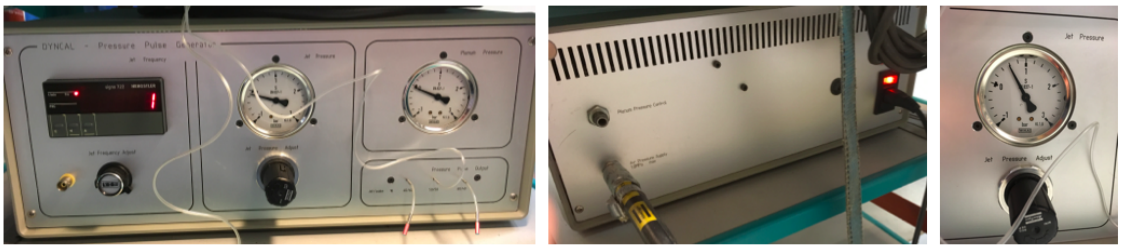

Figure 2.51 – Pressure pulse generator in KTH

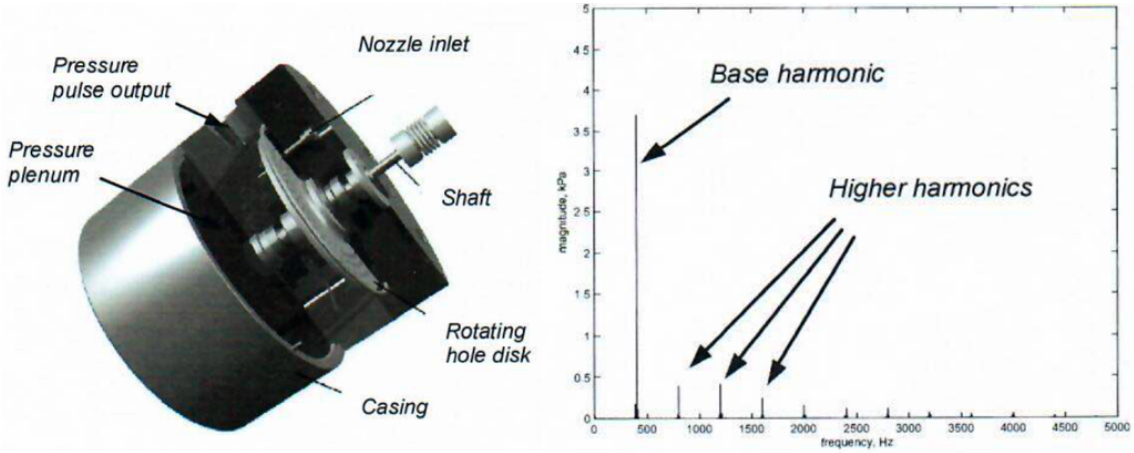

Figure 2.52 – Rotating disk inside the generator and typical frequency spectrum [75]

2. **Pressure line**: pressure inlet (constant value chosen with the valve) in the middle of Figure 2.51.

3. **Connection tubes** (fixed): Flexible vinyl tube that connects the pressure pulse generator to the T connector (tube with $d = 1$ [mm] and $L = 0.4$ [m]).

4. **Test tube**: Measurement system to be characterized (vinyl tube), with variable shape, L and D

5. **T-connector**: Device (build by Scanivalve©) T063-T to connect the reference pressure line to the reference sensor and the tested tube (Figure 2.53).

6. **Transducers**: Kulite XCQ-062 (flush mounted transducer from Kulite Semiconductor Products Inc.©, $p = 1.6$ [bar] absolute maximum), reference (in black in Figure 2.50) and tested (in red). These sensors have to be statically calibrated as said in the review. This is done using a DPI063 (Figure 2.56), that gives the translation [Pa]↔[mV], by generating a pressure with a piston and reading the value in [mV] on the screen. This was done to minimize non-linear effect uncertainties (drift, hysteresis,...).

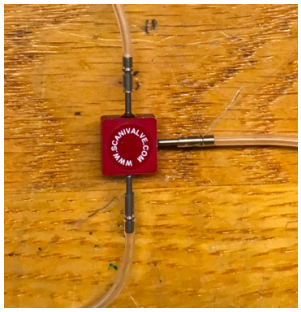

Figure 2.53 – Scanivalve©T063-T in KTH

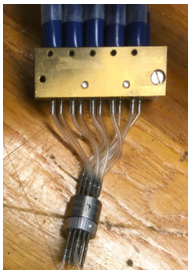

Figure 2.54 – Transducers (inside gold chamber) connected with blue VGA cables, in KTH

7. **Acquisition system**: Reference and test transducer were connected to the acquisition system: Slice Pro USB controller DTS SPU0020, Slice Pro SIM DTS SPS0036 (Figure 2.55). This plug and play system allows an easy connection of the transducers to the computer.

Figure 2.55 – Acquisition system Slice Pro USB controller DTS©SPU0020, Slice Pro SIM DTS©SPS0036

Figure 2.56 – Druck©DPI063 static calibrator in KTH, 100 [Pa] accuracy

8. **Computer connection and software**: The software used was DTS©SliceWare, Version 1.08. Each transducer has to be added in the software, with its static calibration (3.3982 and 3.4292 [kPa/mV]). The sampling frequency and measurement duration were fixed at $f_{samp} = 20$ [kHz] and $t = 10$ [s] for each test. In DTS SliceWare software, a real-time signal of reference and measured pressure is shown (in fact, only the voltage [mV], but converted after in [Pa] thanks to static calibration). This typical signal is a square-wave of one frequency. Signals (reference and test) have to be close to each other. Obviously, the longer the tubes test, the more the signal is damped so red signal will be lower in amplitude than the black one and shifted (phase decay). Huge differences can come from a leakage in tube connections and have to be avoided. After arming, recording and disarming acquisition system by the software, results can be exported in `.csv` data sheet.

Post-processing After saving data in `.csv`, post-processing is done by automatically reading data. The file `calib data.txt` containing calibration factor is used to convert recorded signal (in [mV]) into the pressure (in [kPa]). The file `cases.txt` contains all chosen frequencies (of the pressure pulse generator, Figure 2.51).

A function is used to get the first (base, Figure 2.52) harmonic of the FFT (by using `fft()` function). The idea is similar to a pass-band filter, a range (0.2 so 20%) around the chosen frequency of the test (in the file `cases.txt`) is selected. If the half of this range is above the chosen frequency, the band starts at $f_{min} = 0.2$ [Hz][10]. If range/2 is below the chosen frequency f, the band starts at $f_{min} = f-$range/2. The band finishes at $f_{max} = f_{min}+$range. Then, the resonance frequency of the 1^{st} harmonic, the amplitude of the FFT and the phase are computed, for both reference and test signals. Finally, the Transfer Function is plotted by repeating this method for all tested frequencies f, adding a point in amplitude and phase graphs at each f,

$$|H(f)| = \frac{|\mathcal{F}_t[p_{sensor}(t)](f)|}{|\mathcal{F}_t[p_{ref}(t)](f)|} \tag{2.30}$$

$$\phi(f) = \phi(|\mathcal{F}_t[p_{sensor}(t)](f)|) - \phi(|\mathcal{F}_t[p_{ref}(t)](f)|) \tag{2.31}$$

The phase is `unwrap()` to have values from 0 to $2\pi, 3\pi, ...$ (not between $-\pi$ and π). Experimental results (amplitude and phase graphs for all tested tubes) will be reported, discussed and compared with the theoretical investigation, other references and other experimental data, in section 2.4.

[10]The case $f = 0$ [Hz] is avoided and the Transfer Function is directly replaced by $H(0) = 1$, thus $|H(0)] = 1$ and $\phi(0) = 0$

2.3.4 ULg calibrator

The objective of this work is also to build a pressure calibrator. As reported in the previous sections, different kinds of pressure calibrator do exist. Nevertheless, they use the same principle: generate a pressure with a particular frequency content, measure the pressure at the pressure tap (reference) and at the end of the tube (or equivalently at the end of the measurement system) in order to construct the transfer function of the tube (or measurement system). In KTH, the calibrator delivers an oscillating pressure at a given (chosen) frequency. It requires to make measurements for each desired frequencies. In our range $f \in [0, 200]$ [Hz] this is not a problem but if the range is wider, this method is time-consuming, to characterize (and calibrate) only one measurement system. This is because the Fourier Transform of a sine function (only one frequency f_0 in the time domain t) is Dirac function δ (in the frequency domain f), as shown in Figure A.8 in Appendix A.3.1. Thus with one amplitude and one phase, only one point is known for the amplitude and phase graphs (for the Frequency Response Function, FRF).

$$\mathcal{F}_t\left[\sin(2\pi f_0 t)\right](f) = \frac{1}{2} i \left[\delta(f + f_0) - \delta(f - f_0)\right] \tag{2.32}$$

Some particular functions (in the time domain) can give continuous functions over a large domain of frequencies such that: sine sweep, uniform noise, impulse,... . Another one that is very easy to generate is the unit step function (Heaviside).

$$H(t) = \begin{cases} 0 & x < 0 \\ \frac{1}{2} & t = 0 \\ 1 & t > 0 \end{cases} \quad \text{and } \mathcal{F}_t[H(t)](f) = \frac{1}{2}\left[\delta(f) - \frac{i}{\pi f}\right] \tag{2.33}$$

The step function brings a large range of frequency of non-zero values of the Fourier Transform. The Heaviside function is discontinuous (or picewisely constant) but is purely theoretical so cannot be observed in "reality", from an experimental point of view. Some limit functions can represent this behavior (progressive increase instead of sharp discontinuity) and are presented in Appendix A.3.1. The question now is how to generate this kind of pressure step? Pressure has to decrease or increase suddenly: this is possible when you make an explosion- bursting a balloon will create this pressure step drop. Indeed, the pressure inside a balloon is higher than the one outside (atmospheric pressure) because of stresses inside the balloon envelope. The time it takes for a balloon to burst is of the order of 1 [ms] as shown in Figure 2.57.

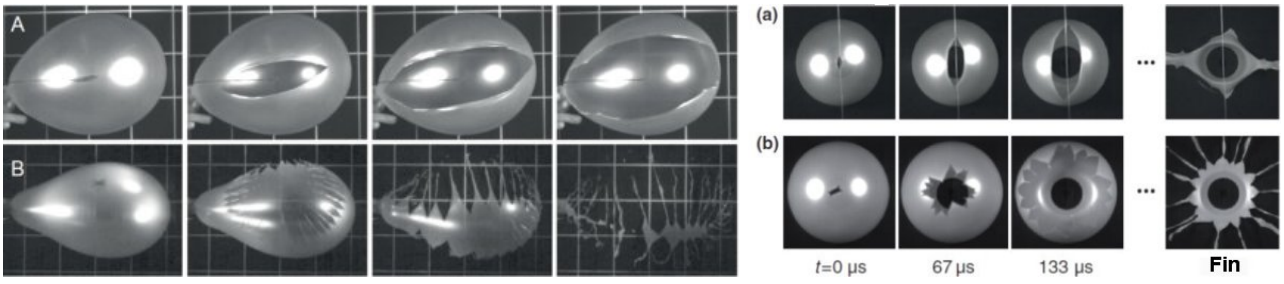

Figure 2.57 – Bursting of a balloon, two kinds: (a) Low-inflated balloon (b) Strongly inflated balloon, each picture separated by 0.3 [ms], from [8]

The balloon is thus an easy, cheap and fast device that can create the desired pressure step. It can be interesting to know the behavior of pressure inside this balloon. The air pressure is obviously constant inside the balloon but depends on the radius of the balloon. Indeed, they are made of rubber, with a certain stress state inside the balloon skin. Theoretical derivation of Figure 2.58 is done in Appendix A.3.2. This behavior is consistent with experiments conducted by [58], with results in Figure A.15 in Appendix A.3.3 (overpressure inside the balloon of the order 1 [kPa]). Figure 2.58 gives the normalized pressure $p^* = \frac{p}{8CH}$ vs radius r^* (with $R = 1$)[11] The pressure is strongly a non-linear

[11] Pay attention to units, p will be in [MPa] if r and R are in [mm].

variation of the radius. There is a strong peak in value around $r^* = 1.23$ ($r = 1.23R$): it corresponds to the difficulty to inflate a balloon at the beginning (corresponding to this critical radius) but after that threshold, it becomes easier because the pressure decrease. Note that here, p is the *relative* pressure (thus the supplementary pressure inside the balloon $p = p_{balloon} - p_{atm}$ compared to the external one (atmospheric)). When the balloon is inflated, for each radius, the pressure inside is above the pressure outside, but less when $r >>$ (anyway the balloon will certainly burst before). By inflating the balloon to a reasonable radius ($r = 5R$ for example[12]), the pressure inside will be sufficient to burst it with a needle. There will be a pressure drop (the relative pressure drops from p to 0, not instantaneously like the unit step function but in a certain finite time, less than 1 [ms], as suggested by Figure 2.57).

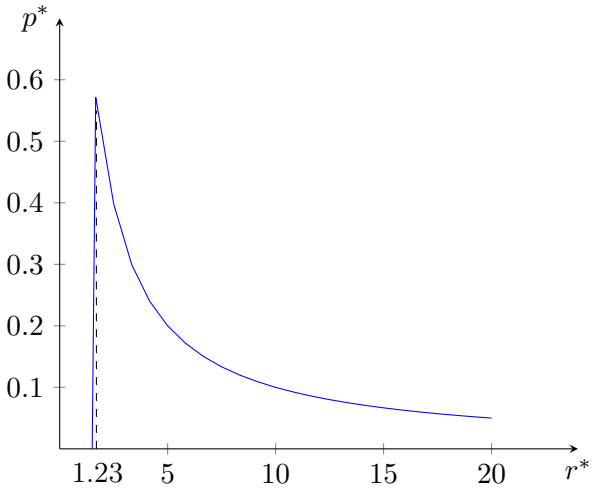

Figure 2.58 – Normalized pressure $p^* = \frac{p}{8CH}$ in the balloon vs normalized radius r^* (with $R = 1$)

Calibration principle According to the work of Paniagua and Denos [53], a burst-balloon device can be built to get a pressure step and convert it in the frequency domain to get the transfer function of the pressure tube/measurement system by comparing pressure at the tap and at the end of the line.

There are different ways to get the frequency content from a time signal:

- By performing a direct FFT (numerically from data)
- By using a parametric system identification

The first one will compute theTF as the ratio between the FFT of the output and the FFT of the input. By sampling a signal with $N = 2^p$ steps, the FFT (and transfer function) is composed of $N/2$ complex numbers (so $N/2$ frequencies). To limit errors, a periodic excitation to compute the FFT is preferred. With a unit step function, this is possible by making an inverse unit step after the first one, to get a boxcar (discussed in Appendix A.3.1). Another drawback of the FFT for a unit step excitation is the Gibbs phenomenon. As seen during the course of Computer Aided Design [28] in Master 1, there is an oscillatory behavior in the graph of the approximation of the step with harmonics (FFT). Close to the step, an overshoot and local maxima/minima alternate (Figure A.13, in Appendix A.3.1). This non-linear behavior makes the computation of the transfer function (ratio of FFT) less precise so that the reconstructed pressure signal is not precisely the reference pressure. These drawbacks with the FFT of a step motivate to use another method: parametric identification which has several advantages:

1. Only a few parameters to store (construction of a polynomial) compared to all discrete points in an FFT
2. No Gibbs phenomenon
3. No need to construct a periodic signal, so that the pressure drop step is sufficient

[12] A simple rubber balloon has typically an initial radius $R = 2$ [cm] so $r = 10$ [cm]

4. Large range of methods to estimate parameters: least-square, maximum likelihood, ...

The dynamic response of a pressure measurement system can be described using a $m-$order linear system model. Indeed, this system is stable, time invariant and linear[13], so it can be modeled by a linear differential equation. Most of the time, pressure transducers show a linear behavior. Non-linear effects appear only at very high pressure amplitudes and gradients, in shock waves for example, according to Schnittfeld [22].

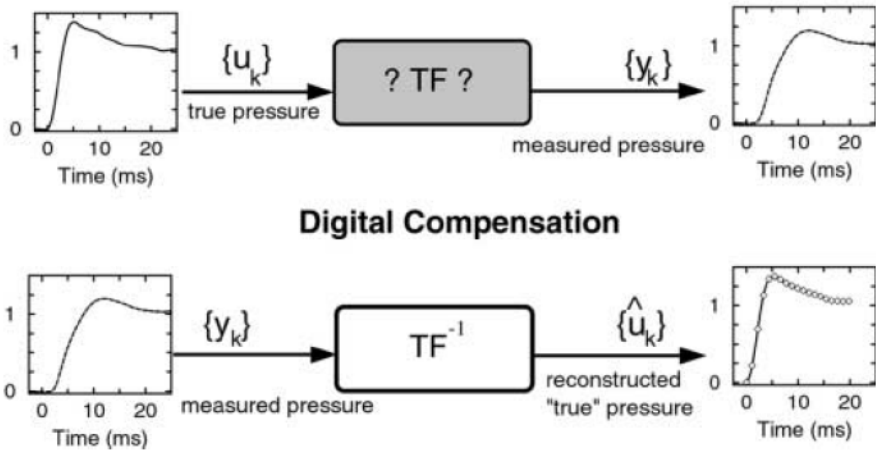

Figure 2.59 – Discrete model of the measurement chain, from [53]

Measured data (of the pressure) are discrete because they are digitalized and sampled at a certain frequency f_s. In Figure 2.59, the input signal (the true pressure at the tap) is $\{u_k\}$ and the output $\{y_k\}$ (pressure measured at the end of the chain). The idea of this method is to find parameters able to model the TF of the system. Then, the digital compensation consists of the reconstruction of a corrected signal $\{\hat{u}_k\}$ starting from the measured one $\{y_k\}$ using the inverse transfer function TF^{-1}.

The discrete model can be expressed by an equation in differences so that y_k can be constructed knowing all previous $k-1$ instant,

$$y_k = \sum_{i=0}^{m} b_i \cdot u_{k-i-d} - \sum_{i=0}^{m} a_i \cdot u_{k-i} \tag{2.34}$$

With m the order of the differential equation, $d = f_s T_d$ the number of samples[14], f_{samp} the sampling frequency, T_d the time delay between the two signals (input and output). Z domain can also be used (Laplace domain (S) for discrete systems). The Z transform of a time series is,

$$Y(z) = \sum_{k=-\infty}^{+\infty} x_k \cdot z^{-k} \tag{2.35}$$

The general form of a differential equation for a continuous-time system is,

$$\sum_{k=0}^{na} a_k \cdot y_k = \sum_{k=0}^{nb} b_k \cdot x_k \tag{2.36}$$

With $na \geq nb$. Thus, the discrete transfer function of a linear system in the discrete Z domain by two polynomials in z, of $m-$order is,

$$\frac{Y(z)}{U(z)} = \frac{b_0 \cdot z^{-d} + b_1 \cdot z^{-1-d} + ... + b_m \cdot z^{-m-d}}{1 + a_1 \cdot z^{-1} + a_2 \cdot z^{-2} + ... + a_m \cdot z^{-m}} \tag{2.37}$$

[13]Assumptions for a system to be described by linear differential equations, as seen in "Modélisation et analyse des systèmes" course in 2^{nd} bachelor

[14]Or "the number of instants for which the output signal remains at 0 level after the input starts rising" [53]

Note that a_i, b_d and d depend on the sampling frequency f_{samp} of data. This equation is very similar to the expression of the RFP, seen in Lecture 4 of the course of Aeroelasticity [32] in Master 2. Indeed, with this method, the FRF (Frequency Response Function[15]) of any dynamic system can be written as:

$$H(\omega) = \frac{b_{nb} \cdot ji\omega)^{nb} + b_{nb-1} \cdot (j\omega)^{nb-1} + ... + b_0}{(\omega)^{na} + a_{na-1} \cdot (j\omega)^{na-1} + ... + a_0} \tag{2.38}$$

Rational function is a generic term to call functions in the form of a ratio of polynomials like equations 2.37 and 2.38. There is a direct correspondence between these equations, with $z = i\omega$, $na = 2n$, $nb = 2n - 1$, $d = 1$ and by reorganizing subscripts of a_i, b_i, where m is the number of modes in the model (so $2n$ is the order of the differential equation m). The polynomial order can be chosen higher than $2n$ to allow for experimental and signal processing errors. The "1" in equation 2.37 comes from a normalization by a_0, so that it does not appear, and other coefficients are of the form $a_i^{new} = a_i^{prev}/a_0$.

These parameters a_i, b_i are based on experimental data, containing noise leading to some error for instant k,

$$e_k = y_k - y_k^{k-1} \tag{2.39}$$

With y_k the exact prediction of equation 2.34 and y_k^{k-1} the experimentally observed value.

$$y_k + \hat{a}_1 \cdot y_{k-1} + ... + \hat{a}_m \cdot y_{k-m} = \hat{b}_0 \cdot u_{k-d} + ... + \hat{b}_m \cdot y_{k-d-m} + e_k \tag{2.40}$$

With $k = 1, 2...N$ instants, there are $N-m-d-1$ equations of this type. Putting theses equations in matrix form and applying an objective function (least-square method), minimizing (assuming $N \geq 2m$ and with $\hat{\Theta}$ the parameter vector $[\hat{a}_1...\hat{a}_m\hat{b_0}...\hat{b}_m]^T$), it gives

$$\frac{\partial}{\partial \hat{\Theta}} \sum_{k=1+m+d}^{N} (e_k)^2 = 0 \tag{2.41}$$

Numerically, 0 is not imposed but an absolute value less than a certain tolerance. After solving this and expressing $z = e^{j2\pi f/f_s}$, transfer function modulus $|H(f)|$and phase ϕ are,

$$|H(f)| = \frac{|Y(f)|}{|U(f)|} = \sqrt{\frac{l_1^2 + l_2^2}{h_1^2 + h_2^2}} \tag{2.42}$$

$$\phi = \arctan\left(\frac{l_2}{l_1}\right) - \arctan\left(\frac{h_2}{h_1}\right) \tag{2.43}$$

$$l_{\substack{1\\2}} = \sum_{i=0}^{m} b_i \cdot \underset{\sin}{\cos}\left[\frac{2\pi f}{f_s}(-i-d)\right] \tag{2.44}$$

$$h_{\substack{1\\2}} = 1 + \sum_{i=1}^{m} a_i \cdot \underset{\sin}{\cos}\left[\frac{2\pi f}{f_s}(-i)\right] \tag{2.45}$$

It can be verified that for a well-calibrated transducer, the gain is equal to 1 at zero frequency ($H(0) = 1$), thus,

$$\frac{\sum_{i=0}^{m} b_i}{1 + \sum_{i=1}^{m} a_i} = 1 \tag{2.46}$$

It is more costly (numerically) to determine these parameters that computing the FFT, because of equations 2.41 but it has to be done only one time for a given measurement system. The "true" (corrected) pressure $\{\hat{u}_k\}$ is directly reconstructed with an iterative process, using the parameters of

[15]The distinction between TF and FRF is a question of variable: TF is used with a general complex variable z or s and FRF is used when this variable is the frequency $z = e^{j\omega}$, with $j = \sqrt{-1}$ and $\omega = 2\pi f$

the transfer function and the measurements y_k. This is simpler than FFT method (start from $y(t)$, make the FFT($y(t)$), divide by FRF $H = \frac{Y}{U}$, make the inverse FFT to get $\hat{u}(t)$). As mentioned before, the advantage of a non-periodic pressure excitation like a step is that only one measure is necessary to get a large range of the frequency domain. The best way to create an almost perfect pressure step rise is to use a shock tube: a diaphragm separates a high and a low-pressure chamber. When it bursts, a shock travels at the speed of sound through the low-pressure chamber. This creates a pressure step almost perfect, able to calibrate frequencies up to 500 [kHz]. Shock tube is thus used for calibration of fast-response probes. Here, such high frequencies are not needed, only the range of [0,200] [Hz] is of interest. For this range, other devices like fast-acting valves or bursting balloon device are preferred, to generate the pressure step. Because of its simplicity to use and build, the last device is chosen. The calibration will be accurate thanks to the parametric method and fast thanks to the nature of the excitation.

Set-up and tools The set-up used to perform this dynamic calibration will now be presented. In Figure A.16 in Appendix A.3.3, a cross section inside the 3D printed cavity is shown on the right (design 1). Above this cavity, a common balloon (in rubber) is maintained by a plug. Inside the cavity, on the left end, a flush-mounted pressure transducer measures the pressure (with a sampling frequency f_{samp}) and data are collected on a computer. At the same time, a pressure scanner DPMS[16] measures the pressure at the end of the pressure tube (or measurement system) that must be characterized. The inlet of this pressure tube is almost in the same location as the flush-mounted pressure transducer (as close as possible but with practical constraints of space). The DPMS is also connected to the same computer, with the same sampling frequency f_{samp} (in order to compare the same frequency behavior (compatible values). Figure 2.60 shows the same principle but with the transducers *inside* the balloon, so without cavity. This design will be used (the complete setup is in Figure A.17 in Appendix A.3.3).

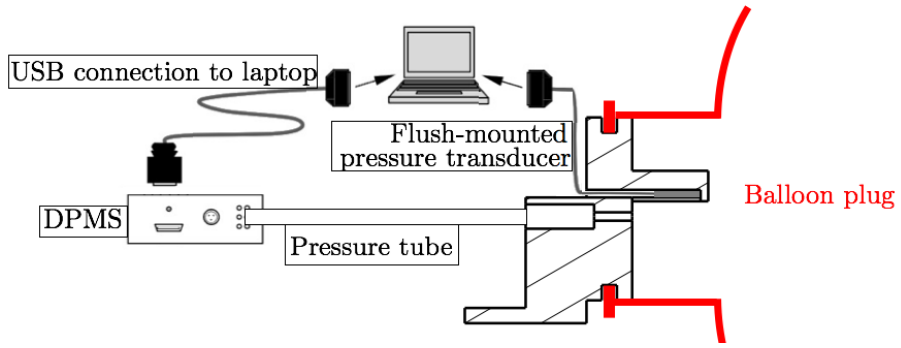

Figure 2.60 – Schematic of the calibration set-up, balloon and measurement tools: design 2

Figure A.18 (left) shows a 3D transparent view of the cavity, printed in 3D for simplicity. The balloon is plugged on top of the cavity, the flush-mounted pressure transducer and the inlet of the pressure tube are at the end of the cavity. This particular shape in "L" is used in order to protect the pressure transducer from balloon debris. Paniagua and Denos [53] say that this kind of design (a chamber) introduces pressure oscillations of 850 [Hz] due to reflections of pressure waves in the chamber. Anyway, oscillations at 850 [Hz] are not in the frequency range of interest, hence not perturbating. A homogeneous pressure state is guaranteed by a small cavity also on the right part of the cavity volume, to ensure a symmetric flow inside the cavity, as mentioned by Vogt and Fransson [75]. The device is rather small and is portable. The balloon explosion is performed using a needle on the middle side of the balloon, where stresses are the highest and leading to the most "clean and repeatable" bursting, as shown in Figure 2.57. A second design can put the pressure transducer and the pressure tube inlet *inside* the balloon. This is too dangerous for the transducer (very sensitive) unless a clever design to protect the transducer is used. This is done by printing in 3D a small envelope around the transducer, the corresponding 3D transparent view and the drawing with dimensions is in Figures A.18 (right) and A.19. The pressure scanner used to get the pressure at the end of the tube is a DPMS, from Turbulent

[16]Dynamic Pressure Measurement System

Flow Instrumentation (TFI)© (photo in Figure 2.61 and connection principle in Figure 2.62). This is a multi-channel pressure measurement system that can measure both mean and time-varying pressures on a matrix of 64 channels (taps). Typical characteristics may include:

- up to 64 channels/module (gold connector in Figure 2.61)
- ±1 [kPa] to ±35 [kPa] (±4" H2O to ±5 [psi]) FS ranges
- 0 [Hz] - several [kHz] frequency response
- 0.1% FS static accuracy at 25[°C] (0.3% over 0 - 50[°C])
- ± 2% accuracy for frequency amplitude (dependent on tube dimensions)

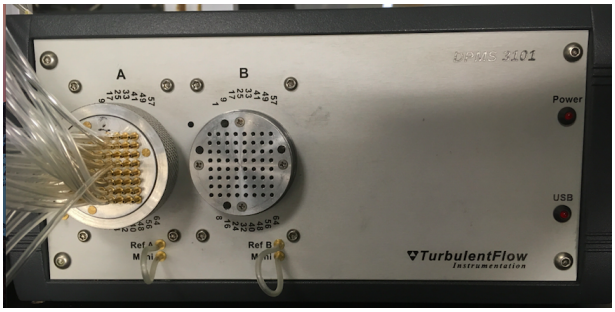

Figure 2.61 – DPMS 3101

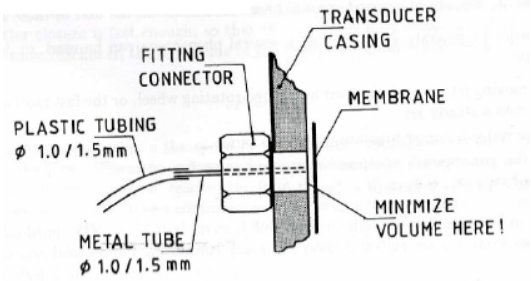

Figure 2.62 – Connection principle of pressure transducer to tube [25]

The DPMS is supplied fully calibrated and ready to use. Calibrations are very stable over long periods of time and a wide range of temperature. In TFI© software, the first window allows choosing the sampling frequency, sampling time and file name, while the second shows in real-time the pressure on 1 chosen of the 64 channels. The flush-mounted transducer is Endevco©8515C-15, a very small sensor (cylinder of 7 [mm] diameter and 1 [mm] heigh, photo in Figure 2.63 and connection principle in Figure 2.64). It is able to measure relative (to atmospheric) pressure in the range of relative pressures [0-2500] [Pa] (so 103.42 [kPa] is absolute).

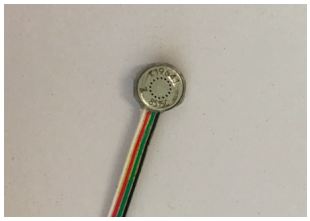

Figure 2.63 – Flush-mounted transducer used to measure reference pressure

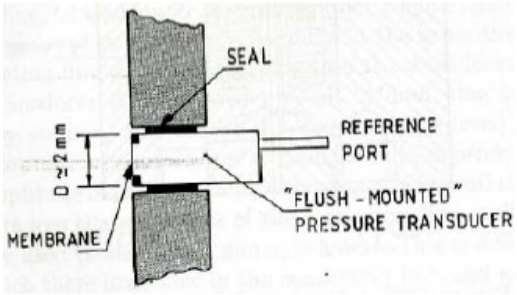

Figure 2.64 – Flush-mounted transducer principle and schematic [25]

Post-processing The sampling frequency and measurement duration were fixed at $f_s = 1000$ [Hz] and $t = 10$ [s] for each test (for DPMS and the flush-mounted transducer). The acquisition for the flush-mounted transducer is made with a National Instrument©DAQ. The synchronization of signals (DPMS and transducer) is made using a shock on the table (creating a small impulse in both recorder pressure). The characteristic step time is very low (less than 10^{-2} [s] so observations will be made on a small time range). A routine is implemented for recorded signals, according to the Rational Polynomial principle described in the calibration principle above.

2.4 Results

In this section, theoretical results (Navier-Stokes equations, RLC and impedance analogy) will be compared with experimental tests performed with KTH and ULg calibrators, in the frequency and time domains. This will put in evidence limitations of the methods, and show the influence of different parameters on the dynamic response: tube length, diameter (0.034-0.054 and 0.057 [in][17] so 0.86-1.37 and 1.45 [mm]) and diameter discontinuity. The reconstruction of pressure (time) signal will also be discussed. All physical parameters are fixed (same value as for the theoretical study, $p_s = 10^5$ [Pa],...). Some parameters will be adjusted to match experimental results:

- Cavity volume V (and effect of diaphragm) for Tijdeman, RLC and impedance analogy. After firsts tests and comparison with theory, cavity volume of transducers was 100 [mm^3] for each case (consistent because the same setup, cavity and transducer is used for each case)
- Attenuation constant $\alpha = A\sqrt{f}$ for impedance analogy (not for cases 8 to 11 because composed of 2 tubes, beyond this theoretical model).

2.4.1 Periodic calibration (KTH)

A strong difference between theory and experimentation is the assumption of an ideal cross section, with a constant area. In practice, the tube is not perfect and small radius variations can give small discrepancies between ideal theory and experiment. This is true mostly for higher frequencies, where higher radius restriction will attenuate even more the pressure signal (lower value of experimental amplitude ratio after $f = 250$ [Hz]). This effect can be cancelled by computing an *effective* tube diameter D_{eff}, taking these variations into account (only a 3.5-5% (on Table 2.5) smaller than the original diameter), suggested in [35] to be between 2 and 5%. Tijdeman [35] uses also this correction. All Figures in the following are computed using this correction. This is not easy to know how this correction will be for a bought tube (with a given diameter, given by the manufacturer) but the range for usual tubes (typical diameter of 1-1.5 [mm]) is corrected by only (3.6-5%). Differences in dynamic response using D or D_{eff} are rather small (Figure 2.65) and mostly around the first peak (not for the phase). The manufacturer does not mention errors on the diameter (they can come from manipulation, folding,...), they can be measured again for each case to ensure results.

Case	L [m]	D [mm]	D_{eff} [mm] (%D)	a
1	1.3	1.45	1.4 (-3.5%)	3.4
2	0.65	1.45	1.4 (-3.5%)	2.8
3	0.1	1.45	1.4 (-3.5%)	2
4	1.3	0.86	0.82 (-4.6%)	16
5	0.65	0.86	0.82 (-4.6%)	16
6	1.3	1.37	1.32 (-3.6%)	3.2
7	0.65	1.37	1.32 (-3.6%)	3.2
8	0.65-0.65	0.86-1.45	0.82-1.4	-
9	0.65-1.3	0.86-1.45	0.82-1.4	-
10	1.3-1.3	0.86-1.45	0.82-1.4	-
11	1.3-0.65	0.86-1.45	0.82-1.4	-

Table 2.5 – Cases studied during experiments and associated parameters (fixed and adjusted)

Figure 2.65 shows the dynamic response of case 1 (*i.e.* a PVC tube with $L = 1.3$ [m] and $D = 1.45$ [m]) and compares results from the theory (Navier-Stokes Tijdeman, RLC analogy, impedance analogy) and experimental data. This tube is typically what is used in practice in many wind tunnel models. The relative small diameter allows a high tube density in models and a length of the order of the meter allows a connection between the model in the wind tunnel section and the pressure scanner (DPMS Figure 2.61) next to it (this configuration will be used for models and applications of Chapters 3 and 4).

[17] Tubes are build by Scanivalve, a US company using imperial units

Moreover, in the scope of the targeted applications (vortex shedding,...), frequencies of interest are not higher than 300 [Hz]. High-frequency phenomena are not part of targeted applications and are more related to noise in the measured signal. This justified the use of case 1 in the range [0,300] [Hz]. Figure 2.65 shows that using optimal and adjusted parameters (V and α), theoretical and simple models agree well with real experimental data, at least around the first peak. Indeed, RLC circuit analogy is only able to represent one resonance (the strongest one being the first peak), due to its simple modelisation. Impedance analogy makes the link between pressure tubes and transmission lines, where reflections are possible, leading to multiple resonances. There is a lack in this analogy concerning parameters α and β. The latter is directly related to the propagation velocity but the former has to be experimentally determined, in parallel to V. Parameters in Tijdeman theory are easier to identify and it leads to less uncertainties and a more accurate shape (closer to experimental data).

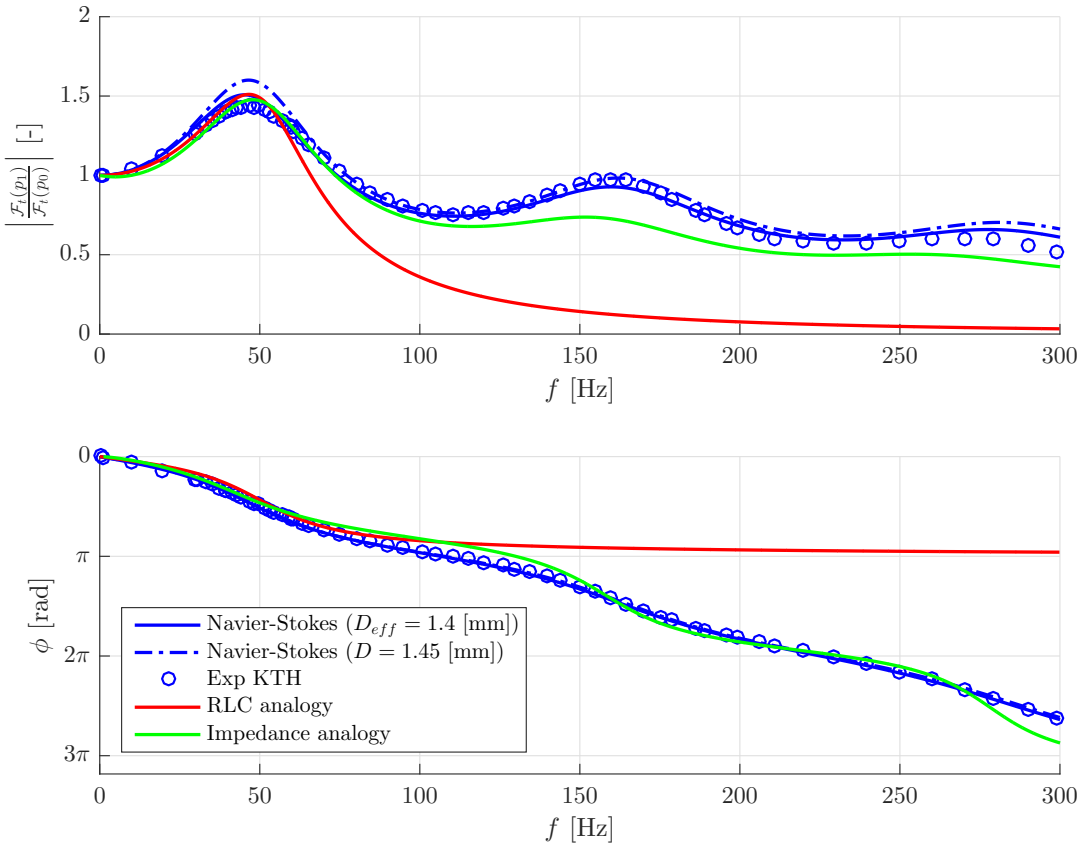

Figure 2.65 – Comparison theory (3 models) - experiment (case 1: $L = 1.3$ [m], $D = 1.45$ [mm])

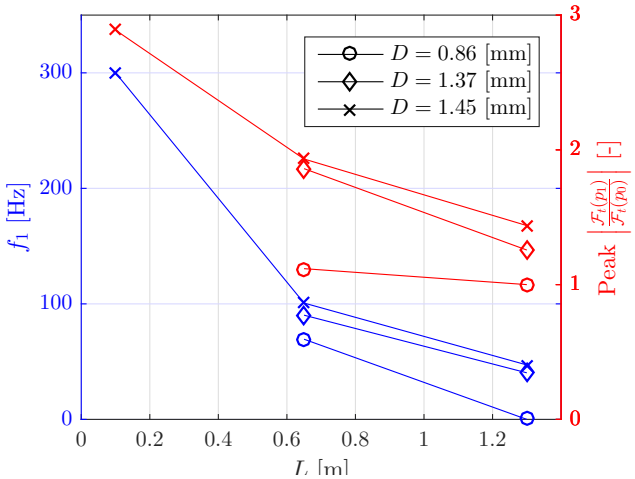

Figure 2.66 – Influence of L and D in first resonance frequency f_1 and peak FFT (experiments)

Figures A.21 to A.26 shows the same comparison but for different cases of L and D (in Appendix A.4). Results are still very close. Figure 2.66 shows a general comparison of the effect of L and D on the resonance frequency f_1 and the associated peak amplitude. The higher L (or the lower D), the lower f_1. The peak amplitude of the FFT correction has a similar dependence. Note that f_1 for case 3 ($L = 0.1$ and $D = 1.45$) is 300 (it is only the upper limit of tested frequencies (by analyzing the shape in Figure A.22, the peak appears after)). There is no resonance for case 4, all frequencies after 0-1 [Hz] are attenuate, and the amplitude decreases rapidly because the tube is too long and narrow. Case 5 (Figure A.24) shows an interesting behavior: the amplitude is close to 1 in a large range of frequency [0,100] [Hz]. For most of the aerodynamics applications, this range can be sufficient and no calibration would be needed because reference signals and measured ones are very close. This is only true for the amplitude. Indeed, the phase lag is rather important, even in the range [0,100] [Hz], around $\pi/2$. Because dynamic pressure is associated with phenomena depending on time, the phase is very important. This is true for example, for the study of vortex shedding, the separation of boundary layer during stall. The phase lag between 2 taps is thus very important and has to be corrected with the same accuracy as for the amplitude. This is the same remark as for the interest to use a restrictor in the tube, correcting the amplitude but not the phase.

Figure A.27 shows experimental data and Tijdeman theory for cases 8 to 11, *i.e.* with a diameter discontinuity. Because of their assumptions, simple RLC and impedance analogies cannot model this change in diameter[18] Theory and experiment match well, using $V_1 = 0$ and $V_2 = 100$ [mm^3]. Small corrections on the diameter have to be done to take into account variations, effective diameters are reported in Table 2.5, always only a few % different from the original one. As observed in theory, diameter discontinuity leads to peaks that superpose each other (relative dependence of D and V with opposite effects). This superposition of 2 peaks gives one peak that appears flattened (flat peak for case 8). Each case show that all frequencies are attenuated because the total tube length is high (between 1.3 and 2 [m]). Lengthening or slimming the tube moves the resonance to lower frequencies, with a lower amplitude (from case 8 to 10). Case 11 has the same total length as case 9 (same peaks location) but diameters are inverted (1.6-1 instead of 1-1.6), giving a lower amplitude peak, even lower than case 10 (which is of a higher length). For these cases, the total length was too long so there was too much attenuation. In practice, tubes of around 1 [m] long are used (similar to case 1) for wind tunnel experiments (see Chapters 3 and 4)). The phase of theory and experiment is also superposed and are rather high, even at low frequency ($\phi = \pi$ at $f = 50$ [Hz]) .

Until now, only results in the frequency domain were presented, to analyze the dynamic response. The purpose of dynamic calibration is to *correct* an unsteady pressure signal in time. As mentioned, 2 ways can be used:

- Applying an IFFT correction: divide the FFT of the measured signal by the correction of the measurement system (using Tijdeman, RLC analogy, the experiment in KTH and ULg,...) and take the IFFT to recover a corrected signal, as much close as possible to the reference one (on the tap).
- Using a parametric system identification (used in experiment in ULg)

Attention must be paid to the time content and also to the shape. Figure 2.67 shows the time signal of the reference and the measured pressure for case 1 at $f = 1$ [Hz]. The pressure is of the form $p = p' + \bar{p}$, with the mean pressure $\bar{p}$ and fluctuation p' (fixed at 6 [kPa], controlled in Figure 2.51). As a comparison, a sine at $f = 1$ [Hz] and an amplitude of $p' = 6$ [kPa], and a mean of $\bar{p}$. As suggested by this Figure, the harmonic pressure delivered by the DynCal pulse generator in KTH is not a perfect sine, it is more a square-wave sinusoidal. It is anyway characterized by one frequency. It is clear that at this very low frequency, the pressure tube does not have any influence, the reference

[18]RLC analogy can do it using more complex circuits, each one representing one tube, connected in parallel. Nevertheless, it requires to solve algebraic equations and RLC results were already compared for a simple tube case. For impedance analogy, a general series of N tubes cannot be modelled but only an inlet restriction, followed by a simple tube without volume. This shows clearly the limitation of this theory, very elegant by the way.

and measured signals are superposed. In the following, the mean pressure will be removed, to study only the unsteady part (fluctuations). Indeed, the mean (steady) pressure value is the one at "$f = 0$" [Hz]: 8 [kPa] in Figure 2.68 (FFT$(p) = 8$ at $f = 0$ and FFT$(p' = p - \bar{p}) \to 0$ at $f = 0$, because $\bar{p'} = 0$, the rest of the FFT is the same, so only p' will be considered in the following). The steady value is obviously not sensitive to fluctuations and dynamic behavior that is studied here.

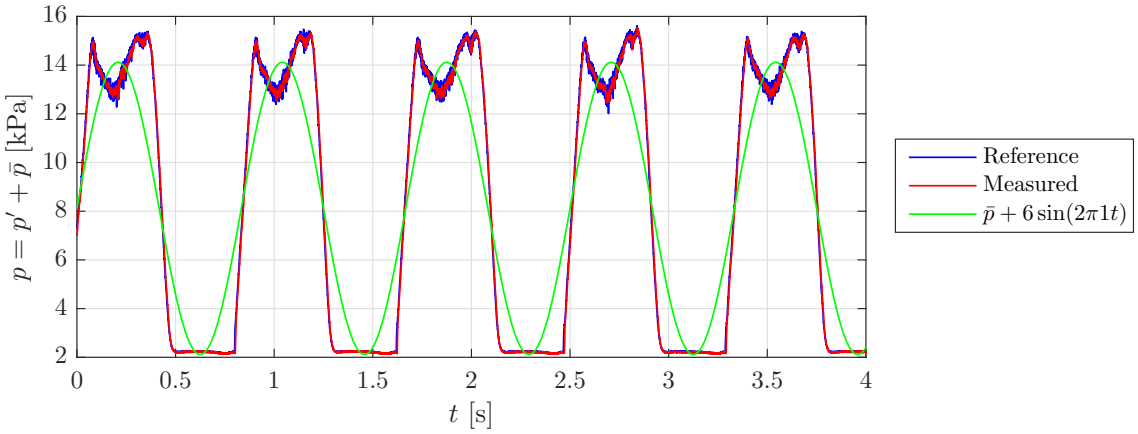

Figure 2.67 – Time pressure signals $p = p' + \bar{p}$ [kPa] at $f = 1$ [Hz]: comparison of reference, measure at the end of the tube and sine signals (Case 1)

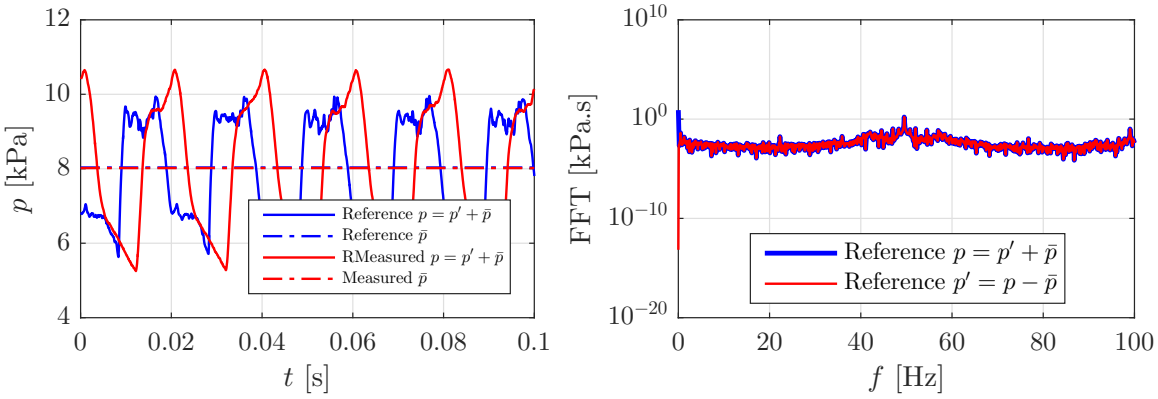

Figure 2.68 – Time pressure signals $p = p' + \bar{p}$ and $\bar{p}$ [kPa] at $f = 50$ [Hz]: comparison of reference and measured at the end of the tube (Case 1), and no influence of mean $\bar{p}$ on the FFT

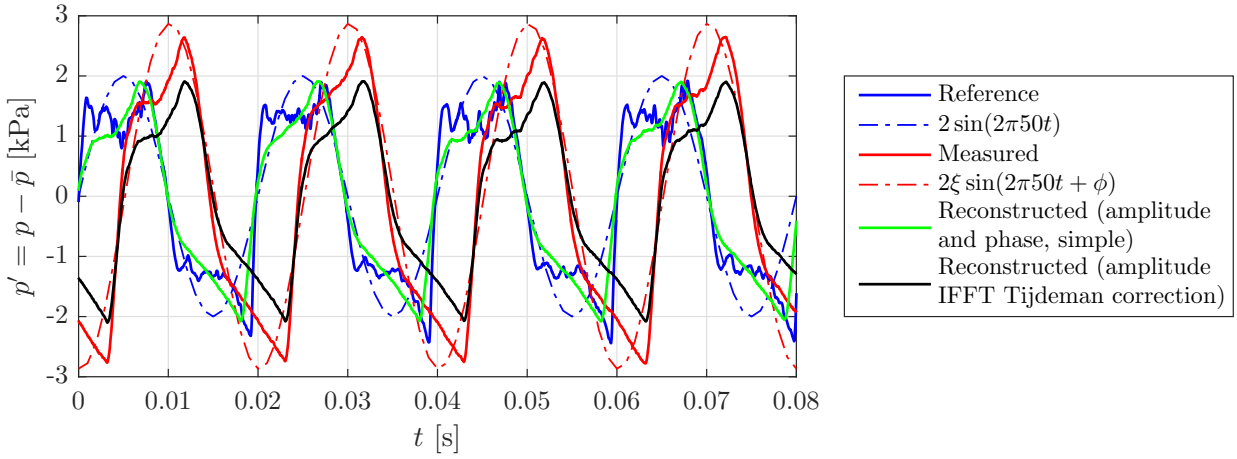

Figure 2.69 – Time pressure signals $p' = p - \bar{p}$ [kPa] at $f = 50$ [Hz]: comparison of reference, measure at the end of the tube, sine and reconstructed signals (simple method (amplitude and phase) and Tijdeman IFFT in amplitude) (case 1)

Figure 2.69 shows the same signals as Figure 2.67 but at $f = 50$ [Hz], which correspond to the peak amplitude ratio of Figure 2.65. The reference and the measured signal are now at different amplitudes (with a ratio of ξ in Figure 2.69) and different phases ϕ.

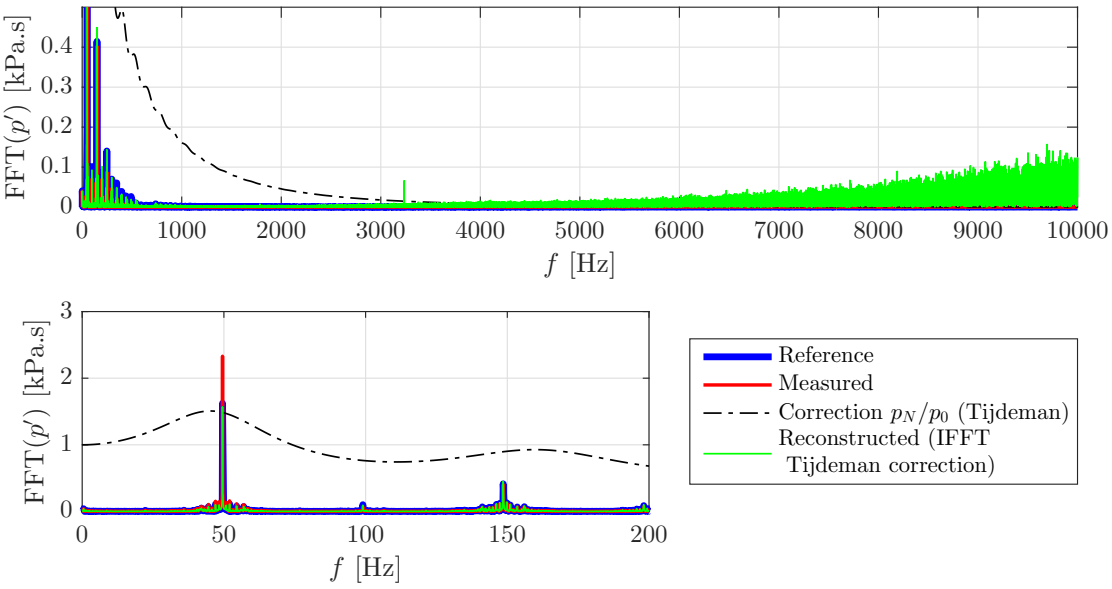

Figure 2.70 – Fourrier Transform of reference, measured, correction and reconstructed signals, range [0,20] [kHz] and zoom (case 1)

The reference signal can be reconstructed from the measured one using the IFFT Tijdeman correction in amplitude, *i.e.* by dividing the Fourier Transform of the measured signal by the amplitude ratio p_N/p_0 (with Tijdeman, Figures 2.65 and 2.70). This will correct only the amplitude, so the corrected signal in dark (Figure 2.69) is not in phase with the reference one (in blue). A correction of the phase is also necessary: the Fourier Transform of the measured signal has to be divided by the complete dynamic response p_N/p_0 (containing amplitude and phase, like Figures 2.72). Figure 2.70 shows that there is a frequency content (non-zero) only for frequencies lower than 500 [Hz] for experimental signals. Anyway, for applications in Chapters 3 and 4 (or in general in experimental aerodynamics), only frequencies lower than 300 [Hz] are required (typical vortex shedding frequency f_{samp} does not exceed tens of [Hz] at low air speed (5-15 [m/s])). Moreover, the reconstructed signal with IFFT correction in green has high values at high frequencies: the FFT of measured signal is very low at high frequency ($\approx 10^{-5}$) but the correction p_N/p_0 too ($\approx 10^{-4}$), so that the ratio is of the order 10^{-1}. Considering such high frequencies has anyway no meaning (the sampling frequency is $f_{samp} = 20$ [kHz], too high) so only the range [0,300] [Hz] has to be considered. Another method to reconstruct the signal is the "simple" one in green in Figure 2.69. Because the pressure signal is sinusoidal (or harmonic with one basic harmonic), all the frequency content is concentrated at this resonance frequency (50 [Hz] in Figure 2.70), other frequencies have a negligible value of FFT. Thus, dividing the amplitude FFT(measured) by the value of p_N/p_0 at $f = 50$ will give a good estimation of the complete correction (which takes into account all frequencies) because only $f = 50$ has an influence. The phase of FFT(measured) is delayed by the phase of p_N/p_0 at $f = 50$. As shown in Figure 2.69, this gives a reconstructed signal very close to the reference one.

Figures 2.71 and 2.72 show the signal reconstruction depending on the cut-off frequency f_c (*i.e.* with a low-pass filter, that cuts off frequencies above f_c). For $f_c = 10$ [kHz], an artificial content in high frequencies is present (Figure 2.70) leading to artificial high frequencies in the reconstructed signal. The extreme case occurs on the opposite if $f_c = 100$ [Hz], containing only the resonance frequency $f = 50$ but no higher frequencies, some oscillations of the reference signal are missed. Figure 2.72 compares Tijdeman and experimental[19] correction at $f_c = 300$ [Hz]. Because Figure 2.65 showed

[19]Experiment data in Figures 2.65, A.21 to A.27 are discrete points; a polynomial fit is thus computed from them, explained in Appendix A.4

very close results for p_N/p_0, this is also true for the reconstructed signal based on this p_N/p_0. The cutoff frequency is high enough to capture the global behavior of the signal (higher frequencies not needed). Nevertheless, there were no small oscillations on the plateau of the measured signal (compared to the reference one). The reconstructed signal based on this measured signal cannot present these oscillations.

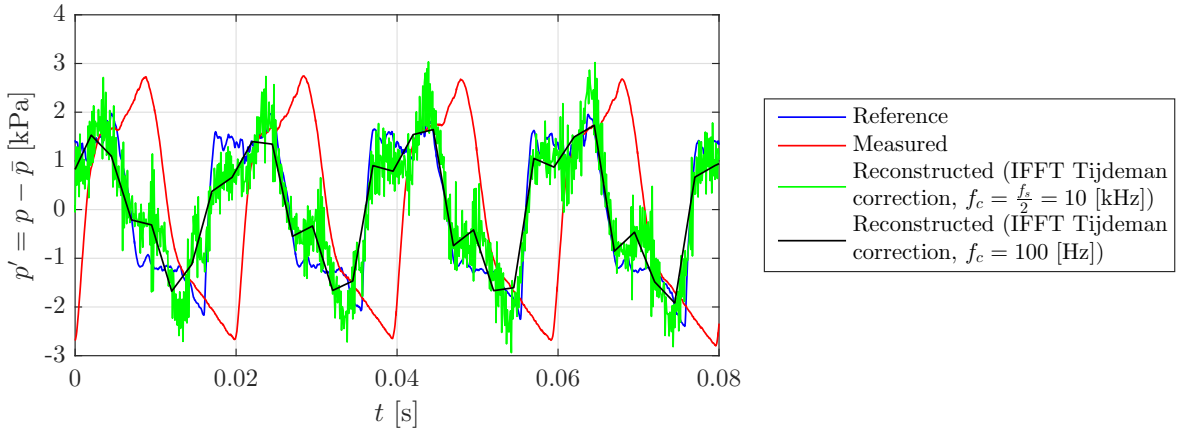

Figure 2.71 – Signal reconstruction at $f_c = 10$ [kHz] and 100 [Hz] (Tijdeman) (case 1)

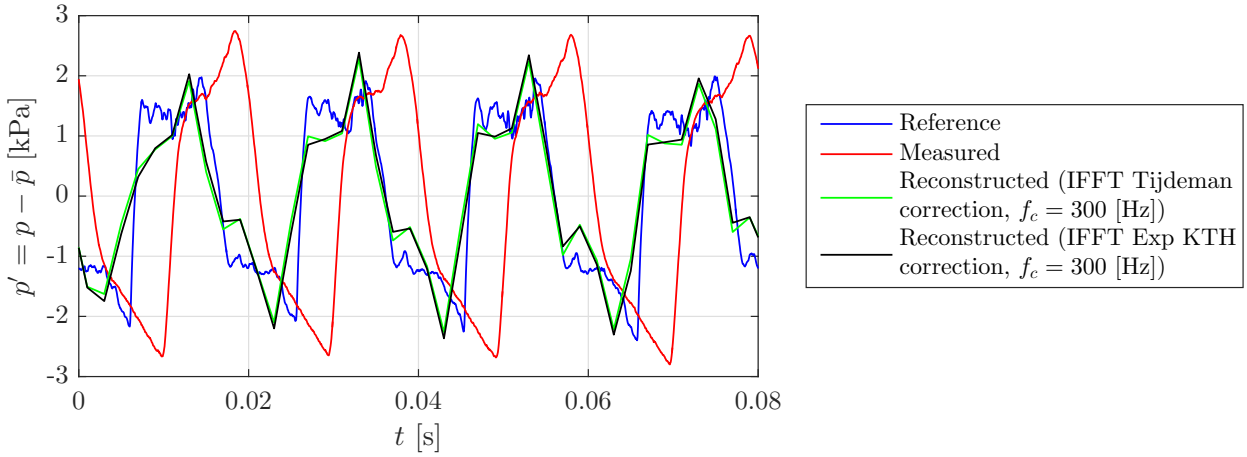

Figure 2.72 – Signal reconstruction at $f_c = 300$ [Hz] (Tijdeman-experiment) (case 1)

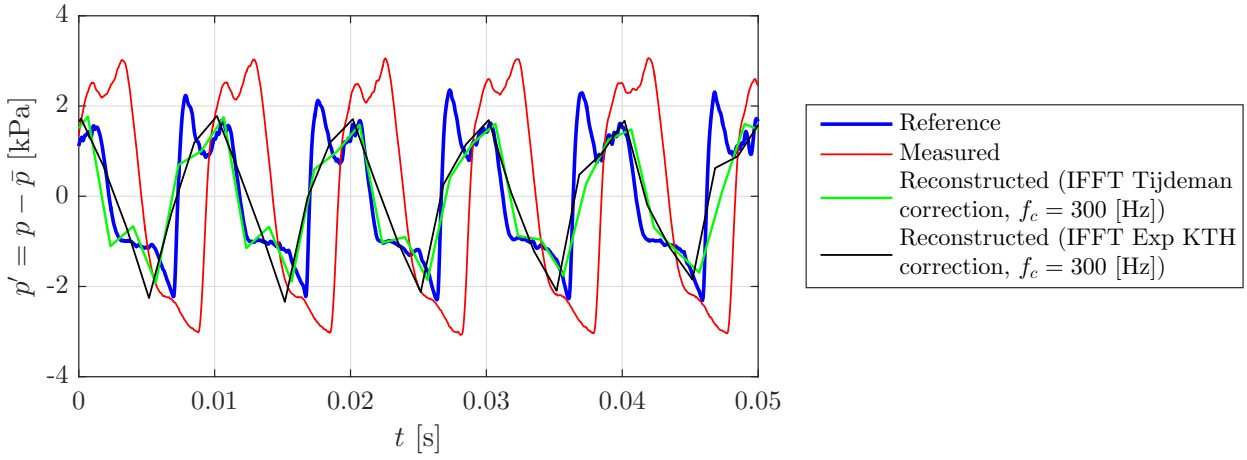

Figure 2.73 – Signal reconstruction at $f_c = 300$ [Hz] (Tijdeman-experiment) (case 2)

Figure 2.73 shows the same procedure as Figure 2.72 but for case 2 (lower L). For this case, reference and measured signals are closer. The correction is close to the reference signal too, with

fewer oscillations than Figure 2.72, because the range [0, 300] [Hz] for case 2 contains only 1 peak (proportionally less frequency content than for case 1). Measured and reference signals are closer at the beginning so that the correction is lower than for case 1, meaningless relative errors (but the frequency content has to be higher than 300 [Hz]). Anyway, typical pressure tube used in the following is case 1. There are some differences at the begin and end of the signal: the measured signal has a different content at high frequency than the reference one and no correction can recover the missing information at the start and at the end of the sampling period (these differences are low). Figure 2.74 shows the probability distribution $\mathcal{P}$ of the fluctuating pressure p' for $f = 1$ and 50 [Hz]. As explained, at 1 [Hz], measured and reference signals are superposed and 50 [Hz] distorts the signal. The lower value of p' at 1 [Hz] is constant (high peak at -0.6 [bar]) but there were oscillations around 0.6 [bar], linked to the fact that the rotating valve delivers an additional pressure to make the upper peaks, and do not produce pressure for the lower part (ambient pressure). For 50 [Hz], reflections inside the tube do not allow the pressure to reach an amplitude as high as for 1 [Hz] (it does not have the time to do it). Figure 2.75 shows time content characteristics as a function of f.

- Kurtosis: $k = \frac{\mu_4}{\sigma^4} = E\left[\left(\frac{p'-\mu}{\sigma}\right)^4\right]$, measures the "taildeness" of the probability distribution around its mean value
- Skewness $\gamma_1 = \frac{\mu_3}{\sigma^3} = E\left[\left(\frac{p'-\mu}{\sigma}\right)^3\right]$ measures the asymmetry of the probability distribution around its mean value
- Standard deviation (equal to the RMS because the mean is zero) $\sigma = \sqrt{E[(p'-\mu)^2]}$ measures the amount of deviation of p' around its mean value

With E the average operator and μ the mean value of the random variable p'. The reference signal is more asymmetric than the measured one but γ_1 stays close to 0 (more at higher f). Time signals for excitation at $f = 1$ [Hz] oscillate on the upper plateau (Figure 2.69) so σ is higher, but it does not mean that there is a high-frequency content. In fact, these oscillations in Figure 2.69 are at a rather low frequency (FFT of signals at $f = 1$ has frequency content around a few [Hz]) but appear relatively high because of the time scale (period 50 times higher than for $f = 50$). These oscillations are thus at only 10 [Hz] and appear to oscillate more but the time scale is higher. The kurtosis and σ follow the shape of the correction p_N/p_0, there are higher differences in shape at resonance.

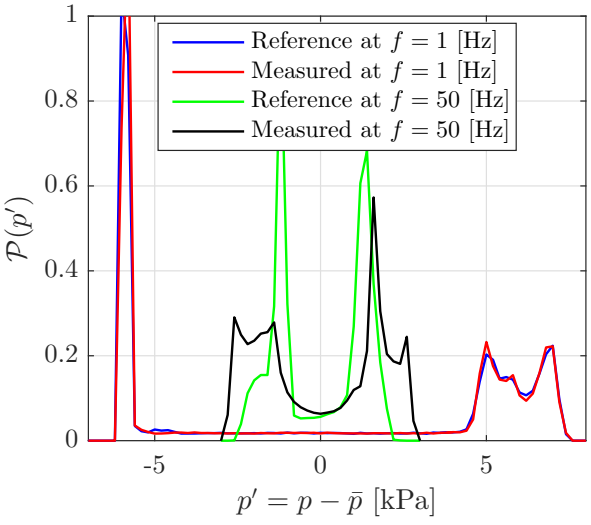

Figure 2.74 – Probability distribution of p' at $f = 1$ and 50 [Hz] (case 1)

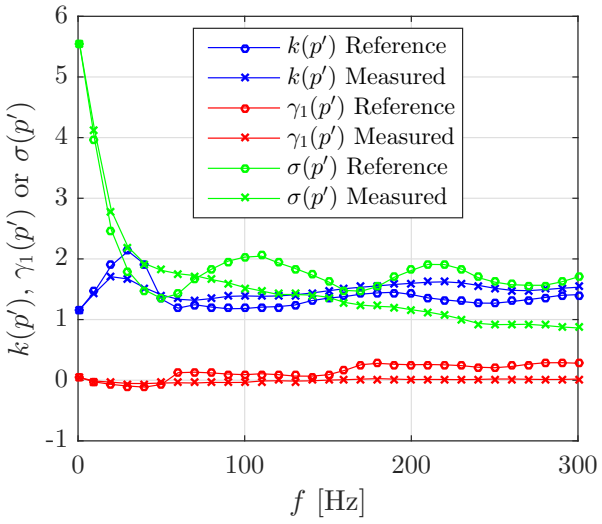

Figure 2.75 – Time characteristics k, γ_1 and σ of signals as a function of f (case 1)

2.4.2 Aperiodic calibration (ULg)

Figure 2.76 compares pressure step generated using the ULg calibrator (burst balloon device) for different tube cases (according to Table 2.5). For each case, pressure and time range are the same (the time range is centered around the step). The influence of L ($\searrow$ left to right graphs) is similar to the one obtained by [53] (in Figure 2.77 left). The shorter the tube, the less delayed the response. The influence of D is visible on Figures 2.76 ($D \searrow$ from above to below graphs) and 2.77 (comparing left and right graphs): the more narrow, the more delayed the response.

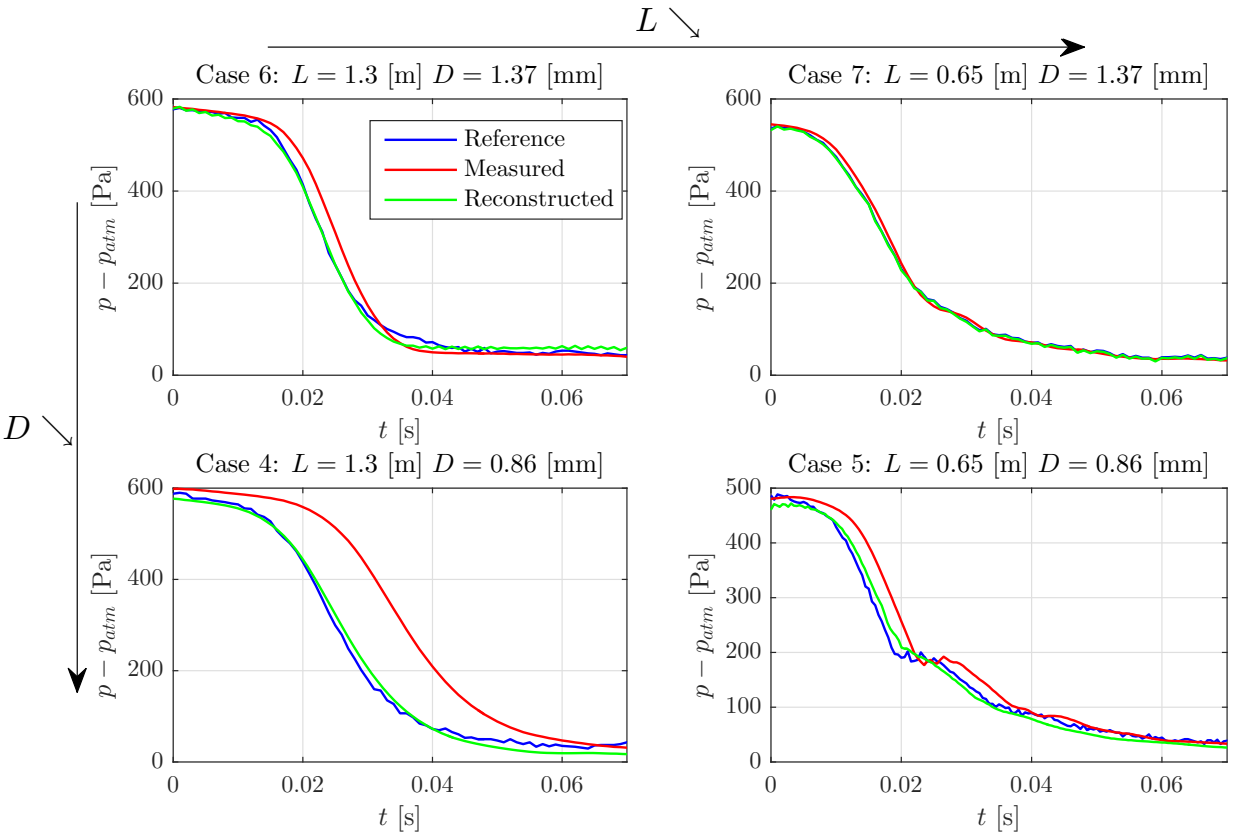

Figure 2.76 – Pressure step signals (reference, measured and reconstructed with RFP correction) for cases 4 to 7 (using the balloon burst calibrator, in ULg)

2.4.3 Comparison

From these step signals, it is possible to construct the RFP, a polynomial fit of the FRF (dynamic response of the tube compared to the reference). The time resolution does not allow to construct a very smooth FRF but it gives an idea of its shape. Figure 2.78 compares FRF obtained with KTH and ULg experiments (periodic and aperiodic signals). The magnitude of ULg case 4 is not exactly at 1 for very low frequency but it should be (linked with some fitting issues). This is also true for case 6, response amplitude for $f < 20$ [Hz] is imposed to 1 to be consistent. The phase is similar but more sensible to fitting.

The reconstructed signal (Figure 2.76) is obtained thanks to RFP fit of the ratio between the measured and reference signals. It is reconstructed starting from the measured signal and applying the correction. Because it is a fit and started from the measured signal, the reconstructed signal appears smoother [20]. The RFP method needs a parameter: the number of modes m. From observations of Tijdeman results and experiment in KTH, an adimensional frequency ω/ω_0 has been studied, and peaks occurred at $\omega = \omega_0 = 2\pi\frac{ma_0}{4L}$ (with the number of modes $m = 1, 3, 5...$). The sampling frequency

[20] Less noise compared to the reference signal, linked to the reference transducer, less precise than the DPMS for low pressure

of both signals is $f_{samp} = 1000$ [Hz] so FFT are in the range [0-500] [Hz]. The number of modes can be deduced with $m = \frac{500}{a_0/(4L)}$. For $L = 1.3$ [m], $m = 8$ and for $L = 0.65$ [m], $m = 4$. Obviously, it is possible to reconstruct the signal by computing the inverse FFT of the ratio between FFT of measured signal and the correction. It is the same as taking the inverse FFT of the FFT of the reference signal, which obviously gives the reference signal. Here, the RFP is fitted and constructed one time and can be used to correct other recorded pressure (during wind tunnel experiments) using the same tube. This is the same principle as the correction made with Dyncal (KTH calibrator), the FRF is computed point by point. The complete response is used to correct pressure signals, not only the ratio of FFT measured/reference from one signal (one point on FRF graph because the Dyncal is mono frequencial).

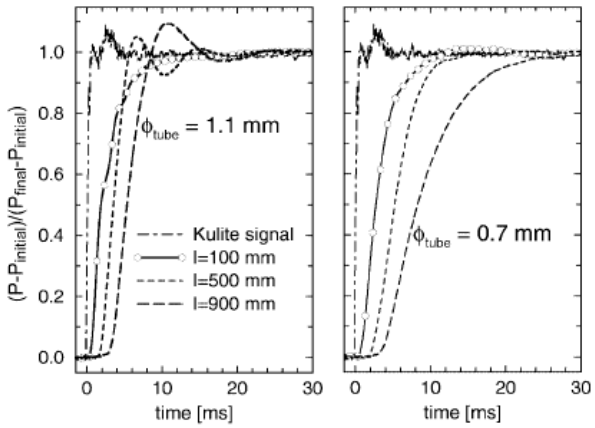

Figure 2.77 – Pressure step signals (reference, measured and reconstructed with RFP correction): influence of tube length and diameter (experiment from VKI [53])

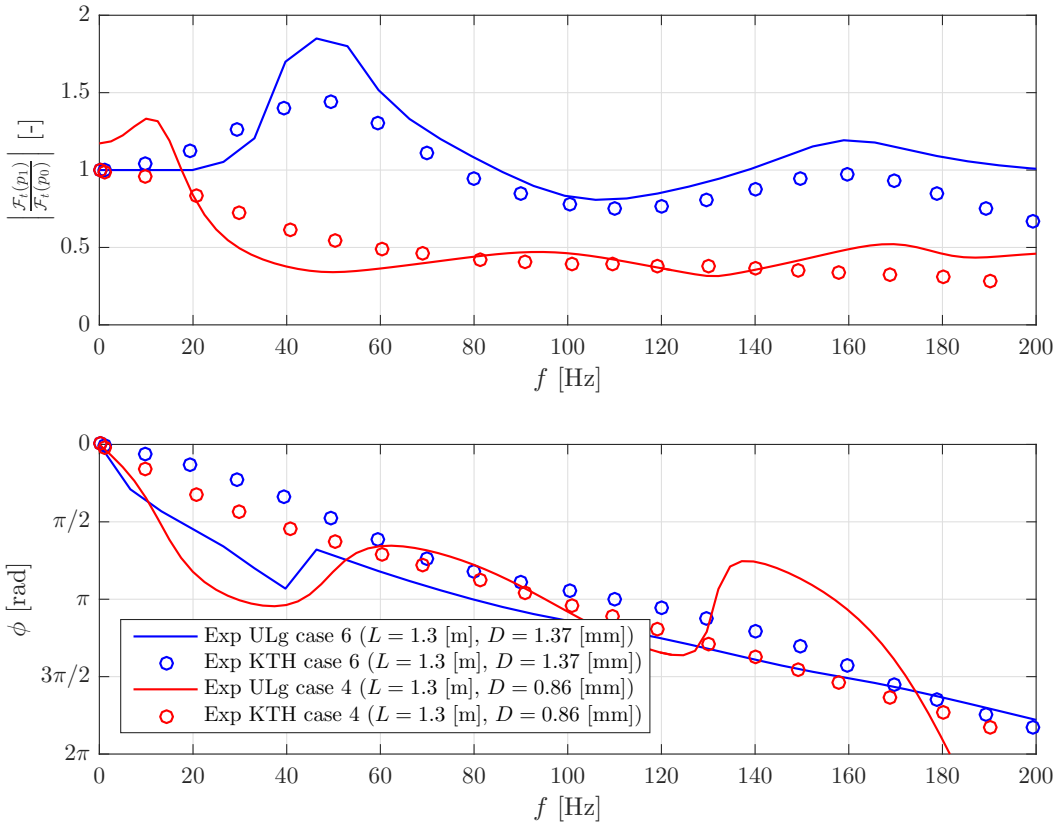

Figure 2.78 – Dynamic response: comparison between experiments in KTH and ULg

2.5 Conclusion

From this comparison theory-experiment, conclusions can be drawn:

- High degree of accuracy (and prediction) of pressure measuring system response thanks to theory (Tijdeman, RLC/impedance analogy). Nevertheless, RLC analogy can only model the first resonance (no reflections).
- Negligible non-linearities in the range considered. Tube material and bending do not have influence on the response (except using Urethane or Vinyl, with different minimum bending radius, to avoid shrinking)
- Lengthening (or slimming) decreases resonance frequency and peak amplitude. Even if the tube volume V_{tube} is constant, a long and narrow tube will attenuates the signal and decrease the resonance frequency, compared with a short and wide one.
- For diameter discontinuity, a combination of both L and D can gives opposite effect depending on the sequence (smaller then wider, or the opposite)
- The construction of amplitude ratio allows the correction of the measured signal. Thanks to IFFT correction, the reference signal can be reconstructed with a good accuracy.
- Phase correction is as important as amplitude correction. For short tube, amplitude ratio is close to 1 (as for restrictors) and the phase is low but too high to be ignored, and a phase correction is necessary. For long tubes, this phase distortion is even worst.
- Pressure calibration is important to know the standard deviation and fluctuations amplitude around a mean value (that is statically determined). This has a strong effect when studying unsteady phenomena (stall, vortex shedding,...).
- Calibration and reconstruction are possible using periodic (experiment in KTH, precise but long) and aperiodic signals (experiment in ULg, less precise, a shock tube is required to get a high time and frequency resolution but is more rapid: one test is enough to get the entire frequency range).

Chapter 3

Wind Turbine Wing

3.1 Introduction

3.1.1 Context

Chapter 2 studied the general principle of unsteady pressure calibration from a theoretical and experimental point of view. This process is particularized to the calibration of tubes typically used during experiments in the Wind Tunnel (ULg), *i.e.* with an internal diameter of 1.37 [mm] and a length of 1.3 [m] (for practical and space reasons). Indeed, the choice to calibrate this type of tube was not arbitrary and directly linked with this first application: the calibration of a Wind Turbine Wing. This section begins by introducing the context of this Wind Turbine Wing, its applications and interests. The general internal structure of a Wind Turbine Blade is rather complex: internal panels are reinforcing the structure when you approach the center of the rotor. Also, there is a huge taper along the span, *i.e.* the airfoil chord varies a lot from the root to the tip. This is directly linked with the lift distribution, which is strongly 3D dependent for a Wind Turbine Blade or equivalently for a wing. Indeed, at the end of the blade of a wing, as the pressure on the lower side is higher than the one on the upper and because there is no more material, the flow is pushed from the lower side to the upper, and it turns because of the incoming flow U_∞.

Figure 3.1 – Typical helicoidal flow create at the blade tip, behind a Wind Turbine (Mexico rotor of MexNext project), from [9]

Tip vortices can be seen in Figure 3.1 for a wind turbine, both show helicoidal flow behind the body. Moreover, because of the finite span of wings and blades, the lift distribution is not constant and is lower near tip because of these vortices. A theoretical infinite (or very huge) wing aspect ratio $\frac{b^2}{S}$ (with b the span and S the wing/blade area) will approach the perfect 2D case (*i.e.* constant lift distribution). The Wind Turbine Wing built for this study is 2D (pressure taps at mid-span with high aspect ratio). For Wind Turbine, this is not easy to make high span blades (resistance constraints, environmental constraints,...). This is why the finite span is counterbalanced by taking a particular shape of the span, taper ratio and airfoils in order to maximize the efficiency of the Wind Turbine. Tip vortices are decreased by taking a thin and sharp blade tip (smoother transition). Moreover, as the Wind Turbine is rotating, its angular speed ω is constant but the linear speed U depends on the location along the span s: $U = s \cdot \omega$. The linear blade speed is thus higher near the tip than near the

rotor. Assuming a constant incoming wind speed, a speed triangle can be constructed, representing the effective airspeed seen by each blade section. The angle of attack and airspeed is higher near the tip than near the rotor. This explains why different airfoils are used along the span: the objective is to generate a constant lift along the span (but obviously not near the tip because of tip vortices) to make the Wind Turbine turning constantly and generate the desired torque. Thus, for sections near the tip, NACA-type airfoils are used: less camber because as the angle of attack and the speed is higher, the same lift will be generated than using a higher camber with a lower speed (near the rotor). Moreover, NACA airfoils are thinner, because the drag has to be minimized (more likely to be higher near tips because of the higher speed).

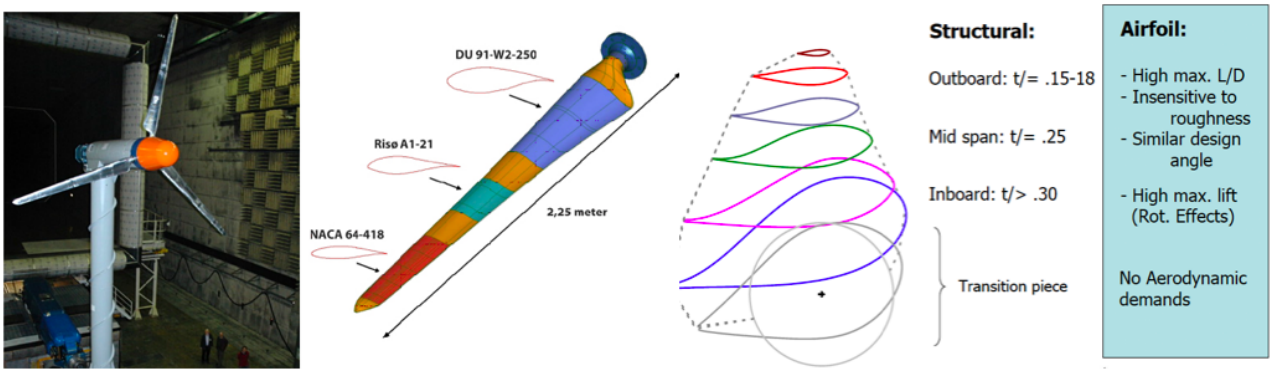

Figure 3.2 – Overview of Mexico rotor in DNW and its blade structure, from [10] and [44]

Near the rotor, thicker profiles of DU-type are used because the drag will be lower (lower speed). These thicker profiles will generate more lift thanks also to the higher camber (to compensate the lower angle of attack and airspeed). Figure 3.2 shows the general use of airfoils along a Wind Turbine Blade and the internal structure of a blade section. Figure 3.2 shows the Wind Turbine made with DU-type airfoils, an overview of Mexico rotor in DNW, the German-Dutch Wind Tunnel [15].

3.1.2 Motivations

This chapter will studied is a special Wind Turbine profile, the DU 96-W-180. This project is in the scope of the PhD of Giulio Vita, in collaboration between Birmingham, TU Delft and ULg. In TU Delft, they develop a series of different airfoils for Wind Turbine Blades (for sections near the rotor, Figure 3.3).

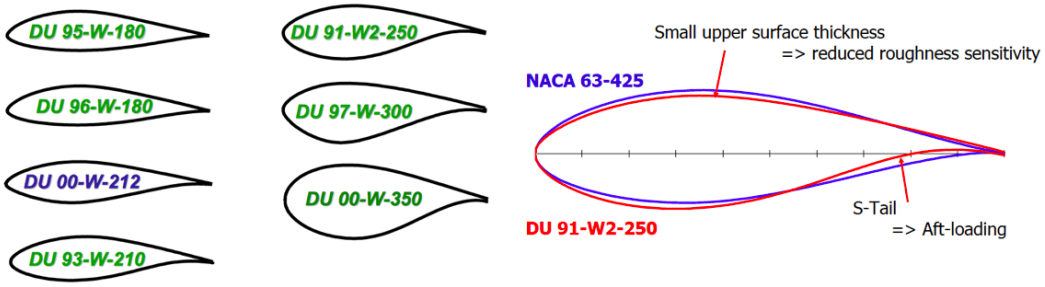

Figure 3.3 – Overview of DU-airfoils studied in TU Delft, from [74]

Giulio Vita is interested in turbulent CFD simulations over this airfoil to see the influence of the turbulence in the incoming flow of the aerodynamics around the airfoil, the turbulence intensity and typical turbulence length scales. He designed 3 different grids with different mesh size to generate different turbulence intensities and length scales in a controlled and comparable way. In February 2017, my internship and Master Thesis started by some measurements with Giulio Vita to characterize the flow behind the grids, *i.e.* with a Cobra Probe for several distances downstream and several heights. He wanted to see the influence of this turbulence on the flow around the airfoil DU 96-W-180. Nevertheless, this work will focus on the flow around the airfoil without grid and particularly study

the stall phenomenon at a high angle of attack which induces separation of the flow, huge vortices creation and some unsteady pressure. This last characteristic will be studied deeply. After the flow characterization, some pressure measurements were taken around the airfoil at different airspeeds and angles of attack, in the scope of the integrated exercise of the course of Aerodynamics (in Aerospace Engineering Master). The added-value of this chapter will be to study the effect of internal channels inside the 3D printed profile. In Chapter 2, the effect of tubes alone was studied, their diameter, length, diameter discontinuities but not the complex shape inside the airfoil. Indeed, when the pressure is measured along the airfoil, PVC tube are used between pressure taps (where the pressure has to be known) and the pressure scanner, which is on the floor. As studied in Chapter 2, the tube will perturb the flow and the pressure measured at the end (by the pressure scanner) is not the same than the one at the pressure tap. This model will be studied according to three points of view (to study the stall but not the turbulence effect):

- **Experimental:** Unsteady pressure measurement on the WT model, using the calibration method studied in Chapter 2
- **Numerical:** Panel method, `XFOIL-XFLR5` software and CFD with `OpenFoam`
- **Theoretical:** Inviscid analytical models can predict the lift at low angle of attack (before the stall). They are discussed in Appendix B.2, to compare results with experimental and numerical models (lift slope at low angle of attack). However, a semi-empirical model for dynamic stall has been studied by Leishman and Beddoes [43], to represent the unsteady lift and drag characteristics of a dynamically stalled airfoil. The principle is based on an indicial formulation, "the onset of vortex shedding during dynamic stall is represented by a criterion for Leading edge (LE) separation (based on the attainment of a critical LE pressure. The TE separation is represented using a Kirchhoff flow model in which the separation point is related to the airfoil behavior." [43] A comparison with Mexico data (Figure 3.2) was done by Pereira [54] but this is out the scope of this study, based on experimental and numerical models.

Comparison will also be made with other references, from TU Delft [74]. Each of these three aspects are associated to advantages and drawbacks (Figure 3.4).

	Experimental	Theoretical	Numerical
Advantages	Deals with real flows Accuracy High Reynolds Number Turbulent flow	Exact solution Boundary conditions	Easy variation of parameters Boundary conditions Seperate effects and phenomena Time required and costs
Disadvantages	Experimental errors Similarity hypothesis Limited test ranges Boundary conditions Time required and costs	Specified conditions Simplified equations Very simple geometries	Numerical errors Low Reynolds numbers Turbulence properties Mathematical models

Figure 3.4 – Advantages/disadvantages of the experimental, theoretical and numerical approaches [44]

Obviously, theoretical models are easy to implement and study, to obtain exact solution but they are associated with strong assumptions and simplifications. Nevertheless, it is always a good point to make the link with it and understand the physics and hypotheses behind. Numerical methods start from theoretical equations that are discretized to be implemented as finite differences, finite elements for example. It allows to take into account any geometry and obtain results directly with a computer (but the cost can vary a lot). Nevertheless, numerical errors can happen (from the discretization, mesh, scheme,...). Turbulence is a hot topic, and mathematical models are required to simplify equations (RANS, see section 3.3.3). In parallel with these methods, the experiment is always necessary, to test a final prototype, or when unknown phenomena are involved,... This method allows a complete study of any situation (Reynolds number, turbulence,...), with accuracy. Nevertheless, the question of scaling has to be well posed[1]; some errors are also inherent with instrumentation. A discussion about the types of errors is made in Appendix B.1.

[1] Adimensional numbers have to be respected to represent the same physics (Buckingham π theorem)

3.2 Wind Tunnel experiment

3.2.1 Model and instrumentation

The first material used is an experimental model. As explained, the setup was used for the lab session and integrated exercise in the scope of Aerodynamics course in 1^{st} Aerospace Engineer Master. The setup is shown in Figures 3.5 and 3.7, a structure made of `Bosch` aluminium profiles (40×40 [mm]) is supporting the wing, at mid-height and mid-width of the Wind Tunnel Test Section 1 (Figure 3.5). Pressure taps are located in the central section of the wing (3.5 and Figures 3.7). Pressure tubes connect pressure taps to the pressure scanner (where pressure is effectively measured, Figure 3.6), all 40 tubes have to pass through the half span of the wing and are then linked to the pressure scanner (Figures 3.7 and 3.5). They are 1.3 [m] long with a diameter of 1.37 [mm], their calibration will be explained in section 3.2.2. A Pitot tube is in front of the wing to measure the free stream velocity U_∞ and pressure p_∞ (Figures 3.7 and 3.5). A connecting rod system is used to fix the wing on the supporting structure, with a rotating degree of freedom (in order to get aerodynamic characteristics depending on the angle of attack). This angle of attack is measured with an electronic spirit level placed on the upper side of the TE of the airfoil. The angle between this upper side and the chord line (thus the angle measured by the spirit level at zero angle of attack) is 12.9 [°] (Figure 3.6).

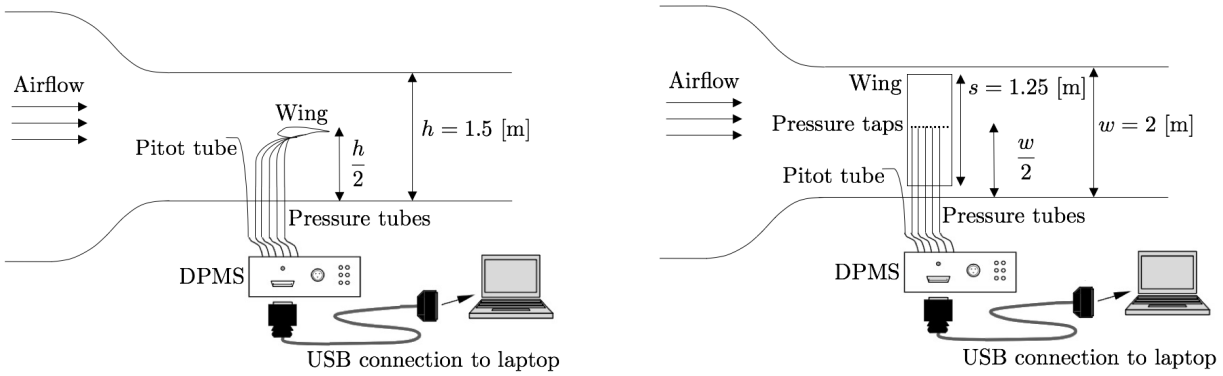

(a) Side view (b) Top view

Figure 3.5 – Schematic of the model inside the Wind Tunnel Test Section 1, with measurement tools

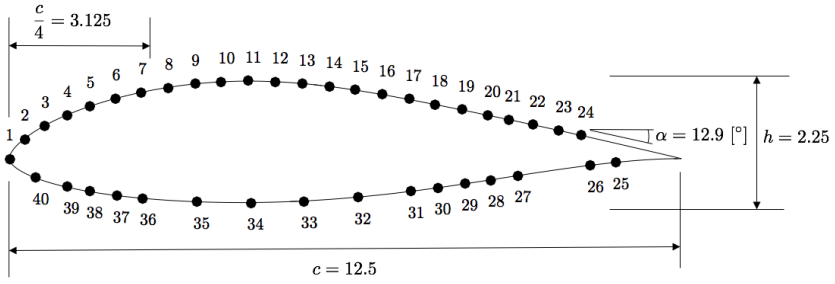

Figure 3.6 – Schematic of the wing central section and pressure taps location, dimensions in [cm]

The solid blockage correction consists in increasing the effective WT airspeed by an increment ΔU_∞ :

$$\Delta U_\infty = \epsilon_{sb} U_{\infty,u} \text{ and } \epsilon_{sb} = \frac{K_1 V_B}{S^{3/2}} = \frac{0.74 \cdot 1.8 \cdot 10^{-3}}{3^{3/2}} = 2.5 \cdot 10^{-4} = 0.025\% \tag{3.1}$$

where $U_{\infty,u}$ is the uncorrected airspeed (Pitot airspeed), ϵ_{sb} the correction factor, $K_1 = 0.74$ for a horizontal model, $S = 2 \cdot 1.5 = 3$ [m^2] is the working section area (Wind Tunnel test section 1 and $V_B = s \cdot A = 1.25 \cdot A = 1.8 \cdot 10^{-3}$ [m^3] is the body volume (with s the span and A the area of the profile). The total correction is rather small because of the small model size compared to the test section. The pressure scanner is the same as the one used is Chapter 2, DPMS (Figure 2.61). The pitot tube is

connected to the the DPMS (one tube for the reference (static pressure p_∞) and the other connected to the matrix of pressure taps, to deduce the free stream velocity from $U_\infty = \sqrt{2(p_{stag} - p_\infty)/\rho}$ (with p_{stag} the stagnation pressure measured at the tip of the Pitot tube), and the total pressure $p_t = p_\infty + q = p_\infty + \frac{1}{2}\rho u^2$. The pressure coefficient is an adimensional measure of the measured dynamic pressure $q = p - p_\infty$,

$$c_p = \frac{p - p_\infty}{\frac{1}{2}\rho U_\infty^2} \tag{3.2}$$

Global quantities (aerodynamic forces) can be deduced from the pressure $p(s)$ and shear stress $\tau_w(s)$ distributions. From the potential flow theory (inviscid assumption), it has ben shown that pressure is the most responsible for lift, *i.e.* inviscid flow is a good approximation for lift (Figure B.8). Nevertheless, drag is composed of pressure and friction parts. Knowing the pressure on each pressure tap (X), it can be integrated to know the lift and the pressure drag (using sin instead of cos in equation 3.3) by projection of each "panel" (mid points between pressure taps), taking into account the incidence α (Figure B.9 in Appendix B.3)[2]

$$c_l = \sum_j \frac{p_j l_j \cos(\theta_j - \alpha)}{\frac{1}{2}\rho U_\infty^2 c} = \sum_j \frac{(p_j - p_\infty) l_j \cos(\theta_j - \alpha)}{\frac{1}{2}\rho U_\infty^2 c} = \sum_j c^- p_j \cos(\theta_j - \alpha)\frac{l_j}{c} \tag{3.3}$$

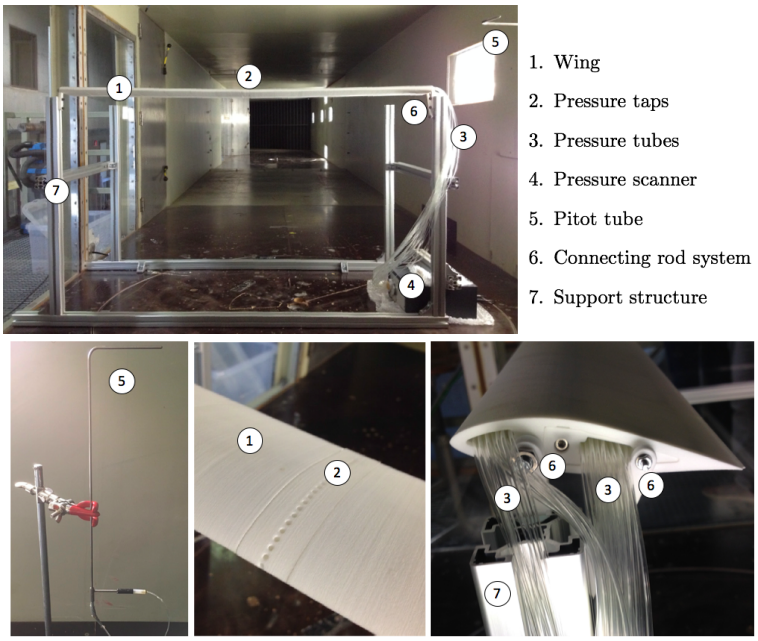

Figure 3.7 – Front and side views of the wing setup inside the Wind Tunnel Test Section 1

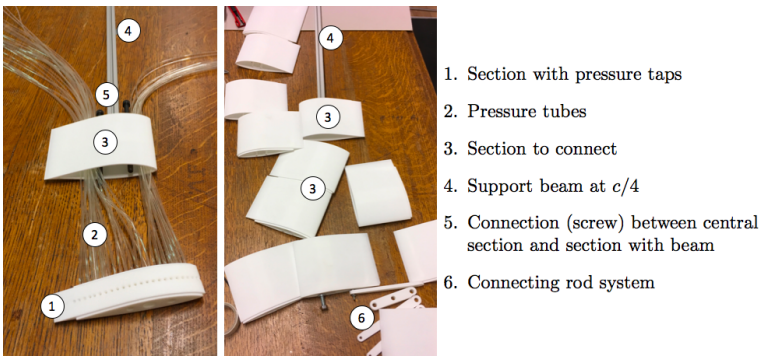

Figure 3.8 – Assembly process and internal structure of the wing setup

[2]Noting that $\oint p ds = \oint p - p_\infty ds$ (integral of a constant around a closed contour is 0).

3.2.2 Calibration of the model

Set-up Figure 3.9 shows the two types of tap used for the profile. Figure 3.10 shows 3D transparent views of the wing model. To measure pressure along the section, pressure channels are 3D printed in the section to connect pressure taps and the tube. These channels are all of the shape of hole 10 (Figure 3.10) except holes 2, 24 and 26. These channels are longer, with bending and diameter restriction, they have thus to be calibrated and compared to the simple channel 10, according to conclusions of Chapter 2. Dynamic response of different holes (and also the effect of tap size, Figure 3.9) will be compared.

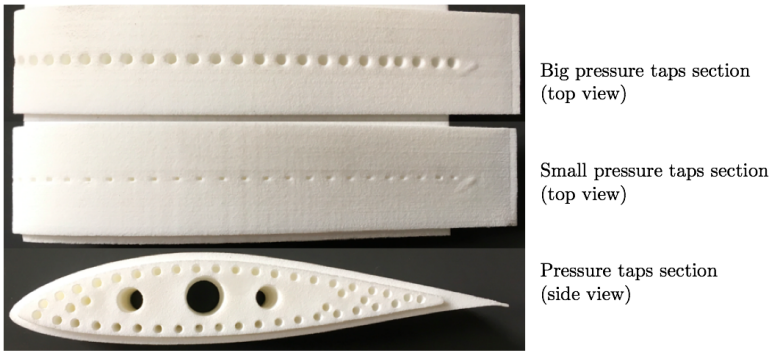

Figure 3.9 – Top and side views of the wing central section with big/small pressure taps

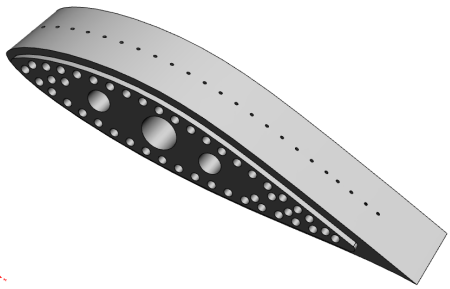

(a) Axisymmetric solid view of the wing central section

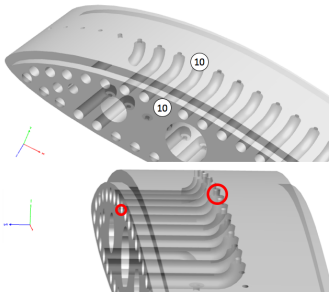

(b) Pressure tap/channel 10

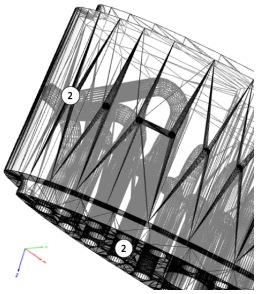

(c) Pressure tap/channel 2

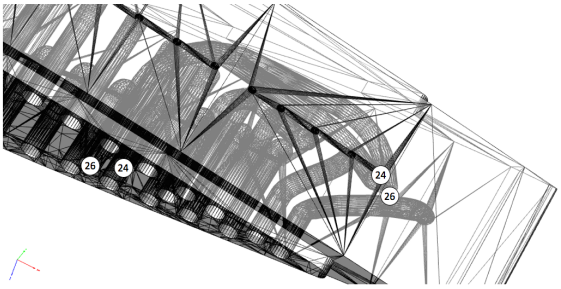

(d) Pressure taps/channels 24 and 26

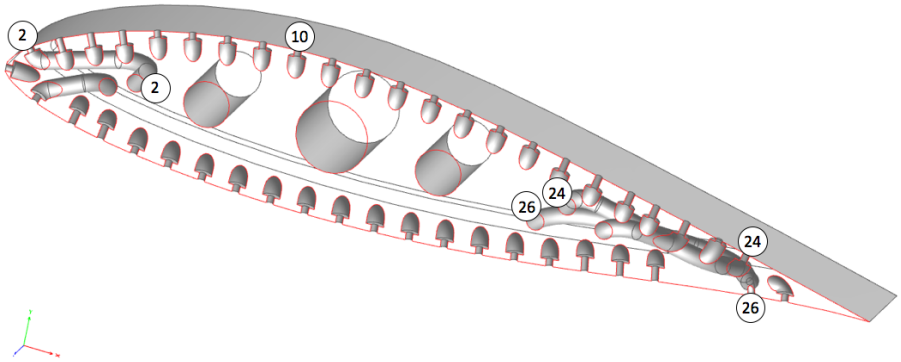

(e) Mid-cross section of the wing central section and summary of all retained (calibrated) channels

Figure 3.10 – Solid, transparent and cut views of the wing central section model and retained channels

The setup used to measure the dynamic response of the model channels is exactly the same as the one used in KTH fo simple tubes. All devices and tools are the same, except the T-connector: for this case, the pressure tube coming from the generator is connected to a cavity reference, inside which the reference transducer is placed (Figure 3.11). A small rubber ring below the reference cavity allows to avoid leakage and guarantees a good connection between reference cavity and wing taps/channels (and a transducer measures the pressure at the end of this tube). The model is clamped in a vice. The reference cavity is schematized in Figure 3.11: a discharge line (outflow tube) allows for the dissipation of the pressure wave and ensures the symmetry of the pressure wave in the cavity (compared to the tap below). Sensors are of the same type as Figure 2.54 (Kulite XCQ-062) but differently connected to the pressure tubes, with a sensor battery (Figure 3.12). Results of calibration will be discussed in section 3.2.2. The setup used for ULg calibrator is the same as Figure 2.60, with the wing fixation in Figure B.10.

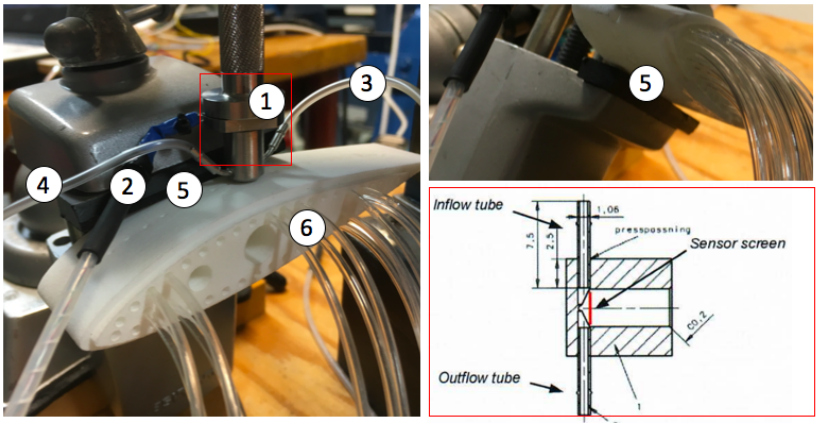

1. Reference cavity
2. Reference transducer
3. Pressure tube from generator
4. Discharge line
5. Wing model clamped on vice
6. Pressure tube with transducer at the end

Figure 3.11 – Setup in KTH for the wing calibration

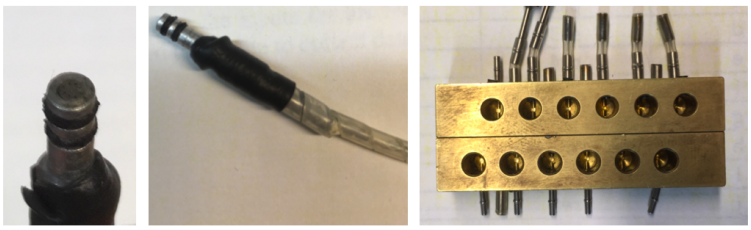

Figure 3.12 – Pressure transducer and sensor battery in KTH

Results This section studies the effect of adding internal channels of the profile to the pressure tubes (studied in Chapter 2). Figure 3.13 compares experimental data and Tijdeman model of case 6 (simple tube alone with $L = 1.3$ [m] and $D = 1.37$ [mm]) with data from profile 1 (*i.e.* airfoil with big taps). All holes show the same dynamic response proving that bending does not influence the response, if the bending radius is high enough to avoid shrink. The Tijdeman model associated to profile 1 is also shown, using two tubes (a small one before the tube of case 6) with $L_1 = 3$ [mm] (begin of taps), $D_1 = 1$ [mm], $V_1 = 0$, $L_2 = 1.35$ [m], $D_2 = 1.37$ [mm]. Shapes of case 6 and profile 1 are similar but the added length of the tube (channel inside the profile) and diameter change at the tap attenuate the response and decrease resonance frequencies. Hole 10 is representative of most profile holes, holes 2-24-26 show more specific shape. Anyway, they show the same response.

Figure 3.14 shows the same results than Figure 3.13 but for profile 2 (small holes, same geometry as Tijdeman profile 1 but $D_1 = D_2/3 = 0.4$ [mm]). The dynamic response is completely different to case 6 (tube alone). The very narrow tap size (Figure 3.10) attenuates a lot the response, for all frequencies. Hole 10 is well estimated with Tijdeman profile 2, hole 24 shows a more attenuated response (narrow part a bit longer, Figure 3.10). This behavior is similar to the response of test blades in Figure 3.15.

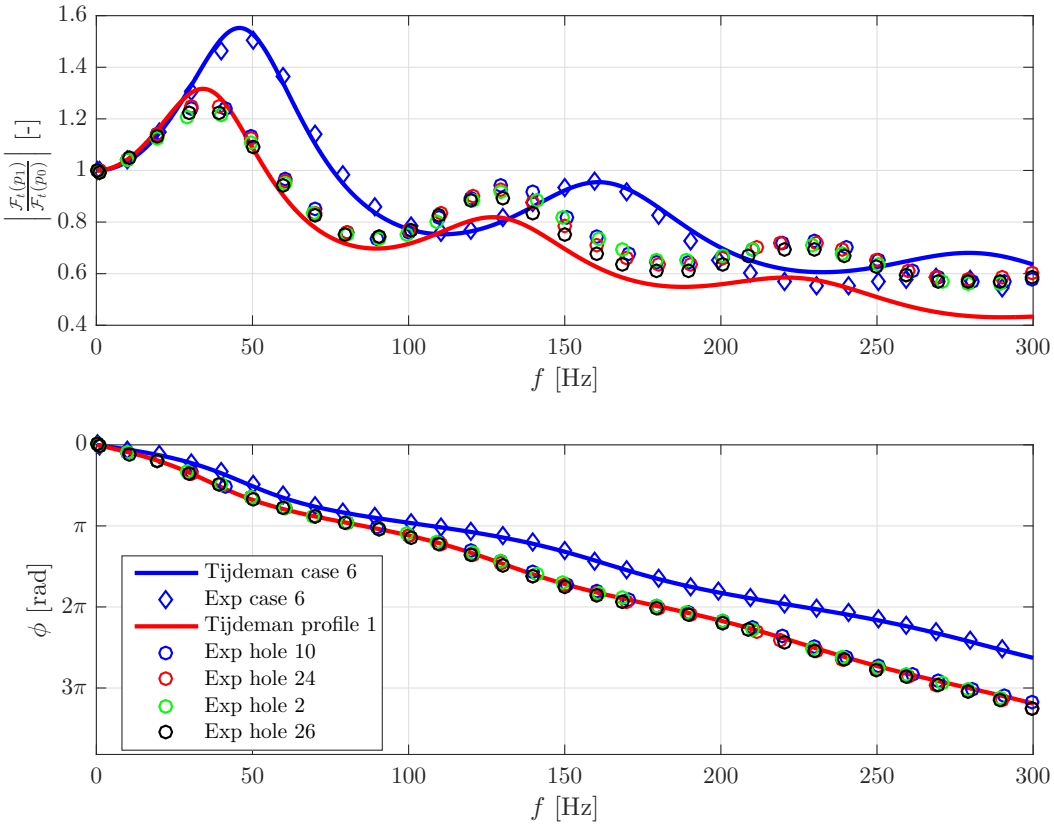

Figure 3.13 – Dynamic response of wing profile 1: comparison of holes 10,24,2,26 and a tube alone (case 6) (experiment and Tijdeman theory)

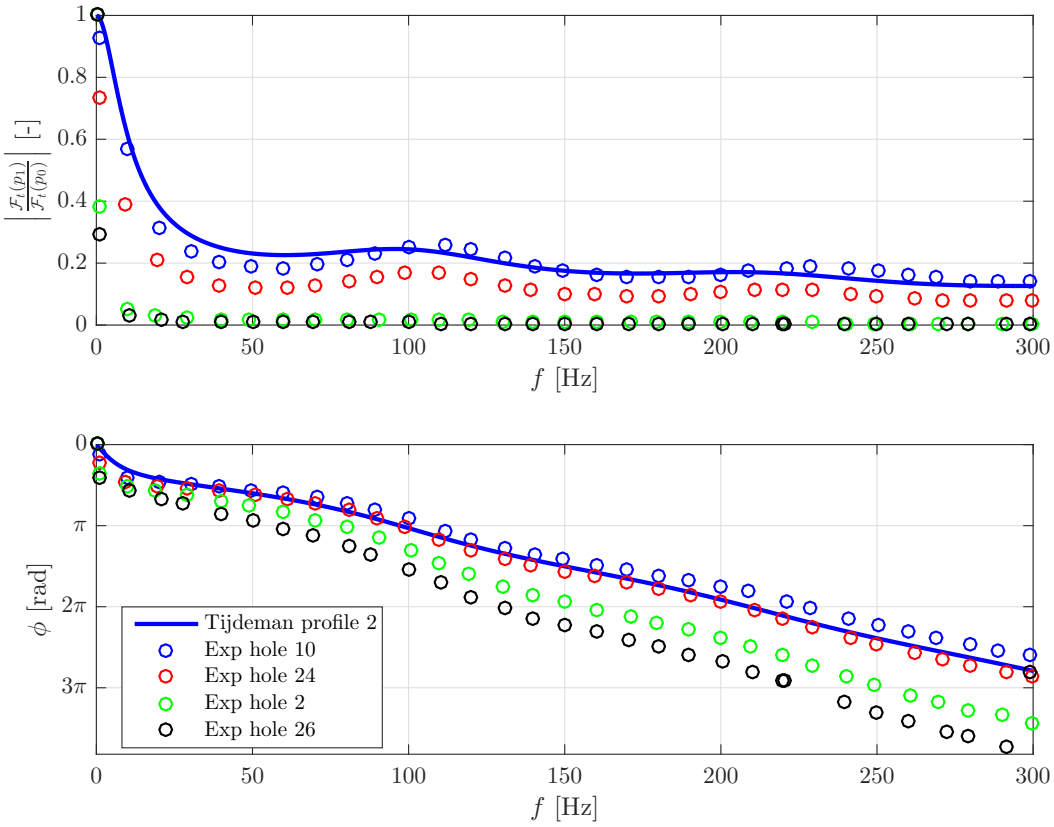

Figure 3.14 – Dynamic response of wing profile 2: comparison of holes 10,24,2,26 (experiment and Tijdeman theory)

To be familiar with the calibration apparatus in KTH, some tests were performed on test blades (Figure B.11 in Appendix B.5, same setup as Figure 2.50). Pressure taps on the blade of 0.4 [mm] diameter are connected by capillarity tube (inside the blade, with 0.5 [mm] diameter) to the blade root. A flexible vinyl tube (inner diameter of 0.8 [mm] and length of 53 [mm]) is used to connect capillarity tube to sensor battery. In Figure 3.15, two lengths of capillarity tube were tested and for both, every frequency are attenuated. The longer the tube, the higher the attenuation. Inner diameters are narrow but the total length is not high (53 [mm] for blades in Figure 3.15 and 1.3 [m] for profile 2 in Figure 3.14, that explains why the response of profile 2 is even more attenuated). For high frequencies, close to 500 [Hz], the amplitudes of the response are close to each other, for both long and short blade tubes. The short tube response is highly monotonic (very low second derivatives), suggesting that influences from pressure reflections due to the short length are negligible. Because of low second derivatives above $f = 100$ [Hz], a few points are necessary to construct the dynamic response (the 10^{th} order polynomial fit is almost straight is this region) so the calibration is faster.

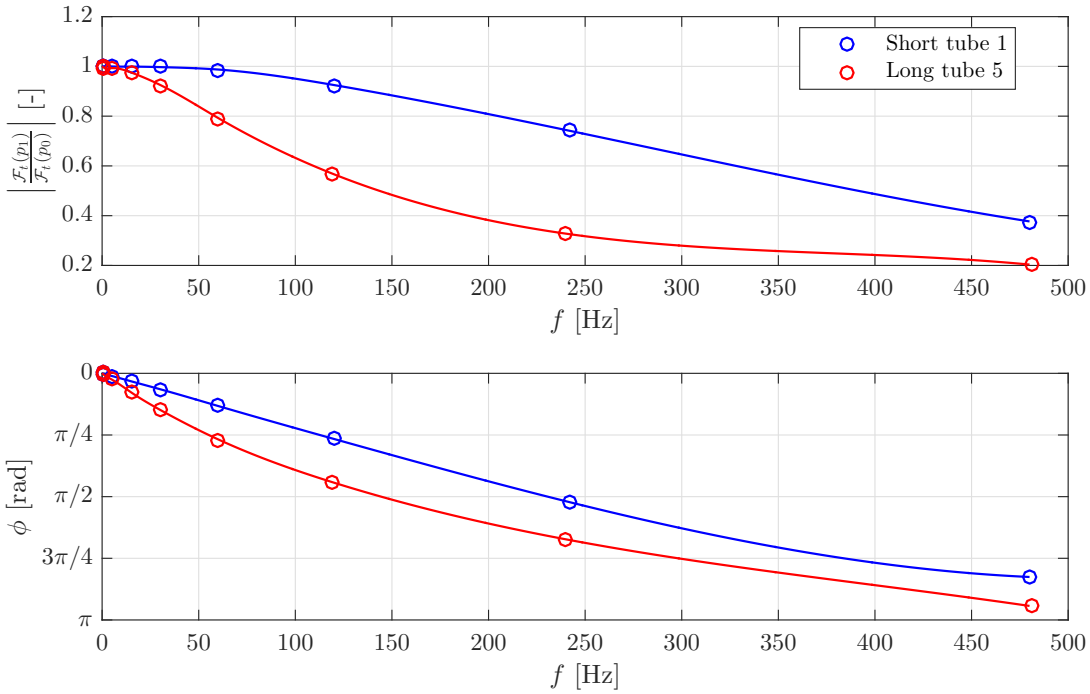

Figure 3.15 – Dynamic response of test blades in KTH: comparison of tube termination, with polynomial fit (10^{th} order)

Figure 3.16 shows pressure time signals (for profile 1, holes 10,24,2,26) at $f = 1$ [Hz], each one superposed with the reference, as expected for this frequency. However, holes 2 and 26 of profile 2 (Figure 3.17) attenuate a lot the signal, even at $f = 1$ [Hz] which was not expected. This suggests that the profile is not well printed or that some obstruction is present. This explains why the response is so attenuated in Figure 3.14 for holes 2 and 26, even at $f = 1$ [Hz] and almost to 0 for higher frequencies. These 2 holes will thus not be considered further. Figure 3.18 shows the pressure signal at $f = 40$ [Hz] for the reference, measured at the end of hole 10 (comparison of profile 1 and 2). Clearly, as observed in Figure 3.14, profile 2 attenuates a lot the response (because of narrower taps) compared to profile 1. Using the FRF correction for each profile, the reference can be reconstructed with a high accuracy (using a cut-off frequency for the low pas filter of $f_c = 300$ [Hz]). Figure 3.19 compares reference, measured and reconstructed pressure step signal obtained with ULg calibrator for both profiles (at hole 10, because of previous remarks). For profile 1, the measured signal is delayed because of the tube length and the inlet diameter restriction. For profile 2, the tap diameter is so narrow that the response is completely delayed, the pressure is no longer assimilated to a strong step but to a damped one. This makes the correction (using RFP fit) difficult to recover the reference signal from the measured one (too much damped). This explains again why measurements on profile 1 are preferred in the following experiments. Nevertheless, differences in signal response due to tap diameter are interesting to study.

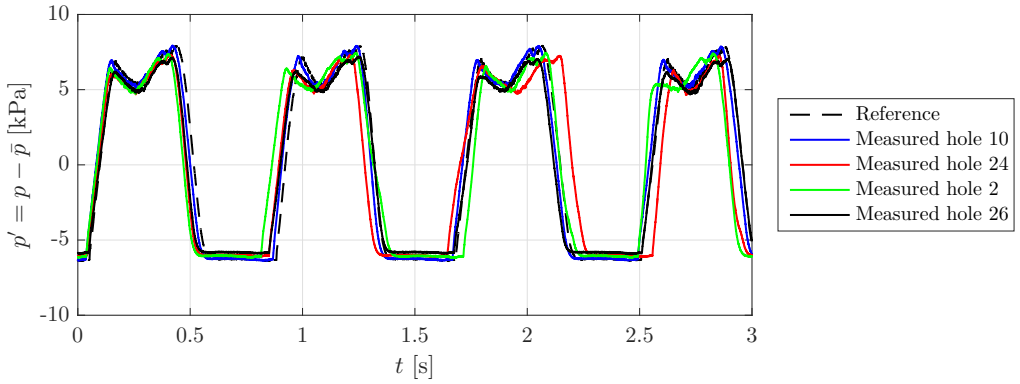

Figure 3.16 – Profile 1 (big taps): Time pressure signals $p' = p - \bar{p}$ [kPa] at $f = 1$ [Hz]: comparison of reference, measure at the end of the tube (holes 10, 24, 2, 26 of Figure 3.10)

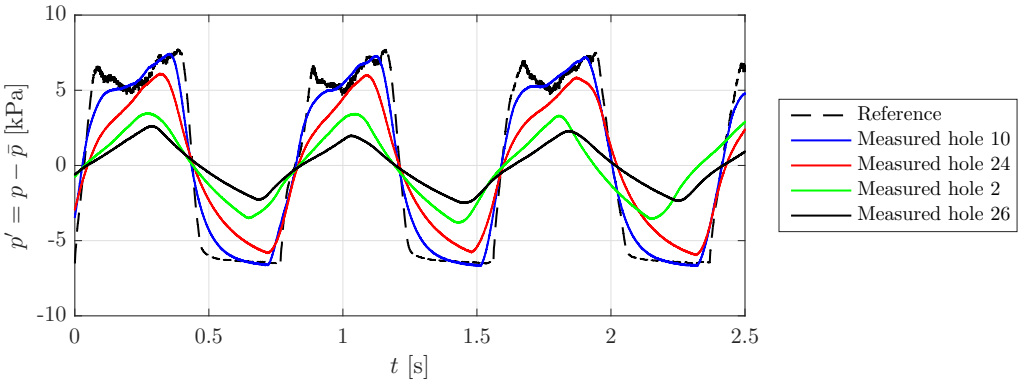

Figure 3.17 – Profile 2 (small taps): Time pressure signals $p' = p - \bar{p}$ [kPa] at $f = 1$ [Hz]: comparison of reference, measure at the end of the tube (holes 10, 24, 2, 26 of Figure 3.10)

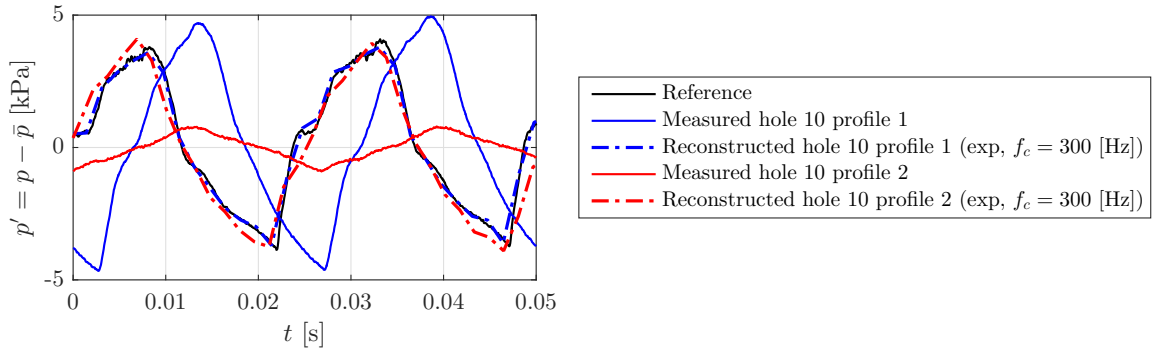

Figure 3.18 – Time pressure signals $p = p' - \bar{p}$ [kPa] at $f = 40$ [Hz]: comparison of reference and measure at hole 10 of profiles 1 and 2: reference, measure and correction

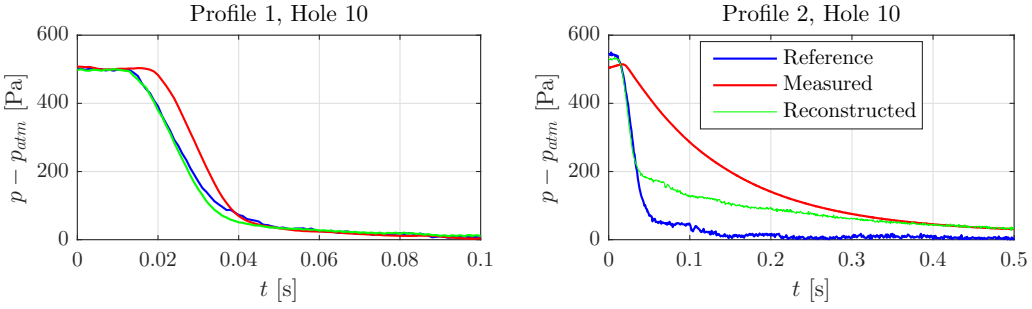

Figure 3.19 – ULg calibrator: pressure step signals at hole 10 of profiles 1 and 2 (reference, measured and reconstructed)

3.3 Numerical models

The purpose is to measure and characterize the flow around the airfoil. Additionally to experiments, some numerical models can compute pressure distribution and global quantities (lift coefficient c_l,...). Analytical (inviscid) models at low angle of attack are presented in Appendix B.2.

3.3.1 Panel method

For a specified body shape, replace its surface by singularity panels (source panels q_i, doublet panels, vortex panels γ), enforce boundary conditions on the discretized geometry (Flow tangency and Kutta), solve numerically a system of equations to compute its aerodynamic characteristics. The body shape is divided into N panels with 3 contributions on each control points: Uniform flow + Source distribution + Vortex distribution (Hess & Smith method). The system of equations is constructed with N flow tangency conditions + 1 Kutta condition (in [64]). Solving it allows to compute the tangential component of velocity on the i^{th} panel of the body as well as the associated pressure coefficient and the lift (from Kutta-Joukowski theorem (circulatory lift theory)),

$$c_p(\bar{x}_i, \bar{y}_i) = 1 - \left(\frac{V_t^i}{V_\infty}\right)^2 \quad , \; c_l = \frac{2\gamma}{cV_\infty} \sum_{j=1}^{N} l_j \tag{3.4}$$

This simple (inviscid) numerical method allows to compute rapidly aerodynamic characteristics. To validate it, a convergence study is made on c_l and c_d compared to the number of panels N used (Figure 3.21). There is no analytical function describing the airfoil (only a set discrete 200 points). These points are interpolated, to reconstruct the airfoil with a desired number of points and so a number of panels N. Figure 3.21 shows the convergence of c_d and c_l with N (computed with equation 3.4, so using vorticity γ, or by integration of c_p (equation 3.3)). Convergence is fast and the initial number of points and panels (200) is sufficient for good results.

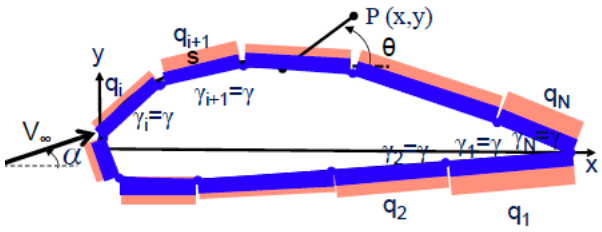

Figure 3.20 – Panel method: source q_j and vortices γ distribution

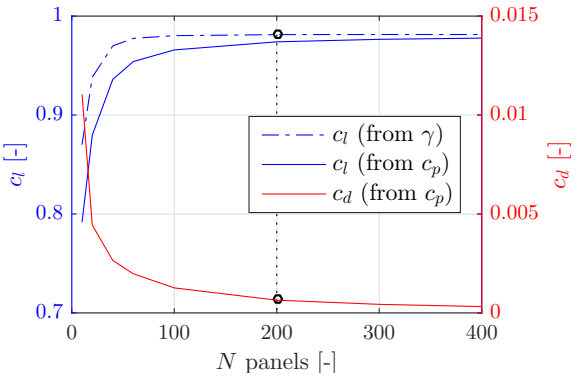

Figure 3.21 – Convergence study: c_l and c_d vs N for DU96w180 profile at $\alpha = 5$ [°]

3.3.2 Xfoil-XFLR5

`Xfoil` is a very useful software to calculate the pressure distribution on the airfoil and hence lift and drag characteristics, given the coordinates specifying the shape of a 2D airfoil, Reynolds and Mach numbers (2D viscous flow). `XFLR5` is a graphical software based on `Xfoil` (direct and Inverse analysis), able also to perform Wing design and analysis based on the Lifting Line Theory, on the Vortex Lattice Method, and on a 3D Panel Method (3D wing). In experimental data, 2 velocities were studied: $U_\infty = 7$ and 15 [m/s]. Results from `XFLR5` are computed for,

- DU96w180 profile coordinate points (200, same as for panel method because this number allows convergence) in `point.dat`.

- `Xfoil` uses a free transition criterion, the e^N method (always active) with a user-specified parameter "N_{crit}" (which is the log of the amplification factor of the most-amplified frequency which triggers transition [16]). It depends on ambient disturbance level in which the airfoil operates and mimics the effect of such disturbances on transition ($N_{crit} = 9$ is taken, for an average WT). Reynolds number $Re = \frac{U_\infty c}{\nu} = 0.6 \cdot 10^5$ and $1.2 \cdot 10^5$, $\alpha = 0$ to 20 [°]
- Mach number $M_\infty = \frac{U_\infty}{a_\infty} = 0.02$ and 0.04 (with $a_\infty = 340$ [m/s], the free stream speed of sound). Specify the M_∞ will take into account compressibility effects, by dividing $c_l, c_p, ...$ by the Prandtl-Glauert correction $\beta = \sqrt{1 - M_\infty^2}$, negligible here because $M_\infty << 0.3$.
- 3D characteristics computed thanks to Prandtl lifting line theory described above (by discretizing the span in N y_0 locations)

3.3.3 Computational Fluid Dynamics

A CFD model, (Unsteady) Reynolds Averaged Navier-Stokes Equations ((U)RANS) with $k - \varepsilon$ is implemented using `OpenFoam`. Assumptions are explained in the following. CFD allows to simulate numerically flow around the profile. It is based on the finite differentiation of Navier-Stokes equations. Here, the unsteady (dynamic) pressure is of interest, thus when the airfoil stalls. For this configuration, the boundary layer is separated, with vortices creation and turbulence being present. A distinction has to be made between steady and unsteady flows:

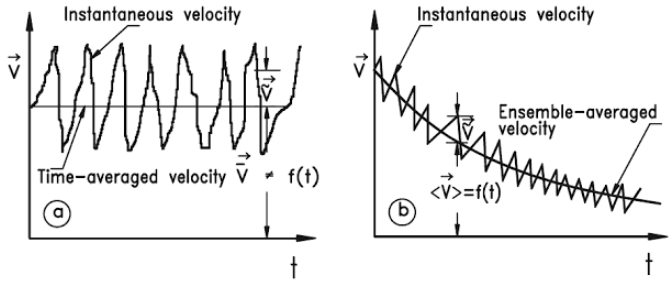

Figure 3.22 – Turbulent flows: Statistically steady (a), unsteady (b) [47]

- Steady: the flow does not depend on time ($\partial_t \cdot = 0$). Steady state is a condition where fluid properties at a point is not a function of time.
- Transient or unsteady flow: time-dependent flow. Turbulence is inherently an unsteady phenomenon by definition, since it involves rapid variations of the fluid properties. However, a turbulent flow can be *statistically stationary* (Figure 3.22): "The random field U(x,t) is statistically stationary if all statistics are invariant under a shift in time." [57]. In other words, statistical properties are constant over time (the mean flow for example, see (U)RANS).

Unsteady phenomena occurring during separation are linked to turbulence (using (U)RANS). There are several methods to compute Navier-Stokes equations in turbulent flows:

- Direct Numerical Simulation (DNS): Solving "exact" NS equations, (up to discretization) at each scales, requires a lot of resources. Indeed, turbulence is characterized by a large amount of different scales, so the numerical mesh has be of this minimal size and is numerically costly.
- (U)RANS: It assumes that in turbulent flow, the instantaneous quantities can be decomposed into mean and fluctuations (Figure 3.23): $u(x,t) = \bar{u}(x,t) + u'(x,t)$ ($= \bar{u}(x) + u'(x,t)$ for statistically steady flow). This leads to averaged boundary layer equations, the same as in a laminar case but with some additional Reynolds stresses $\propto \overline{u'v'}$. This adds 6 unknowns so the system has to be closed, for example using Boussinesq assumption and turbulent viscosity ν_T: $\overline{u'v'} = -\nu_T \frac{\partial \bar{u}}{\partial y}$. Prandtl's mixing length assumption (mixing length) states that $\nu_T = (\kappa y)^2 \left| \frac{\partial \bar{u}}{\partial y} \right|$, with κ the von Karman constant.

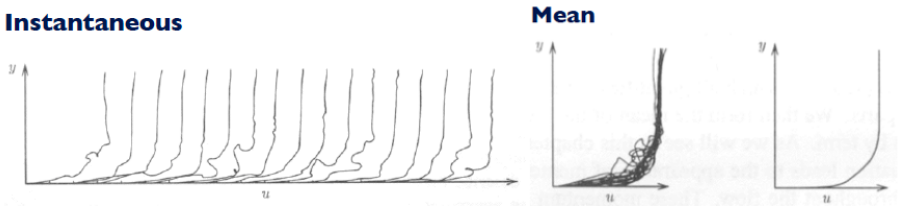

Figure 3.23 – Reynolds decomposition [72]

Other models can be used, such has Spalart-Allmaras, $k-\omega$ SST or $k-\varepsilon$ (used here). This is a two equation model to avoid the empiricism associated with the mixing length,

$$\begin{cases} \frac{\bar{D}k}{Dt} = \nabla \cdot (\nu_k \nabla k) + 2\nu_e \bar{e} : \bar{e} - \varepsilon \\ \frac{\bar{D}\varepsilon}{Dt} = \nabla \cdot (\nu_e \nabla \varepsilon) + 2\nu_e \bar{e} : \bar{e} \left(C_{\varepsilon 1} \frac{\varepsilon}{k}\right) - \varepsilon \left(C_{\varepsilon 2} \frac{\varepsilon}{k}\right) \end{cases} \tag{3.5}$$

With, $\nu_e = C_\mu \frac{k^2}{\varepsilon}$, $\nu_k = \frac{1}{\sigma_k}\nu_e$, $\nu_\varepsilon = \frac{1}{\sigma_\varepsilon}\nu_e$, $C_\mu = 0.09$, $\sigma_k = 1$, $\sigma_\varepsilon = 1.3$, $C_{\varepsilon 1} = 1.44$, $C_{\varepsilon 2} = 1.92$, $\bar{e}_{ij} = \frac{1}{2}\left(\frac{\partial \bar{u}_i}{\partial x_j} + \frac{\partial \bar{u}_j}{\partial x_i}\right)$ and $k = \frac{1}{2}\bar{u'^2}$ the turbulent kinetic energy [29]. This model is already implemented in the software used here for CFD, `OpenFoam`. The geometry has to be specified, as well as the mesh, using `Gmsh`. Figure 3.24 shows the chosen C-grid and its dimensions with parameters for the number of elements on edges: N_C (without progression) and N_R (without progression along the chord, with progression $p_V = 1.05$ of vertical edges and progression $p_H = 1.01$ for the horizontal one, behind the airfoil). The generated mesh is in Figure B.12 in Appendix B.3). Boundary conditions are essential to have a well-posed problem, on table 3.1.

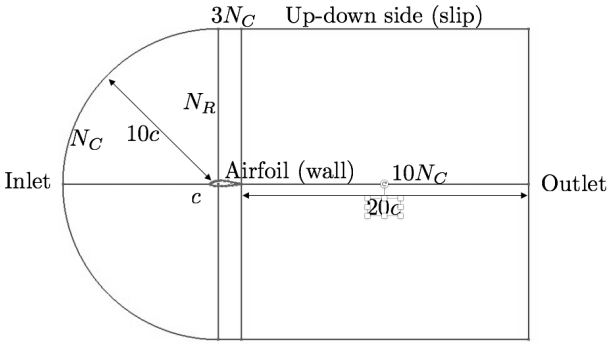

Figure 3.24 – Domain geometry and boundaries of the wing

	Inlet	Outlet	Airfoil	Up-down side
Velocity U	7 or 15	zero gradient	0	zero gradient
Pressure p	zero gradient	0 (p_{ref})	zero gradient	zero gradient
Turbulent viscosity ν_T	calculated (+init)	calculated (+init)	calculated (+init) (nutkWallFunction)	calculated (+init)
Turbulent kinetic energy k	fixed value (+init)	zero gradient	calculated (+init) (kqRWallFunction)	zero gradient
Turbulent dissipation ε	fixed value (+init)	zero gradient	calculated (+init) (epsilonWallFunction)	zero gradient

Table 3.1 – Boundary conditions of the wing model domain

Once a turbulent quantity is calculated (using `OpenFoam` function), it has to be initiated, using a rule of thumb for example [29] (using $U = 15$ [m/s]),

$$k = \frac{1}{2}U'^2 = 0.28 \ , \ \varepsilon = \frac{C_\mu^{0.75} k^{1/2}}{l} = 13.94 \ , \ \nu_T = \frac{C_\mu k^2}{\varepsilon} = 5{\cdot}10^{-4} \ , \ U' \approx 5{-}10\%U \ , \ l = 5{-}10\%c \tag{3.6}$$

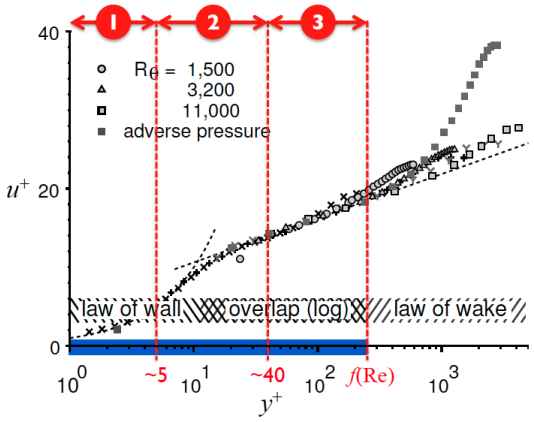

Figure 3.25 – Velocity profile of turbulent BL in semi-log plot [72]

For the boundary layer resolution, the 1^{st} mesh along the airfoil is chosen such that $y^+ = \frac{u^* y}{\nu} =\leq 1$, with $\bar{u}^+ = \frac{\bar{u}}{u^*}$ (wall unit, Figure 3.25), $u^* = \sqrt{\tau_w/\rho}$ (friction velocity). The viscous sublayer ($y^+ < 5$) follows the law of wall and numerically y^+ has to be lower than 1. In this region, $\bar{u}^+ = y^+$ and $\tau = \mu\frac{\partial \bar{u}}{\partial y} - \rho \overline{u'v'}$ (Very thin region adjacent to wall, turbulence negligible (wall), laminar, shear stress mostly constant, linear velocity profile [72]). This can be estimated from correlations of flow around a flat plate (Blasius, [72]) or the grid spacing calculator from NASA [17]. With $U = 15$ [m/s] ($Re = 1.2 \cdot 10^5$) and a reference length $c = 0.125$ [m], the 1^{st} mesh size is estimated at $1.97 \cdot 10^{-4}$ [m]. In CFD, uniform mesh with an aspect ratio of 1 are the best one for the flow (according to [73]). High aspect ratio has to be avoided except for the mesh at the boundary layer where there is a high vertical velocity gradient but not horizontally (Figure 3.26 and 3.27).

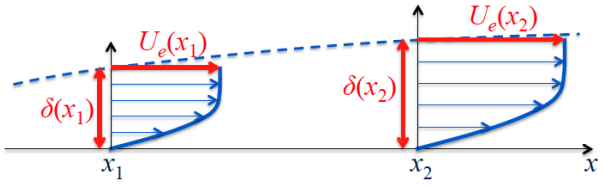

Figure 3.26 – Velocity profile U_e in boundary layer δ [72]

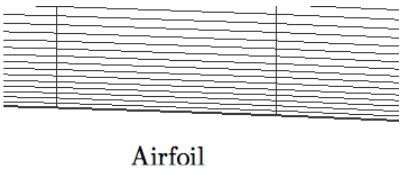

Figure 3.27 – Mesh close to airfoil

Moreover, the Courant-Friedrichs-Lewy (CFL) condition is a necessary condition for convergence of partial differential equations (usually hyperbolic PDEs) numerically solved by the method of finite differences [73], in one or $n-$ dimension, (with C_{max} taken to 1 usually [30])

$$C = \frac{U\Delta t}{\Delta x} = \Delta t \sum_{i=1}^{n} \frac{U_I}{\Delta x_i} \leq C_{max} = 1 \tag{3.7}$$

With Δt the time step, Δx the smallest length (determined by the condition $y^+ \leq 1$ above). For the time discretization, `OpenFoam` allows different schemes. To have an accurate and stable solution, these schemes were selected (high-order central are the most precise, according to the theory of the course of CFD in Master 2 [73])

- Convective terms: Velocity: 2^{nd} order upwing, turbulent variables ($k - \varepsilon$): 1^{st} order upwind
- Diffusive terms: 2^{nd} order central (Crank-Nicolson)
- Gradients: 2^{nd} order central

The iterative procedure is done using the principle of "outer" solver (linear set of equations) and one "inner" solver (for velocity and pressure fields). `OpenFoam` linear solvers are implemented and, here, preconditioner is used (`PBiCG`: preconditioned (bi-)conjugate gradient with `DIC`: diagonal incomplete-Cholesky (symmetric)). Once every initial and boundary conditions are set in folder `/0`, mesh and constants in folder `constant/` (ν_{air} and turbulence model $k - \varepsilon$), discretization scheme in `/system/`,

simulations are launched with `pisoFoam` (using RANS) and results are viewed with `paraView`. Results for the profile at 0 angle of attack and $U = 15$ [m/s] will be used to validate the numerical model (*i.e.* the mesh size, time step, discretization scheme). Figure 3.28 shows the convergence of c_l using different meshes and time step. Mesh 2 and $\Delta t = 10^{-5}$ are selected for the following. As shown in Figure 3.28, a transient phase of 0.05 [s] is necessary to reach the steady lift. Indeed, during a short time, after an impulsive start, there is a region of large vorticity, 'Flushed' downstream. A thin sheet of strong vorticity rolls up to create a starting vortex. The flow leaves the TE smoothly (Kutta) to reach the steady state. According to Kelvin theorem $\frac{D\Gamma}{Dt} = 0$, $\Gamma_4 = -\Gamma_3$. Wagner and Kussner indicial functions are able to represent the progressive increase of lift to its steady value (Figure 3.29) and so the one in Figures 3.28 and 3.30 (starting vortex)..

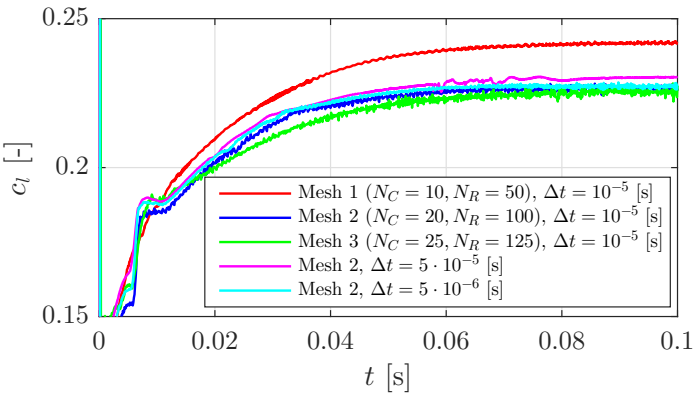

Figure 3.28 – Convergence study on mesh and time step

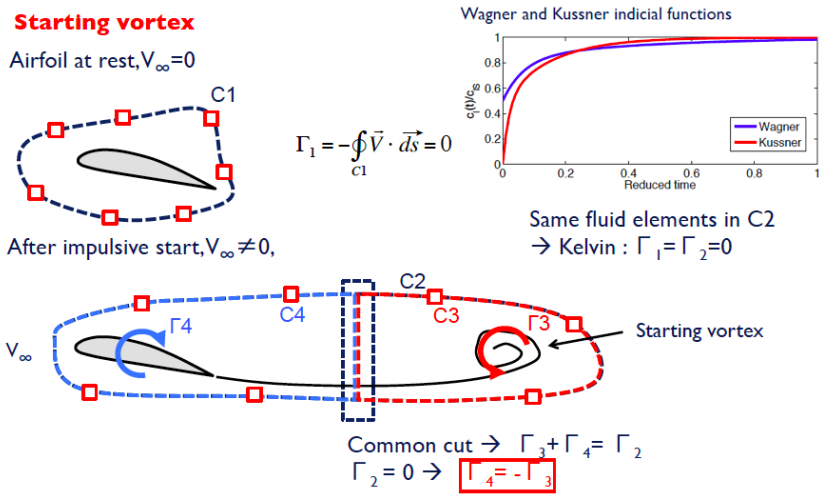

Figure 3.29 – Starting vortex phenomenon, Kelvin's theorem and Wagner function [65]

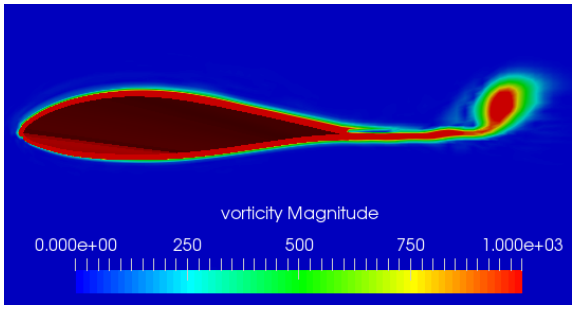

Figure 3.30 – DU96W180 at $\alpha = 0$ and $U = 15$ [m/s]: vorticity at $t = 0.01$ [s]

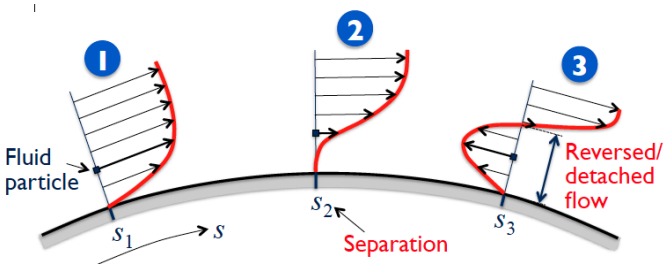

Figure 3.31 – Separation of boundary layer [72]

In the following, the stall phenomenon occurring at a high angle of attack will be studied. It happens when the boundary layer separates, due to an adverse pressure gradient $\frac{dp}{ds} > 0$ (reversed flow so $tau_w = \mu \left.\frac{du}{dy}\right|_{y=0} < 0$), illustrated in Figure 3.31. The separation point occurs when $\left.\frac{du}{dy}\right|_{y=0} = 0$, at an inflexion point of pressure or shear distribution.

3.4 Results

This section will compare and discuss all results (experimental and numerical methods) in the scope of stall. The pressure calibration results (from section 3.2.2) will be used to present results after. Every hole number of the wing profile mentioned in this section are related to those of Figure 3.6.

3.4.1 Pressure distribution

Every taps are now dynamically calibrated (with the correction of hole 10 for all taps (same geometry), except holes 2,24 and 26). The influence on the pressure measured at taps will be studied but firstly the mean pressure will be studied (of steady type). Indeed, as explained before, the mean of the pressure time signal is not sensitive to dynamic effects (the mean is the value of the FFT at "$f = 0$" [Hz]).

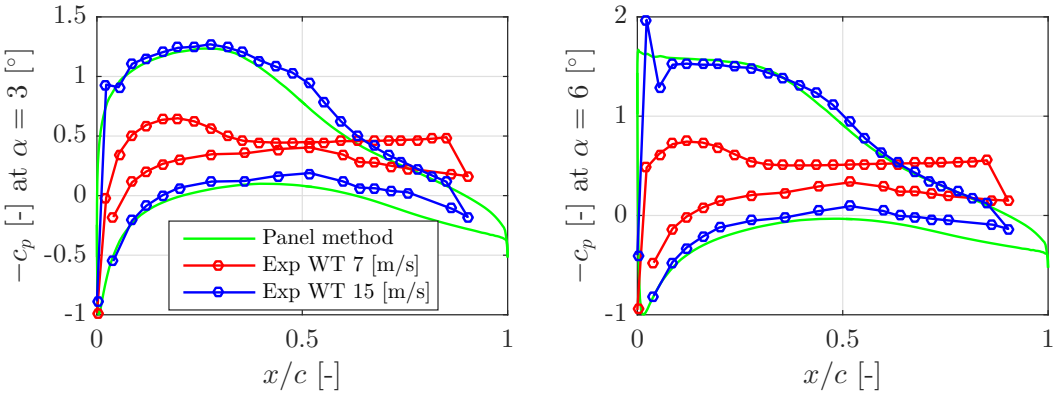

Figure 3.32 – Pressure distribution of wing profile 1 at $\alpha = 3$ and 6 [°]: comparison of panel method and experiment at $U_\infty = 7$ and 15 [m/s]

Figure 3.32 compares the pressure distribution (pressure coefficient $-c_p$ along the normalized chord x/c of wing profile 1) computed by panel method (inviscid) and experimental data of Wind Tunnel at $U_\infty = 7$ and 15 [m/s] for angles $\alpha = 3$ and 6 [°]. Pressure distribution of airfoils are similar, they have all a $-c_p = -1$ at the stagnation point (here at $x/c = 0$, at hole 1). Indeed, Bernoulli's principle (for incompressible flows) states that the stagnation pressure p_{stag}[3] is equal to the dynamic pressure q_∞ plus the static pressure p_∞. In this case, the stagnation pressure is also equal to the total pressure p_0[4]. Thus $c_p = \frac{p_{stag} - p_\infty}{q_\infty} = \frac{q_\infty}{q_\infty} = 1$. The upper profile side (extrados) is called the suction side because of the negative pressure on it, sucking the profile and creating the lift. The lower side (intrados) is the pressure side. The pressure difference (between upper and lower sides) is higher when the thickness is higher (thickness effect in Joukowski airfoil). The highest velocity $U_\infty = 15$ represents a higher Reynolds number ($Re = \frac{Uc}{\nu} = 1.2 \cdot 10^5$), thus with inertia forces $\propto Uc$ much higher than viscous effects $\propto \nu$. This case is close to an inviscid case, illustrated by the very close results of exp WT 15 [m/s] and panel method (purely inviscid model) on Figure 3.32. On the contrary, exp WT 7 [m/s] gives a lower Re ($0.6 \cdot 10^5$) and the distribution is highly different and thus strongly Reynolds dependent. Usually, airfoils are Reynolds dependent but not as much as for this particular profile. The DU96W180 profile is used in the blade span part close to the root and to the rotor because speeds are lower there and require a high thickness to produce enough lift (speed triangle). Because of the upper side geometry (high thickness and camber), the flow is strongly accelerated on it. The problem is that at low velocity, this geometry induces that the laminar boundary layer on the rear part (after the maximal thickness

[3] Pressure at the stagnation point, *i.e.* where the flow velocity is zero.

[4] For compressible flows, $p_{stag} = p_0$ if the fluid at stagnation point is isentropically brought to rest [50]

point, close to hole 10) separates (because of a recirculating flow, due to adverse pressure gradient, Figures 3.31 and 3.33). This corresponds to the beginning of the plateau of the pressure distribution at low speed, around $x/c = 0.3$ (Figure 3.32). The plateau corresponds to the recirculating flow region, with bubble and divided streamline. The boundary layer is subjected to a transition between laminar and turbulent (where the pressure has a step-like shape, the transition point is the point at which $-c_p$ starts to decrease after the plateau (Figures 3.33 and 3.35 at around $x/c = 0.7$). Then, the flow is reattached (turbulent boundary layer). The pressure distribution is again close to the inviscid one, viscous effects are associated to boundary layer transition and separation (with a step like shape in the pressure distribution). Indeed, turbulent Boundary layer (BL) more stable to separation (Figure 3.34), the momentum is higher close to the wall and the increased friction drag is compensated by a lower pressure drag (as a golf ball) [72]. As suggested by Figure 3.34, turbulence is associated to a "fuller" velocity profile, higher velocity gradients at the wall and thus larger wall shear stress. The diffusion (higher momentum) is enhanced by turbulent fluctuations so the turbulent BL is thicker and grows faster. If the plateau in pressure distribution continues (no transition, nor reattachment), the flow is still detached (Figure 3.32 for $u_\infty = 7$ [m/s]).

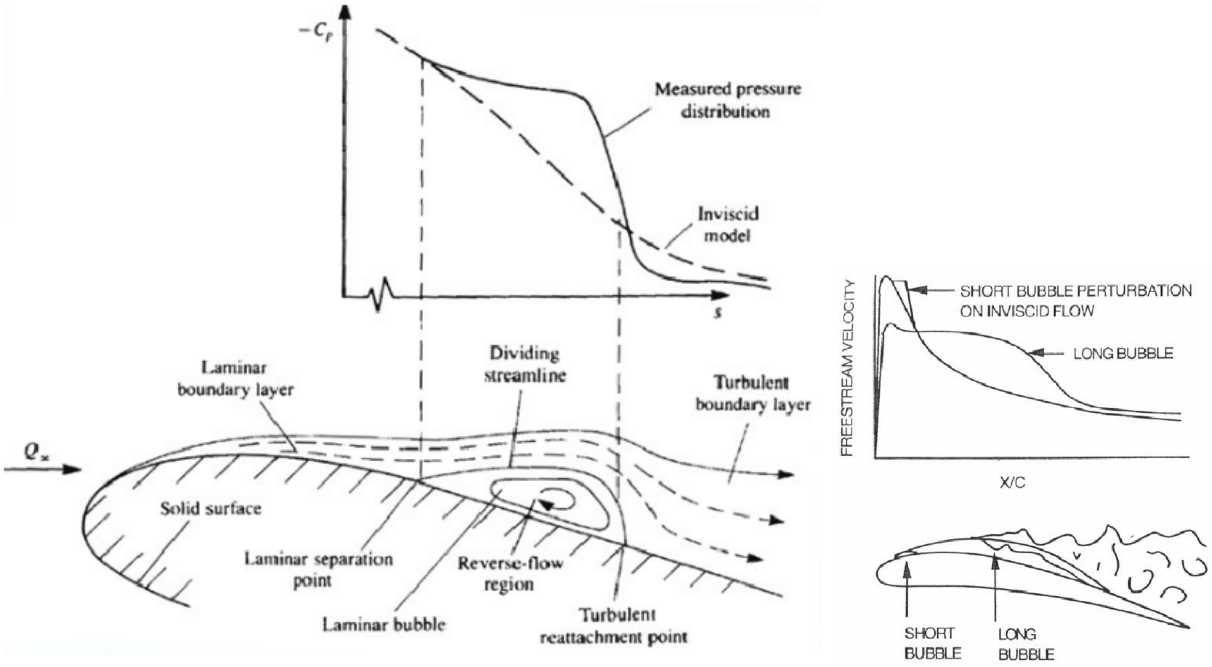

Figure 3.33 – Effects of laminar separation bubble on pressure distribution and separation bubble effects on suction side velocity distribution [11]

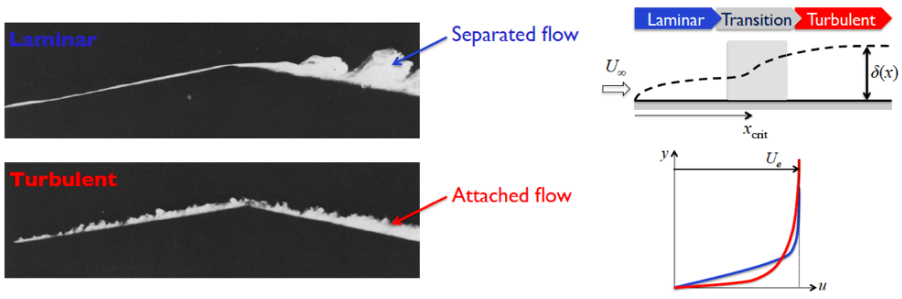

Figure 3.34 – Boundary layer separation around a sharp corner, transition of boundary layer (laminar to turbulent) and associated velocity profiles [72]

This turbulence can be modelled in `Xfoil` software with the parameter N_{crit}. As explained, it is usually fixed at 9 for averaged WT, dirty conditions (more turbulence in the free stream flow delivered by the WT) are obtained using $N_{crit} = 4 - 8$ [16]. Figure 3.35 shows the influence of N_{crit} on c_l

and $-c_p$ at $\alpha = 0$ for both velocities. At a high Reynolds number, differences are not high, because this case is close to the inviscid one (for the global shape only, Figure 3.32 shows the step of the pressure distribution of exp WT 15 [m/s], associated to transition, because even if Re is high, viscous effects are negligible but still present). For lower Re on Figure 3.35, N_{crit} has a strong influence. For $N_{crit} = 4$ (higher turbulence), there is some convergence issues in c_l computation. Because of the higher turbulence, the pressure distribution reattaches sooner than for $N_{crit} = 9$ (step translated to the left in Figure 3.35 right). The Wind Tunnel in ULg has a rather low turbulence level (0.1%), $N_{crit} = 4$ induces too much turbulence than the reality thus $N_{crit} = 9$ will be fixed for the following. Moreover, it should be pointed out that `Xfoil` is not really accurate at low Re.

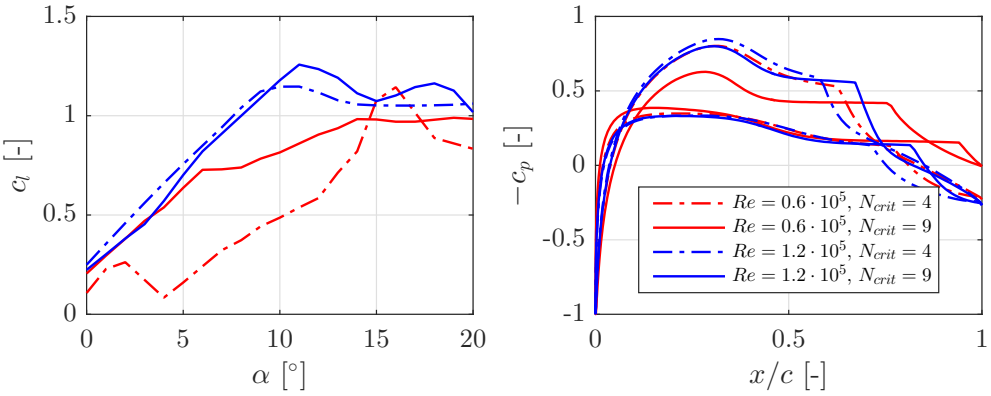

Figure 3.35 – Lift coefficient c_l vs angle of attack α and pressure distribution $-c_p$ at $\alpha = 0$: comparison of Re and N_{crit} effects, `Xfoil` results

Figures B.13 and B.14 in Appendix B.5 compare results from `Xfoil` and CFD: pressure/velocity distribution, boundary layer and streamlines for $\alpha = 0$ and 8. For these cases, the flow (streamlines) is attached for the high Re (as the two first graphs in Figure 3.36). As explained, at low Re, the boundary layer is thicker, the pressure distribution appears flatter. Figure 3.36 compares pressure distribution obtained with experimental data, panel method, `Xfoil` and CFD (for both U_∞ and $\alpha = 0, 8, 12$ [°]). All results are quite close. Nevertheless, the step in pressure associated with the transition is less visible in experimental data and CFD. It is absent for panel method (inviscid case). Reynolds dependence discussed before is clearly identifiable. The lower Re induces more viscous effects, slowing down, even more, the flow. The laminar BL is detached over a large region (from $x/c = 0.4$ to 0.8 at $\alpha = 0$, from 0.3 to 0.7 for $\alpha = 8$) and the transition occurs quite far (at $x/c = 0/8$ for $\alpha = 0$ and 0.7 for $\alpha = 8$). The turbulent BL is still attached after, thus the airfoil does not have stalled. This induces that the pressure difference is lower (and so the lift) even without stall (at higher α). For the higher Re, the flow is still attached at $\alpha = 0$ and 8. However, at $\alpha = 8$, the pressure distribution starts to be lower, from the TE. A plateau is formed, associated with separated flow, starting from TE (the pressure for $0 < x/c < 0.3$ is still superposed to the panel method (attached, almost inviscid case).

At $\alpha = 12$, the separation bubble propagates a lot from the trailing to the LE, and the pressure distribution drops (compared to an inviscid case). Stall point is reached, the pressure distribution and lift will drop for a further angle of attack increase (more recirculations). The transition point is around $x/c = 0.15$, then the turbulent BL reattaches but separates at around $x/c = 0.5$ (plateau) and the airfoil stalls. This can be seen also in Figure 3.37 for $Re = 1.2 \cdot 10^5$ and $\alpha = 12$, the turbulent BL increases a lot compared to $\alpha = 8$ and separates so the wing stalls. For $Re = 0.6 \cdot 10^5$, the laminar BL separates but transition occurs at $x/c = 0.6$ with an attached turbulent BL, so the wing does not stall. Figure 3.38 shows pressure, velocity distribution, boundary layer growth and separation phenomenon at $Re = 0.6 \cdot 10^5$ and $\alpha = 20$. `Xfoil` and CFD show similar results: the turbulent BL is very thick and separates to form a divided streamline (bubble) at $t = 0.05$ [s] (this phenomenon happens continuously, Figure 3.38 is only one snapshot). This bubble propagates and vortices are ejected after, streamlines are not attached and smooth anymore, unsteadiness is involved (studied just hereafter, associated to the dynamic calibration).

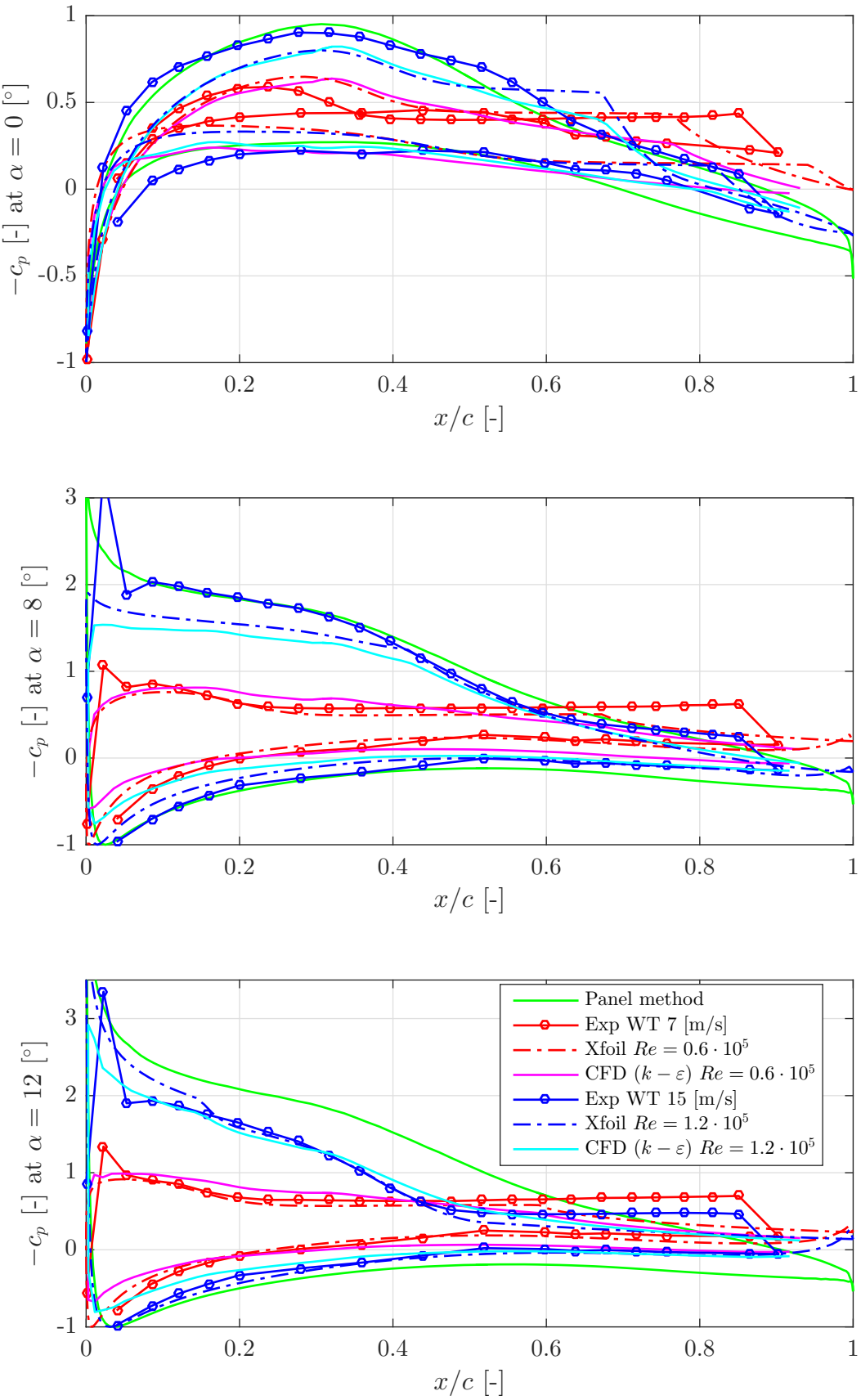

Figure 3.36 – Pressure distribution of wing profile 1 at $\alpha = 0, 8$ and 12 [°]: comparison of panel method, experiment, `Xfoil` and CFD at $U_\infty = 7$ and 15 [m/s]

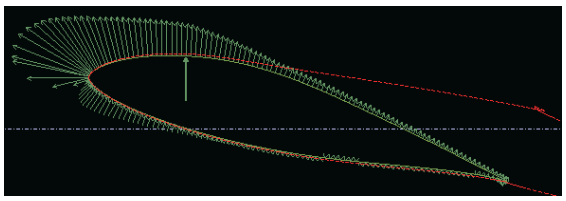

(a) `Xfoil` $Re = 0.6 \cdot 10^5$

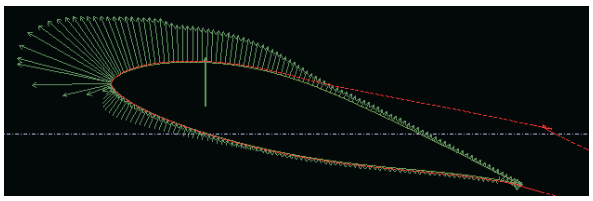

(b) `Xfoil` $Re = 1.2 \cdot 10^5$

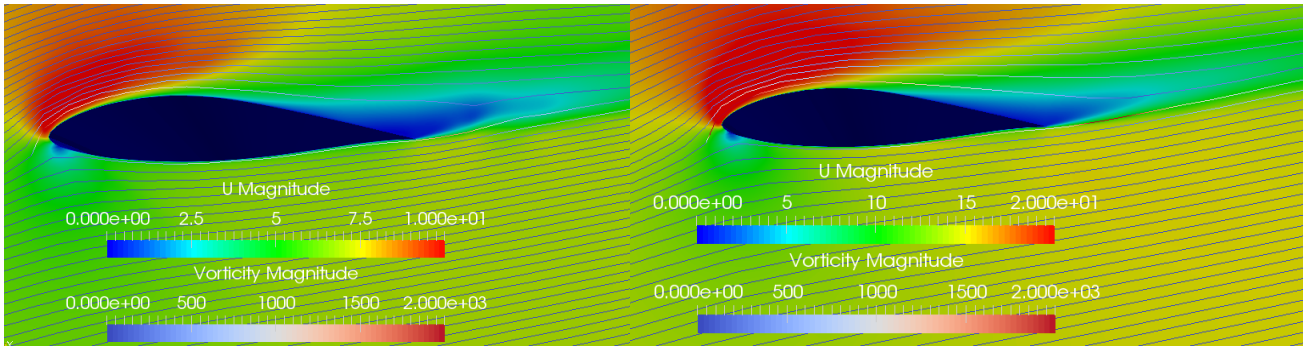

(c) CFD $Re = 0.6 \cdot 10^5$

(d) CFD $Re = 1.2 \cdot 10^5$

Figure 3.37 – Pressure (arrows in `Xfoil`) and velocity distribution (CFD), boundary layer (red line in `Xfoil`), streamlines with vorticity (CFD): comparison `Xfoil`- CFD at $\alpha = 12$ [°]

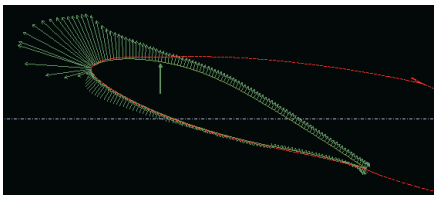

(a) `Xfoil` (pressure with arrows, BL in red)

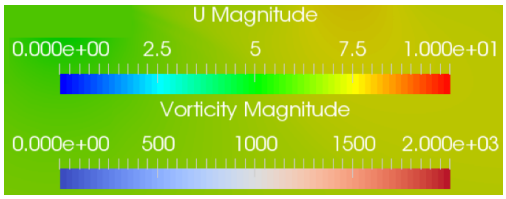

(b) Legend of CFD pictures below

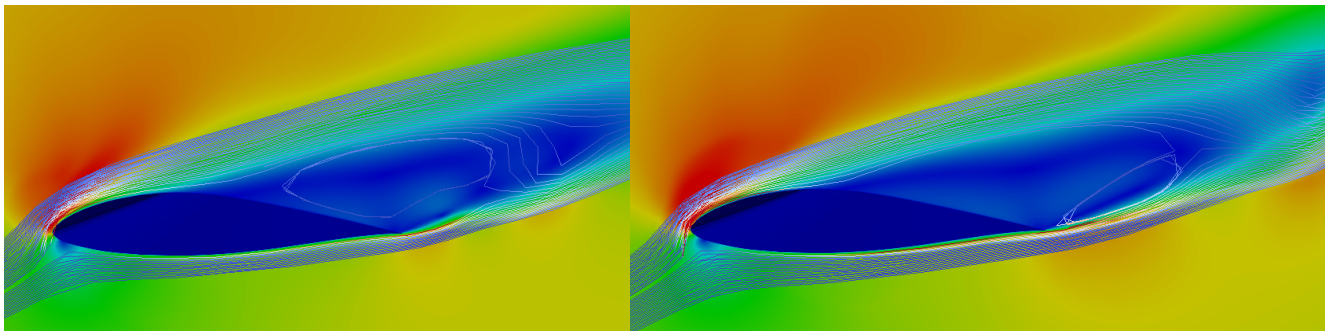

(c) U (CFD) at $t = 0.05$ [s]

(d) U (CFD) at $t = 0.06$ [s]

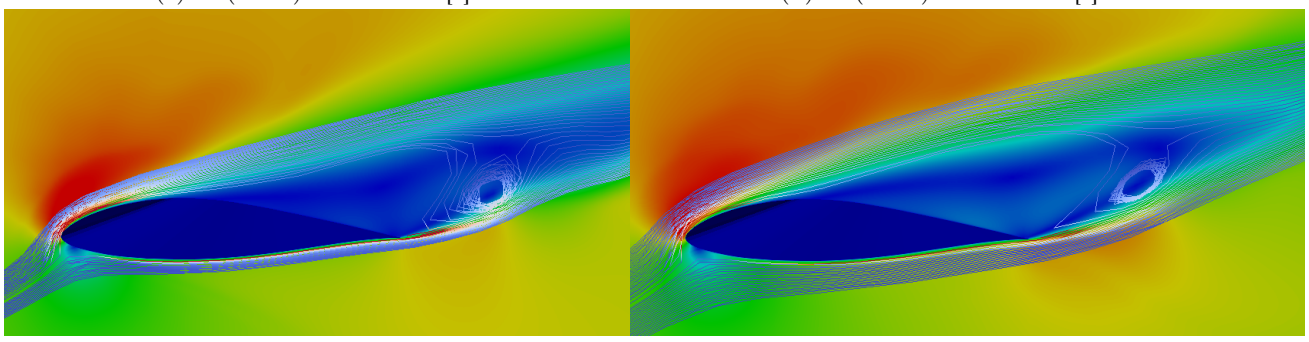

(e) U (CFD) at $t = 0.07$ [s]

(f) U (CFD) at $t = 0.075$ [s]

Figure 3.38 – Pressure and velocity distribution, boundary layer, streamlines with vorticity: comparison `Xfoil`-CFD at $\alpha = 20$ [°] and $Re = 0.6 \cdot 10^5$, separation phenomenon

Figure 3.39 shows a summary of the mean pressure evolution $\bar{c}_p$ of different taps (with numbering of Figure 3.6) at several α for both U_∞. Hole 1 is the stagnation point at $\alpha = 0$ ($-c_p = -1$) but this point moves with increasing α: it corresponds to hole 40 at $\alpha = 10$ (for $U_\infty = 15$). Tap 26 is on the lower side and obviously, nothing particular happens there, the c_p is constant for both U_∞. The pressure at holes 6 to 10 shows the same kind of shape as the one of the lift c_l, increasing with α and stalls near 10 (for $U_\infty = 15$). The general stall happens when taps on the highest location stalls as well (6 to 10). Holes 16 to 24 show constant pressure (in turbulent BL, just after the transition near hole 15). The most interesting observation is the different pressure evolution for taps 20-24 and 14-16, near the stall at $\alpha = 10$: c_p increases at taps 20-24 and decreases at taps 14-16, showing the adverse pressure gradient inducing the separation. For $U_\infty = 7$, most taps on the upper side measure the same pressure (corresponding to the plateau), with a similar evolution with α as c_l, because laminar BL has separated, the transition occurring near the TE.

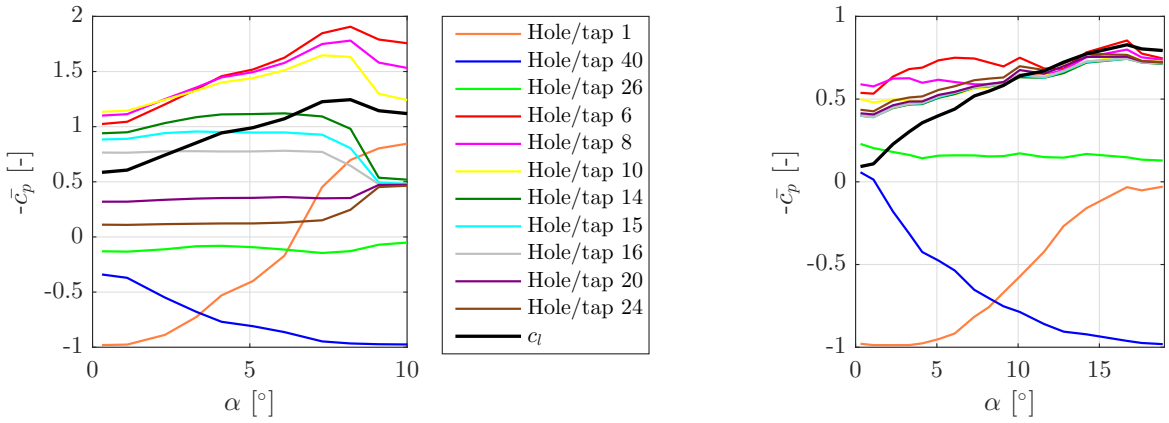

(a) $U_\infty = 15$ [m/s] (b) $U_\infty = 7$ [m/s]

Figure 3.39 – Experimental mean pressure and lift coefficients ($\bar{c_p}$ and $\bar{c_l}$) vs angle of attack α

Figures 3.40, B.15 and B.16 show experimental pressure fluctuation ($c'_p = c_p - \bar{c}_p$) at hole 15 for both U_∞ in time and frequency domains with the measure and the reconstruction thanks to the dynamic response correction (pressure calibration of Figure 3.13), for $\alpha = 0, 8, 12$. A comparison is also made with CFD results. At $\alpha = 0$, streamlines are attached so no high-pressure fluctuations are expected: this is the case for CFD results. However, the experiment shows fluctuations of the order 10^{-2} while a steady case is expected. These fluctuations come from measurements errors (systematic). This can be deduced from a systematic oscillation at resonance frequencies $f = 12$ and 22 [Hz]. These oscillations can also come from the roughness of the profile. Indeed, 3D printed holes add a certain artificial roughness that can produce small pressure fluctuations downstream.

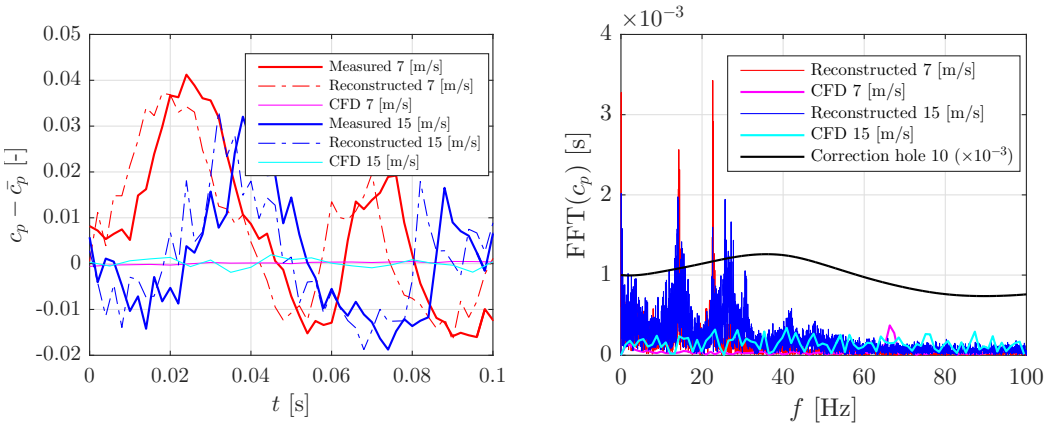

Figure 3.40 – Experimental pressure coefficient fluctuation $c'_p = c_p - \bar{c}_p$ at hole 15 and $\alpha = 0$: measured and reconstructed signals for both U_∞, comparison with CFD (in time and frequency domains), dynamic response correction (pressure calibration of the profile at hole 10)

At a higher angle $\alpha = 8$ (Figure B.15), the pressure profile at high Re starts to separate (Figure 3.36), inducing higher fluctuations c'_p at a wider range of frequencies (a lot of frequencies are excited, random and chaotic behavior, characteristic of turbulence). At a low Re, there is less turbulence (transition occur near the TE) and the laminar BL separates (Figure 3.36), the two resonance peaks are still present. Pressure fluctuations of CFD results is higher than for $\alpha = 0$ (order of $10^{-2} - 10^{-1}$) and similar to those of the experiment. For $\alpha = 12$ (Figure B.16), both Re show pressure fluctuations of order more than 10^{-1}, for a large range of frequency. Turbulence is clearly present and the turbulent BL is detached for the highest Re. CFD results show also fluctuations for a wide frequency range.

Figure 3.41 shows time characteristics σ, k and γ_1 of experimental signals depending on U_∞ and α. For $U_\infty = 15$, they are easily understandable. The standard deviation is low at low angles of attack ($\alpha = 0 - 7$) because the flow is attached, fluctuations come from measurement errors, they are thus quite constant for both direct measured and reconstructed signals (with calibration correction). This is the same for kurtosis (measuring the "tildeness" of the probability distribution, constant at 3.2, typical for a gaussian distribution) and skewness (asymmetry of the probability distribution, close to 0 here, so no asymmetry). For higher α, recirculations and turbulence are increased, creating more fluctuations and a higher σ. The purpose of dynamic calibration is thus to correct these amplitude fluctuations. The kurtosis is not so much affected by the calibration but the skewness well. Indeed, thanks to the calibration, the probability distribution remains symmetric even at stall (assuming a Gaussian distribution of turbulent fluctuations at separation). An interesting observation is that hole 24 shows the highest fluctuations. This is consistent as this hole is the closest to TE, where the BL starts separating. Another point is the relatively low fluctuation of c_l. As a global quantity, it acts like a "filter" and attenuates fluctuations of pressure taps alone. Indeed, it takes all taps into account (also those with very low fluctuations, such as holes 26-40 on the lower side, the BL remains always attached there).

For $U_\infty = 7$, time characteristics are similar but the transition from low to high α (at stall) is less evident. Fluctuations (deviation σ, tildeness k and asymmetry γ_1) are higher and more variable than those at $U_\infty = 15$. Indeed, even at low α, Reynolds effects (low Re) induces that the laminar BL has separated (constant pressure for most taps on the upper wing side), thus with recirculations and fluctuations. Again, the pressure correction plays on σ and also on the skewness of c_l: the measured c_l was not symmetrically distributed but well the corrected one.

Figure B.17 shows the same characteristics as Figure B.16 but only for $U_\infty = 7$ and for holes 15 (upper wing side) and 35 (lower side) at $\alpha = 20$, corresponding to the stall at low Re. The pressure at hole 35 varies according to remarks of Figure 3.40, with 2 resonance frequencies but low amplitudes. The pressure at hole 15 varies more and over a larger range of frequencies (recirculations and stall). The lift varies less (again a kind of filter).

Important remark: the lift coefficient c_l is computed according to equation 3.3, by making a summation of c_p around the profile (extrapolation of an integral). Because of the linearity of the summation and mean operators, there is no difference between computing the mean as

- Mean of the c_l from the instantaneous c_l
- Mean of instantaneous c_p at each tap and then performing the integration

The computation of the standard deviation involves quadratic operator so σ of the instantaneous c_l is not necessarily the same as σ of each c_p integrated along the airfoil. Physically, it is more consistent to compute the instantaneous lift c_l by integrating every c_p at each instant. After, the σ of the instantaneous c_l is computed. For the reconstruction of the signal, the calibration correction is applied on each c_p to recover the true pressure signal (as in Figures 3.40 to B.16) and the instantaneous lift c_l is computed from integrating each c_p.

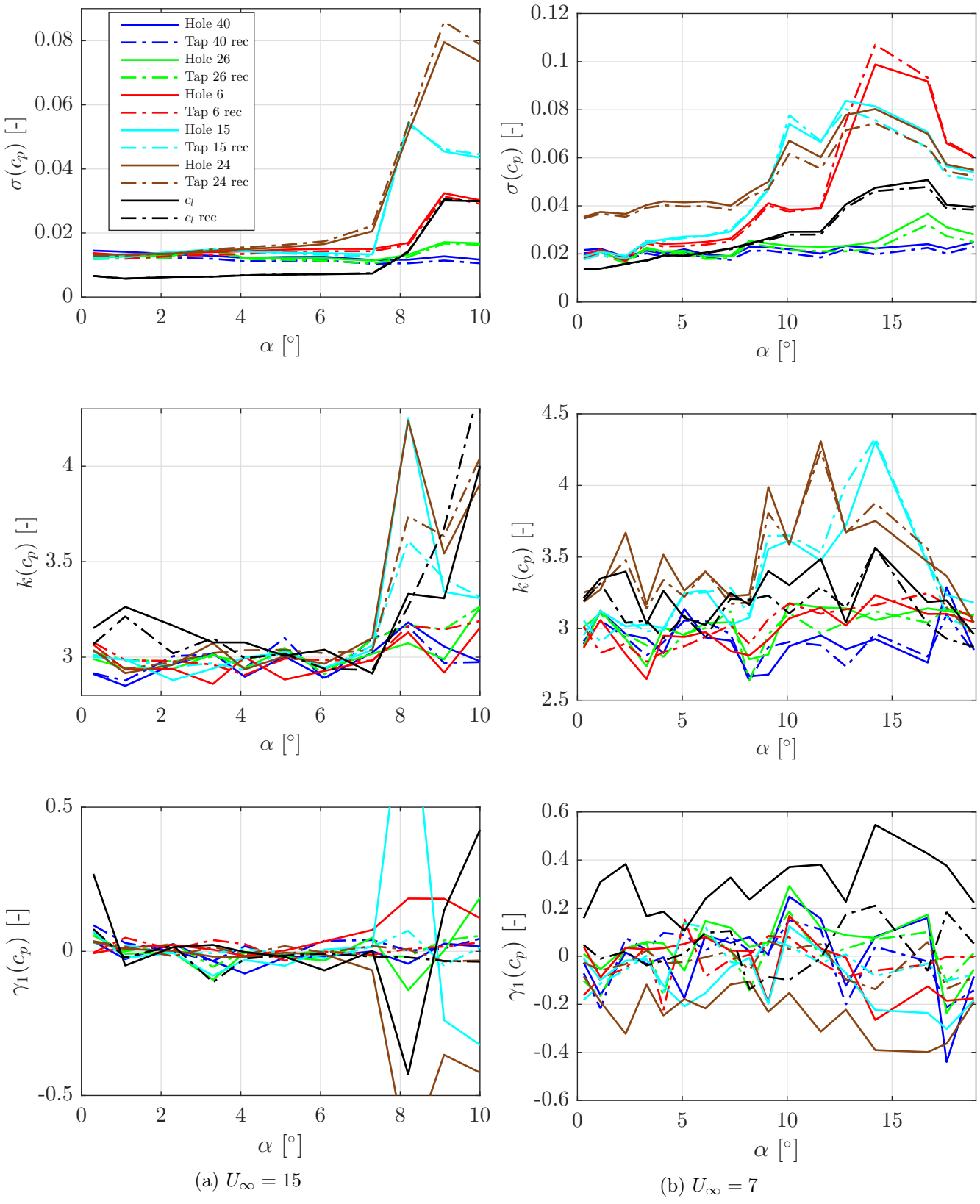

(a) $U_\infty = 15$ (b) $U_\infty = 7$

Figure 3.41 – Experimental time characteristics of pressured measured and reconstructed at different holes for both U_∞: standard deviation σ, kurtosis k and skewness γ_1

3.4.2 Global quantities

A useful way to present aerodynamic results is to use global quantities: lift c_l and drag c_d coefficients. It allows to have a quick overall view (without the need to study each pressure taps individually). figure 3.42 shows c_l' fluctuations at $\alpha = 12$ (stall for the high Re), they are lower than fluctuations

of pressure at hole 15 for same conditions. Figure 3.43 shows 3D characteristics from `XFLR5` (lift C'_L and induced drag C'_{Di} along the span y/b for both U_∞ at $\alpha = 6$ and 12[5]. Due to wing tip vortices, the closer from the wing tip, the higher the induced angle, the higher the downwash, the higher the induced drag and the lower the lift. This effect increases with U_∞ and α. Because the wing aspect ratio is high, 3D effects are quite low. Indeed, Figure 3.44 shows that there is not so many differences between

- Experimental lift at mid-span
- The 2D lift c_l computed with `Xfoil/XFLR5`
- The mid-span lift (where experimental taps are located) that takes 3D effects into account C'_L
- The complete 3D lift C_L

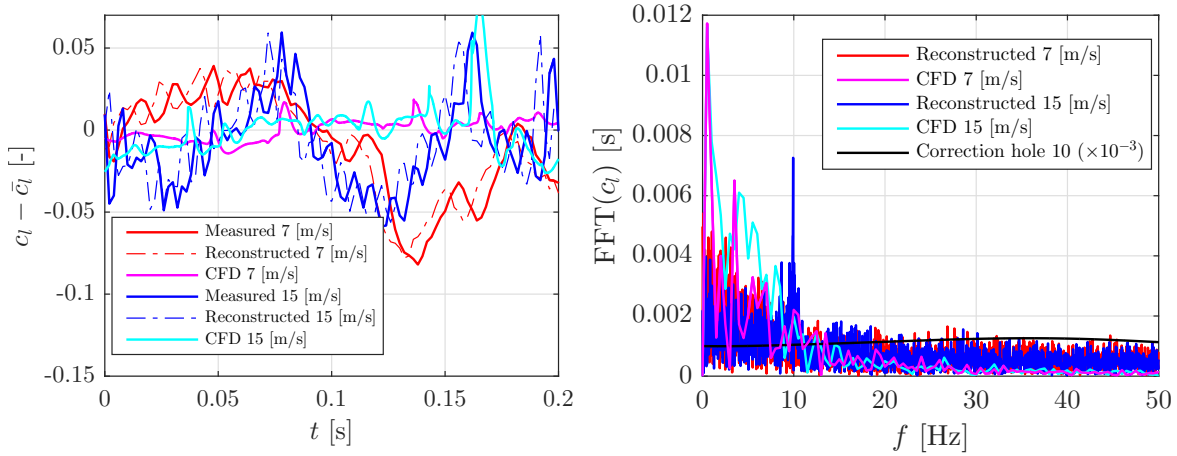

Figure 3.42 – Experimental lift coefficient fluctuation $c'_l = c_l - \bar{c}_l$ at $\alpha = 12$: measured and reconstructed signals for both U_∞, comparison with CFD (in time and frequency domains), dynamic response correction (pressure calibration of the profile at hole 10)

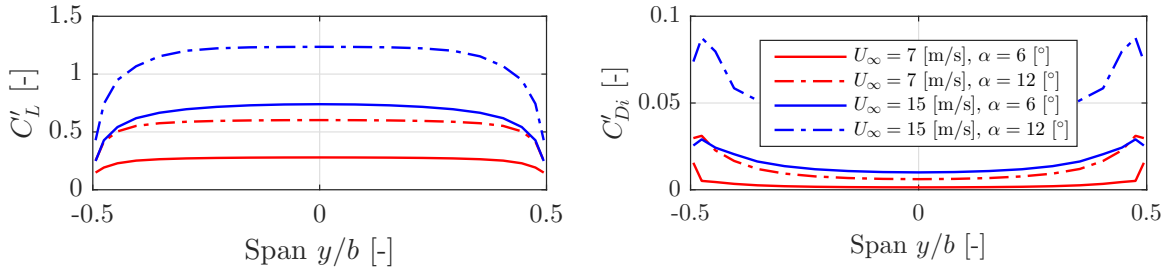

Figure 3.43 – `XFLR5`: Influence of angle of attack and velocity on 3D wing characteristics along the span: lift C'_L, induced drag C'_{Di}

Experiment and 3D lift C_L and C'_L at mid span are quite close for $Re = 0.6 \cdot 10^5$. For $Re = 1.2 \cdot 10^5$, 3D effects are increased (Figure 3.43) and there is a bit more difference compared to 2D lift. Figure 3.45 makes the same comparison but for the drag. The 2D drag c_d is decomposed into pressure drag (due to separation, that increases with α) c_d^p + viscous drag c_p^v (non-zero even at $\alpha = 0$, no d'Alembert paradox). The 3D drag C'_D at mid span is the 2D drag c_d + the induced drag C'_{Di} at mid span. At lower Re, viscous effects are higher and hence the drag. Error bars on Figure 3.44 and 3.45 are computed from the calibrated and corrected time signals (σ increases at stall for both c_l and c_d at both U_∞). Figure 3.46 is useful to make a comparison and a summary of what was discussed until now: comparison of theoretical, experimental and numerical lift coefficient c_l. Near the stall, experiment,

[5] C'_L is the 2D lift (on each span location) but taking into account 3D effects

`Xfoil` and CFD are close to references (Lindeboom [44] and van Rooij [74]). These references use a bit higher Re, but anyway at a sufficiently high Re, results are close to the inviscid case and the stall (associated with viscous BL separation) does not depend too much on Re. For a lower Re ($0.6 \cdot 10^5$) there is no results in reference and `Xfoil` is less precise at. Theoretical models are inviscid and hence cannot model the stall. The slope of the high Re real case is however well estimated with Joukowski airfoil and panel method. They are quite close and are able to model both thickness (lift slope) and camber (lift at zero angle) effects. The thin cambered airfoil theory is able to model estimate the lift at zero angle but it assumes a thin airfoil so the lift slope is not high enough. Figure 3.47 summarizes the same observations but for the drag. Experiment-`Xfoil`-CFD results are quite close except for `Xfoil` at low Re. Moreover, `Xfoil` predicts always laminar separation bubbles (step in pressure distribution) but it was not always clearly observed in experiments. Indeed, the lower Re, the higher viscous effects and so the viscous correction that `Xfoil` adds, leading to higher errors.

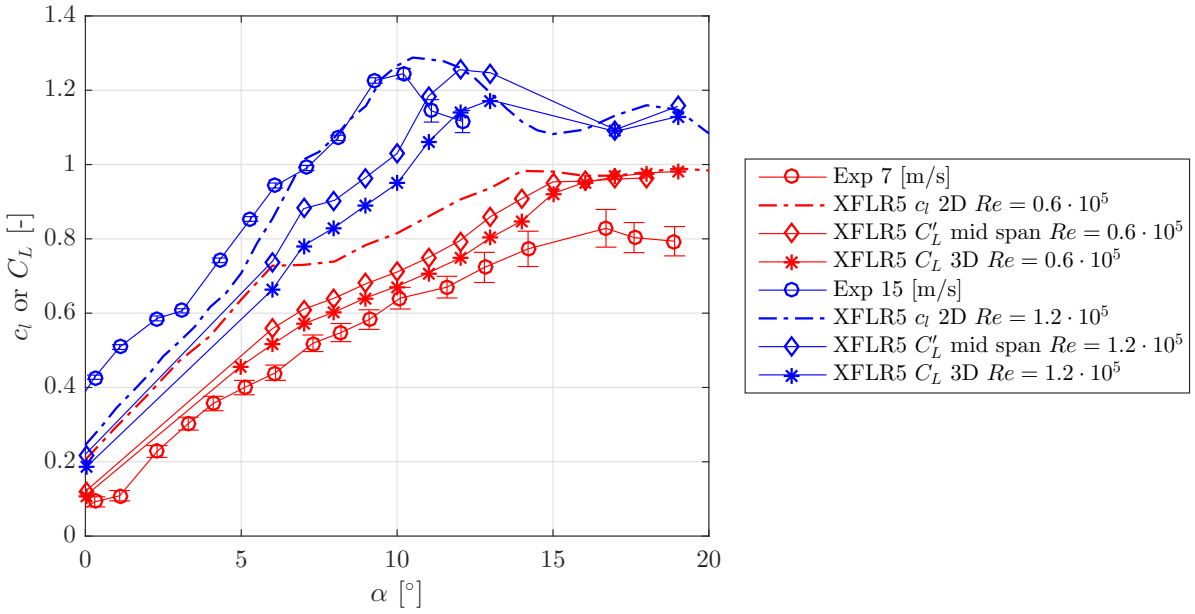

Figure 3.44 – Lift coefficient C_L vs angle of attack: comparison of assumption (2D-3D) on experiment and XFLR5

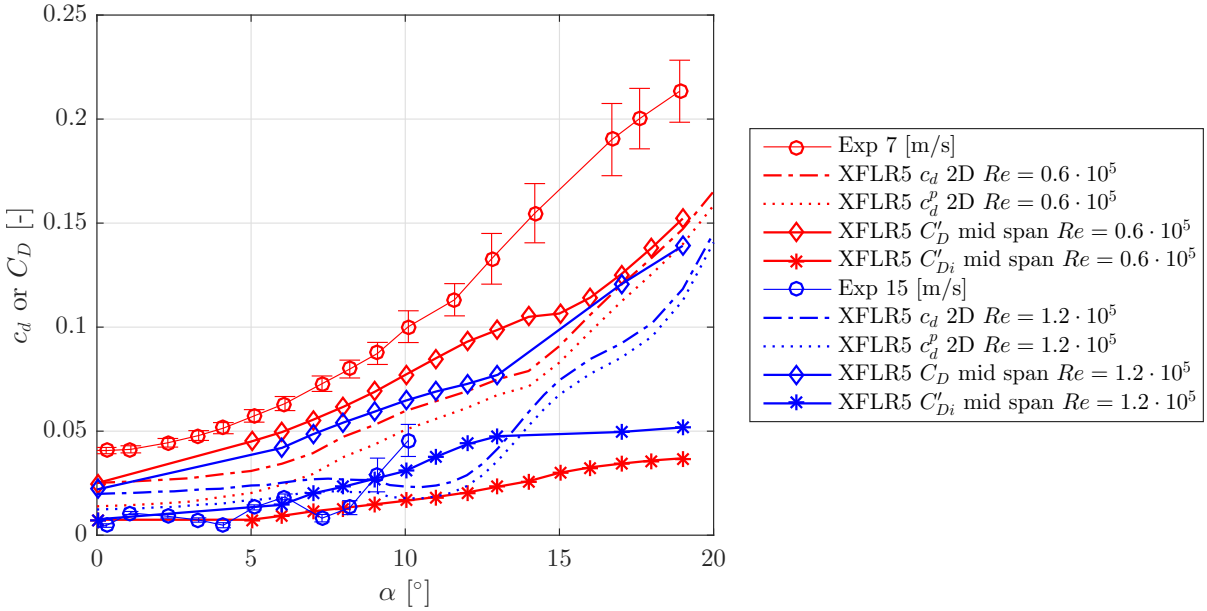

Figure 3.45 – Drag coefficient C_D vs angle of attack: comparison of assumption (2D-3D) on experiment and XFLR5, pressure, viscous and induced components

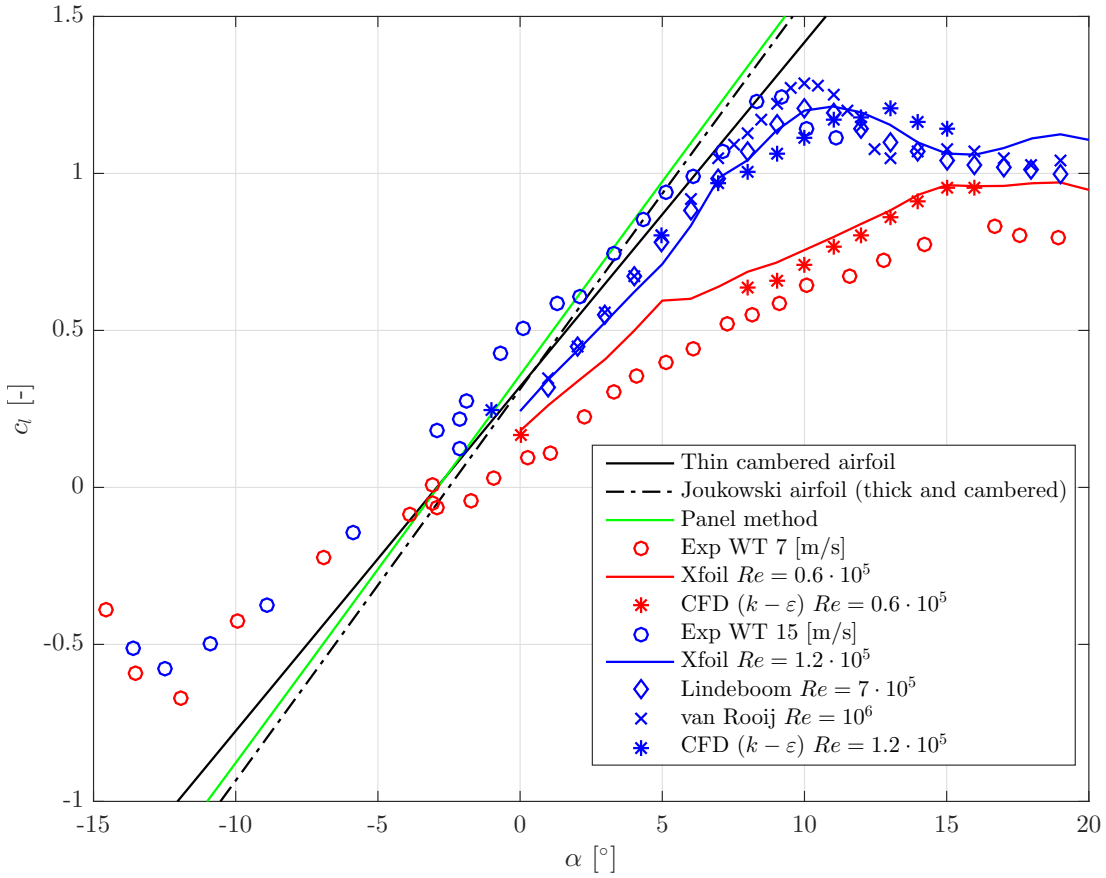

Figure 3.46 – Lift vs angle of attack: comparison of theory, references, experiment, CFD and Xfoil

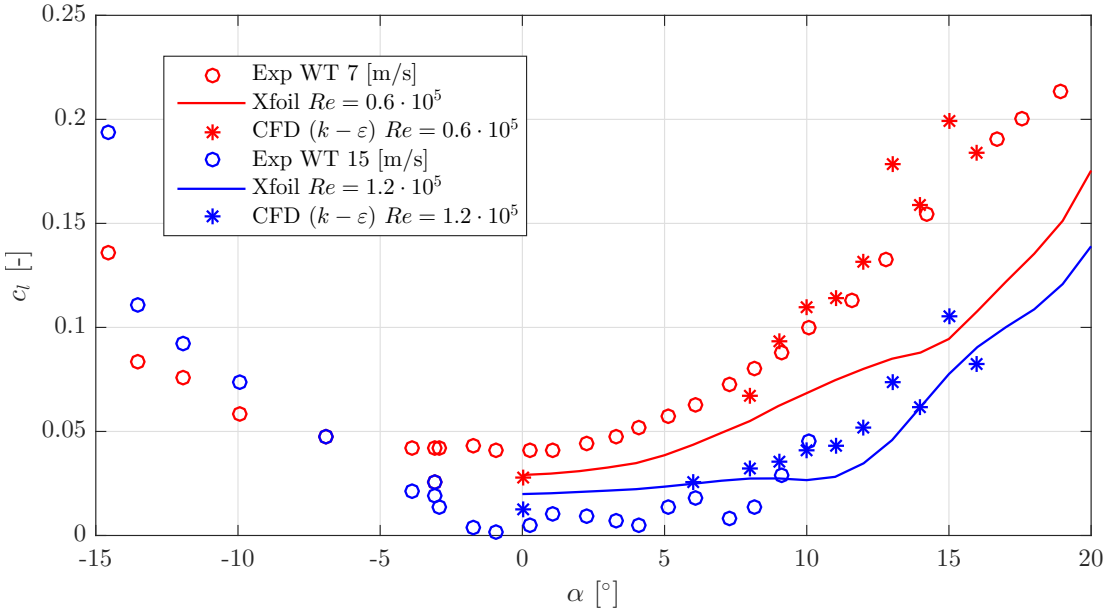

Figure 3.47 – Drag vs angle of attack: comparison of theory, references, experiment, CFD and Xfoil

Another interesting remark is the type of stall involved here. The pressure distribution was characterized by rounded suction peaks and moderate pressure gradients, with the turbulent BL initially separating close to the TE. The separation point then moves progressively to the LE. This is called TE stall (Figure 3.48 (a)), characteristics for thick airfoils (NACA 4421,...). The lift curve is progressively curved at stall. As observed, the separation point was near $x/c = 0.5$ at $\alpha = 12$ (maximum lift). Figure 3.48 (b) suggests another type of stall, more abrupt: LE stall. In this case, the laminar BL separates abruptly, associated to a separation bubble. There are two cases. In the first one, by increasing α,

the bubble length decreases to a critical point and suddenly bursts into a large region (almost on the entire chord). An incompatibility between BL and external flow makes the reattachment failing. In the second case, there is a separation of the turbulent BL (a short distance downstream of the bubble) because of its weakened state. Figure 3.48 (c) and (d) shows thin airfoil stall (sharp and blunt LE). The principle of transition-separation for a sharp LE airfoil is the same as for other stalls but reattachment is not as rapid as in the second case above. For a blunt LE airfoil, a short bubble is formed and bursts into a long one (corresponding to point A in Figure 3.48 (d)). Finally, "combined" stalls can happen, with separation at both LE and TE, distinction between stall types is thus not always clear. Some devices can be added to change lift and drag performances: LE camber suppress LE stall, TE camber increase LE suction and the tendency to stall there. Vortex generators can also be added to increase the lift by forcing the flow to stay attached for a higher angle (Figure 3.49, with DU91-W2-250, a profile similar to DU96W180). It creates a vortex that delays the separation by removing part of low speed BL.

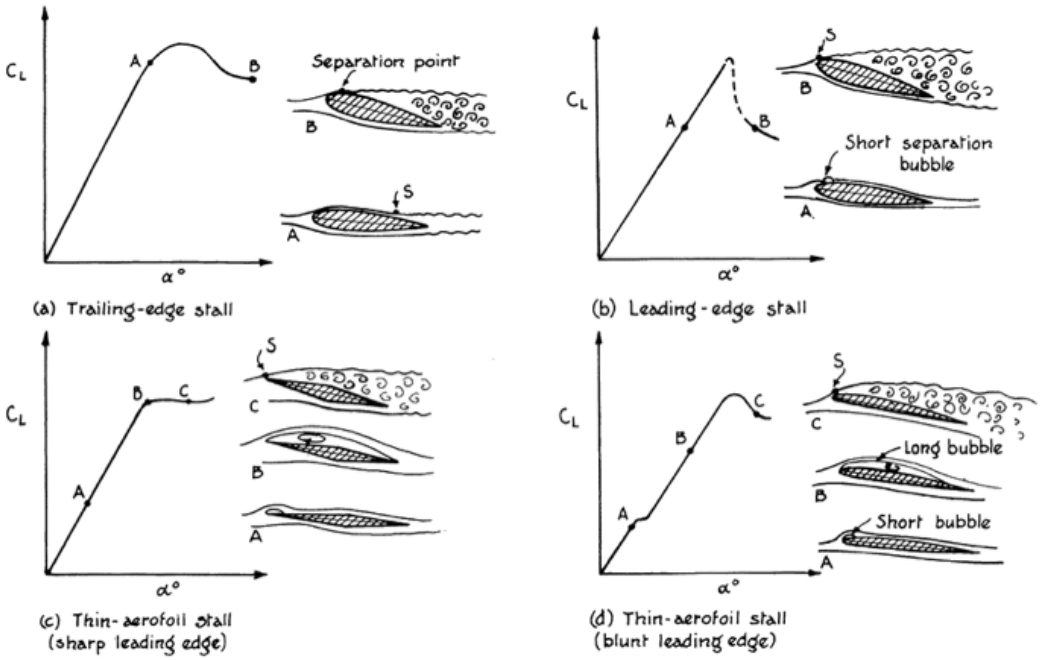

Figure 3.48 – Sketch of the four different stall types [56]

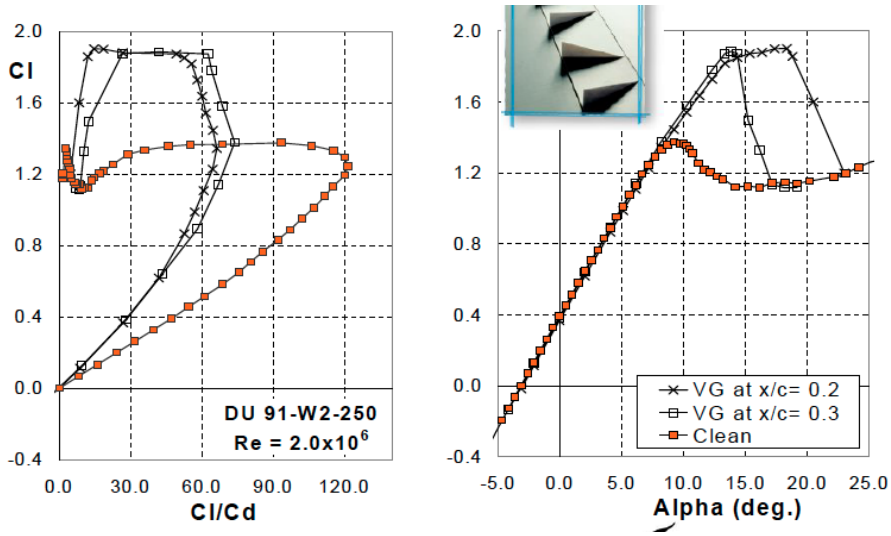

Figure 3.49 – Vortex generators influence on polar plots of DU91-W2-250 [74]

3.5 Conclusion

Some important points can be retained from this first dynamic pressure calibration application,

- Pressure taps can distort the signal due to diameter restriction, over a certain length. If channels are 3D printed, their shape has to be chosen such that no shrink can happen. The most optimum way to take into account dynamic calibration in an aerodynamic model is to use the same tubes (same length and diameter) to measure the pressure at a given location.
- Comparison of diameters was interesting for Chapter 2 but experiments in Wind Tunnel Laboratory in ULg are made using tubes of a given diameter ($D = 1.37$ [mm]). The calibration was studied comparing taps diameter. Indeed, if there is not enough space inside the model for tubes (too high density of tubes, tangle), channels can be 3D printed and taps diameter have to be chosen. As observed thanks to dynamic calibration, the response is highly delayed and attenuated using profile 2 (small taps). A careful calibration has thus to be done to take into account unsteady effects (static/steady properties are conserved).
- For phenomena in the range $f \in [0, 200]$ [Hz], the amplitude ratio is very close to 1 for $L < 0.5$ [m] (Figure A.24) thus if dynamic calibration is not performed, only slight errors on phase will be done. However, for higher tube length L, amplitude and phase are higher and dynamic calibration is mandatory.
- Comparison of reference and measured signals is also useful to see if shrinkage or leakage are present in the tube/tap, to avoid unphysical measurements.
- Dynamic calibration is useful to correct unsteady characteristics such as standard deviation or kurtosis during the stall. The lift coefficient works like a filter, fluctuations during stall are lower than those of each pressure taps coefficient.
- This allows to identify the type of stall, starting from the TE.
- Comparison with CFD validates the results (fluctuations of CFD results are lower because there are no instrumentation errors, that create noise)
- Theoretical models are useful to predict the lift at low angles of attack. However, viscous effects leading to stall cannot be theoretically modelled. Numerical methods like `Xfoil-XFLR5` adds a viscous correction and are able to detect this stall. However, the lower the Re, the higher the viscous effects, the higher the needed correction and therefore a greater likelihood of error.
- This profile is strongly Reynolds dependent. Pressure distribution, lift and drag vary with Re. The highest $Re = 1.2 \cdot 10^5$ is close to inviscid case (low viscosity) and the lift slope is very close to theoretical results,

  - Panel method and Joukowski airfoil model well thickness (lift slope) and camber (lift at $\alpha = 0$) effects
  - Thin cambered airfoil theory can only model camber effect

  The lower $Re = 0.6 \cdot 10^5$ shows a lower lift slope, and so pressure distribution. A large stalled laminar BL is present on the upper surface and reattaches as a turbulent boundary layer on the rear part (close to TE). The complete stall (separation of turbulent boundary layer) occurs for higher ($\alpha = 20$ for $Re = 0.6 \cdot 10^5$ and $\alpha = 12$ for $Re = 1.2 \cdot 10^5$).

Chapter 4

VIV grid

4.1 Introduction

4.1.1 Context

In aerodynamics, the distinction is often made between two types of bodies: airfoil (streamlined) and bluff (blunt) bodies. The former type refers to what was studied in Chapter 3, *i.e.* wings for which the flow is attached and assumed steady for low angles but shows separation due to viscous effects at higher angles (turbulence, unsteadiness,...). The latter is linked to bodies that are not "aerodynamically" shaped, in the sense that the flow is separated at each angle or velocity, that large vortices are created in the wake and that the pressure distribution around the body is unsteady. Most of civil structures (buildings, bridges,...) are bluff bodies where the flow is complex to study but necessary because loading around the structure has to be known, for dimensioning, resistance, displacement, or noise reasons. The last phenomenon is often a strong issue in civil structures because they are placed on the ground, close to where people are living or working. Sometimes, noise can be very disturbing and has to be avoided.

4.1.2 Motivations

Indeed, a grid was built and placed on a house to hide a terrace. It is composed of Aluminium rectangular cylinders horizontally spaced by 4 [cm] to guarantee that the terrace behind remains hidden. This grid is built with esthetic constraints, taking into account structural loads, the grid is dimensioned and fixed on four extreme points into the house facade (Figure 4.1). However, no aerodynamic study was performed. At certain periods of the year, the owners of this house realized that the grid generated an intense noise. This undesirable phenomenon creates a strong sound, continuous but appearing to stay at a constant frequency, between 50 and 100 [Hz]. Once it happens, it is like a huge guitar or harp with several chords of the same length, creating a strong mono frequencial sound, annoying the whole neighborhood.

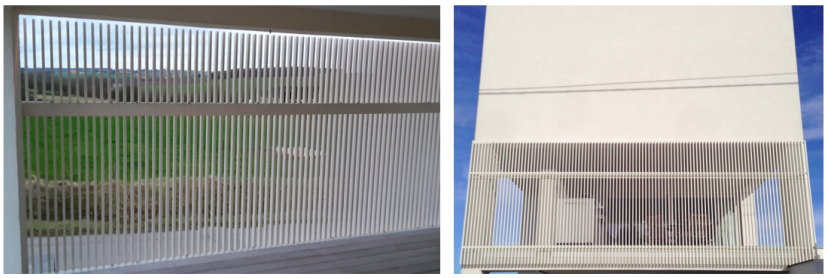

Figure 4.1 – Real grid on site, from inside (left) and outside (right)

They first thought that the phenomenon came from the air resonance inside cylinders, exactly as when one blows across the top of an empty bottle (called Helmotlz resonance). They decided to close the ends of the cylinders but the noise remained so the physical phenomenon behind is not Helmoltz

resonance. So, where does this noise come from, if not from Helmoltz resonance ? Why is it present on this grid ? Which parameters can influence this noise ? How to prevent it ? All these questions are interesting to solve and are no straightforward. A complete characterization of this grid has to be made to understand the phenomenon and solve it. The starting point of this Chapter is thus the study of this grid in its initial configuration but some parameters will be added, to see their effects and how they can be changed to solve this noise problem. This would also allow to extend the results of the study to structures of the same kind (rectangular cylinders in flow). Involved phenomena (vibration, vortex shedding, separation) are unsteady and the work performed in Chapter 2 will be used and applied here. The study included the following steps:

- A theoretical investigation with references, in order to understand more the phenomenon, particularly rectangular cylinders in flow
- *In situ* measurements to make the link between the noise, vibration of cylinders, wind strength and direction. Development of a WT model, based on the real grid, to reproduce real conditions and study other configurations
- Use of numerical methods to compare and validate results, by studying structural (modal) properties of the grid on one side (using FEM, with `SamcefField`©) and fluid dynamics around the grid on the other (using CFD, with `OpenFoam`).

4.2 Aeroelastic instability: VIV

For such a structure, two kinds of phenomena are present. Firstly, structural and inertia forces are linked to the mechanical behavior of the structure. Secondly, aerodynamic forces are acting on the structure because of the flow around it. The study of the interaction of inertial, structural and aerodynamic forces is called *Aeroelasticity* (Collar's triangle in Figure 4.2). Both phenomena will be introduced theoretically in this section and applied to one rectangular cylinder. The complete grid will be studied in experimental and numerical studies.

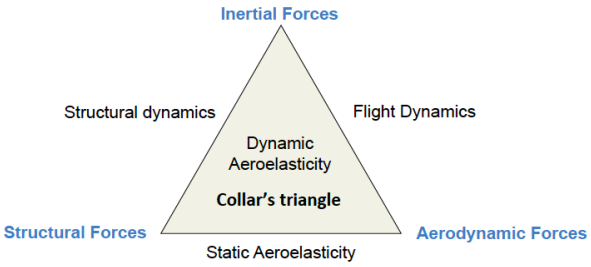

Figure 4.2 – Collar's triangle [66]

4.2.1 Structural forces

Euler-Bernoulli beam theory (engineer's beam theory or classical beam theory) is a simplification of the linear theory of elasticity which provides a simple means of calculating the load-carrying and deflection characteristics of beams. The transverse vibrations of the beam in bending can be deduced with kinematic assumptions,[34]

1. The beam cross-section is not deformable
2. The transverse displacement on it is uniform and, for simplicity's sake, is limited to the transverse displacement in the Oxz plane: $w = w(x)$, $v = 0$
3. The axial displacement component results from the rotation of the cross-section. The rotation is such that the cross-sections remain orthogonal to the neutral axis: $u(x, z) = -z\frac{\partial w}{\partial x}$ (equivalent to neglecting the shear deformation of the material)

By computing the beam kinetic $\mathcal{T}$ and potential $\mathcal{V}$ energies, the equation of free vibration of the beam is deduced from Hamilton's principle ($\delta(\mathcal{T}-\mathcal{V})=0$) by assuming harmonic motion $w(x,t) = w(x)\sin(\omega t)$ and neglecting the rotatory inertia of the cross-sections (no wave propagation in the beam), for a bipinned beam (Figure 4.3b)

$$\frac{d^4w}{dz^4} - \omega^2 \frac{m}{EI} w = 0 \text{ with } \begin{cases} w = 0 \\ M = EI\frac{d^2w}{dz^2} = 0 \end{cases} \quad (\text{at } z = 0 \text{ and } l) \tag{4.1}$$

Indeed, a pinned connection fixes the displacement and let the rotation free. The simplification is shown in Figure 4.3a, rectangular cylinders (cross section in Figure 4.3b) are horizontally spaced by $esp = 0.04$ [m] and welded on a L-profile. This welding is done on one face only, the three other ones are free and it can thus be seen as a pinned connection. The total cylinder length is 2.34 [m] but the welded fixation are spaced by 1.35 [m], there are 2 free lengths on both extremities of 0.5 [m] (only one shown). They are associated with higher frequencies modes so they are not considered in this simplification (this will be checked in FEM study). In equation 4.1, ω is the eigenfrequency,

$$\omega_n = \mu_n \sqrt{\frac{EI}{ml^4}} \text{ with } \mu_n = n\pi \text{ for bipinned beam} \tag{4.2}$$

- Young Modulus (Aluminium) $E = 7 \cdot 10^4$ [MPa]
- Cross Section Inertia $I = \int y^2 dA = \frac{DB^3}{12} - \frac{((D-2e)(B-2e)^3)}{12} = 7.8552 \cdot 10^{-8}$ [m^4]
- Mass per unit length $m = \rho A = \rho(DB - (D-2e)(B-2e)) = 0.7128$ [kg/m]
- Beam length $L = 1.35$ [m]

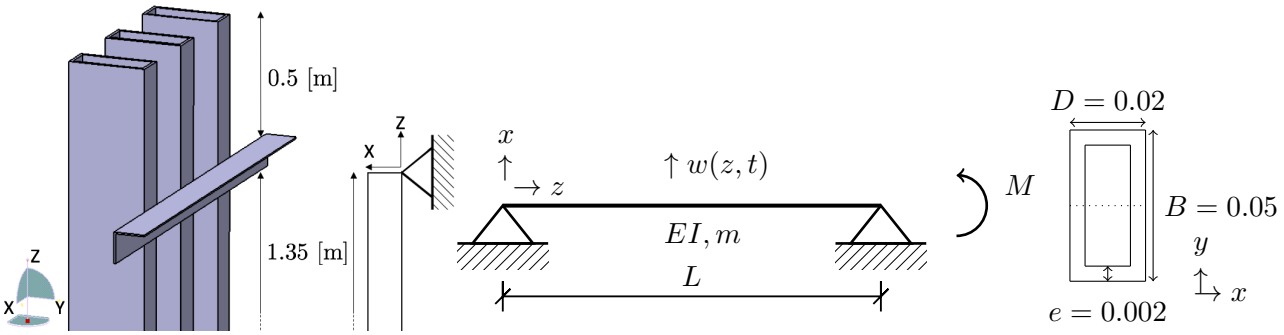

(a) 3D fixation simplification

(b) Bipinned beam, cross section and notations [m]

Figure 4.3 – Cylinder structure simplification (from the real views in Figure C.1)

4.2.2 Fluid forces

Introduction: flow around a cylinder As studied in the previous Chapter, a useful number to characterize the flow is the Reynolds number $Re = \frac{U_\infty D}{\nu}$ (here based on the cross flow dimension D). It is a measure of the boundary layer thickness and transition between laminar and turbulent flows. The most well-documented flow around a bluff body in the literature is the one around a circular cylinder. The pressure distribution is doubly symmetric for potential flow (Figure 4.4): Steady lift force and no drag (D'Alembert Paradox). In reality, the fluid is viscous, and, as discussed previously, the BL can separate when adverse pressure gradient happens (at $\theta \approx 80$, the pressure distribution reaches a plateau for $Re = 10^5$). The flow depends on the Re (inertial/viscous forces, Figure 4.5):

- For low Re (1-100), the flow is creeping, vorticity created in the BL is totally dissipated near the body [66], there is no separation for $Re < 5$, while for $Re > 40$ a vortex street
- Around $Re = 150$, a transition to a turbulent wake occurs
- For higher Re (150-10^6), viscosity has an effect in the vicinity of the body and a large amount of viscosity is not dissipated near the body

Due to no-slip condition (viscous effect), vorticity is created along the BL which separates from the cylinder surface to form a free shear layer in the wake, containing the vorticity (Figure 4.6). The vorticity causes the shear layer to roll up into a vortex. Indeed, the flow speed outside the wake is much higher than inside. The origin of the vortex shedding process is a shear layer instability (inviscid mechanism) [66]. The whole wake is affected and vorticity is continuously produced. This vortex formation is done on both cylinder sides, forming an unstable pair that alternates. It happens at a well-defined frequency, the vortex shedding frequency f_s. There is a linear dependence between f_s and U_∞, through the Strouhal number:

$$St = \frac{f_{vs} D}{U_\infty} \tag{4.3}$$

Where shedding frequency $f_{vs} = 1/T_{vs}$ (shedding period). This number is constant only in a limited range of Reynolds numbers (Figure 4.7). $St = 0.2$ in the subcritical region but it increases in the critical regime (one of the separation points starts to become turbulent). The shed vortices impact the aerodynamic forces. The lift coefficient C_L is defined perpendicular to the flow direction (Figures 4.6 and 4.8) from the lift force $C_L = F_L/(1/2\rho U_\infty^2 D)$. As the shedding process is continuous and alternating, and the flow is symmetric, the lift oscillates around 0 (periodically, with T_{vs}). The drag C_D oscillates around its mean value $\overline{C_D}$ at $T_{vs}/2$.

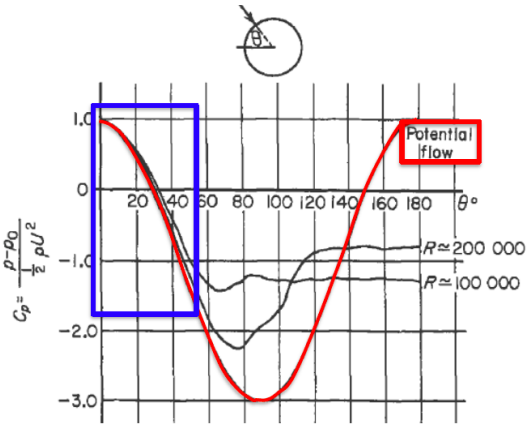

Figure 4.4 – Pressure distribution around circular cylinder, Re influence [66]

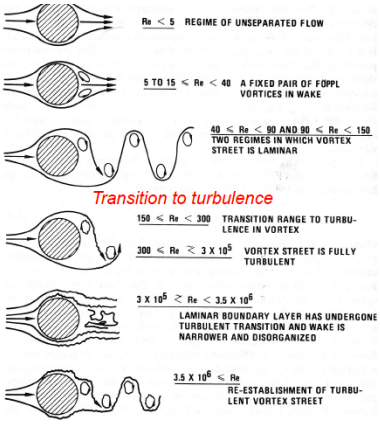

Figure 4.5 – Regime of fluid flow across smooth circular cylinders [42]

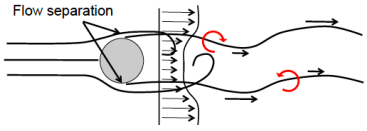

Figure 4.6 – Vortex shedding process around circular cylinder [66]

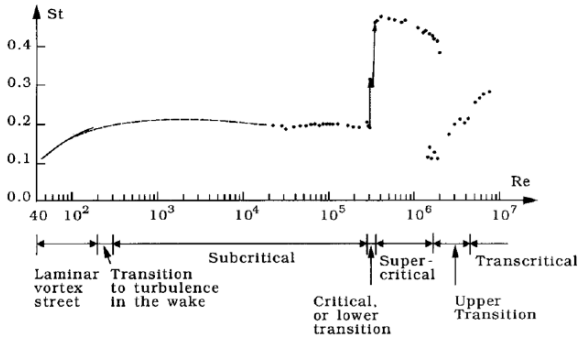

Figure 4.7 – St vs Re (cylinder) [38]

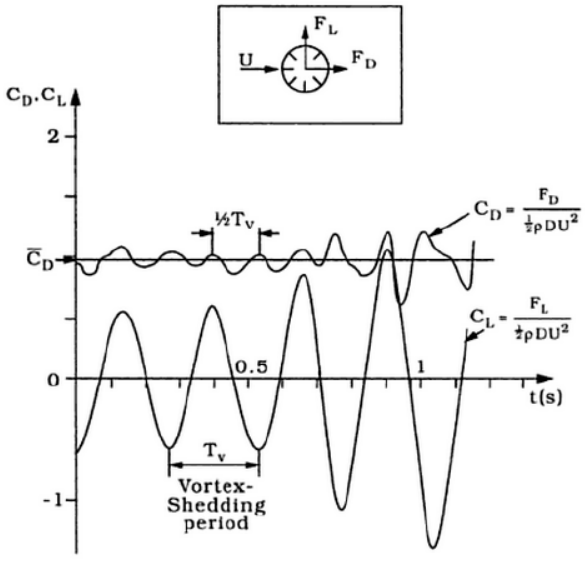

Figure 4.8 – Aerodynamic forces around cylinder [38]

Rectangular cylinder characteristics Compared to circular cylinders, the flow around rectangular cylinders is less well documented. Nevertheless, because of the grid cylinders shape, the aerodynamic behavior of a rectangular cross section will be studied (depending on the angle of attack α_∞). While the separation point of a circular cylinder moves depending on Re (θ location), the separation point for a rectangular cylinder always occurs at the sharp edges (Figure 4.9).The actual geometry is in Figure 4.10, compared with Figure 4.11 (conventions of [23]). Figure C.2 shows the 3D flow around a rectangular cylinder, with end effects. Assuming a long cylinder, characteristics and vortex shedding are 2D at mid span.

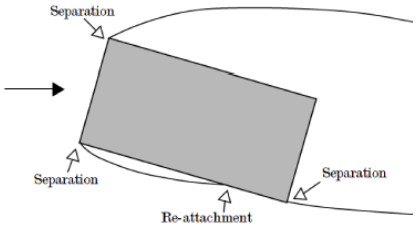

Figure 4.9 – Flow around a rectangular cylinder at incidence [66]

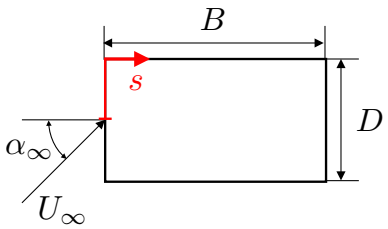

Figure 4.10 – Cross section of a cylinder model: actual geometry and notations

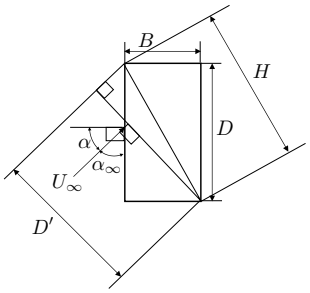

Figure 4.11 – Cross section of a cylinder model, adaptation of geometry to compare with [23]

The slenderness ratio $\frac{B}{D}$ is fixed at $\frac{50{\cdot}10^{-3}}{20{\cdot}10^{-3}} = 2.5$. The best way to study this kind of flow (on a bluff body) is to talk with *adimensional* quantities: the aspect (slenderness) ratio: $\frac{B}{D}$ and the Strouhal number defined previously: $St = \frac{f_{vs}D}{U_\infty}$, with D [m] being the cross flow dimension. Dimensions in the definition of St are crucial and need to be well identified in order to compare the same things when using other references (as done in [70]). This is the object of the following equation (4.4). In [23] and in Figure 4.12a, Strouhal numbers of different combinations of $\frac{B}{D}$ and α were measured. As said, $\frac{B}{D} = 0.4$ is fixed and studies the effect of α. The geometry in [23] in Figure 4.11 is rotated from 90° compared to 4.10 and the ratio $\frac{B}{D}$ is reversed. It follows that $\alpha = 90 - \alpha_\infty$. Other references also use this kind of definition for St: the cross-stream dimension D'. Figure 4.12a shows that St' is around 0.18 for α in the range of interest [20°,70°]. This $St' = \frac{fD'}{U_\infty}$ has to be adapted for the definition used here, defining D instead of D' as the dimension in St. A trigonometric study in Figure 4.11 shows that:

$$D' = \sqrt{B^2 + D^2}\cos\left(\alpha - \arctan\left(\frac{B}{D}\right)\right) = 53.85 \cdot 10^{-3}\cos(\alpha - 21.80) \tag{4.4}$$

Two equivalent ways can be used to correct St' into St: (1) By proportionality: $St = St'\frac{D}{B'}$ (2) By defining a new vortex shedding frequency associated to a Strouhal at $U_\infty = 1$ [m/s]: $f_{s,1} = St'\frac{1}{B'}$ leading to the corrected $St = \frac{f_{s,1}D}{1}$. These two methods give the same results, which is coherent. The transposition of notations from [23] (and [48]) is made in Figure 4.12b. The convention of Figure 4.12a [1] shows that St' is rather constant in a large range of α, but by changing D' for each α (equation 4.4), the effect of α is not emphasized and the convention of Figure 4.10 will be used for the rest of this study. In Figure 4.12b, St increases with α_∞ until 0.1 at 15 [°], vortices are more often ejected (f_{vs} is higher) because they cannot reattach after (the cylinder is no more horizontal). The higher α (after $\alpha = 15$), the sooner the flow reattaches on the lower surface (Figure 4.9) and the lower f_{vs} and St.

Figure 4.13 shows the influence of slenderness ratio B/D at $\alpha_\infty = 0$. For low B/D, the after body is very short, vortices are continuously and rapidly generated. When the ratio increases, the afterbody influences more the vortex shedding (closer to the wake) and St decreases. An interesting observation is the discontinuity around $B/D = 2.5 - 2.8$. The St increases suddenly from 0.06 to 0.15. The afterbody is long enough so that vortices reattach just at the end (near sharp edges on the right), and the situation seen by vortices at the end of the rectangle is equivalent to the one with a low after body B/D. For $B/D > 3$, the same process occurs, St decreases.

[1] With fixed $B/D = 0.4$ equivalent to $B/D = 2.5$ using convention of Figure 4.10

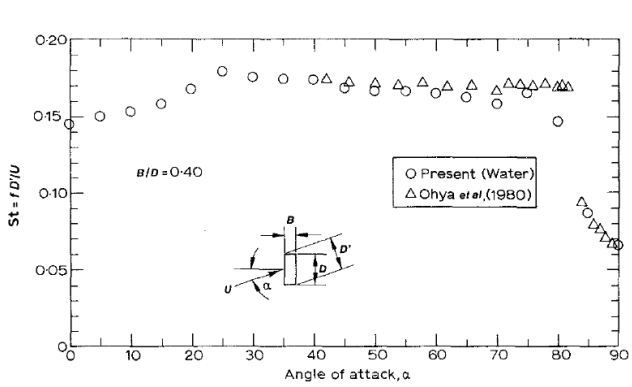

(a) St' vs α, geometry conventions of Figure 4.11 (Knisley [23]) $\left(\frac{B}{D} = 0.4\right)$

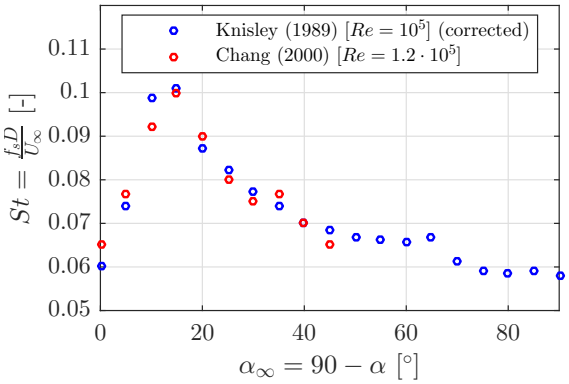

(b) St vs α_∞, geometry conventions of Figure 4.10 and correction of Figure 4.12a [23] $\left(\frac{B}{D} = 2.5\right)$

Figure 4.12 – Rectangular cylinders with fixed B/D: Strouhal numbers as a function of the angles of attack (comparison of references [23] and [24])

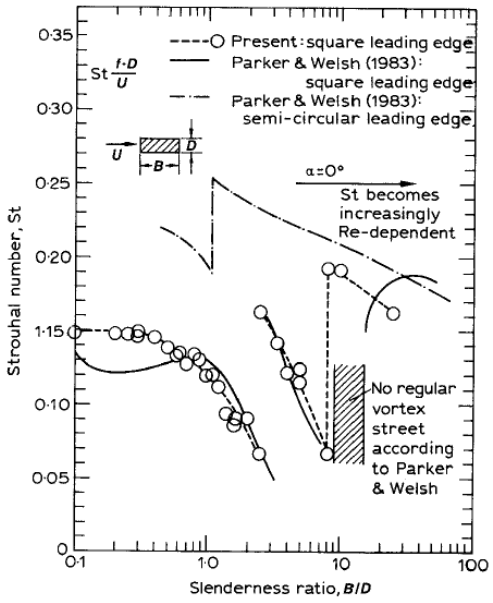

(a) Influence of leading edge [23]

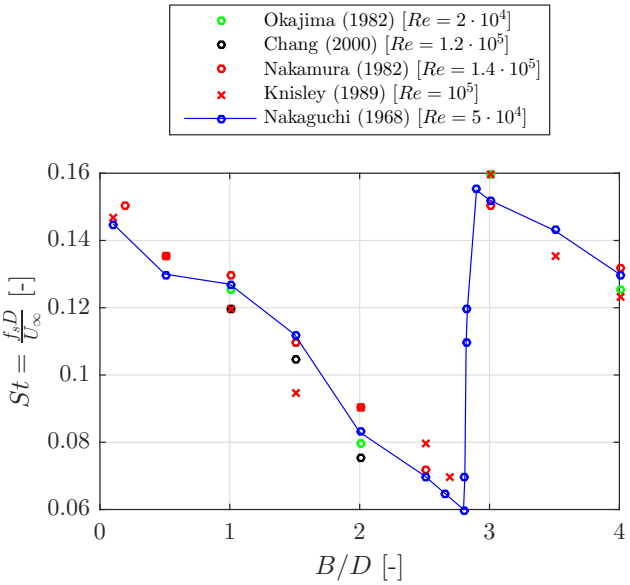

(b) Experimental references [19][24][49][23][36]

Figure 4.13 – Strouhal number St vs slenderness ratio B/D, at zero angle of attack, comparison of experimental results

4.2.3 Fluid-structure interaction

VIV phenomenon A free cylinder in flow can be seen as a simple linear oscillator (Figure 4.14). A dimensional analysis shows that the motion of a 2D linear structure in a subsonic, steady flow can be described as [66] (symbols are important, the same notation is conserved for the rest of this work):

$$\left[\frac{A}{D}, \frac{f_s}{f_s^0}, \frac{f_{vs}}{f_s^0}\right] = f(U_r, Re, m_r, \eta_s) \tag{4.5}$$

- f_s = free motion frequency ("s" stands for structural) in flow (at $U = U_\infty \neq 0$)
- f_s^0 = free motion frequency (at $U_\infty = 0$), independent of U_∞ (but not of the fluid properties)
- A = amplitude of the free motion
- f_{vs} = frequency of the vortex shedding process (with motion)
- $U_r = \frac{U_\infty}{f_s^0 D}$ the reduced velocity
- $m_r = \frac{m_S}{m_F}$ (m_S,mass (p.u. length) of the structure [kg/m] and $m_F = \rho S = \rho BD$, mass (p.u. length) of the fluid with density ρ), represents the susceptibility of flow induced vibrations

- $\eta_S = \frac{\text{energy dissipated per cycle}}{4\pi \times \text{total energy of the structure}}$
- $Sc = \frac{\pi}{2}(1 + m_r)\eta_S$, Scruton number ($\sim$ reduced damping)
- $SG = 4\pi^2 St^2 Sc$, Skop-Griffin number

With parameters fixed $D, f_s^0, m_r, \eta_S, \nu, \rho$ but U_r and Re varies with U_∞. It is possible to report in a graph (Figure 4.15) the evolution of f_s and f_{vs} according to U_r. When a certain critical U_r is reached, there is a matching of frequencies: the structure is excited at its still air free motion frequency $f_s = f_s^0$ and the vortices are shedded at $f_{vs} = f_s^0$. Because of the St relation, f_{vs} increases linearly with U_∞ and when $f_{vs} = f_s^0$ the matching creates a lock-in range where the cylinders is excited at $f_{vs} = f_s^0$ by the fluid (vortices) and excites itself at $f_s = f_s^0$.

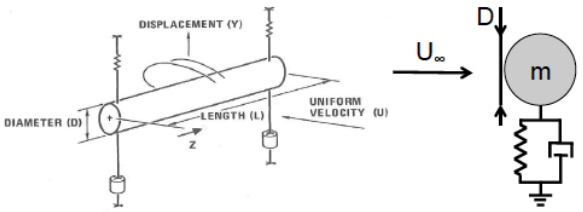

Figure 4.14 – Cylinder in a 2D steady flow, and linear oscillator model [66]

There are two key quantities to characterize VIV:

- A_{max}: max amplitude of the y motion, reached at $U_r = 1/St$
- Lock-in range: also occurs around $U_r = 1/St$

For small variations of U_∞ in a Re range, Re effect can be neglected. There remain only U_r, m_r and η_S effects, summarized into SG number

$$\left[\frac{A_{max}}{D}, Lockin(U_r)\right] = f(SG) \tag{4.6}$$

Figure 4.16 shows that $A_{max} < 1$ or 2 D (even for very low mass-damping combination) and $A_{max} \sim 0$ for heavy/damped structures The lock-in range decreases if SG increases so that VIV is a self-limited phenomenon.

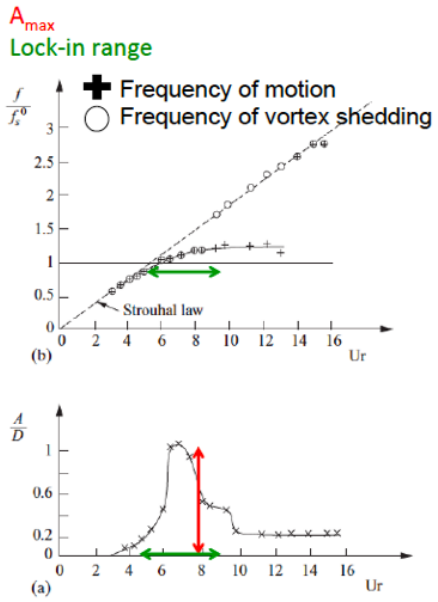

Figure 4.15 – VIV curves: (a) Lock-in range and frequencies (b) Amplitude A_{max} and lock-in range [52]

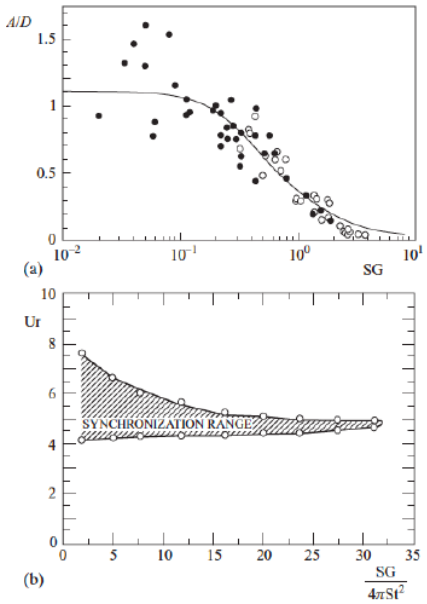

Figure 4.16 – VIV curves: (a) A_{max}/D vs SG (b) Lockin[U_r] vs Sc [52]

Galloping phenomenon In addition with VIV, galloping is another aeroelastic phenomenon. It is a velocity-depend, damping controlled instability, with transverse or torsional motions. It goes with the quasi-steady assumption: "the motion of the structure is slow compared to the motion of the fluid. The flow has time to adapt to the motion of the structure. Lift and Drag in the course of oscillation are the same at each α as the value measured statically during wind tunnel experiments". The criterion is thus a large reduced velocity: $U_r = U_\infty/(fD)$. Some authors have studied the meaning of "large U_r":

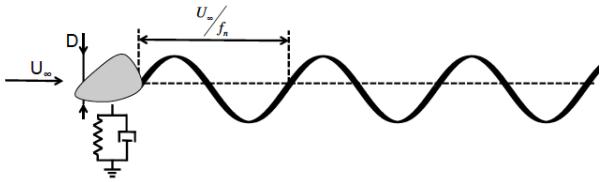

Figure 4.17 – Fung quasi-steady proposition [70]

- Fung (1955) : Figure 4.17 $U_\infty/f_n > 10D \rightarrow U_r = U_\infty f_n D > 10$
- Blevins (1977) : $f_{vs} > 2f_n$, using St definition and taking $St = 0.2$, $U_r > 10$ (same result but different physical reasoning)
- Nakamura & Mizota (1975) : $U_r = U_\infty/(fD) > 2U_{cr}^{VIV} = 2\,(U_\infty/(f_n D))_{cr}$ (for square prism), if not respected, interaction between VIV and galloping

Performing a stability study, the system is unstable if increasing motion (angle $d\alpha > 0$) leads to increasing vertical force ($dF_y > 0$), Den Hartog's criterion: $\frac{dC_L}{d\alpha} + C_D < 0$. A galloping curve (Figure 4.18 with hysteresis) can be found using non-linear equation of motion and polynomial fit, with $A = \frac{dC_{Fy}}{d(Y'/U)}\Big|_{Y'/U=0} = \frac{dC_{Fy}}{d\alpha}\Big|_{\alpha=0} > 0$ (Den Hartog, $-\frac{dC_{Fy}}{d\alpha} = \frac{dC_L}{d\alpha} + C_D$). The threshold for galloping (critical reduced airspeed) is $U_{cr}^{gallop} = \frac{2\beta}{nA}$, typically > 10, with $\beta = \delta/(2\pi)$ (δ = log-decrement) and $n = 1/m_r$.

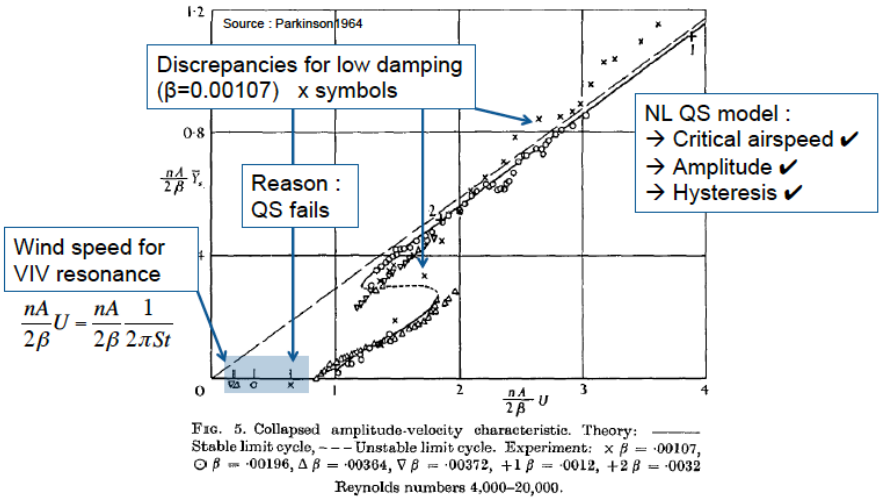

Figure 4.18 – Universal galloping curve for square prism (Parkinson & Smith (1964)) [33]

Because the noise created by the grid does not come from Helmoltz resonance, it most likely comes from vibrations of the structure (the sound is only a vibration of air). After studying these fluid-structure phenomena (VIV-galloping), it is clear that vibrations associated to the noise come from these aeroelastic effects. The purpose of the experimental study will be to identify which phenomenon is involved, by comparing critical reduced speeds U_{cr}^{VIV} and U_{cr}^{gallop} by computing an amplitude A/D vs speed U_r curve (Figure 4.19). If critical speeds are too close to each other, interaction between VIV and galloping may occur and the resulting oscillation amplitude would be higher than a single phenomenon prediction.

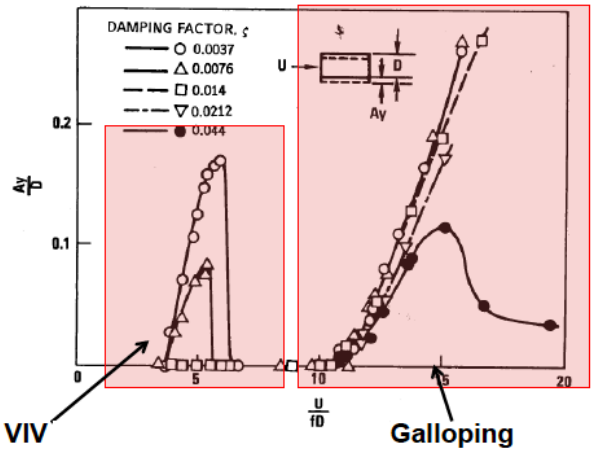

Figure 4.19 – Amplitude A/D vs reduced speed U_r for a rectangular cylinder [52]

Cylinders interference Previous results studied the flow and interaction for one cylinder. However, the grid is composed of 106 cylinders, spaced by $esp = 0.04$ [m] (*i.e.* $2D$). The proximity of cylinders will obviously create some interference in the flow. Zdravkovich [46] studied oscillations of two interfering circular cylinders. He discussed some interesting results, depending on their relative position (side-by-side or tandem, in Figure 4.20). By focusing on side-by-side positions:

- $1 \leq T/D \leq 1.2$: the two cylinders behave like one single body, only a single vortex street is formed downstream
- $1.2 \leq T/D \leq 2.2$: a biased gap flow (bistable) is formed, narrow and wide wake alternate between the two cylinders, f_{vs} is different in the two wakes
- $T/D \geq 2.2$: f_{vs} is the same in the two wakes but are coupled in out-of-phase (symmetry between the two cylinders)

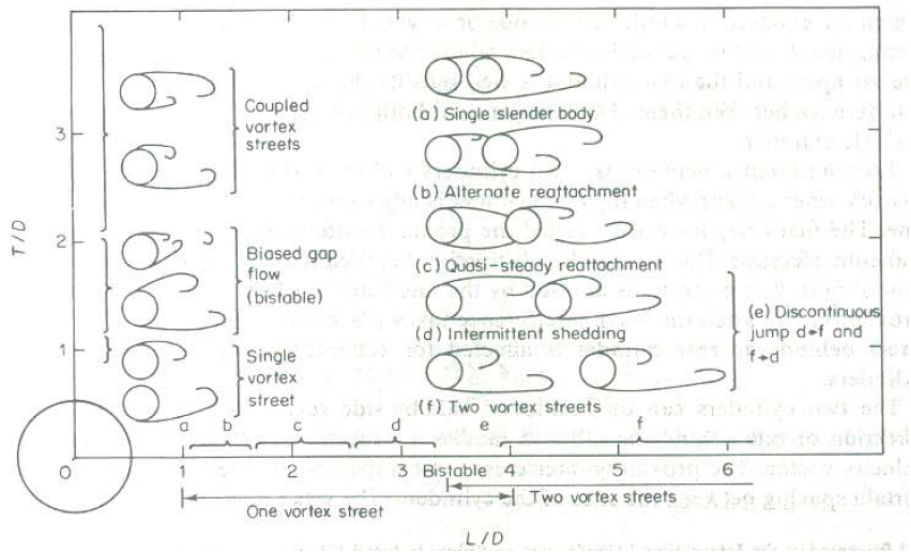

Figure 4.20 – Classification of flow regimes in side-by-side (T/D) and tandem (L/D) arrangements for stationary cylinders [46]

As studied above, vortex shedding is the most common fluid excitation for cylinders. The arrangement influence f_{vs} and St can vary from 0.1 to 0.38 (reduced speeds from 2.6 to 10). The cylinder with the higher St starts to oscillate at the lower U_r, whereas the second cylinder may remain stable (even if cylinders are the same). The oscillations of one cylinder can also affect the vortex shedding of the second one. Figure 4.21 shows the typical VIV response, depending on T/D. For low reduced

speed (W in Figure 4.21), forces are close and there is no high oscillation amplitude. When $W > 45$[2], the irregular cylinders displacement bring them into the biased gap flow region. Large transverse displacements and forces occur (but different drag forces for the two cylinders). When cylinders are more spaced, this instability is less steep and occur for a higher reduced speed W. All critical reduced airspeeds are reported in Figure 4.22, depending on the cylinder arrangement. The more spaced the cylinders are, the higher the reduced speed W, except for $T/D = 1.125$ (higher W than the one for $T/D = 1.25$). When cylinders are highly spaced, they behave like if they were alone.

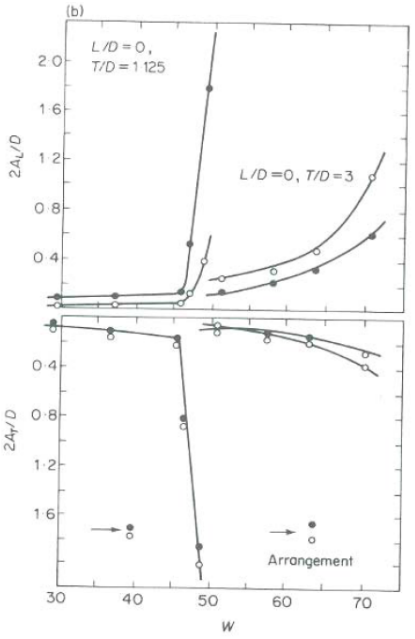

Figure 4.21 – Response to fluid-elastic excitation [46]

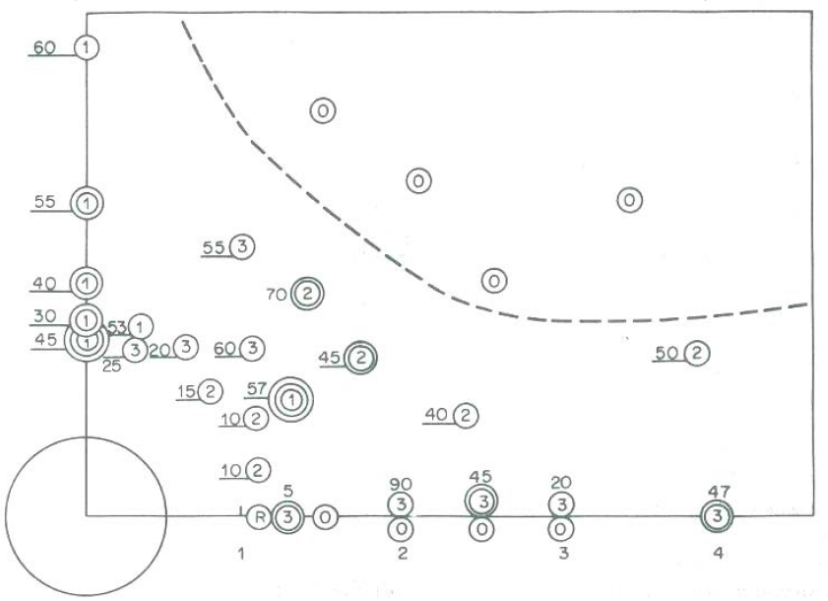

Figure 4.22 – Arrangements tested for fluid-elastic excitation; The type of response is written within circles and critical reduced velocity ext to them, for each arrangement [46]

These results suggest that cylinders interferences influence the critical reduced speed U_r (and also St because the VIV threshold occurs at $U_r = 1/St$). The arrangement T/D will be studied after as spacing parameter. Because rectangular cylinders are studied, the parameter angle of attack α will also be studied (not present for the purely symmetric circular cylinder studied by Zdravkovich [46]).

4.3 Numerical models

In this section, numerical tools will be used to study the grid (composed of rectangular cylinders, studied in previous section) from structural and fluid points of view. A FEM model of the real grid will be built, to compute its modal properties. A WT grid model will be built and also numerically study, the design is explained in section 4.5.1. Moreover, the fluid behavior around rectangular cylinder will be modelled using CFD. This section present these model assumptions and implementation, results are presented in dedicated sections (section 4.4.2 for the real grid and 4.6 for the WT grid model).

4.3.1 Finite Element Model

The mechanical (vibration) study of the grid was studied with strong simplification (only one bipinned cylinder of $L = 1.35$ [m]). Using FEM, it is possible to discretize beam in elements (with its neutral fiber) and to construct any shape to study its dynamic response (eigenfrequencies). It is possible using `LMS Samtech©SamcefField Rev8SL5`. The `Analysis Type` is selected to Modal. The simple cylinder is drawn using a `wire` as neutral fiber and `beam` behavior. Pinned boundary conditions are applied and a simple `mesh` is generated (and fixed after convergence study). The theoretical simplification will be compared with the same cylinder but with free extremity cylinders of 0.5 [m]. Moreover, the complete

[2]Definition of reduced velocity W is multiplied by 2π compared to the one used in this study

real grid will be modelled (106 cylinders fixed on two L-profiles, clamped on four points in the wall). A comparison will also be made with the WT grid model (11 cylinders fixed on a football goal like support). To validate this model, a convergence study is done, by inspecting the first eigenfrequency depending on the number of elements along the cylinder length (Table 4.1).

Averaged mesh length [m]	0.5	0.4	0.1	0.01
Mesh number [-]	3	4	14	135
First eigenfrequency f_1 [Hz]	66.29	65.7	65.42	65.42

Table 4.1 – Convergence study on simple cylinder model in `SamcefField` (one bipinned beam)

After this validation, the real grid is modelled in `SamcefField`: 106 cylinders of 2.35 [m] total length, welded on two L beams (cross section 0.04×0.04 [m^2] and 2 [mm] thickness), clamped on extremities (parallel and vertically spaced by $L = 1.35$ [m]). The WT grid model described in the section 4.5.1 is also modeled in `SamcefField` using the same principle (but only clamped to the ground, on the U lower side). Numerical results will be compared to the experimental data (from accelerometers) in section 4.5.2. Figure 4.23 shows eigenfrequencies obtained with `SamcefFiel` for a simple bipinned cylinder. It proves that using a cylinder of $L = 1.35$ [m] with or without free extremities (for a total length of 2.34 [m]) does not change the first eigenfrequency (bending in x direction, with the lowest inertia, $f_1 = 66$ [Hz]). The mode associated to the free extremities is at $f_2 = 92$ [Hz] (kind of independent mode of a clamped-free beam). The third mode is the bending in y direction ($f_3 = 137$ [Hz]), the fourth is a bending in x with 1 central node ($f_4 = 178$ [Hz]) and so on. The simple beam theory, with values in section 4.2.1, gives $f_1 = 67$ [Hz], which is consistent because of the same assumptions and modelisation.

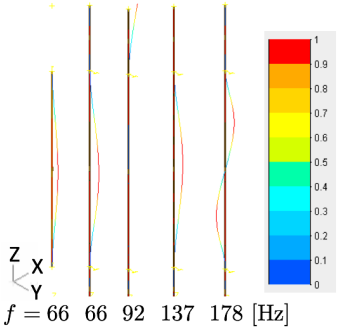

Figure 4.23 – Eigenmodes (adimensionalized, ratio in legend (max = 1)) and frequencies (for one cylinder with $L = 1.35$ [m]) with `SamcefField` without (1^{st}, left) and with (2^{nd} to 5^{th}) free extremities

4.3.2 Computational Fluid Dynamics

As done in Chapter 3, a CFD study will also be performed for the WT grid model, to compare with experimental results. It will be useful to know the velocity, pressure,... contour and mostly the lift-drag time variation and the pressure distribution around the cylinders. The same model as in Chapter 3 will be used ((U)RANS $k-\varepsilon$). Numerical and iterative scheme is the same as in Chapter 3. Boundary conditions are the same as for Chapter 3 Table 3.1, using the following initial conditions for inlet [26]:[3]

$$k = \frac{3}{2}(I_u U\infty)^2 = 0.0024\ ,\ \varepsilon = \frac{C_\mu k^{3/2}}{0.1} = 1.17\ ,\ \nu_t = C_\mu \frac{k^2}{\varepsilon} = 4.43 \cdot 10^{-7} \tag{4.7}$$

A convergence study is made on a mesh composed of one cylinder ($B/D = 2.5$) at $\alpha = 0$ (geometry in Figure 4.25 but with only one cylinder). Every simulation is performed at $U_\infty = 5$ [m/s] (from observed results in section 4.6 in site and in WT model, critical speed is close to 5 [m/s]). Figure 4.24 compares c_l and c_d for one cylinder at $\alpha = 0$ depending on the mesh (the time step is fixed at

[3]With $I_u = \frac{U_1}{U_\infty} = 0.8\%$ (turbulent intensity) and turbulent length scale $L/D = 0.0045$ (Ong 2012 [45]).

$\Delta = 10^{-5}$ to respect CFL condition $u\Delta t/\Delta x < 1$ for each mesh size Δx). Mesh 2 uses value in Table 4.2, Mesh 1 uses a mesh three times coarser than Mesh 2 (Mesh 3 a mesh 1.5 times finer). Because the flow is symmetric ($\alpha = 0$), the mean lift c_l is 0 (Figure 4.24) and oscillates at f_{vs}. The drag c_d has a positive mean value (around 0.84) and oscillates at $2f_{vs}$ (but with a lower level of oscillation). From this convergence study, mesh 2 is conserved for the following results. The final mesh domain (with 10 cylinders) is represented in Figure 4.25, the grid is studied in 2D (cut plane at cylinders mid-height), with the number of elements and the progression used in the final mesh (after the convergence study on one cylinder) in Table 4.2.

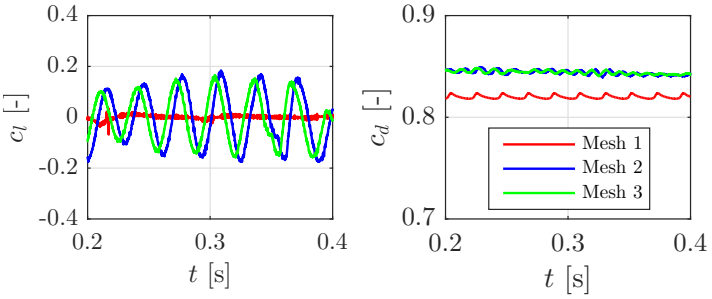

Figure 4.24 – Convergence study on mesh and time step

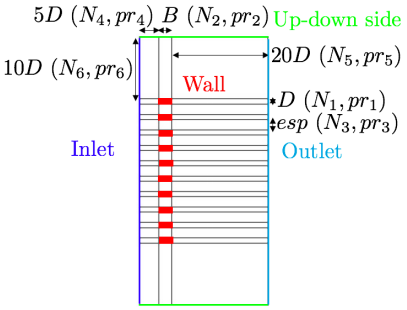

Figure 4.25 – Grid domain geometry and boundaries

i	1	2	3	4	5	6
N_i	20	50	40	50	50	50
$prog_i$	1	1	1	0.9	1.07	0.95

Table 4.2 – Number of element and progression used in final mesh of Figure 4.25

4.4 *In situ* measurement

This section will present all methods used to characterize and study the grid from a fluid-elastic point of view (both structural and flow characteristics). Firstly, experimental measurements taken on the real grid will be analyzed to identify for which conditions the grid vibrates (wind speed and direction). Afterwards, the WT model will study the same conditions and test other configurations, to highlight the influence of incidence and cylinder spacing.

4.4.1 Instrumentation

The response of the real grid (full-scale measurement) during the noise-event (grid vibration) is measured using instrumentation in Figure 4.26.

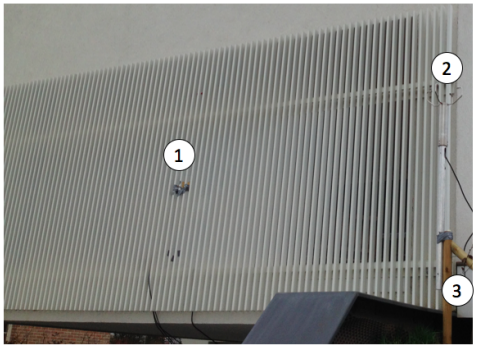

1. Accelerometers
2. Anemometer
3. Acquisition station

Figure 4.26 – Measurement set-up on the real grid

1. Three accelerometers: PCB-Piezotronics© 3713B112G, sampled at $f_s = 640$ [Hz], placed at mid-height of 3 central cylinders of the grid (Figure 4.26)
2. An anemometer to measure the air speed U_∞ and direction α_∞
3. An acquisition system (computer and internet connection) to send data from the site to the Wind Tunnel, during one week.

4.4.2 Results and discussion

Modal properties Figure 4.27 shows some interesting modes of the real grid. As the grid is composed of a lot of cylinders and beams, and degrees of freedom, it will show the same number of eigenmodes as the number of elements (each one with very close frequencies when they represent the same kind of deformation, for example, bending in y of cylinders). Because the cylinders are fixed on 2 support beams (the longest element in the model) they show very low frequency mode for the whole structure (first mode with 1 antinode at $f = 1$ [Hz], higher mode with 5 antinodes at $f = 22$ [Hz] and a more complex pattern with a combination of antinodes in several directions at $f = 43$ [Hz]). There is a lot of modes around $f = 64$ [Hz] that show the same kind of deformation (bending in x), differences can come from in and out of phase cylinders (Figures 4.27d and 4.27e). The mode of free extremities is also present, at a higher frequency $f = 84$ [Hz]. There are (global) modes of the whole grid at low frequencies, but the modes of interest (those of cylinders) are very close to a situation where cylinders are bipinned, alone (by comparing $f = 66$ alone in Figure 4.23 and $f = 64$ in the grid). This motivates the design of the WT model, discussed in section 4.5.1.

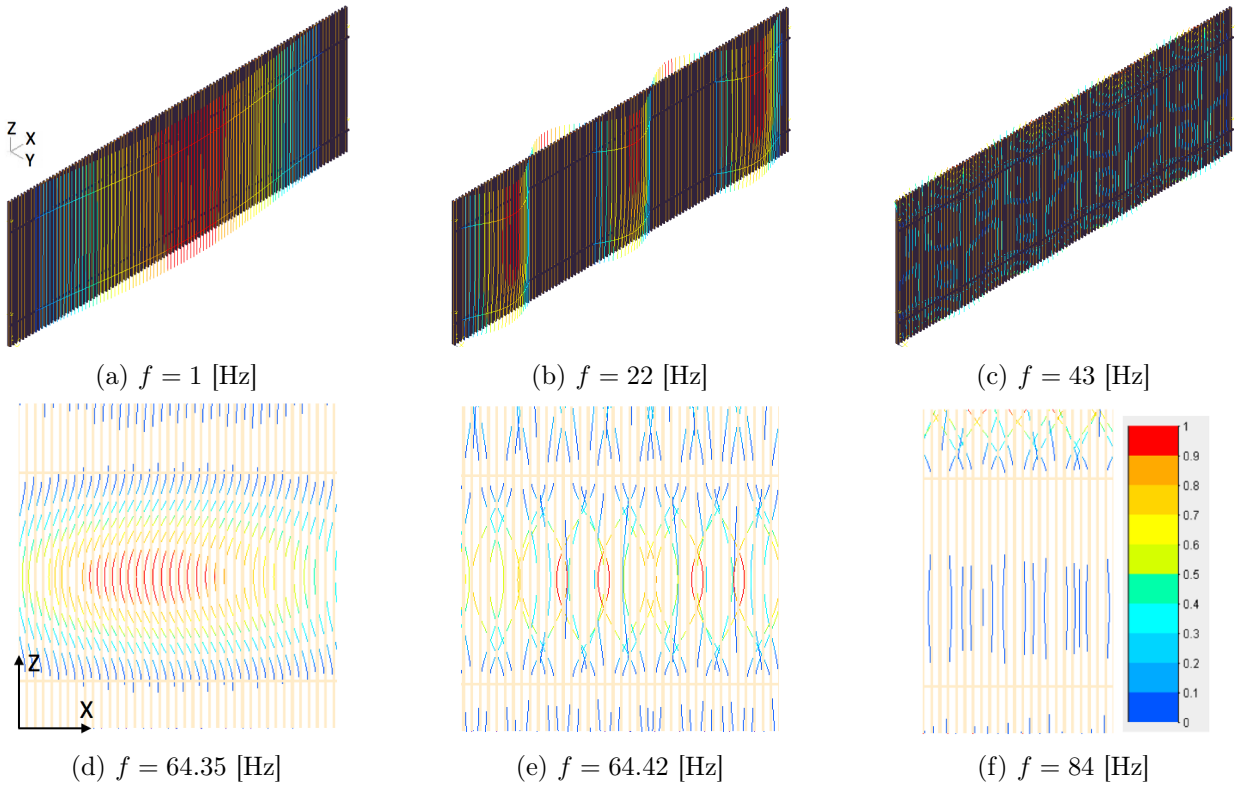

(a) $f = 1$ [Hz] (b) $f = 22$ [Hz] (c) $f = 43$ [Hz]

(d) $f = 64.35$ [Hz] (e) $f = 64.42$ [Hz] (f) $f = 84$ [Hz]

Figure 4.27 – Eigenmodes and frequencies of the real grid, with `SamcefField`, deformation ratio in legend (max = 1)

Fluid-structure interaction Three accelerometers continuously record acceleration (in x direction, during 7 half days), at the same time as the wind speed and angle, to make the link between them. The two first cylinders were filled with sand, to see the influence of the mass[4] and damping on the response (increasing m and η_S increases SG number and decreases A_{max}/D and Lockin(U_r)). The sampling is made at 640 [Hz] and the recording is done through 10 minutes files.

[4]By $m = \rho_{sand}(B - 2e)(D - 2e)L = 1500 \cdot 0.046 \cdot 0.016 \cdot 2.34 = 2.58$ [kg]

Figure 4.28 shows a global view of the 7 half days of measurement (around 80 [h]), using a time window of 1 [min] where quantities are averaged (U_∞ and α_{infty}) or statistically analyzed ($\ddot{x}_{max}$ or $\sigma(\ddot{x})$). Indeed, gust and wind variation are typically constant in this interval. It can be interpreted from this figure that the acceleration increases sharply (peak values above 0.5 [g][5]) for a certain condition: every time $U_\infty > 5$ [m/s], this instability occurs. The direction varies a lot when the wind is at low speed but for $U_\infty > 5$ [m/s], a dominant wind, the direction is also more dominant (typical west wind in Belgium) but this is less evident than the correspondence $\ddot{x}_{max} - U_\infty$. Zones of interest are called events, where the acceleration is high. The dynamic response will be more deeply analyzed for a representative event, between 75 and 78 [h] (the last half day).

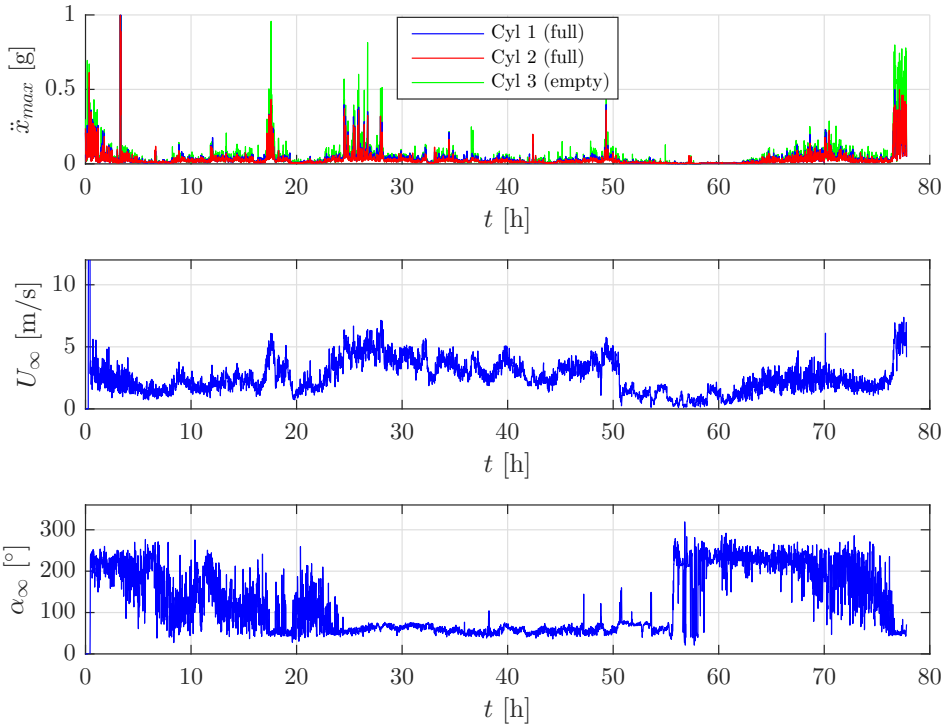

Figure 4.28 – Response *in situ* (peak acceleration) during 7 half days, wind speed and direction

Figure 4.29 shows a typical VIV curve (as Figure 4.19), the acceleration (Root Mean Square (RMS)) increases a lot for each cylinder around $U_\infty = 5$ [m/s]. Cylinder 3 has higher A_{max}/D and Lockin(U_r) because of lower mass and damping. Figure 4.30 shows a zoom on the event of Figure 4.31: cylinder 3 oscillates two times more than cylinders 1 and 2 (out of phase, as the mode at $f = 64$ in Figure 4.27d).

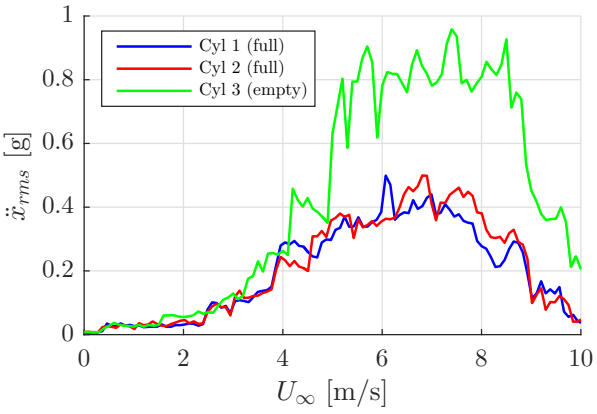

Figure 4.29 – VIV curve: $\ddot{x}_{rms}$ envelope as a function of U_∞ during event at $t = 77$ [h] (Figure 4.31)

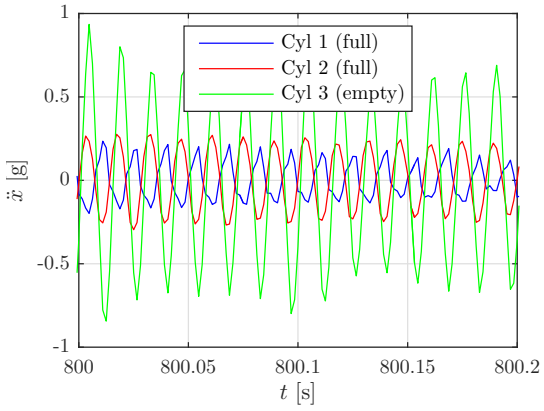

Figure 4.30 – Comparison of accelerometers (zoom in event at $t = 77$ [h] (Figure 4.31))

[5] 9.81 [m/s^2]

Figure 4.31 shows properties during an event (the last half day, around $t = 77$ [h]): acceleration of accelerometers 1 to 3 during the time, probability density $\mathcal{P}$ of $\ddot{x}$ and $|FFT(\ddot{x})|$, and comparing to U_∞. Full cylinders (1 and 2) show lower oscillations amplitude (SG is higher thus A_{max}/D is lower, between -0.5 and 0.5 [g]) compared to cylinder 3 (between -1 and 1 [g]). However, during events (oscillations), cylinders are excited at their resonance frequency (around $f = 60$ [Hz], consistent with modal study (with `SamcefField`) with $f = 64$ [Hz]). As observed, events happen when $U_\infty \geq 5$ [m/s] (most of the time in Figure 4.31, as suggested by $\mathcal{P}(U_\infty)$).

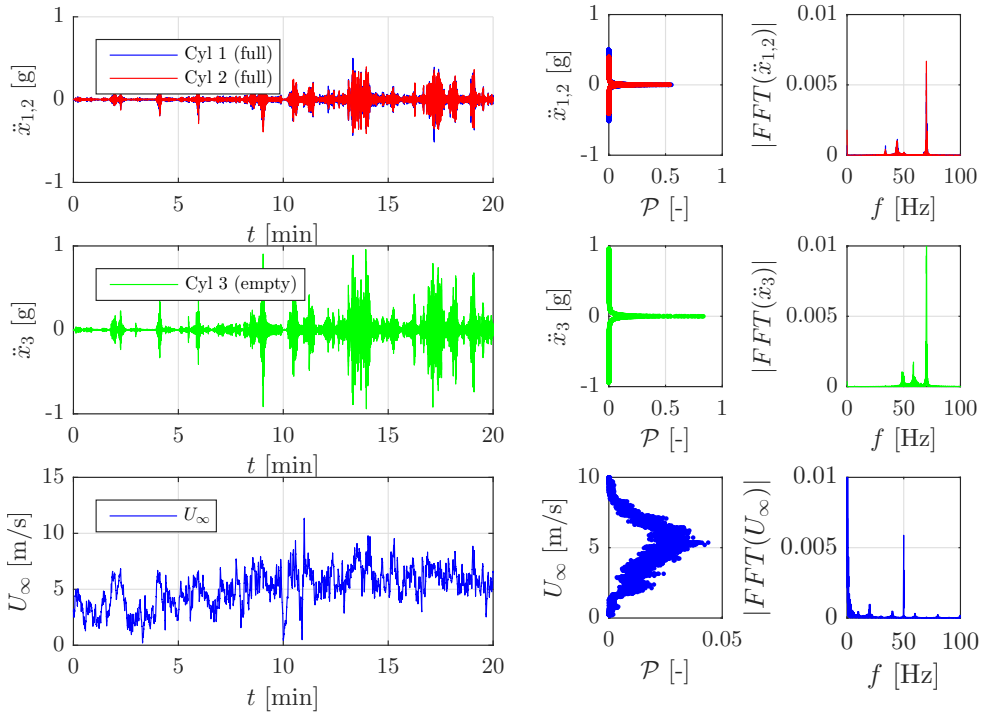

Figure 4.31 – Response *in situ* of 3 accelerometers during event at $t = 77$ [h], wind speed: probability distribution and FFT

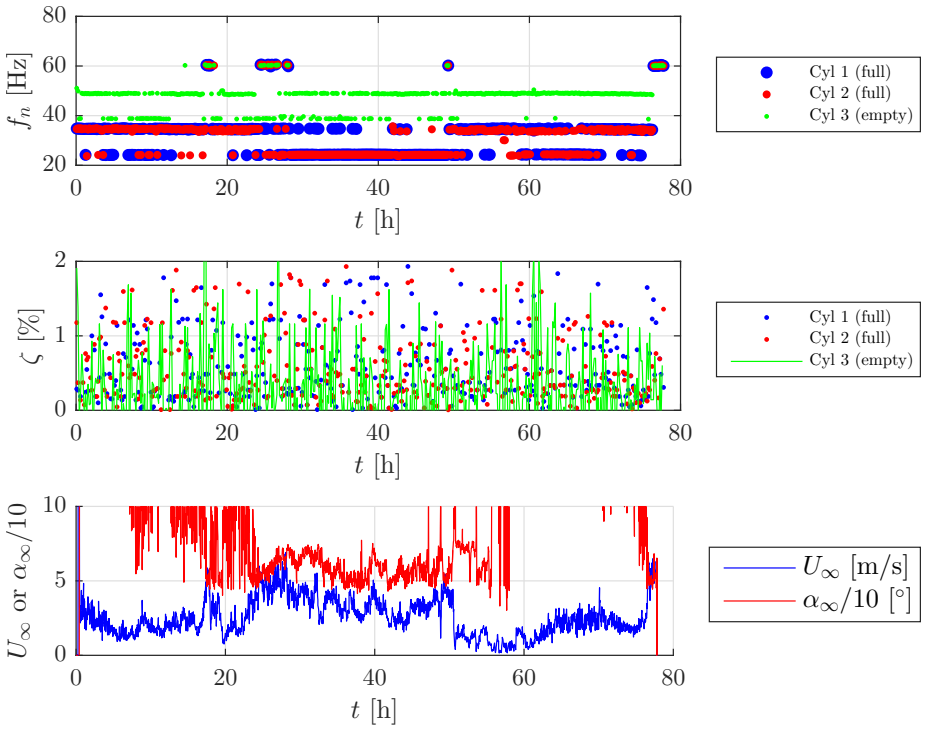

Figure 4.32 – Eigenfrequency f_n and damping ratio ζ during 7 half days *in situ* (with U_∞ and α_∞)

Figure 4.32 shows eigenfrequency and damping ratio for each 10 [min] recording, during the 7 half days. At each event, $f_n = 60$ [Hz] for each cylinder and the damping ratio decreases (it is not clear in Figure 4.32 but more in Figure 4.33). Figure 4.33 shows modal properties during event (the last half day, around $t = 77$ [h]) for each 10 [min] recording (red line). It is obtained by averaging modal properties for each window (each 10 [min] recording is divided into windows of $win = 5$ [s]). Modal properties are written in terms of $St = f_n D/U_\infty$ and ζ. When nothing happens (low speed), St and ζ are higher (a higher damping means a lower amplitude, St is high because U_∞ is very low). When the instability (event) occurs, St of each cylinder is close to 0.22 and the damping is lower for cylinder 3 (around 0.2%, consistent with higher oscillations, the mass, the damping and SG are lower, leading to higher A_{max}/D and Lockin(U_r)). After these observations, the grid is clearly subjected to VIV. Galloping occurs at $2\zeta/(nA)$, with $A = 2.69$ for a square cylinder (from Nakamura [77] not the case here but it gives a good guess). The (reduced) threshold for galloping is thus 12 (with $n = 1/m_r = 0.0017$ and $\zeta = 0.01$, from Figure 4.33) while the critical reduced speed for VIV is $U_r = 1/St = 1/0.22 = 4.55$. Galloping is not present for the speed of interest. This results for St is interesting. Indeed, the St for a rectangular cylinder alone in the flow is between 0.06 and 0.1 (Figure 4.12), a grid effect is present and modifies the vortex shedding behavior because of cylinder interference. The WT model is hence useful to study this effect.

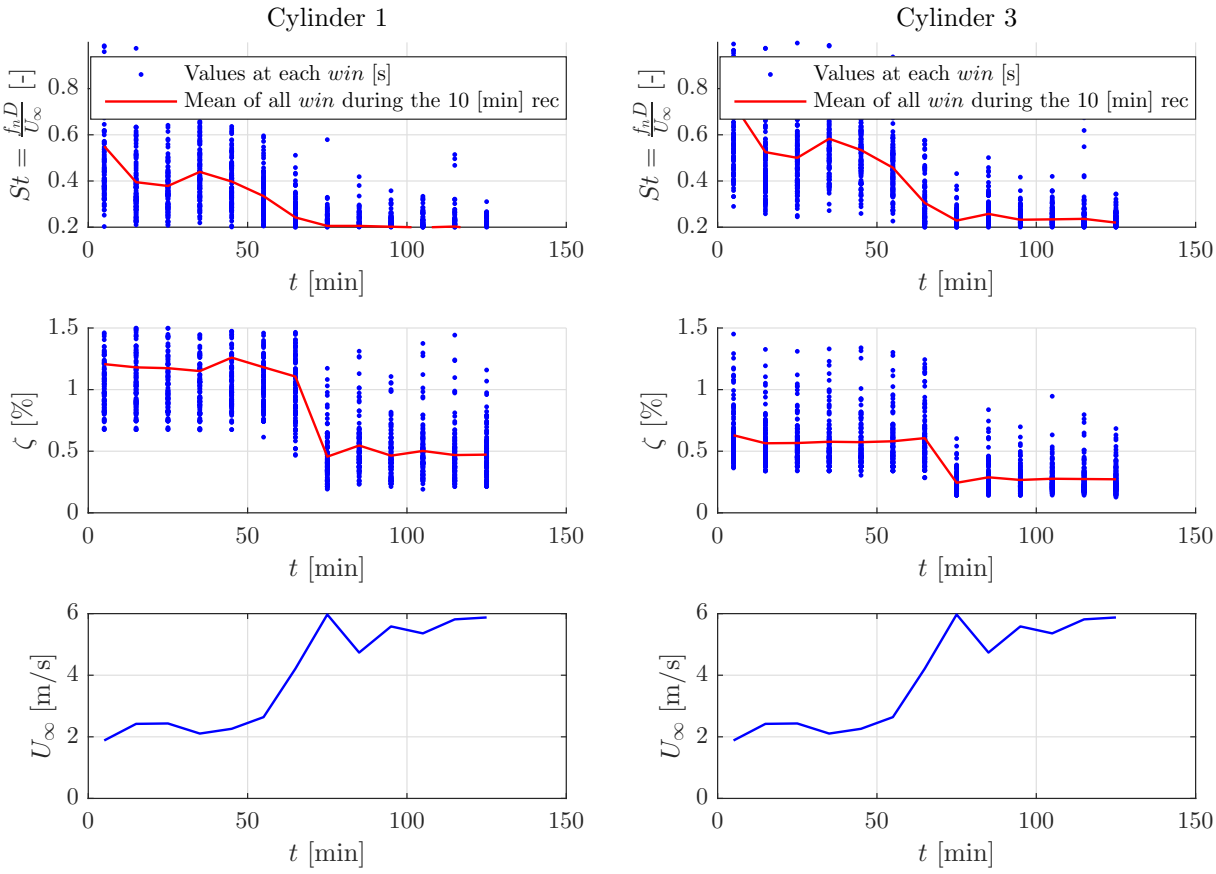

Figure 4.33 – St and ζ statistics *in situ* (zoom in the event of Figure 4.31) and U_∞

4.5 Wind Tunnel Model

Observations of the real grid behavior motivates the design of a WT grid model, to reproduce real conditions and better understand the phenomenon. Such a model can plays in an *active* way, *i.e.* imposing wind conditions (speed and incidence) rather than measuring random real ones. This model is also built such that cylinders can me moved horizontally to study the spacing parameter T/D and the influence on cylinders interference.

4.5.1 Design and instrumentation

Figure 4.34 shows the model build for WT testing, a 1:1 scale of the original grid. The model is composed of 11 Aluminium cylinders, with a section $B = 0.05$ [m] $\times$ $D = 0.02$ [m] (hollow section, with 2 [mm] thickness) and length of $L = 1.43$ [m], spaced horizontally by $esp = 0.04$ [m]. Cylinders are fixed to a support structure (Football goal-like shape), composed of hollow square cylinders in Aluminium (section 0.04×0.04 [m^2], thickness 3 [mm]). The fixation is made with M3 screws, connecting cylinders to extruded Bosch©Profiles (section 0.04×0.04 [m^2]), allowing a free choice of the horizontal location of cylinders (to study the parameter spacing esp). To guarantee the same fixation type and strength, a setting torque tool (Facom©R208-25) is used to screw with a constant torque of 15 [Nm]. The real model uses welded cylinders on support, not perfect but with a similar stiffness compared to M3 screw (necessary to allow the spacing esp). The grid model is screwed on the turning table, to study the parameter angle of attack α).

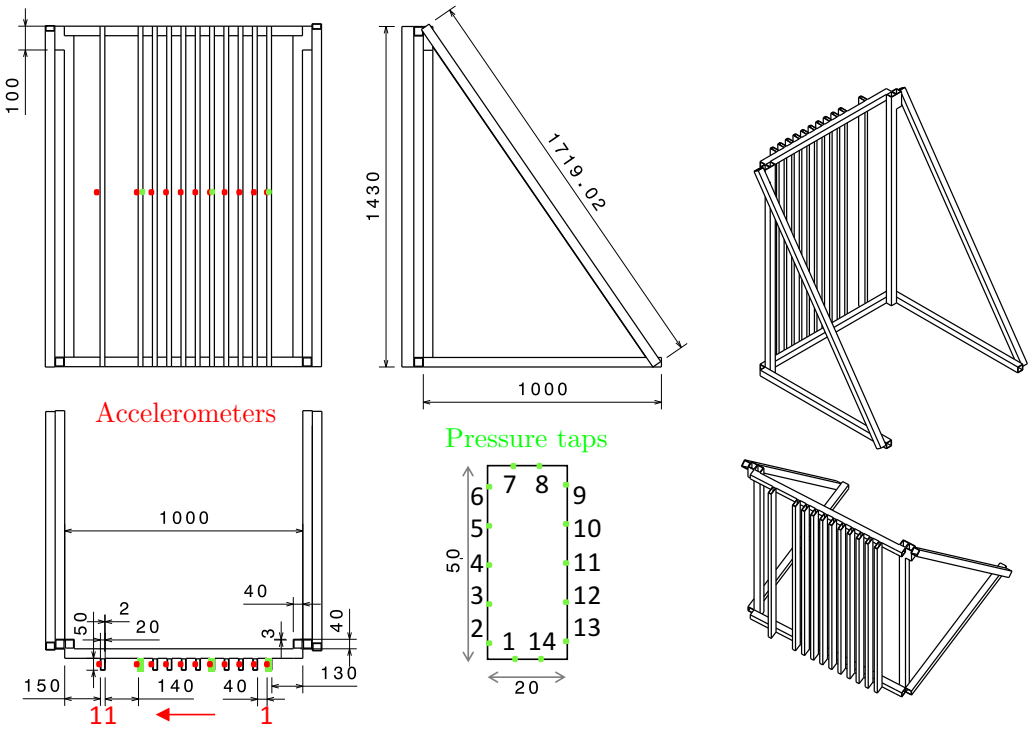

Figure 4.34 – Drawing of the grid model build for WT testing: top, side, front and axisymmetric views, locations of accelerometers, pressure taps and cylinders numbering, dimensions in [mm]

Only 11 cylinders are used, for practical reasons (WT test section 2 has dimensions of 2.5 [m] $\times$ 1.8 [m]. The purpose of this study is to analyze the fluid-structure interaction (VIV) for rectangular cylinders as well as the grid effect (not only one cylinder but interactions of the grid). For consistency and organization, cylinders are numbered according to Figures 4.34 and 4.35 for the whole Chapter. The FEM analysis of modal properties justifies the equivalence of the WT model and the real one (section 4.3.1). Using 10 cylinders is sufficient to obtain a similar flow on the central part. There are interactions between cylinders in neighborhood and external cylinders are far enough from the central ones to neglect ends effects on these central cylinders. Comparison of measurements on site and in the WT will be discussed later. The characterization of the grid will be complete, in the sense that fluid and mechanical characteristics will be measured, with the setup shown in Figure 4.35.

- Structure: Accelerometers (red locations in Figures 4.34 and 4.35) for accelerations measurements on each cylinder, to deduce modal properties (eigenfrequencies f_s and damping ratio). They are PCB Piezotronics ©302A02, loaned by V2i. Their sensibility (different for each accelerometer in [mV/g]) is directly put in an V2i executable). Figure C.3 shows accelerometers location on the model, inside the WT Test Section 2. The sampling frequency is $f_{samp} = 640$ [Hz].

- Fluid:
  - Turbulent Flow Instrumentation ©Cobra Probe 100 series: This probe is able to measure the three velocity components (and so vortex shedding behind cylinders f_{vs}) with a high accuracy and fastly thanks to a very thin head of cobra-like shape. Figure C.5 shows its geometry, reference port and acceptance cone. Figure C.6 shows the acquisition made with the Device Control Software. The sampling frequency is $f_{samp} = 500$ [Hz].
  - Telescopic Hot Wire Probe Kimo©- SFC-900: It allows to measure precisely the free stream air speed in the WT U_{HT}, knowing the airspeed chosen on the WT controller U_C, in Figure C.7: $U_{HT} = 0.82U_C - 0.46$.
  - Pressure taps (green locations in Figures 4.34 and 4.35: 5 along each cylinder chord B and 2 along cross flow dimension D, thus 14 in total). Turbulent Flow Instrumentation ©DPMS (same used in Chapter 2, in Figure 2.61) is used to measure the pressure. The connection between taps and DPMS is made with PVC tubes (corresponding to case 6 in Chapter 2, $L = 1.3$ [m] and $D = 1.37$ [mm]) to measure the pressure distribution around the rectangular cylinder at mid-height, on 3 cylinders. In a first case, cylinders 1, 5 and 10 in Figures 4.34 and 4.35 and, in a second one, cylinders 4,5,6. It will emphasize vortex shedding generation and interaction (phase between vortex of two adjacent cylinders). Figure C.4 shows the pressure instrumentation. The sampling frequency is $f_{samp} = 500$ [Hz]. Recorded pressure signal will be dynamically calibrated thanks to IFFT correction discussed in Chapter 2.

The studied parameters will be: airspeed U_∞, angle of attack α and space esp (adimensionalized to T/D) (turbulence characterization and study is not the purpose of this work, but the one of Giulio Vita), pressure time signals will also be studied and calibrated.

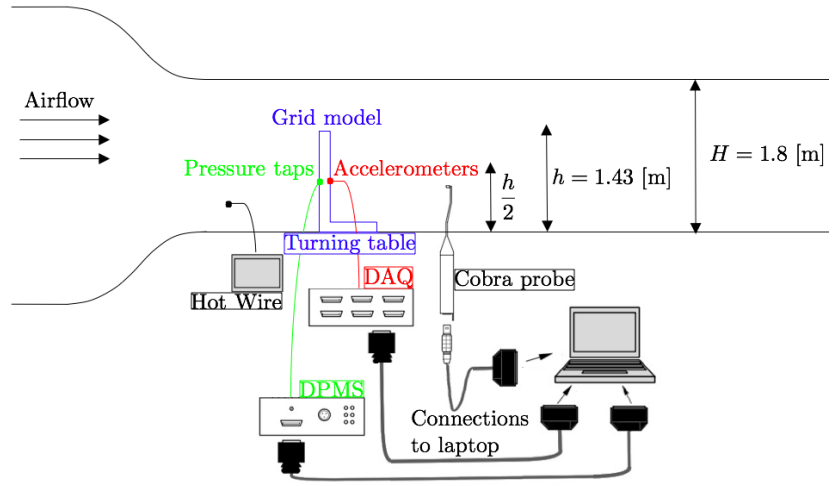

(a) Side view

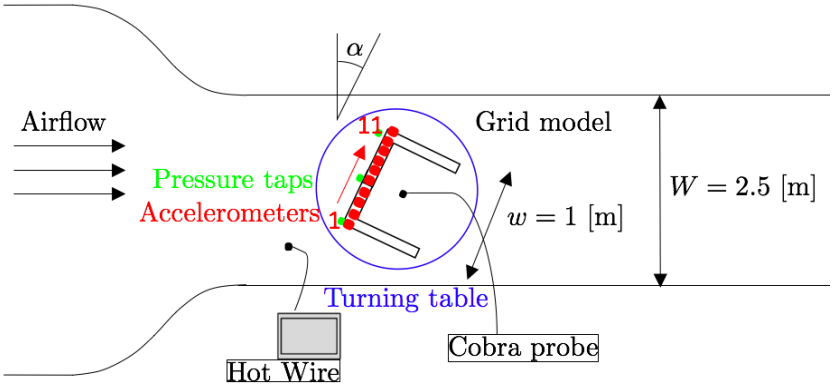

(b) Top view

Figure 4.35 – Setup of the grid model inside the WT Test Section 2, with measurement tools

4.5.2 Results: modal properties

FEM study The model structure was studied in terms of modal properties before to be manufactured. Figure 4.36 shows several modes of the model. As for the grid, some overall support modes are present at a lower frequency (translation at $f = 18$ and bending of support at $f = 49$ [Hz]). Modes of interest are bending in x direction at frequencies very close to those found in theory and with `SamcefField` model of the real grid. Higher modes are also present, similar to those of a single bipinned beam (y bending, x bending with 1 node,...).

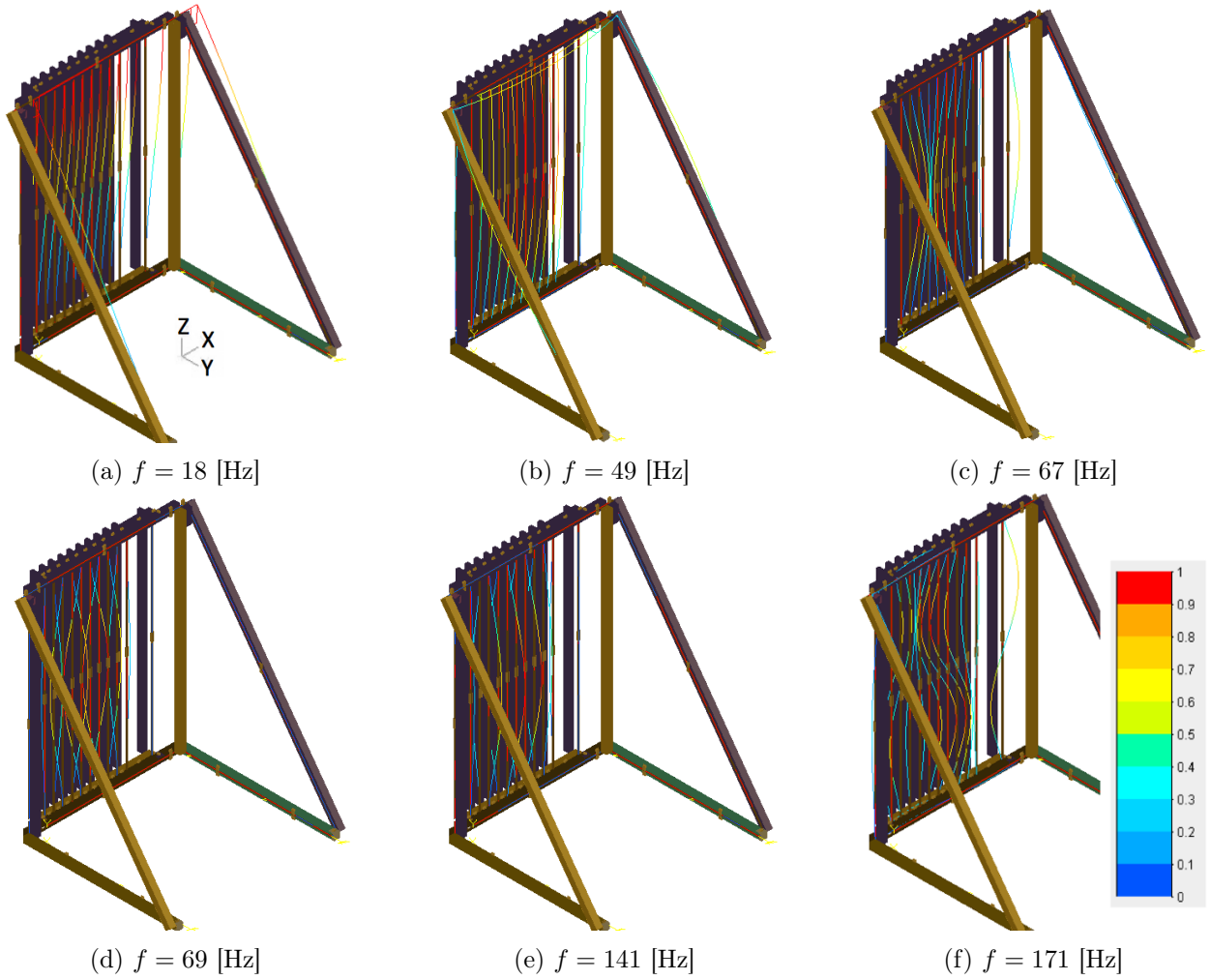

(a) $f = 18$ [Hz] (b) $f = 49$ [Hz] (c) $f = 67$ [Hz]

(d) $f = 69$ [Hz] (e) $f = 141$ [Hz] (f) $f = 171$ [Hz]

Figure 4.36 – Eigenmodes and frequencies of the WT model, with `SamcefField`

Wind-off study The WT model can be studied in terms of modal properties, using accelerometers in wind-off conditions ($U_\infty = 0$, numbering in Figure 4.35). Figure 4.37 shows the typical free response (decay) after an impulse in x directions on each cylinder (but only 1,5,10 are shown). The dominant eigenfrequency is clearly identifiable and it corresponds to 61 [Hz] (the most energetic mode in Figure 4.38, the same for each cylinder). Another lower frequency mode can be seen also, with beat phenomenon (at $f = 15$ [Hz] in Figure 4.38). It corresponds to a global mode of the whole structure (in Figure 4.36a). Cylinder 5 seems more damped than 1 and 10 (decreases more rapidly in Figure 4.37). Figure 4.39 compares damping ratio of cylinders, using four methods:

- Half Power 1: using the Q-factor method, the damping ratio is deduced from $\zeta = \frac{1}{2Q}$ with $Q = \frac{f_n}{f_a - f_b}$ (with f_a and f_b frequencies when $FFT = \sqrt{2} FFT_{max}$, *i.e.* at the eigenfrequency f_n). Several decays (impulses) were performed on each cylinder, to validate the test. This generates several FFT and ζ. Half Power 1 shows the mean and standard deviation (error bar) from these FFT, for each cylinder.

- Half Power 2 uses the same formula but performed on the mean FFT (of all FFT, from all tests). This mean FFT is computed by making a mean of amplitude and phase and then reconstructing the FFT as $FFT = |FFT| \cdot e^{i\phi}$. There is only one (mean) value for ζ.
- Exponential fit: it computes the envelope of the free decay (Figure 4.37) by fitting a time decreasing exponential of the form ae^{-bt}, where $b = \zeta\omega_n \Rightarrow \zeta = b/(2\pi f_n$
- Log-decrement: using the time response (4.37), it is possible to deduce the damping from the formula between two peaks: $\zeta = \frac{1}{2\pi}\log(x_n/x_{n+1})$. This is done for every adjacent peak of the decays, leading to several values of ζ (for each cylinder). Its mean and standard deviation are reported in Figure 4.39.

Figure 4.39 shows that Half Power 1 and 2 give very close results (same method but small differences depending on the way to average it). Exponential fit and log decrement give close but not perfect results. The behavior is nevertheless conserved and damping ratio is always a touchy thing. Most cylinders are low damped but 4,5,6 seem more damped. The screw strength is as constant as possible thanks to a setting torque tool but some differences can remain. A grid effect can also be pointed out: central cylinders are more damped than those on extremities. It is important for the following results: differences in damping (structural parameter) can have influence on the response in VIV curve (acceleration amplitude A/D vs speed U_r). This amplitude is inversly proportional to the damping, by multiplying the A/D by ζ, only fluid effects can be studied.

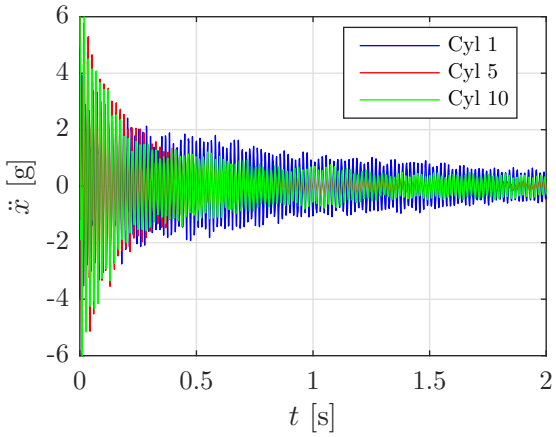

Figure 4.37 – Free response (decay) for cylinders 1,5 and 10 ($U_\infty = 0$) (in WT)

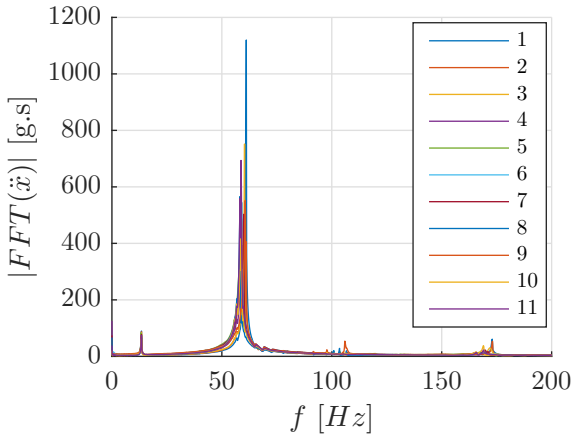

Figure 4.38 – Amplitude of FFT of cylinders acceleration $\ddot{x}$ ($U_\infty = 0$) (in WT)

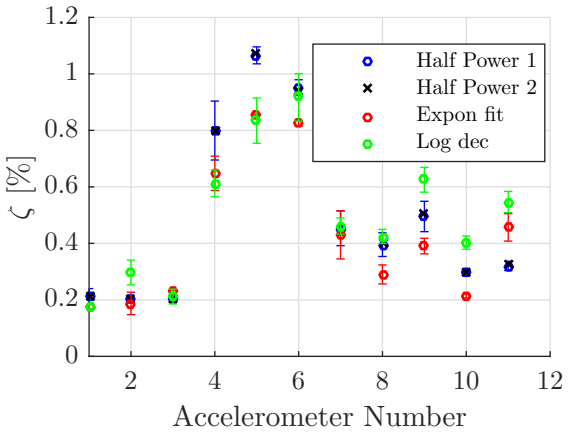

Figure 4.39 – Damping ratio ζ of cylinders: comparison of methods ($U_\infty = 0$) (in WT)

4.6 Comparison

After defining all methods and models, their results will be compared. Measurements taken on the WT grid model will be discussed by making parallel with those from the real grid (section 4.4.2). Firstly, fluid-elastic interaction will be studied (acceleration measures as a function of airspeed). The spacing parameter T/D will be studied, to make a link with single cylinder in the flow (the incidence to). A pressure analysis will then be performed, using the dynamic calibration, to compare experimental and CFD results of the flow around the WT grid model. For experimental measurements, frequencies will be compared (in term of Strouhal number St): f_s (structural, with accelerometers) and f_{vs} (vortex shedding, with Cobra Probe) to f_s^0 (structural at rest). When results are shown, the numbering of cylinders of Figures 4.35 and 4.34 is used.

4.6.1 VIV in WT model: grid effect

Using the WT model, a deep study of the grid can be done. Three parameters will be studied: U_∞, α and *esp*. First of all, VIV curves can be drawn by measuring cylinder acceleration as a function of airspeed (the best way to compare oscillating signals is to use the RMS, for n discrete values $x_{rms} = \sqrt{\frac{1}{n}(x_1^2 + ... + x_n^2)}$). Figure 4.40 shows cylinders response as a function of the airspeed. Exactly as the real grid, the grid model vibrates the most around $U_\infty = 5$ [m/s], with $\ddot{x}_{rms}$ of several [g] (left graph). Each cylinder does not have the same damping ratio thus multiplying $\ddot{x}_{rms}$ by ζ allows to study fluid effects only. Moreover, it is more convenient to work with adimensional (reduced) airspeed $U_r = U_\infty/(f_n D)$ (right graph). If displacement x is computed, it is convenient to adimensionalize it by D, (but here, acceleration are used, assuming a mono frequencial motion, $x = \ddot{x}/(2\pi f_n)^2$). Cylinders at the center of the grid (4 to 6) vibrate the most. They are independent to end effects (cylinders 1,2 and 9,10 at extremities vibrate less, they are influenced by a non-symmetric flow even at $\alpha = 0$ (see CFD results)). $U_r = 4 - 5$ at the maximum amplitude, conditions in the WT reproduce well the real situation. Indeed, Figure 4.41 is the adimensional version of Figure 4.29 ($\zeta\ddot{x}_{rms}$ vs U_r, because of the multiplication by ζ, the resulting amplitude of cylinders 1,2,3 is the same [6]). The critical reduced speed U_r is around 4 for both WT and real grids. Oscillation amplitude is however a bit lower in the real grid. Indeed, the wind is not as constant as the one in the WT, the incidence, speed and turbulence level are not perfectly uniform (variations of U_∞ and α_∞ in Figures 4.28). Therefore, all the wind energy is not used to excite the structure. The range of U_r that excites the structure (lock-in) is larger for the real grid. Indeed, even if the anemometer measures a higher windspeed (just next to the grid), the local speed on cylinders can be a bit different (and close to 5), leading to excitation. From *in situ* measurement, the windspeed is very often close to 5 during event.

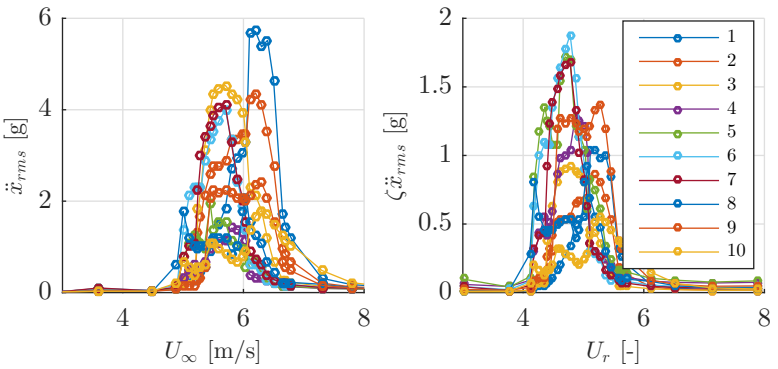

Figure 4.40 – WT grid model: VIV curve for $\alpha = 0$ and $esp = 0.04$ [m] ($T/D = 2$ [-]), legend with cylinders number, dimensional (left) and adimensional (right) quantities

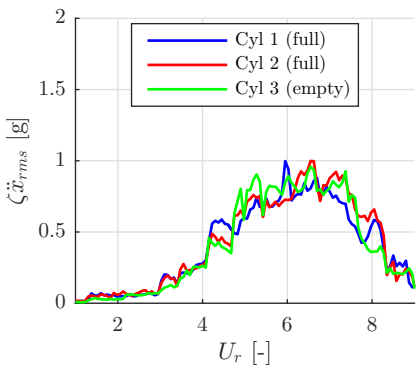

Figure 4.41 – Real grid: VIV curve, $\ddot{x}_{rms}$ envelope as a function of U_∞ for event at $t = 77$ [h] (adimensional plot of Figure 4.29)

[6] Cylinder 3 vibrates 2 times more than 1 and 2 but the associated ζ is 2 times lower

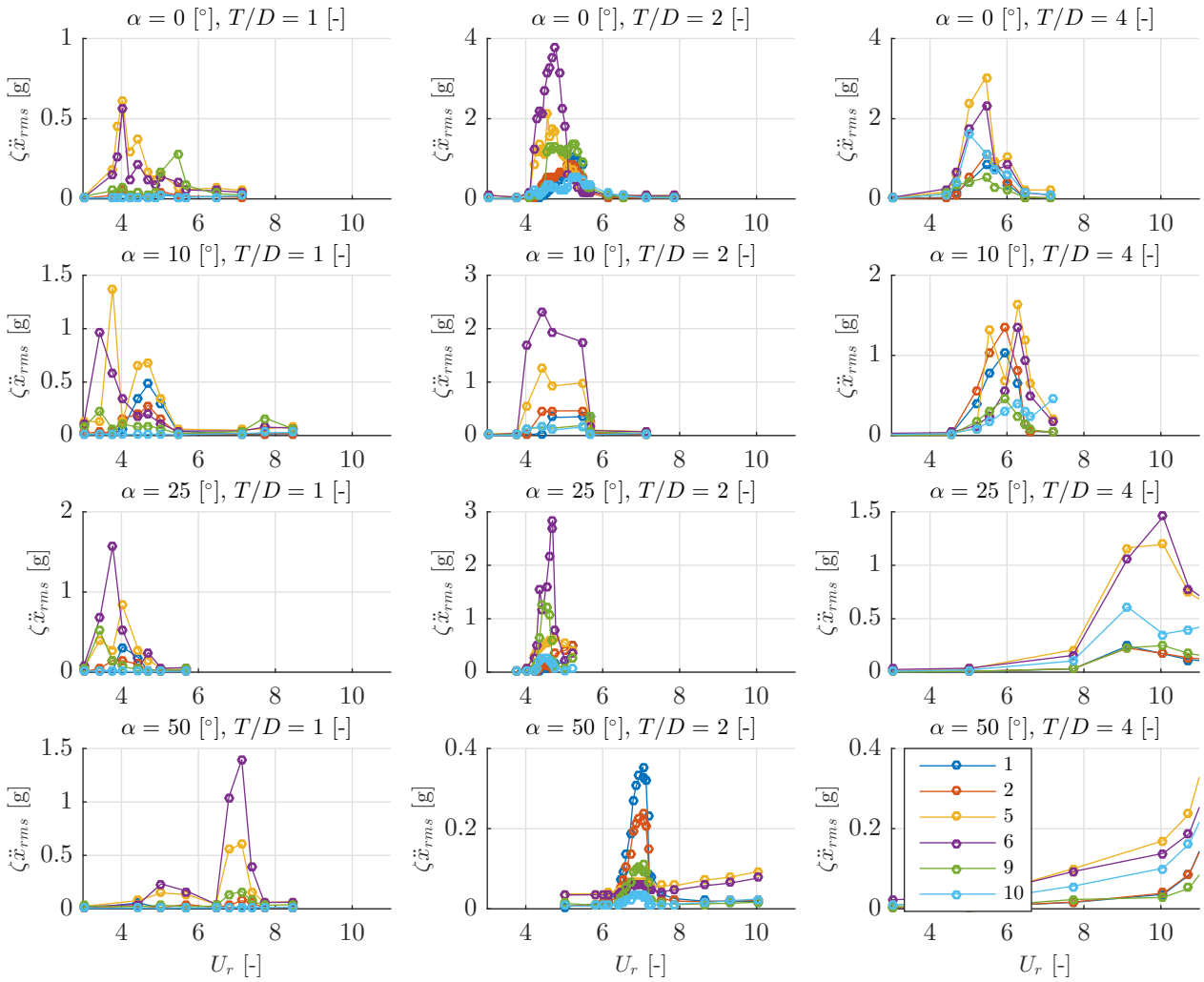

Figure 4.42 – VIV curve: α and T/D effects on WT model

Figure 4.42 shows the effect of α and T/D on cylinder response. The higher T/D, the higher U_r^{crit} and the lower St[7]. Indeed, when T/D is lower, the flow is more accelerated between cylinders (by the conservation of flow). The flow seen by the cylinder is thus more rapid than the free stream and it will reach the critical airspeed necessary to reach VIV (fixed by the St) for a lower free stream than a single cylinder alone in the flow. U_r^{crit} is lower and St appears higher for interfering cylinders than for a single one ($St = 0.22$ for $T/D = 2$ at $\alpha = 0$ whereas $St = 0.06$ for a single cylinder). This is enhanced by the biased gap flow suggested by Zdravkovich [46]. Moreover, the higher α, the higher U_r as well, in a stronger way compared to T/D. When cylinders are at incidence, the first ones come a bit in front of the others. The wake of upstream cylinders is influenced by downstream cylinders (true for a subsonic flow but nor for a supersonic one where the information cannot travel upstream). Vortices ejected by upstream cylinders encounter downstream cylinders, are deviated and less often ejected (the BL is thinner). f_{vs} and St are lower and U_r is higher. This is not the only influence, flow separation depends also strongly on α. For $\alpha = 10$, (in Figure 4.12 St increases for $\alpha = 10$), separation produces more often vortices, on each cylinder sides and f_{vs} and St increases (U_r decreases). This decrease of U_r at $\alpha = 10$ compensates the increase discussed above and U_r remains quite constant. Cylinders 1-2 and 9-10 show similar response at $\alpha = 0$. When α increases, cylinders 9-10 are influenced by all cylinders upstream (orientation in Figure 4.35 and vibrate less. For $\alpha = 50$, cylinders 1-2 vibrate more because they are directly exposed to the flow, other are in the wake of these first cylinders. The case $\alpha = 50$ and $T/D = 4$ is the most extreme, combined effects of α and T/D increase U_r and decrease St.

[7] $U_r = 1/St$ when VIV occurs

From this study of WT model, the variation of St with α and T/D can be summarized in Figure 4.43 (because $U_r = 1/St$ when instability begins, St are deduced from VIV curves (Figure 4.42)). St decreases when T/D increases, as well when α increases (in a stronger way). These values give the critical reduced velocity of VIV using $U_r = 1/St$, which have to be avoided (oscillations and noise are unwanted). The Strouhal for the real grid is at 0.2 (for $T/D = 2$ and $\alpha = 0 - 50$ [°]).

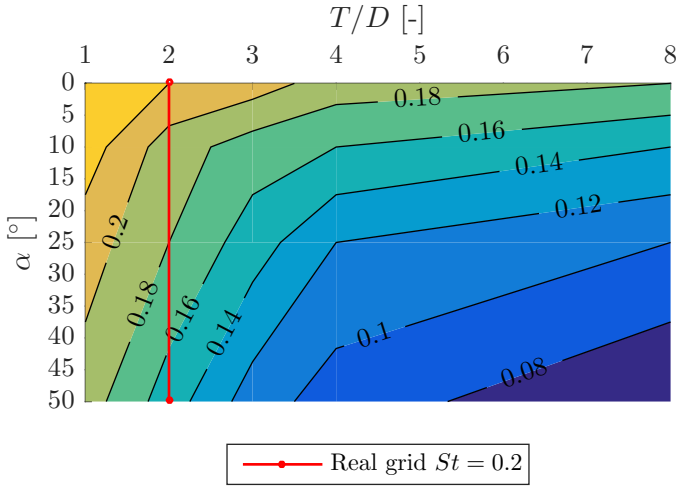

Figure 4.43 – WT grid model: Contour plot of Strouhal number St depending on α and T/D, comparison with the real grid

4.6.2 Limit case of single cylinder

In term of VIV curve, Figure 4.44 shows the same dependence with α and T/D. For $\alpha = 50$, U_r^{crit} is very high (around 15). When T/D increases, U_r^{crit} increases and St decreases ($St = 0.22$ for $\alpha = 0$ and $T/D = 2$ and St decreases to 0.18 for $T/D = 8$).

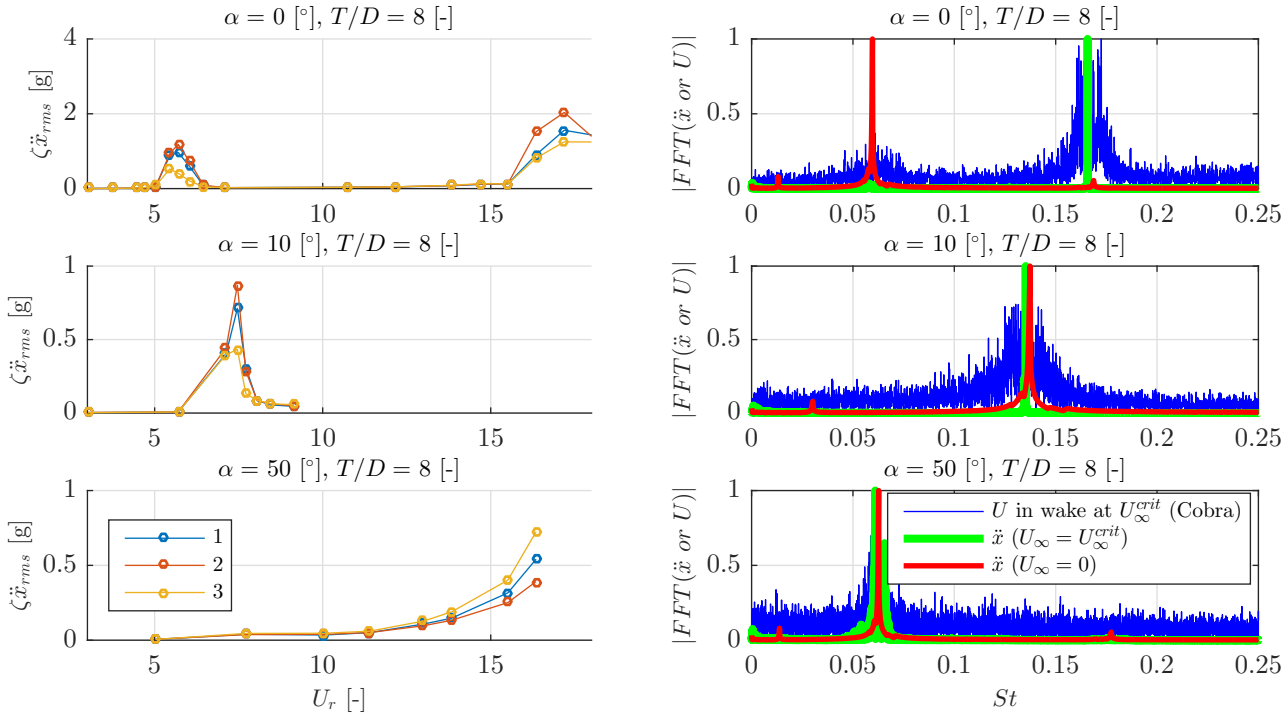

Figure 4.44 – WT grid: VIV curve ($T/D = 8$, 3 cylinders), FFT for cylinder 2 in term of St

Figure 4.44 shows FFT in term of $St = fD/U_\infty$ when VIV occurs, *i.e.* when $U_\infty = U_\infty^{crit}$. For this case, there is a matching of natural frequencies (in term of St) of FFT of:

- U, the velocity in the wake (measured with Cobra Probe), at $U_\infty = U_\infty^{crit}$, at f_{vs}
- $\ddot{x}$, the cylinder 2 acceleration, at $U_\infty = U_\infty^{crit}$, at f_s
- $\ddot{x}$, the cylinder 2 acceleration, at $U_\infty = 0$ (free decay), at f_s^0

By comparing with 4.12, $St(\alpha = 10) = 0.12$ and $St(\alpha = 50) = 0.06$ also. The case $\alpha = 0$ is very interesting. Indeed, the VIV curve shows two peaks, one at $U_r = 6$ ($St = 0.16$) and the other at $U_r = 16$ ($St = 0.06$). On first approach, it could remember the Figure 4.13 with the discontinuity in St occurring at B/D between 2.5 and 3 (for $\alpha = 0$)[8]. Nevertheless, **it does not mean that St is discontinuous here**, it comes from the fact that the structure has 2 resonance modes (one at 60 and another at around 170 [Hz]). In Figure 4.45[9], there is one frequency matching at $U_r = 5.4$, corresponding to the first mode $f_s^0 = 60$ and $St = 0.18$. There is another matching at $U_r = 16.3$ but associated to the second mode ($f = 180$ [Hz]) and the St is conserved (0.18). In fact, U_r in Figures 4.44 and 4.45 ($\alpha = 0$) should use the corresponding f_s^0: the first peak in the VIV curve is well at $U_r = U_\infty/(f_s^0 D) = 6.5/(60 \cdot 0.02) = 5$ but the second should be at $U_r = U_\infty/(f_s^0 D) = 20/(170 \cdot 0.02) = 5.5$, the same U_r^{crit}, hence the same St. **In conclusion,** at $\alpha = 0$ and $T/D = 8$, the Strouhal is $St = 0.18$ but the instability occurs for 2 different U_r because 2 different modes are excited, VIV curve has 2 peaks. The St is on the upper part of the discontinuity plot of St vs B/D (at $\alpha = 0$) in Figure 4.12. The plot of $FFT(\ddot{x})$ at $\alpha = 0$ and $T/D = 8$ in Figure 4.44 states for the second instability (second peak in the VIV curve), second matching in Figure 4.45).

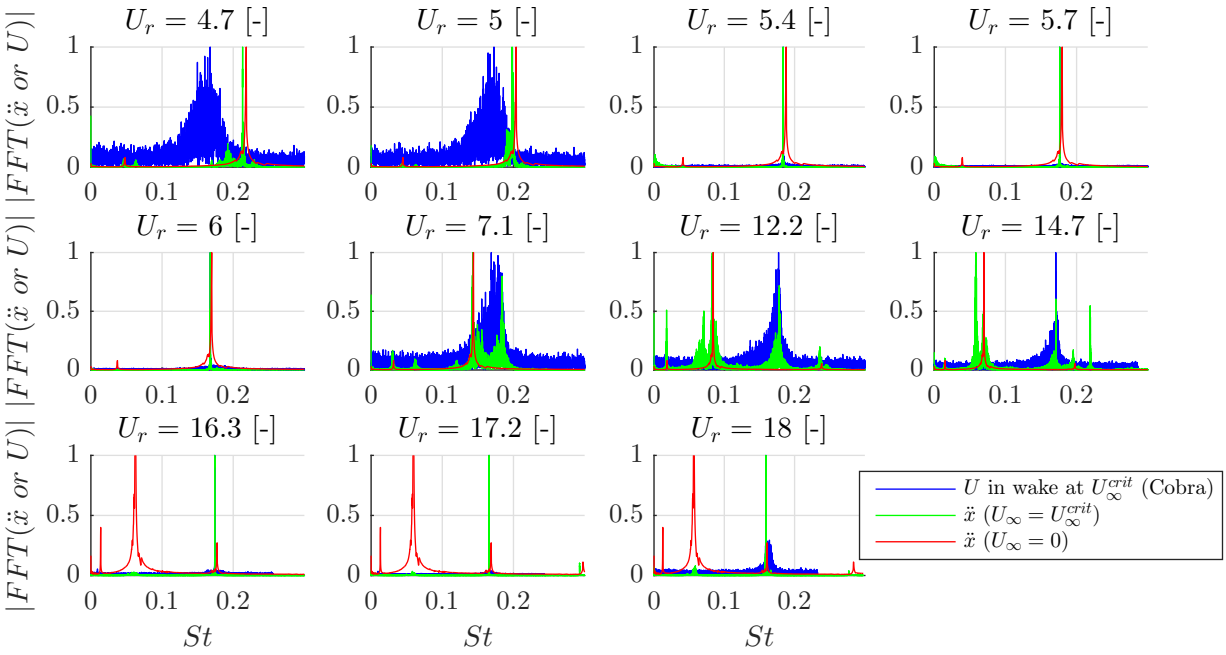

Figure 4.45 – WT grid: frequency matching in term of St for $\alpha = 0$ and $T/D = 8$

Figure 4.46 shows the flow around a single cylinder for varying B/D (CFD results). For B/D, the flow is separated everywhere after the upstream sharp edges and vortices ejection is well identifiable (at low $St = 0.11$ in Figure 4.48). For $B/D = 2.5$ and 3, the after body is so long that the flow reattaches at the end, vortices ejection and St increases (0.115 and 0.125 in Figure 4.48). Figure 4.47 shows lift

[8]For B/D slightly lower than 2.5, f_{vs} is low (vortices ejection slowed down by after body influence) and it becomes suddenly high for slightly higher B/D, when the flow reattaches close to sharp edges at the end of the body, as if the afterbody was very small (similar St to very low B/D).

[9]The two peaks in Figure 4.44 are linked with a double *structural* mode. Figure 4.45 shows $FFT(\ddot{x}$ or $U)$ in term of Strouhal $St = fD/U_\infty$. The velocity is the wake (blue) follows well the Strouhal relation (St is constant when the velocity increases). There is a frequency matching at $U_r = 5.4 - 6$. The structure is excited (VIV occurs) and the Strouhal is 0.18 ($1/U_r = 1/5.4 = 0.18$) for this case (all frequencies match at $St = 0.2$). The frequency at rest f_s^0 is constant (it decreases in term of St when U_∞ increases). The principal mode is at $f = 60$ [Hz] (thus corresponds to $St = fD/U_\infty = 0.06$ at $U_\infty = 20$ [m/s] ($U_r = 16.3$ [-] in Figure 4.45)). However, there is another structural mode at around $f_s^0 = 180$ [Hz] (small peak at $St = 0.18$ for $U_r = 16.3$). It term of St (at $U_\infty = 20$ [m/s] ($U_r = 16.3$ [-])) it corresponds to $fD/U_\infty = 0.18$, thus the St is constant.

and drag time variation and FFT in term of St. The lift oscillates at f_{vs} and the drag at $f_{vs}/2$. Figure 4.48 compares St vs B/D at $\alpha = 0$ from references (experiment and other CFD studies). This simple CFD shows St of the same behavior but not as precise as other references or experiment.

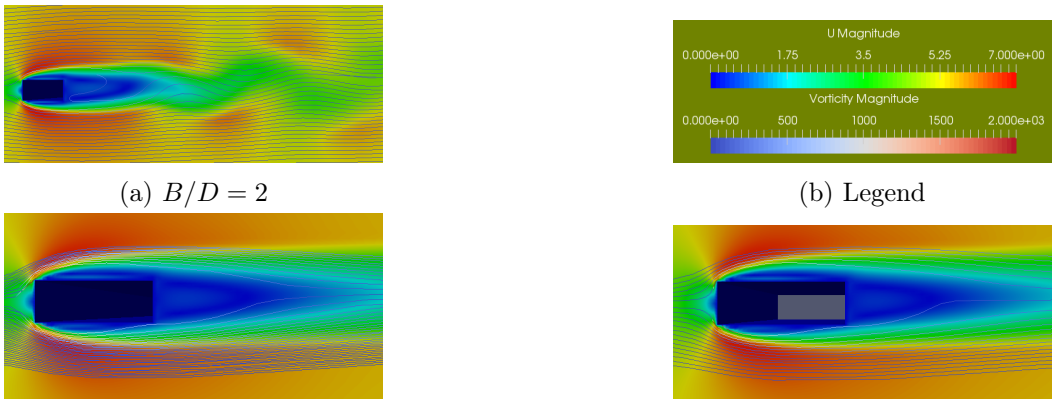

(a) $B/D = 2$

(b) Legend

(c) $B/D = 2.5$

(d) $B/D = 3$

Figure 4.46 – CFD: flow around cylinder at $\alpha = 0$ depending on B/D, at $t = 0.2$ [s]

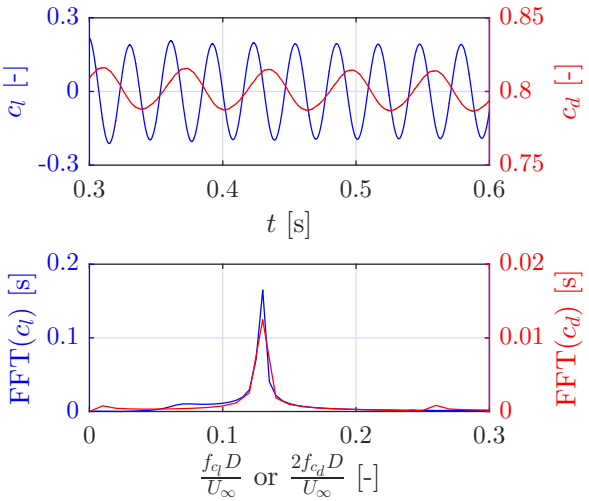

Figure 4.47 – Lift c_l and drag c_d for $B/D = 2.5$ at $\alpha = 0$ and FFT (in term of St), CFD

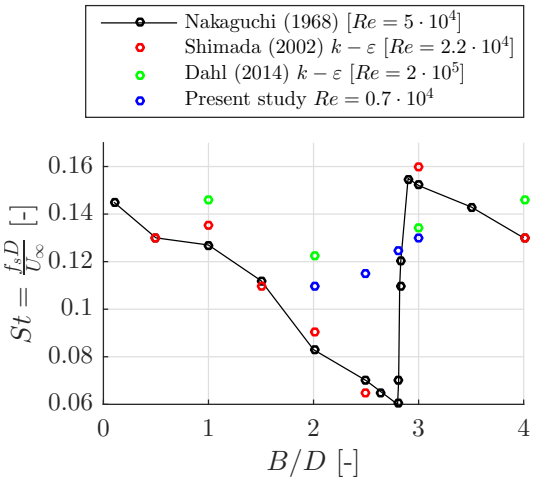

Figure 4.48 – St at $\alpha = 0$ obtained with CFD: comparison with references [36][26][61]

4.6.3 Pressure analysis

Another interesting quantity to study is the pressure. As explained, a rectangular cylinder is a bluff body, with flow separation at the upstream sharp edges. Along the after body, the flow is unsteady and a dynamic calibration (from Chapter 2) has to be made on pressure tap measurement (using tubes of $D = 1.37$ [mm] and $L = 1.4$ [m]). Figure 4.49 shows an example of pressure time signal (relative, $p - p_\infty$) for cylinders 1,5,10 at hole 2 for $\alpha = 0$ and $T/D = 2$ (numbering in Figure 4.34, the tap just after separation point (corners)). It shows that dynamic calibration changes quite a lot the oscillation amplitude. Indeed, the frequency of vortex shedding is around 60 [Hz] for each cylinder, which is close to the resonance peak of the Dyncal correction (using experimental data done in KTH) in Figure 4.50. The correction done using Tijdeman theory is very close, because a simple tube of a constant diameter is used, without tap restriction (this was not the case in Chapter 3). As observed in VIV curves (Figure 4.42), cylinder 5 oscillates more in term of pressure also. Because of the symmetry at $\alpha = 0$, hole 2 of cylinder 1 corresponds to hole 13 of cylinder 10 (same pressure amplitude in this case). However, hole 2 of cylinder 10 is at the grid extremity, without cylinder interference. In the rest of this study, all pressure signals are dynamically corrected.

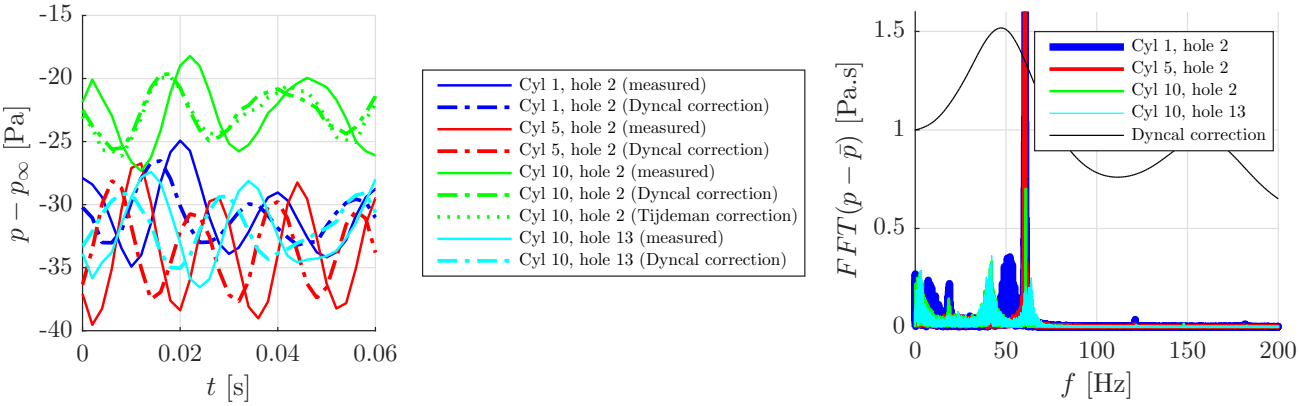

Figure 4.49 – WT grid: Pressure at holes 2, 13 of cylinders 1,5,10, with dynamic correction, for $\alpha = 0$, $T/D = 2$ and $U_\infty = 5$ [m/s]

Figure 4.50 – WT grid: FFT of Figure 4.49

Figure 4.51 is very interesting to compare experimental and CFD results, for cylinders 1,5,10 for $T/D = 2$. The first column shows mean pressure distribution ($\bar{c_p}$ vs adimensional curvilign coordinate s/D, defined in Figure 4.10). The second one shows the lift time signal c_l and the last one shows the FFT in term of $St = fD/U_\infty$.

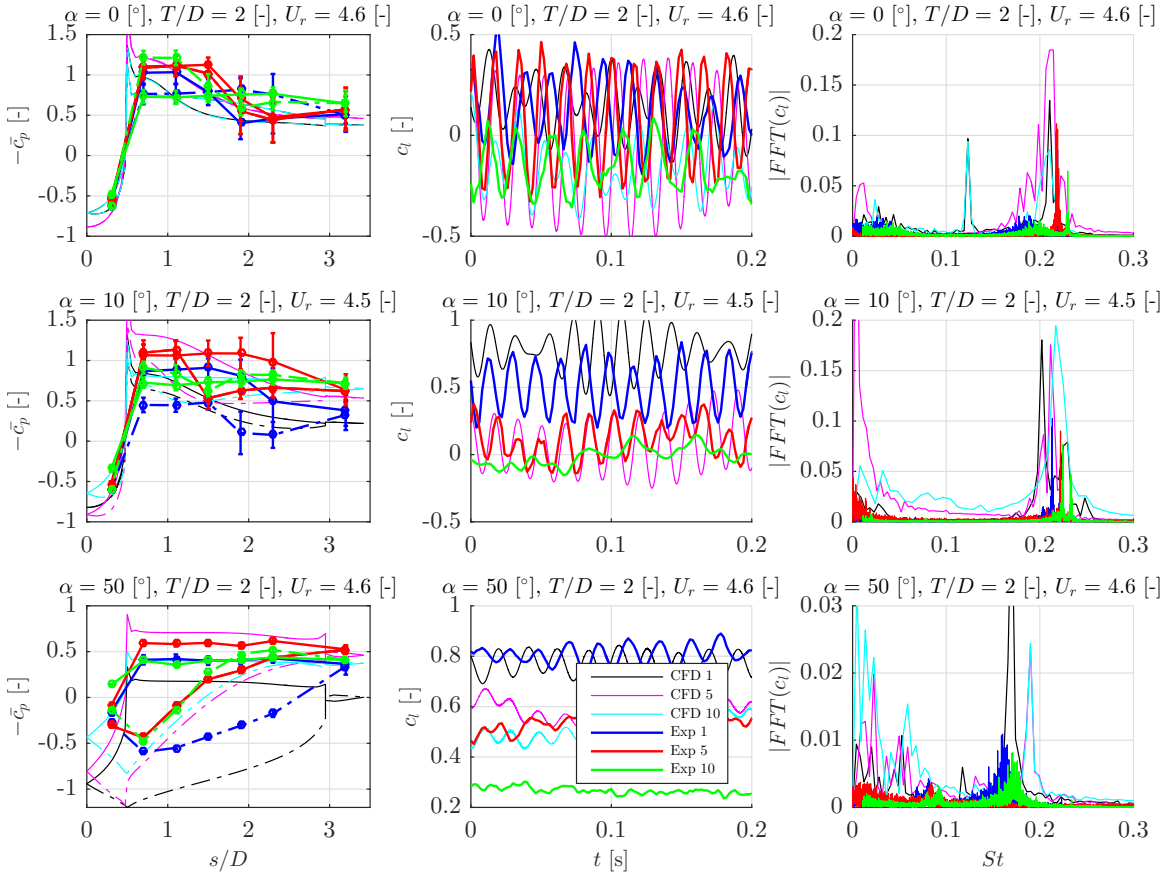

Figure 4.51 – Mean pressure distribution for $\alpha = 0, 10, 50$ at $T/D = 2$ for cylinders 1,5,10 (pressure coefficient $-\bar{c_p}$ vs adimensional curvilign coordinate s/D), instantaneous lift c_l and $|FFT(c_l)|$ in term of $St = fD/U_\infty$: comparison experiment (WT)-CFD, cylinder lower side in (-) and upper side in (-.)

At $\alpha = 0$, the flow is symmetric in the grid (cylinder 5 with superposed pressure distribution of upper and lower sides and zero mean lift). However, cylinders 1 and 10 are at grid extremities and the flow on the external side is not symmetric: $\bar{c_p}$ on upper and lower side is not symmetric,, the mean lift is slightly negative for cylinder 10[10] but oscillates at the same frequency for cylinders 1,5,10 ($St = 0.21$).

[10]Positive for cylinder 5, the accelerated flow between cylinders 1 and 2 sucks cylinder 1 upper side, thus positive lift

The flow is separated on both cylinder 5 sides (plateau in $\bar{c_p}$ for $s/D = 0.5 - 2$), vortex ejection and interference with other cylinders a makes a drop in $-\bar{c_p}$ for $s/D = 2 - 3$ (also separated flows with plateau). The flow is separated along the whole upper side of cylinder 10 and the lower side of cylinder 1 (extremity side). When cylinders are at incidence, the mean lift is positive (but less for cylinder 5, constrained by interfering cylinders) and St decreases (U_r increased in VIV curves). For $\alpha = 50$, all upper sides are separated (plateau) and the lower side of cylinder 1 is under positive pressure (negative $-\bar{c_p}$). CFD and experiment show that the stagnation point (for $-c_p = -1$) moves from $s/D = 0$ to $s/D = 0.8$ (on the rectangle upperside). Cylinder 10 is in the wake of all other upstream cylinders, the flow on the lower side is perturbed and the resulting lift is lower. This decreases in lift is more important for experiment than for CFD. There is also a shift in $\bar{c_p}$ for cylinder 1 between CFD and experiment but other results are quite close, the model is validated. St from lift (in term of f_{vs}) decreases from 0.21 to 0.16 when α increases from 0 to 50, being consistent with observations from VIV curves (in term of acceleration, f_s).

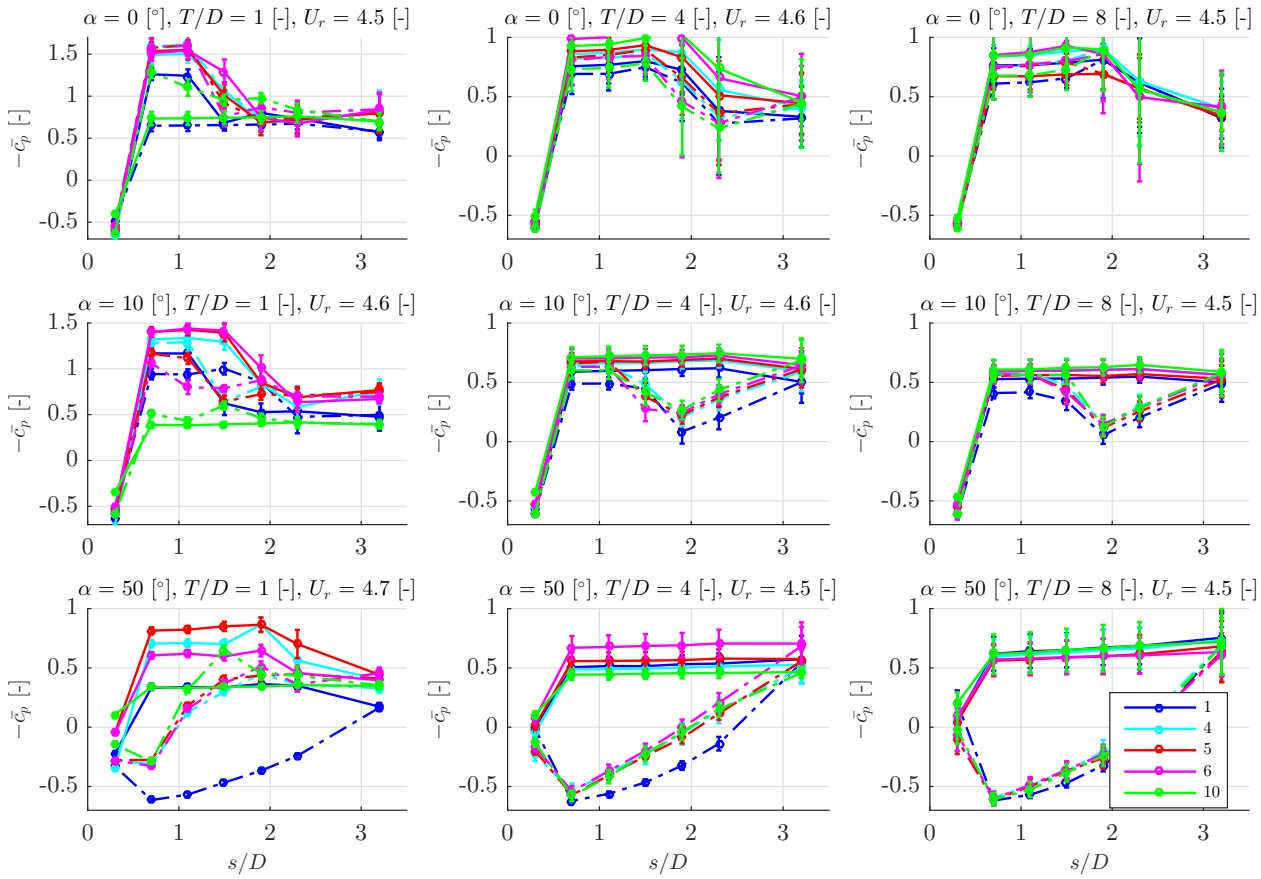

Figure 4.52 – WT grid: Mean pressure distribution for $\alpha = 0, 10, 50$ at $T/D = 1, 4, 8$ for cylinders 1,4,5,6,10 (pressure coefficient $-\bar{c_p}$ vs adimensional curvilign coordinate s/D), cylinder lower side in (-) and upper side in (-.)

The pressure distribution can be studied in more details using other T/D (1, 4 and 8), for cylinders 4 and 6 in addition to 1,5,10: the pressure around the three central cylinders and the two extremities has been studied (Figure 4.52)). At $\alpha = 0$, the higher T/D the more symmetric the pressure distribution (upper-lower sides) and the more superposed the pressure for all cylinders. In other words, when T/D increases, the grid effect decreases, cylinders are so spaced that they behave as if they were completely alone. The pressure distribution for each cylinder tends to the one for a single cylinder. For $T/D = 1$ at $\alpha = 0$, the upper side of 10 is separated (plateau) as well as the lower side of 5. Pressure distribution of 4,5,6 is very similar for each situation $(\alpha, T/D)$. This validates the fact that the flow in the central part of the grid is independent of the cylinder and this is even truer when the grid contains more cylinders (end effects are completely neglected, and the flow in the whole grid is the one observed for cylinders 4,5,6). The lower T/D, the higher the influence of interfering cylinders and

the stronger the step shape of pressure on cylinders 4,5,6. Indeed, at $\alpha = 0$ and $T/D = 2$, $-\bar{c_p}$ makes a step from 1.7 ($s/D = 0.5 - 1.5$) to 0.7 ($s/D = 1.5 - 3$). This corresponds to the first separation of flow on upper (or lower) side. A second separation, at a different pressure, happens when the separation wake of one cylinder (on its lower side) encounters the separation wake of the cylinder just below (on its upper side). The two separation wakes (from the lower side of the top cylinder and the upper side of the bottom cylinder) start thus independently just after the first corner (at $s/D = 0.5$), then they influence each other and merge at around $s/D = 1.5$.

When T/D increases, this step shape pressure distribution is decreased. For $T/D = 2$ (Figure 4.51), $-\bar{c_p}$ goes from 1 to 0.5 at $s/D = 2$. For $T/D = 8$ (limit case of a single cylinder), $\bar{c_p}$ is almost constant along the whole upper and lower side ($s/D = 0 - 5 - 2.5$). This corresponds to a completely separated flow along the cylinder (behind corners at $s/D = 0.5$), with no interference with other cylinders (single cylinder). When α increases, the pressure distribution of cylinders 4,5,6 is no more symmetric. Pressure on the lower side (cylinders 4,5,6) separates just after the first corner ($s/D = 0.5$) but reattaches after (around $s/D = 1 - 1.5$), for $\alpha = 10$ and $T/D = 1, 4, 8$. There is almost no wake on this lower side of the top cylinder (5) and it interferes less on the pressure on the upper side of the bottom cylinder (4) (for $T/D = 1$). Therefore, the first plateau of the step shape pressure is longer for $\alpha = 10$ and $T/D = 1$ ($s/D = 0.5 - 1.5$ compared to 0.5-1 for $\alpha = 0$). This is even truer for $\alpha = 50$, the pressure is attached on the lower side and perturbs less the upper side of the bottom cylinder (longer plateau, $s/D = 0.5 - 2$, the upper side is separated almost as if it was alone). For $\alpha = 10 - 50$ and $T/D = 4 - 8$, the upper side is completely separated. For $\alpha = 10$, the lower side separates just after corner ($s/D = 0.5 - 1$) and reattaches after ($s/D = 1 - 2.5$). For $\alpha = 50$ the flow on the lower side is attached (the real distance along which separation occurs is not captured by the coarse pressure tap distribution). Other references studied the mean pressure distribution $\bar{c_p}$ (Figure 4.53) for a single cylinder at $\alpha = 0$ and $B/D = 5$ (instead of 2.5 here). Their obtained results are consistent with those of this study: stagnation point $c_p = 1$ at $s/D = 0$, pressure drop at the corner ($s/D = 0.5$) and separated flow after the corner ($s/D = 0.5 - 3$). There is then a reattachment near the end of the after body ($s/D = 4$) because of the high aspect ratio in these references (5 instead of 2.5), leading to an increase of St as discussed before (Figure 4.48).

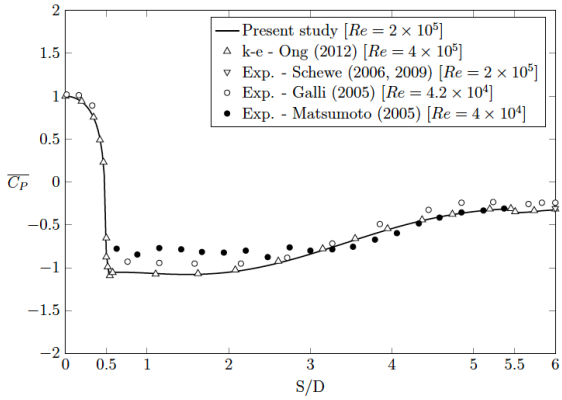

Figure 4.53 – Mean pressure distribution for an alone cylinder at $\alpha = 0$ with aspect ratio $B/D = 5$(pressure coefficient $\bar{c_p}$ vs adimensional curvilign coordinate s/D): results from references [26]

By measuring at the same time the pressure around the adjacent cylinders 4,5,6, the vortex shedding behavior can be studied in term of phase and synchronization between cylinders. Figure 4.54 shows time variation of pressure $-c_p$ at corners of cylinders 4 and 5 at $\alpha = 0$ and $T/D = 1, 3, 4$ (corners colors and contours legend in Figure 4.54). When cylinders are close to each other ($T/D = 1$), it corresponds to the single vortex street region (Figure 4.20). The upper side of cylinder 5 (in blue) and the lower side of cylinder 6 (in magenta) are in phase. The lower side of cylinder 5 (in red) and the upper side of cylinder 4 (in green) are together in phase but out of phase with blue and magenta. Cylinders are so close to each other and interference is so high, that symmetric sides of two adjacent cylinders are

synchronized in term of vortex shedding (red-green or blue-magenta). The flow is separated everywhere but the pressure for upstream corner (in Figure 4.54 (-)) is different from the one at downstream corner (in Figure 4.54 (-.)). This corresponds to the step shape pressure of Figure 4.52 (different separated flow at $s/D = 0.5$ (upstream corner) and $s/D = 3$ (downstream corner)). When cylinders are more spaced ($T/D = 3$), it corresponds to a biased gap flow, or coupled vortex street (Figure 4.20). Magenta and red are in phase, in opposition with blue and green. Vortex shedding is no more synchronized in alternating channels[11]. However, upper sides of all cylinders are in phase, lower sides are also in phase but upper-lower ejection alternates, because cylinders are more spaced. Cylinders influence still each other by the fact that the pressure at upstream and downstream corner is still different (but less than it was for $T/D = 1$). The same kind of synchronization happens for $T/D = 4$ but adjacent cylinders do not influence each other (same pressure at upstream and downstream corners, plateau in pressure distribution). Vortices are alternatively ejected between upper and lower cylinder sides. The same study but at incidence ($\alpha = 25$) is done in Appendix C.3.1.

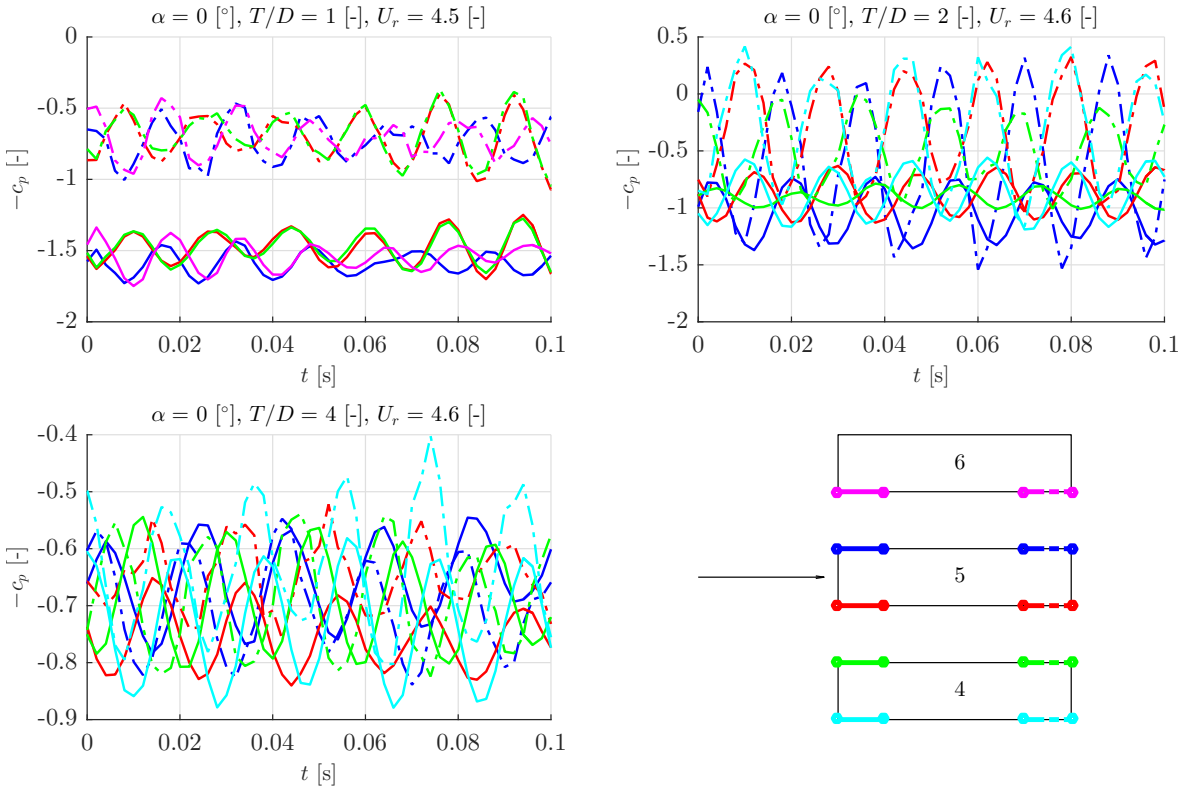

Figure 4.54 – WT grid: pressure $-c_p(t)$ at corners of cylinders 4,5,6 at $\alpha = 0$ and $T/D = 1, 2, 4$

Figure 4.55 shows the vorticity magnitude (measure of the vortex shedding) for the 10 cylinders grid at $\alpha = 0, 25, 50$ and $T/D = 1, 2, 3, 4$. At $\alpha = 0$, the synchronization is identifiable: for $T/D = 1$, cylinder interferences are huge, channels between cylinders are in phase. When $T/D = 2$, a complex biased gap flow occurs (as suggested by [46]): cylinders have an alternating (bistable) vortex ejection behavior (one out of two cylinders). When $T/D = 3, 4$, cylinders become independent and the flow behaves as if the cylinders were alone. At $\alpha = 25$, there is no more symmetry in the flow, vortex ejection from each lower cylinder sides becomes synchronized (in alternation with the upper side). Cylinder 10 is completely in the wake of 9 for $T/D = 1, 2$ and a huge separated zone behind it occurs. Indeed, this angle corresponds to an intermediate angle that the flow can make when it separates from upstream corner of the bottom cylinder to downstream corner of the top cylinder ($\arctan(2/5) = 21$ for $T/D = 1$ and $\arctan(4/5) = 38$ for $T/D = 2$). For $T/D = 3, 4$, interferences begin to occur at $\alpha = 25$. At $\alpha = 50$, cylinder 10 is completely in the wake of 9 for $T/D = 3$ also ($\arctan(6/5) = 50$). Cylinder interferences are higher and cylinders are in the wake of each other even for $T/D = 4$.

[11] For $T/D = 1$, for which channel between cylinder (cylinder so close that the space between them forms a channel) showed synchronized vortex ejection, one out of 2 cylinders

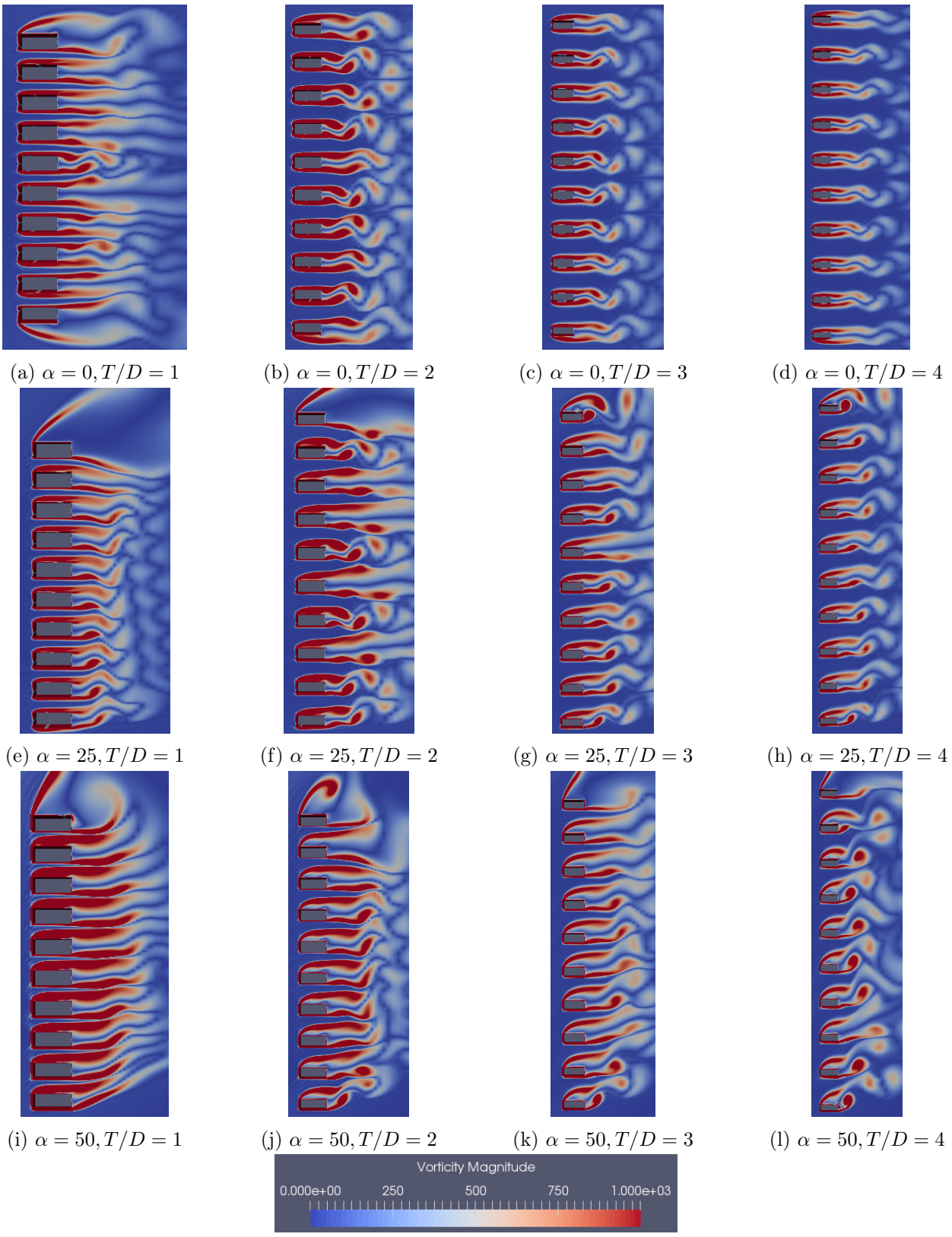

(a) $\alpha = 0, T/D = 1$ (b) $\alpha = 0, T/D = 2$ (c) $\alpha = 0, T/D = 3$ (d) $\alpha = 0, T/D = 4$

(e) $\alpha = 25, T/D = 1$ (f) $\alpha = 25, T/D = 2$ (g) $\alpha = 25, T/D = 3$ (h) $\alpha = 25, T/D = 4$

(i) $\alpha = 50, T/D = 1$ (j) $\alpha = 50, T/D = 2$ (k) $\alpha = 50, T/D = 3$ (l) $\alpha = 50, T/D = 4$

Figure 4.55 – Vorticity magnitude around the grid at $U_\infty = 5$ [m/s]: α and T/D effect (CFD results)

Figure C.9 in Appendix C.3.2 shows velocity magnitude for same paraùeters as Figure 4.55. Figure 4.56 shows streamlines and velocity magnitude around central cylinders of $T/D = 2$ depending on α. At $\alpha = 0$, the vortex shedding is symmetrically alternating between upper and lower sides. At $\alpha = 25, 50$, vortices are ejected from downstream lower side corner and upstream upper side corner, with the wake interfering with the top cylinder.

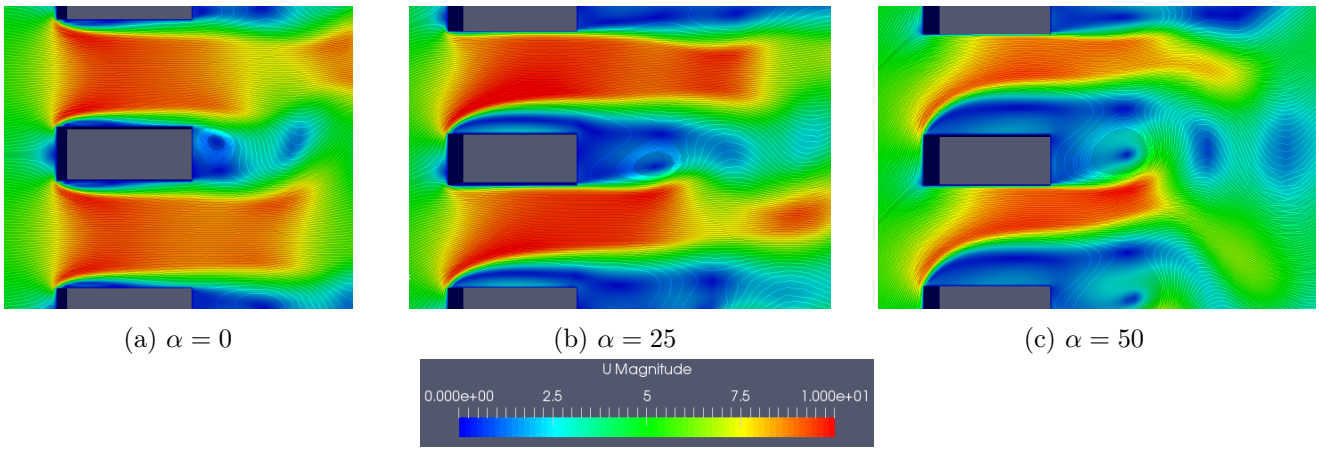

(a) $\alpha = 0$ (b) $\alpha = 25$ (c) $\alpha = 50$

Figure 4.56 – Velocity magnitude and streamlines around the grid for $T/D = 2$ at $U_\infty = 5$ [m/s] (CFD)

The pressure measurement and CFD results are added to results of section 4.6.1, to produce Figure 4.57. It summarizes all principal results: it shows the frequency matching in term of St between:

- f_{vs}: wake (Cobra Probe) and c_l (from c_p integration on pressure taps and from CFD), at U_∞^{crit})
- f_s: acceleration at U_∞^{crit}, using accelerometers
- f_s^0: acceleration at $U_\infty = 0$, using accelerometers

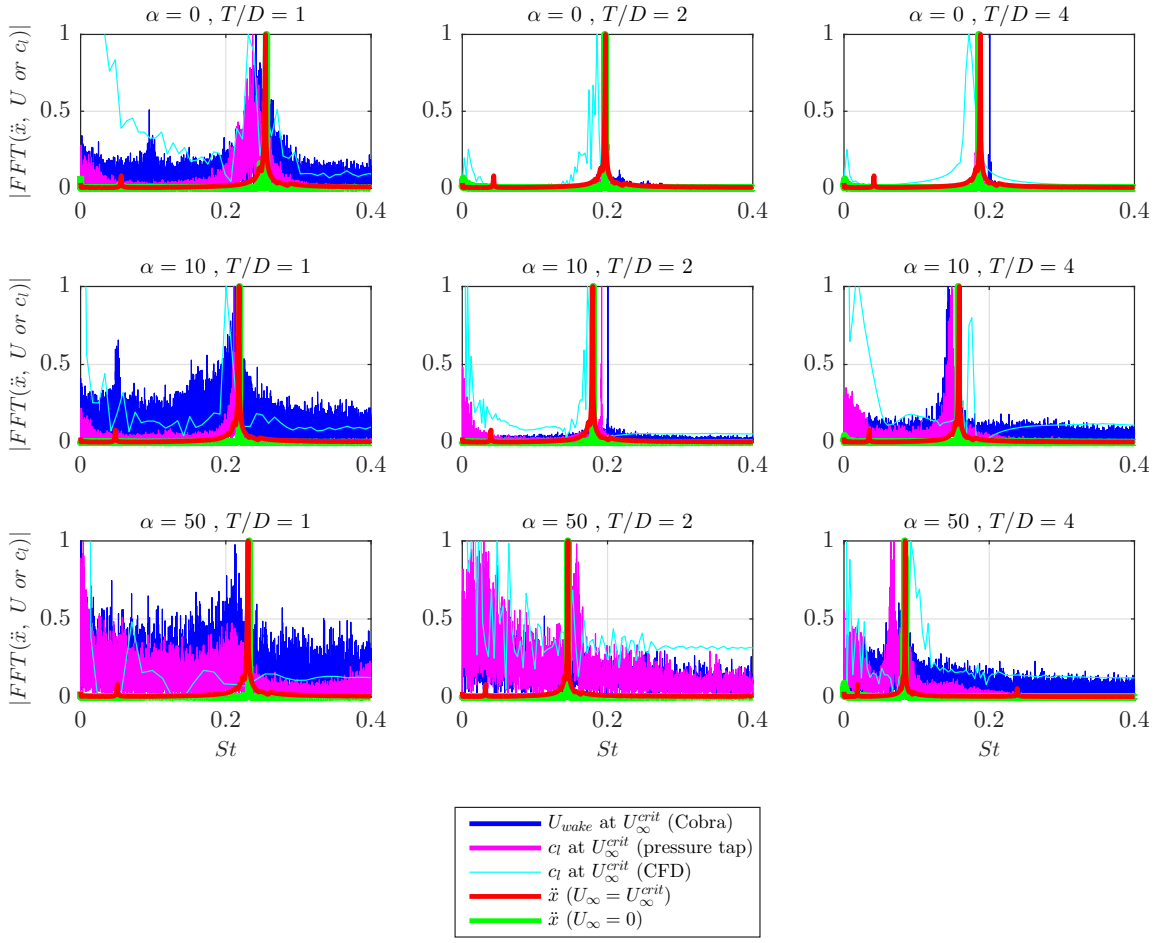

Figure 4.57 – FFT of recorded signals in term of Strouhal number St: α and T/D effect, comparison of f_{vs} (wake and pressure, at U_∞^{crit}), f_s (acceleration at U_∞^{crit}) and f_s^0 (acceleration at $U_\infty = 0$), for cylinder 5

Results are consistent, except CFD at $\alpha = 50, T/D = 1$. This case is anyway more complex, with higher noise in experimental results (the flow has to turn a lot into a narrow channel). CFD results

are obtained just at $U_\infty = U_\infty^{crit}$ (starting of VIV), the phenomenon of lockin (f_{vs} and f_s locked at f_s^0 over a range of U_r in Figure 4.15) is not captured by CFD (f_{vs} follows the Strouhal relation). For $T/D > 4$, cylinders behave as if they was alone ($St = 0.18$ as in Figure 4.48 upper line), consistent with [46] results (Figure 4.58, proximity/interference region for $T/D < 4$).

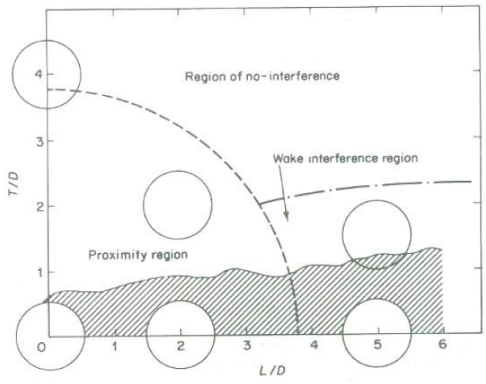

Figure 4.58 – Characteristic regions of two interfering cylinders [46]

4.7 Conclusion

From this study, several results and interpretations can be highlighted:

- Fluid-structure interaction is a very interesting topic. Because of the complexity and the coupling of flow and structural properties, it is not easy to predict. Indeed, when civil engineering structures are built, bluff bodies are often used: the purpose is not to optimize an aerodynamic shape, submitted to high airspeeds but it uses to respect structural capabilities, in an urban environment (low speed on the ground). Aerodynamic behavior of such structures is not always studied and it can lead to undesirable but interesting phenomena. Indeed, the grid on site composed of rectangular cylinders, already installed on the house, makes a huge noise under certain conditions. From accelerometer and wind measurements on site, a link between noise event and wind conditions were made. When the wind comes at angles between 0 and 50 [°] with a minium speed of 5 [m/s], cylinders vibrate suddenly a lot, producing the noise. For these conditions, the vortex shedding process (ejection of vortices from the point of separation (because of rectangular corners)) is synchronized with the eigenfrequency of the structure (resonance frequency without flow). Vortex ejection excites the structure at its resonance frequency, which in turn triggers the flow and the vortex shedding, and so on.

- Structural properties of the grid were studied. Thanks to beam theory and FEM, the first mode that excites all cylinders in the same way happens at around $f_s^0 = 60$ [Hz]. This first mode of bending is equivalent, considering a bipinned cylinder alone or cylinders in the whole grid. Because of the structure, some global modes happen also (bending of beams that support cylinders) but at very low frequencies, not excited by fluid conditions. From measurements on site, the amplitude of oscillation is maximum at $U_\infty = 5$ [m/s] and the damping is minimum. For these critical conditions, $f_{vs} = f_s^0 = f_s = 60$ [Hz] (vibration of cylinders at their resonance when $U_\infty = 5$). Using adimensional numbers allows to generalize conclusions for other dimensions (if these numbers are conserved). Using the reduced critical speed, $U_r = U_\infty/(f_s^0 D) = 4.7 = 1/St$ and Strouhal number $St = f_{vs}D/U_\infty$. The flow around a rectangular cylinder as been studied by other references but not in a more complex structure, with interactions and interferences between adjacent cylinders. Direction (α) and space between cylinders (T/D) has been studied to see their influence on the instability process and critical VIV speed U_r (the inverse of the Strouhal number St). A WT model has been build to study α and T/D. It consisted of a 1:1 scale of the real grid (same cylinder length and cross section) but composed of 10 cylinders. A previous FEM study showed that the structural characteristics were the same (resonance frequency around

$f_s^0 = 60$ [Hz]). This has been validated by experimental wind off measurements (accelerometer on each cylinder measuring the free decay to impulse excitation).

- End effects are present at grid extremity cylinders, leading to asymmetric flow even at $\alpha = 0$. Grid effect and representative cylinder response was observed for central cylinders (they vibrate more than extremity cylinders). Increasing T/D decreases cylinder interference: U_r increases (and St deceases). The limit case was observed for $T/D = 4 - 8$, with U_r and St very close to those obtained for a single cylinder (compared also with references). With the cylinder cross section aspect ratio used here ($B/D = 2.5$, single cylinder at $\alpha = 0$) a very interesting behavior happens: the St is constant at 0.18 but 2 peaks are present on the VIV curve (2 resonance frequencies). When α is increased (until 50), parts of cylinders come in front of others. Because the whole grid is turned by α, cylinders are upstream of others. Their wake interferes (wake of upstream cylinder constrained by the presence downstream cylinder), ejecting vortices at a lower frequency (lower St and higher U_r). A single cylinder at incidence has anyway a smaller St. Indeed, separation points are different: upstream corners (from upper and lower sides) for low incidence but upper upstream - lower downstream corners for higher incidence and vortices are ejected less often.

- The pressure study along cylinders allows to understand how the flow behaves, depending on α and T/D. For high T/D, the flows around each cylinder converge to the same distribution (as if they were alone), whatever the cylinder position in the grid. A symmetric pressure distribution at $\alpha = 0$ (separated flow from the upstream corner) is found. For higher α, all upper sides are separated, and the stagnation point moves on the lower side. When cylinder are close to each other ($T/D = 1$), a strong interaction happens: the flow around central cylinders is completely different to the one around extremity cylinders. The separated flow of each cylinder sides is interfering with the one of adjacent cylinder, the pressure distribution has a step shape (the lower T/D, the sharper the step). For small T/D, the flow is accelerated in channels (space between cylinders), the flow seen at these channels is higher than the upstream speed. The vortex shedding (linear to speed) is higher than the one expected for a single cylinder at the same free stream speed. Grid instability happens at a lower speed than the one for a single cylinder and is associated to a higher St ($U_r = 1/St$). Lowering T/D artificially increases St.

- The synchronization of flow and vortex ejection between adjacent cylinders was also studied thanks to the dynamic calibration. Indeed, by looking precisely at time variation of quantities, they have to be corrected in amplitude and phase. The dynamic calibration ensures that fluctuations around the mean quantity and mainly the phase are correct. Indeed, the type of vortex ejection (depending on T/D) and cylinder interaction is studied in term of synchronization of pressure fluctuations, strongly linked with phase. The comparison with CFD results allows to validate the results and to visualize easily the flow and vortex ejection according to α and T/D. At $\alpha = 0$, low T/D is characterized by a single vortex street: channels between cylinders are so narrow that the flow is synchronized there (upper side of bottom cylinder and lower side of top cylinder are synchronized), and alternates one channel out of 2. For $T/D = 2$, vortices alternate between upper and lower sides but in a more complex way (bistable). For $T/D = 3$, a coupled vortex street happens: all upper sides are in phase with each other (out of phase with lower sides). For $T/D = 4$, vortices alternate between upper and lower side, independently for adjacent cylinders (as if they were alone). Increasing α forces the flow on each lower sides to be attached but separated at the downstream corner. Separation on the upper sides happen always at the upstream corner. The vortex shedding is synchronized between lower side, out of phase with upper sides.

- Knowing grid characteristics (mainly St, fixed), it is possible to find solution to VIV instability. Indeed, critical reduced airspeed is fixed (by $U_r = 1/Dt$). Nevertheless, if U_∞ and f_s^0 (or D) are increased by the same amount, the ratio (U_r) remains constant. The flow is the same (same adimensional number St) but conditions are different: if the structural resonance frequency f_s^0 (or diameter D) in increased, the speed at which VIV instability occurs is higher. For this grid

placed on the ground, wind speed of for example 10-15 [m/s] does not happen often (compared to 5 [m/s]). Thus, by increasing 2 or 3 times the resonance frequency of cylinders, critical speed will be shifted to higher values, less likely to happen in Belgium at the ground level. Increasing f_s^0 can be done by inspecting the formula from beam theory: decreasing the cylinder length (by placing a connection beam at mid length for example), or by increasing the bending stiffness EI (by increasing E[12] or by increasing inertia I, using a larger cross section). Another way to increase f_s^0 is to change cylinder boundary conditions: if the welding of cylinders on the support is reinforced so that it acts like a rigid clamping, cylinders will be more rigid (higher f_s^0). The problem of playing with f_s^0 is the fact that the structure is changed (geometry, material,..). Adding a beam at the cylinders mid length allows to conserve the existing structure but changes the "design". Other parameters can be used to lower the VIV: the mass and the damping. Indeed, cylinders on site filled with sand present oscillations two times smaller than those of the empty cylinder. Increasing the mass and damping (leading to increase SG) does not play on the critical speed (instability still occurs) but decreases vibration amplitude and the lockin range. The addition of sand increases the mass and also the damping (vibration dissipation in sand by internal friction). Another way to increase the damping is the use of damper on the grid (small suspended mass).

[12] f_s^0 is proportional to E/m (m is the mass per unit length (proportional to density ρ)), E/m can be changed using another material (with higher E/m), steel is useless because has the same E/ρ as Aluminium

Chapter 5

Conclusion

The principal contribution of this master thesis is to propose guidelines for dynamic calibration of pressure measurement systems. In experimental aerodynamics, a useful quantity to measure around aerodynamic bodies is the pressure. It allows to know the flow around the body: where peak pressure occurs, where the flow separates,.... Some pressure transducers are flush-mounted and miniature. They can be placed on the model surface without perturbating the flow. Nevertheless, they are not as small as pressure tap (typically 5 [mm] of diameter). The solution is to use a pressure scanner, placed next to the Wind Tunnel model but far enough to not perturb the flow. Pressure tubes are then used to connect the pressure scanner to the location where the pressure is wanted (tap on the model).

Static (or mean) pressure is exactly known with this system (it corresponds to the value at "$f = 0$ [Hz]") but time varying components (fluctuations around the mean) are perturbed by the tube. Exactly like organ pipe, RLC circuit or transmission lines, a pressure tube is characterized by resonance frequencies, due to the wave propagation. Each pressure tube has a certain dynamic response in the frequency domain: a Transfer Function, defined as the ratio between the signal at the end and the signal at the entry of the tube (in frequency domain, the Fourier Transform of the time signal). The response of each tube will be different, depending on its geometry. Chapter 2 was dedicated to the study of this Transfer Function. When this calibration is done, pressure tubes can be used to measure unsteady pressure signals, directly corrected thanks to results of Chapter 2. Typical unsteady phenomena are associated to separated flow, stall, turbulence, vortex shedding. Chapter 3 is a direct application of unsteady pressure: a stalled wind turbine wing, subjected to Reynolds effect. Chapter 4 is another application, associated to the vortex shedding instability of a bluff body: a grid composed of rectangular cylinders (in opposition with the wing, a streamlined body).

5.1 General conclusions

In Chapter 2, a deep theoretical study was performed on the dynamic response of pressure tubes based on reference works. Tijdeman [35] starts from Navier-Stokes equations, for the flow in a tube. Assuming a laminar flow, small disturbances, small diameter compared to the tube length, ends effects are neglected and the ratio between the end and the begin of the tube is computed. By fixing physical properties (air at room temperature), this pressure ratio depends mostly on the tube length, diameter and end cavity volume (representing the pressure sensor cavity). This theory is able to model a series of N successive tubes, with a given geometry for each. The dynamic tube response can be computed with the Transfer Function (in an analytical form), with a complex value for each frequency. Its representation is typically made using its amplitude and phase (vs the frequency). Delio [31] shows a correspondence between fluid and electricity differential equation. The resistor represents pressure loss in the tube, the inductance the dynamic balance of flow and the capacitor the cavity (sensor) volume. A simple tube (only one tube-cavity system) can be modeled, but only with one resonance frequency. Taback [39] makes also a parallel between wave propagation in a pressure tube and in a transmission line. The tube diameter, length and cavity volumes are equivalently represented by an impedance. This allows to model reflection of wave propagation and thus a dynamic response with

several resonance peaks (as Tijdeman study but contrary to the RLC circuit, with only one resonance).

In addition to theoretical models, experimental measurements were performed. A review of existing devices was made. The principle is to measure the pressure at both extremities of the pressure tube and compare them in term of frequency content. A pressure signal with a frequency content (unsteady) is applied to the tube entry. The Transfer Function is the ratio between the Fourrier Transform of the measured signal at the tube end and the one of the reference signal, at the tube entry. When the Transfer Function of the tube is known, pressure signal measured thanks to the this tube can be corrected by dividing its Fourrier Transform by the Transfer Function and taking the inverse Fourrier Transform of the result. This principle is used for the calibrator in KTH (Stockholm University). This calibrator uses a periodic pressure generator, that gives a mono frequencial pressure signal at the tube entry. The Transfer Function is computed point by point for each frequency. Another method used is to construct a polynomial Transfer Function (with fitting coefficients), knowing as the Rational Fractional Polynomial (RFP). This method is used for the calibrator designed and build at the ULg. This calibrator uses an aperiodic pressure signal by creating a step. The Transfer Function is constructed by fitting RFP coefficients using data from one test only, because the step function has a wide frequency content (compared to the mono frequency of the periodic KTH generator). Practically speaking, this pressure step is created using a bursting balloon device (high pressure inside the balloon, explosion, lower (atmospheric) pressure). Comparison of these methods gives close results.

The studied parameter values were chosen in a way directly linked to the application scope. The frequency range of the Transfer Function could be very wide but higher frequencies than those observed in measurements are useless. Typically, the frequency range associated to separated flow or vortex shedding (applications of Chapters 3 and 4) is in the range [0-300] [Hz]. There is no need to compute the dynamic response associated with higher frequencies. Higher frequencies are anyway associated with measurement errors (noise). From theoretical results, higher frequencies are anyway highly attenuated by the tube and it acts a bit like a low pass filter. With the KTH calibrator, each frequency is obtained with one test, which can takes a while if a lot of frequencies are tested. Knowing the frequency range of interest before making measurements allows to optimize the time and the way they are taken. Moreover, other studies have shown that the pressure tube material (metal or vinyl) has no influence on the response. This is the same for the tube bending: there is no influence of the number of bending points or location if there is no shrinkage or sudden diameter change. This is respecting the minimum tube radius of curvature, provided by tube manufacturer, guaranteeing the absence of shrinkage.

Results from Chapter 2 show that lengthening or slimming the tubes has a similar effect: the first resonance frequency (the highest and the most energetic) decreases together with its associated peak amplitude. If very long and narrow tubes are used, almost all frequencies are attenuated (amplitude ratio well below 1 and high phase shift). This has to be avoided because the amplitude ratio is used as a divisor of the measured signal. If the amplitude response is close to one, the ratio will not vary too much, but if the response is very low, imprecisions on the denominator can amplified those on the results. Most of the time, the same tubes are used (in term on material and diameter). The only geometrical parameter is thus the tube length. The equivalent sensor cavity volume is constant (associated with the particular pressure sensor used) but has to be computed by adjusting the parameter in the theoretical model in such a way that the response is the same as the experimental one. The influence of this volume is an attenuation of the resonance peak (the extreme theoretical case of a zero volume corresponds to infinite resonance, as in an organ pipe). The volume of the tube is fixed by its length and diameter. Even if this volume is constant, a long and narrow tube will attenuates the signal and decrease the resonance frequency, compared with a short and wide one. For diameter discontinuity (modelled using two tubes, with a zero volume between), a combination of length and diameter can gives opposite effect depending of the sequence (smaller then wider, or the opposite) because of opposite effects. For a smaller tube followed by a wider one there is a higher amplitude because less friction in the wider tube, but the wider tube acts like a volume from the point of view of the smaller tube.

Phase correction is as important as amplitude correction. For short tubes, the amplitude ratio is close to 1 (as for restrictors) and the phase is low but too high to be ignored, and a phase correction is necessary. For long tubes, this phase distortion is even worst. Pressure calibration is important to know the standard deviation and the amplitude of fluctuations around a mean value (that is statically determined). This has a strong effect when studying unsteady phenomena (stall, vortex shedding,...). Theoretical and experimental results are close to each other, because one pressure tube is a simple measurement system.

In Chapter 3, a 3D printed wind turbine wing profile has been studied. Pressure taps and channels are directly printed. Diameter change and complex channel shapes are built because of space constraints. Pressure tubes are connected to the end of these channels. The measurement system is not only composed of a simple pressure tube and it has to be experimentally calibrated. The diameter restriction at pressure tap has a strong influence on the response. For the profile with small taps, all frequencies are attenuated (amplitude below 1) and some holes (40 in total around the profile contour) are obstructed. The profile with larger taps has almost no diameter restriction and the response is closer to the one obtained with a simple pressure tube. This profile was used to make Wind Tunnel measurements (the other had too small taps) at low (7 [m/s]) and high (15 [m/s]) airspeeds (or Reynolds number). The pressure distribution is integrated along the contour to get the lift and the drag (depending on the incidence and the Reynolds number).

Dynamic calibration is useful to correct unsteady characteristics such as standard deviation or kurtosis during stall. The lift coefficient works like a filter, fluctuations during stall are lower than those of each pressure taps coefficient. Comparison with CFD validates the results (fluctuations of CFD results are lower because there is no instrumentation errors that create noise). Theoretical models are useful to predict the lift at low angles of attack. However, viscous effect leading to stall cannot be theoretically modelled. Numerical methods like `Xfoil-XFLR5` add viscous correction and are able to detect this stall. However, the lower the Re, the higher the viscous effects, the higher the needed correction and therefore a greater likelihood of error. This profile is strongly Reynolds dependent. Pressure distribution, lift and drag vary with Re. The highest $Re = 1.2 \cdot 10^5$ is close to inviscid case (low viscosity) and the lift slope is very close to theoretical results: Panel method and Joukowski airfoil model well thickness (lift slope) and camber (lift at $\alpha = 0$) effects. Thin cambered airfoil theory can only model camber effect. The lower Re shows a lower lift slope, and hence pressure distribution. A large stalled laminar BL is present on the upper surface, and reattaches as a turbulent boundary layer on the rear part (close to TE). The complete stall (separation of turbulent boundary layer) occurs for higher angle ($\alpha = 20$ for the low Re and $\alpha = 12$ for the high Re). The type of stall is from the trailing edge.

Chapter 4 studied a real problematic: a grid composed of 100 rectangular cylinders equally spaced (of two times the rectangle cross flow dimension) placed in front of a house, subjected to the wind. A huge noise produced by this grid was observed by the owners. Noise is associated to air vibration, produced by the grid vibration. The purpose is thus to study from where these vibrations come from and how it can be predicted. Vibration is an unsteady phenomenon and the dynamic calibration of Chapter 2 has to be directly used.

Firstly, real conditions were studied and accelerometers were placed on site. For seven half days of measurement, a correspondence between high amplitude oscillations (called event) and wind condition was found: when the speed was between 5 and 8 [m/S] with a direction of 0-50 [°]. From a theoretical context, such oscillations happen during VIV (vortex induced vibration). Indeed, when the flow around a rectangle is separated from upstream corners, vortices are ejected. This process follows the Strouhal relation (linear dependence of the vortex shedding frequency and the airspeed). A particular body is characterized by a Strouhal number St. Once the velocity increases, the frequency of vortex shedding increases as well and when it reaches the resonance frequency of the structure (at rest), the excitation

occurs: fluid excites the structure which in turn excites the fluid and so on, fluid-structure interaction happens. The modal properties of the structure was thus studied (resonance frequency and damping) using several methods: beam theory (cylinders on the grid are equivalent to a bipinned beam alone, at $f_s^0 = 60$ [Hz]) and FEM with `SamcefField` (comparing the whole real grid, a simple bipinned beam and the WT model). This model was built to reproduce real conditions of the grid (model at scale 1:1 but with 10 cylinders instead of 100, structural properties being the same thanks to the FEM study). These predictions on modal properties were validated by experimental wind off tests (by measuring the free decay after an impulse on each cylinder, without wind).

Real conditions of the grid were reproduced, using additional parameters: airspeed, incidence, spacing between cylinders. The instrumentation consisted of accelerometers on each cylinder (measuring vibration amplitude), a Cobra Probe in the wake of the grid (measuring the vortex shedding), a Hot Wire upstream of the grid (to know exactly free stream conditions) and pressure taps around cylinders at mid height (to know the flow around it, the vortex ejection). VIV curves (amplitude vs airspeed) show that decreasing the spacing between the cylinders decreases the critical reduced speed ($U_r = U_\infty/(f_s^0 D) = 1/St$), corresponding to a higher St. When cylinders are close to each other, the flow is accelerated in the channels between the cylinders, the speed seen by the cylinders is thus higher than the upstream one. The instability occurs at a free stream speed lower than the one for a single cylinder (normally $St = 0.07$ and $U_r = 16$ for a single cylinder but the grid with a spacing of $T/D = 1$ shows $St = 0.24$ and $U_r = 4.2$ at zero angle of attack). The limit case of the grid is when the spacing is a least 4 or 8 times D, in this case the flow behaves as if the cylinder was alone.

These results were computed at zero incidence, by varying the airspeed. The incidence has also a strong effect: when it increases, the critical reduced airspeed increases (St decreases). Indeed, at incidence, the flow on the lower side stays more attached, the separation occurring at the downstream corner (and separation on the upstream upper corner). The vortex ejection happens less often and St decreases. This has been validated by studying the pressure distribution depending on the incidence and the spacing. It shows that every cylinder converges to the same pressure distribution when the spacing increases. The cylinder interaction at low spacing is characterized by a change in the characteristic plateau of a separated flow (a step shape is observed, showing the interaction of adjacent cylinder wake). Using the dynamic pressure calibration, the phase (synchronization) of vortex shedding process can be studied. By comparing with CFD results, it shows that a small spacing is characterized by a single vortex street (high interference) and when it increases, the flow is bistable and tends to a coupled vortex street and finally to independent vortices ejection. From this study, a datasheet of St for all configurations (incidence and spacing) was computed. It gives the critical speed associated to the configuration, and so the conditions to avoid.

5.2 Perspectives

Along this study, the dynamic calibration was studied and implemented to direct problematic and situations, to better understand them. It prompts however some additional questions.

Chapter 2 studied the dynamic response, to correct the signal *after* measurements, in a passive way. A more optimal way to make unsteady pressure tests could be to act in an *active* way, *i.e.* to build a pressure measurement system that takes into account the signal distortion and correct it geometrically. This is possible by designing and printing directly channels containing a restrictor. This is a small diameter restriction that allows to obtain an amplitude ratio very close to 1 over a large range of frequency. This system does not play enough on the phase, and a small shift is still present. It could be interesting to find a direct way to correct this phase. It could be also a user friendly interface: when you use a pressure measurement software, you are asked to enter the reference of the pressure tube you use (so that the diameter, critical bending radius are known) and its length. The software will automatically correct the signal during recording.

During Chapter 3, Reynolds effect on the wing was studied. Nevertheless, another parameter can influence the separation point and the boundary layer behavior: the roughness. It could be interesting to study the influence, by computing a Reynolds number that takes the roughness into account (using an equivalent roughness dimension). Moreover, pressure taps can influence also this roughness. It could be interesting to see the influence of their size on the flow, by comparing several profiles (with their associated calibration). A CFD simulation of different pressure taps size can also be compared.

Chapter 4 studied deeply the grid effect. Observations can be used to correct the phenomenon, *i.e.* get rid of oscillations by shifting critical speed to higher values (that happen less in Belgium). The reduced speed is constant for a grid/cylinder configuration but by increasing eigenfrequency f_s^0, U_∞ (critical) is increased. Several solutions can be implemented to increase f_s^0: reduce the cylinder length, find a material with higher specific stiffness(E/ρ) or increase the cross section inertia. Another kind of solution (if the design has to be conserved) is to play on the Skop-Griffin number SG. If the structure is heavier and more damped, SG increases and the instability occurs at the same speed but oscillations are of lower amplitude. The question is how to link the vibration amplitude to the noise. By how much to increase the structure mass so that the structure can sustain this weight and the noise is enough reduced ? Noise study and comparison to vibration amplitude is not well know It can be very interesting to study, to increase the comfort of citizens, or build structure with multiple purposes of: structural purpose or an artistic appeasement using music...

> *Music has charms to soothe the savage breast*
>
> William Congreve (1697)

Appendix A

Pressure calibration

A.1 Theoretical models

Derivation of RLC analogy Equation 2.10:

- Fluid motion in tube: dynamic balance (inertia and wall friction τ_w)

$$A(p_1 - p_2) = \rho_s L \frac{dU}{dt} A + \pi D L \tau_w \tag{A.1}$$

  Assuming that the wall friction coefficient is the same in unsteady and steady conditions (strong assumption), the steady pipe flow gives

$$\pi D L \tau_w = A \Delta p \tag{A.2}$$

  Where Δp is the steady pressure pipe loss

  - distributed: $\Delta p = 4 C_f \frac{L}{D} \rho \frac{U^2}{2}$ with $C_f = \frac{16}{Re}$
  - localized: $\Delta p = \xi \rho \frac{U^2}{2}$ with ξ depending on the location (pipe inlet, outlet, ...)

  Rearranging equation A.1 (for laminar flow),

$$\frac{p_1 - p_2}{\rho} = L \frac{dU}{dt} + 32 \nu \frac{L}{D^2} U + \left(\frac{4}{3} + \sum \xi \right) \frac{U^2}{2} = L \frac{dU}{dt} + k_1 U + k_2 \frac{U^2}{2} \tag{A.3}$$

- Fluid in cavity: mass conservation between tube and cavity. The cavity volume Vol varies with time because of the transducer membrane (related to σ in [35]) through the variation of p_3 (relative pressure to ambient p_s). Polytropic compression happens in the cavity $\frac{dp}{p} = n \frac{d\rho}{\rho}$ with $p = p_3 + p_s$

$$UA = \frac{1}{\rho} \frac{d}{dt} (\rho Vol) = \frac{dVol}{dt} + \frac{Vol}{\rho} \frac{d\rho}{dt} = \frac{dVol}{dp_3} \frac{dp_3}{dt} + \frac{Vol}{\rho} \frac{d\rho}{dt} = \left(\frac{dVol}{dp_3} + \frac{Vol}{n p_s} \right) \frac{dp_3}{dt} \tag{A.4}$$

  The pressure can be deduced,

$$p_2 = p_3 = \frac{1}{\frac{dVol}{dp_3} + \frac{Vol}{n p_s}} \int U A dt = \frac{1}{C} \int U A dt \tag{A.5}$$

  Eliminating $p_2 = p_3$ and combining line-cavity equations leads after integration to

$$L \frac{d^2 U}{dt^2} + (k_1 + k_2 U) \frac{dU}{dt} + \frac{A}{\rho C} U = 0 \tag{A.6}$$

  Thanks to the initial conditions ($t = 0$: $U = 0$, $\frac{dU}{dt} = \frac{p_1}{\rho L}$). This equation is exact but non-linear so a numerical scheme is necessary. Non-linear terms can be neglected assuming that

– The laminar flow and velocity are sufficiently low ($L >>$ or $D <<$) so that the dynamic pressure drop ($\propto U^2$) can be neglected compared to the laminar pressure drop ($\propto U$). Term $k_2 << k_1$ and equation A.6 can be linearized.

– The change in pressure in the cavity p_3 is adiabatic ($n = 1.4$) and the changes in pressure and density, compared to the initial values, are small so that $\frac{dVol}{dp_3} << \frac{Vol}{np_3}$

A.2 Experimental investigation

Shock-tube equations Assumptions for shock tube equation derivation:

- Perfect gas law
- Adiabatic flow
- Isentropic relations applicable
- Constant properties (specific heat)
- Instantaneous bursting of the diaphragm
- Inviscid flow (negligible viscous forces)

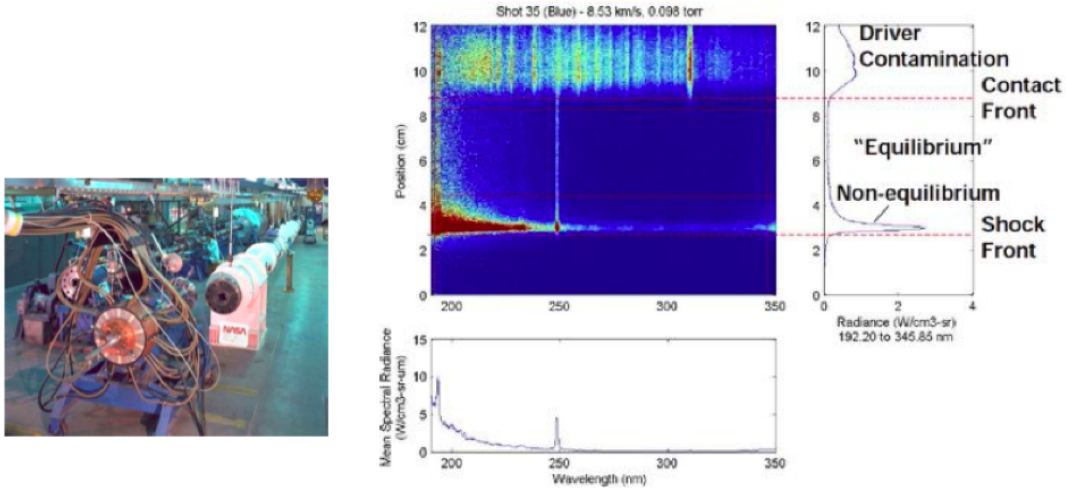

Figure A.1 – Electric Arc Shock Tube (EAST) facility at NASA ARC: snapshot of radiating flow measured by means of a spectrometer [68]

The pressure step measured by a transducer fixed on a side wall of the tube is (air in the tube)

$$p_2 - p_1 = \frac{7}{6}(M_1^2 - 1) \tag{A.7}$$

With p_1 and p_2 in Figure 2.40c and M_1 the shock wave Mach Number (depending on velocity U_1 and temperature T_1). The pressure behind the reflected shock wave measured by a transducer fixed at the end wall of the tube is,

$$p_5 - p_1 = \frac{7}{3}p_1(M_1^2 - 1)\left(\frac{2 + 4M_1^2}{5 + M_1^2}\right) \tag{A.8}$$

Quantitatively, the dwell time[1] for the NIST [21] shock tube ($L = 7$ [m]) is 0.1 [ms] when p_5 is 20 [MPa]. The low-frequency limit (from which there are values) is a few hundred [Hz] for the NIST tube. For amplitude, limits are about 20 [MPa] and the upper-frequency limit is some hundred [kHz] (above 500 [MHz] according to Paniagua and Denos [53]).Figure 2.40b shows the normalized density distribution across a shock wave[2] as a function of a normalized position x/λ_∞, where $\lambda = a/f$. Density

[1] Time during which the pressure is held constant

[2] in Argon gas at $M_\infty = 9$ (Mach Number $M_\infty = \frac{U_\infty}{a_\infty}$ where U_∞ is the free stream velocity and a_∞ the speed of sound in free stream conditions)

is directly related to pressure using state relations (for perfect gas). The density rises continuously in shockwaves. The shock thickness is of the order of the mean-free-path (average distance between two successive collisions of a molecule). An important observation is the failure of the fluid dynamical description because the flow is rarefied [68]. Discrete points come from Alsmeyer experiment, red line from Navier-Stokes equations simulation (Computational Fluid Dynamics), blue line from Boltzmann equation simulation (Direct Simulation Monte-Carlo) and green-line from Euler equations. Navier-Stokes equations can be written in a compact vector form as [68],

$$\partial_t U + \boldsymbol{\partial_x} \cdot \boldsymbol{F} + \varepsilon \boldsymbol{\partial_x} \cdot \boldsymbol{F}^d = 0 \text{ with } U = (\rho, \rho \boldsymbol{u}, \rho E)^T \text{ and } \boldsymbol{F} = (\rho \boldsymbol{u}, \rho \boldsymbol{u} \otimes \boldsymbol{u} + p\mathbb{I}, \rho \boldsymbol{u} H)^T \qquad \text{(A.9)}$$

With $\boldsymbol{u} = (u, v, w)^T$ (velocity components), ρ the density, E the energy, H the enthalpy. The Euler equations are obtained as the limit of the NS equations when the dissipative terms vanish ($\varepsilon \to 0$, no viscosity). NS and Euler solutions match in inviscid regions upstream (region 1 in Figure 2.40b) and downstream (region 2) of a discontinuity where gradients vanishes ($\boldsymbol{F}^d = 0$).

Parameters Tube material and bending do not have influence on the dynamic response.

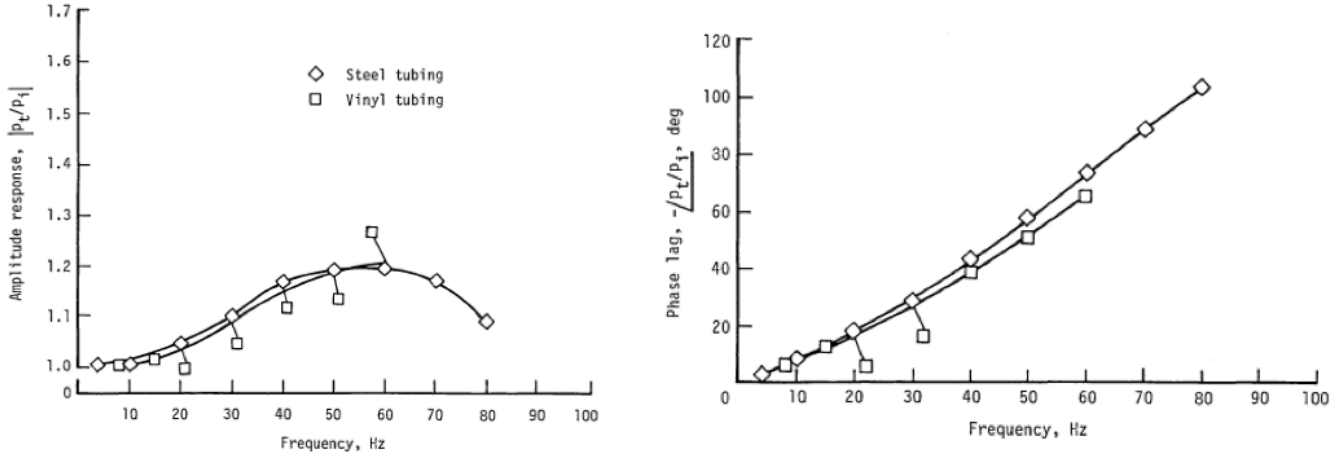

Figure A.2 – Effect of the tube material on Transfer Function [76]

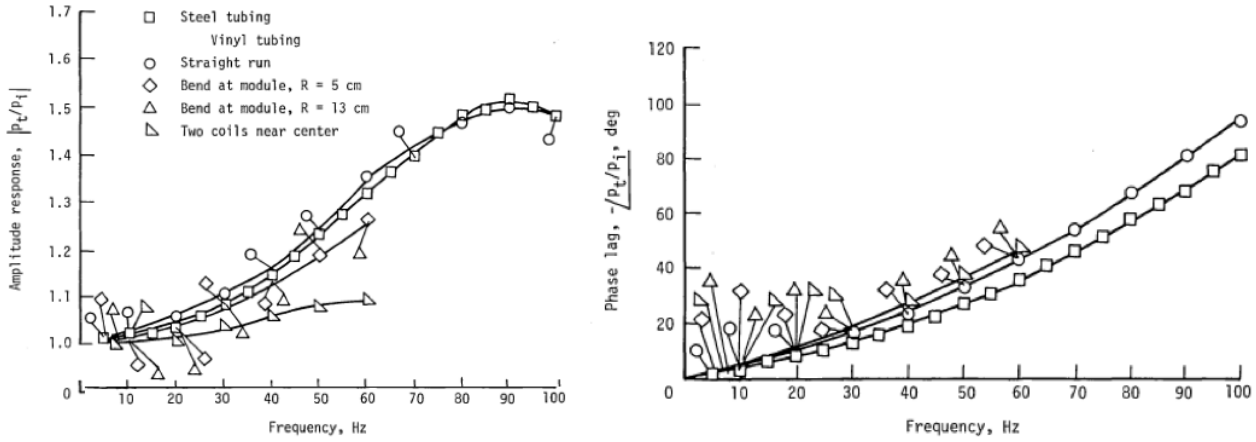

Figure A.3 – Sinusoidal response for 0.09-em inside-diameter vinyl tubing that was 61 em long: influence of tube shape [76]

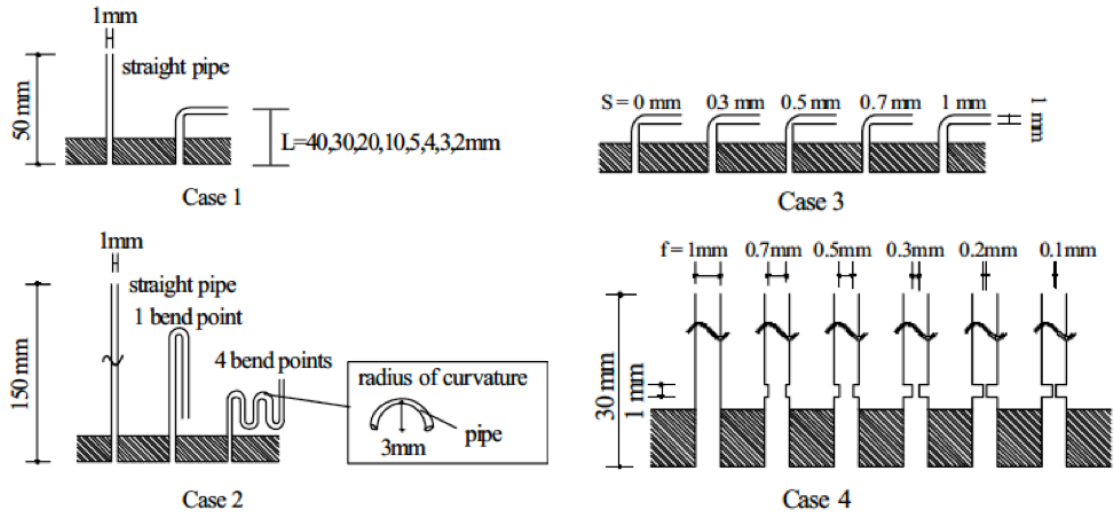

Figure A.4 – Experimental cases (inner diameter of pipe=1 mm, radius of curvature at bending point=3 mm). Case 1: Effects of the location of bend point (L: length from the pressure tap to bending points). Case 2: Effects of number of bend point (total length of pipe=150 mm). Case 3: Effects of inner diameter at bend point (S: diameter of inserting brass bar when pipe bend). Case 4: Effects of partial shrink [78]

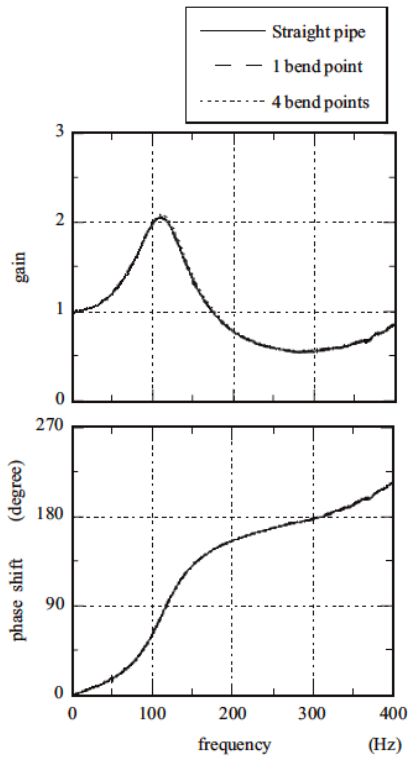

Figure A.5 – Case 2: Transfer functions of pipes with different number of bend point (pipe length=15 cm, tube length=35 cm)

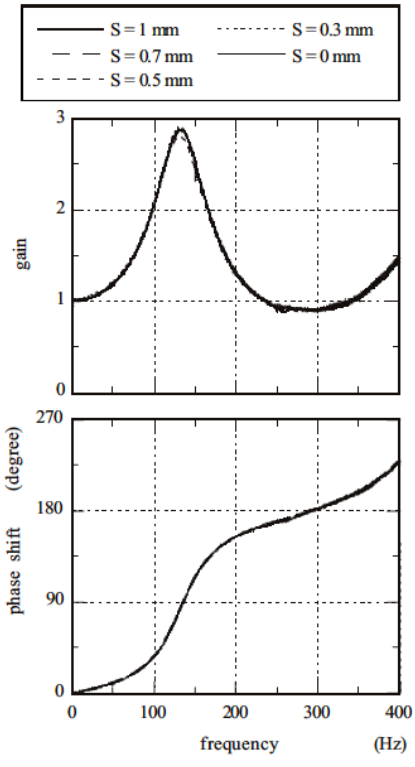

Figure A.6 – Case 3: Transfer functions of pipes with different sectional areas at bend point (pipe length=3 cm, tube length=47 cm)

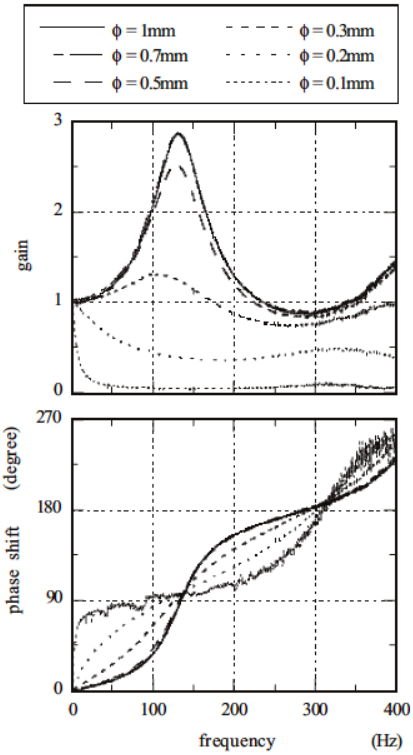

Figure A.7 – Case 4: Transfer functions of pipes with different sectional area (pipe length=3 cm, tube length=47 cm)

A.3 ULg calibrator

A.3.1 Analytical functions for pressure generation

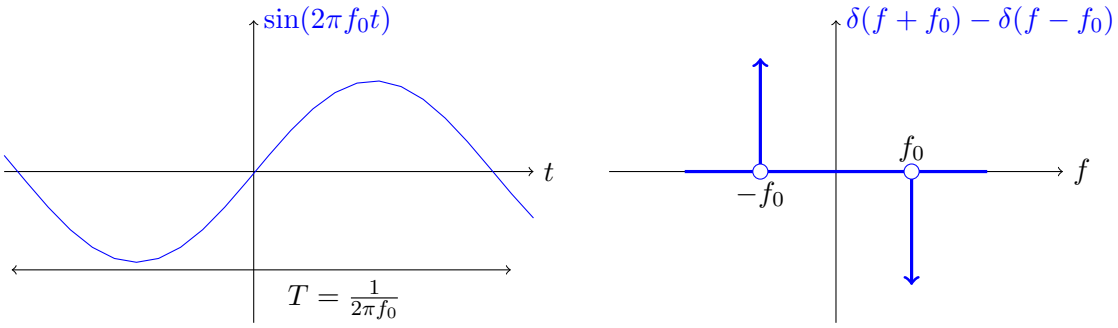

Figure A.8 – Schematic representation of Sine function in time domain and its Fourier Transform (Dirac function in frequency domain)

Of course, in the frequency domain, only positive values of f are meaningful. Some particular functions (in time domain) can give continuous functions over a large domain of frequencies such that: sine sweep, uniform noise, impulse,... . Another one that is very easy to generate is the unit step function (Heaviside),

$$H(t) = \begin{cases} 0 & x < 0 \\ \frac{1}{2} & t = 0 \\ 1 & t > 0 \end{cases} \tag{A.10}$$

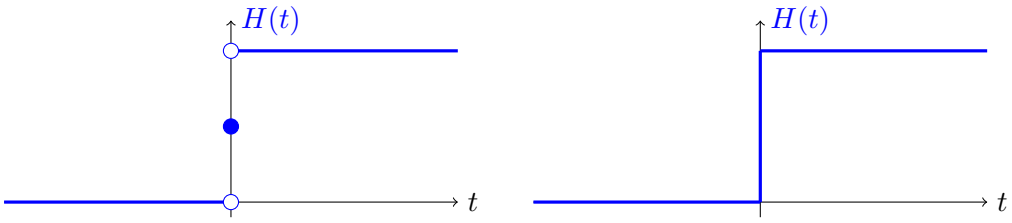

Figure A.9 – Schematic representation of limit functions that approximate the Heaviside function in the time domain, from equation A.12

It represents either a piecewise constant function or a generalized function as shown in Figure A.9. The Fourier Transform of the Heaviside function is given by (Figure A.10):

$$\mathcal{F}_t[H(t)](f) = \frac{1}{2}\left[\delta(f) - \frac{i}{\pi f}\right] \tag{A.11}$$

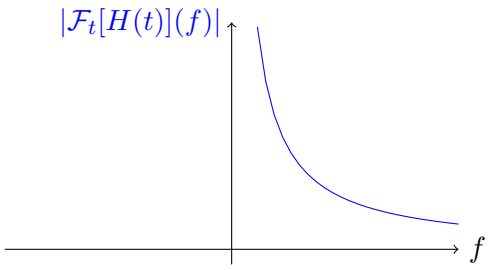

Figure A.10 – Schematic representation of the Fourrier Transform of the Heaviside function in the frequency domain

This function can be defined as a limit for $t \to 0$ of some continuous functions (where $Si(t)$ is the sine integral function):

$$H(t) = \begin{cases} \frac{1}{2} + \frac{1}{\pi} \lim\limits_{x \to 0} Si\left(\frac{\pi t}{x}\right) \\ \lim\limits_{x \to 0} \frac{1}{1+e^{-\frac{t}{x}}} \\ \dots \end{cases} \qquad \text{with } Si(t) = \int_0^t \frac{\sin(x)}{x} dx \tag{A.12}$$

The shape of these approximations with parameter $x \to 0$ is shown in Figure A.11. from a experimental point of view, they are more likely to happen.

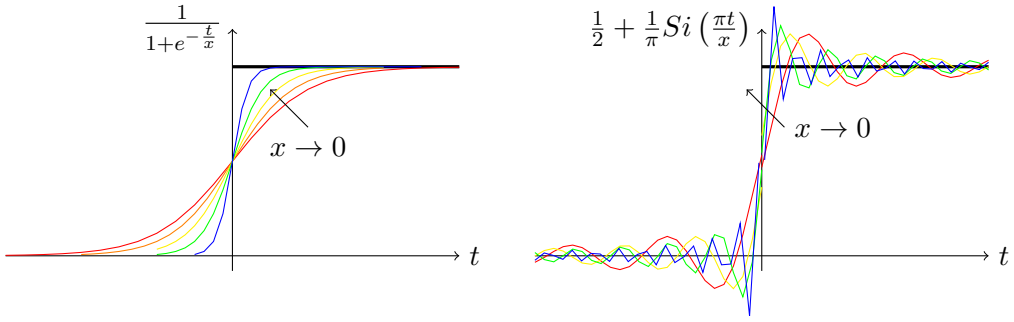

Figure A.11 – Schematic representation limit functions that approximate the Heaviside function in the time domain, from equation A.12

The Fourrier transform of a boxcar (window function) is a *sinc* function (Figure A.12). With a balloon, this window can be done by attaching an already inflated balloon on the plug but closed (so that the pressure is the ambient one). Then, by opening suddenly the balloon, the pressure inside it is transferred inside the test chamber (of a negligible volume compared to the one of the balloon) leading to a rising pressure step. After, the balloon is bursted, leading to a dropping step. A window pressure signal is created and its Fourrier Transform is a $sinc = \frac{\sin(f)}{f}$ periodic functon.

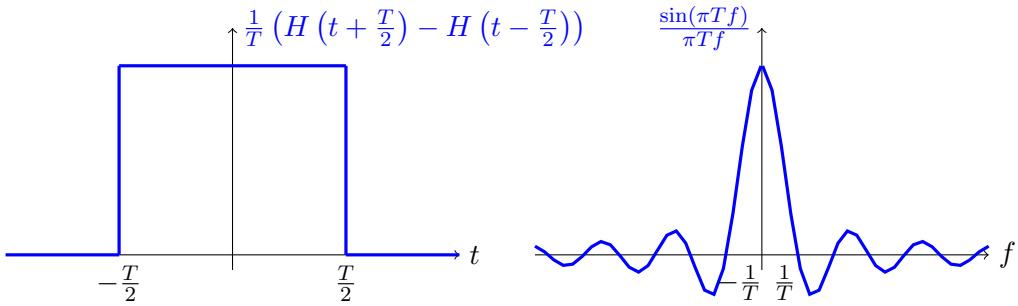

Figure A.12 – Schematic representation of windows function in the time domain and its Fourier Transform in the frequency domain

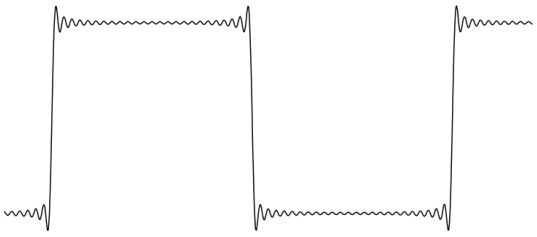

Figure A.13 – Illustration of Gibbs phenomenon, approximation of window function with 25 harmonics (Si function, equation A.12), from [28]

A.3.2 Pressure inside a balloon

The pressure inside a balloon made of rubber will be derived here, depending on the size (radius) and material behavior. As seen during the course of "Mécanique des milieux continus" [51], considering that the balloon is spherical, an equilibrium can be made on the balloon skin, to get the pressure (Figure A.14) from the stress σ. Performing a force equilibrium,

$$p\ r\ dr\ rd\phi = 2\sigma \sin\left(\frac{\phi}{2}\right) h\ r\ d\theta + 2\sigma \sin\left(\frac{\theta}{2}\right) h\ r\ d\phi \approx 2\sigma h\ r\ d\theta d\phi \Rightarrow p = 2\sigma \frac{h}{r} \tag{A.13}$$

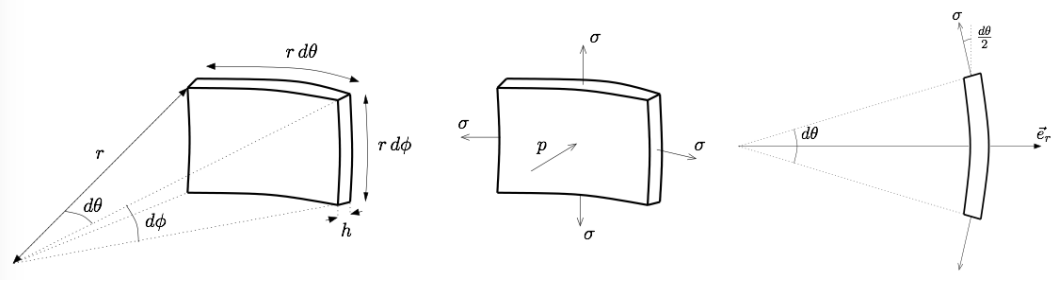

Figure A.14 – Elementary element of balloon in spherical coordinates, from [51]

Stress σ inside the balloon skin can be deduced, assuming a constitutive law for the rubber skin, given by a hyperelastic potential,

$$W = C\left(2E_{11}^{GL} + 2E_{22}^{GL} + \frac{1}{1 + 2E_{11}^{GL} + 2E_{22}^{GL} + 4E_{11}^{GL}E_{22}^{GL}} - -1\right) \tag{A.14}$$

Where E_{AB}^{GL} is the AB component of the Green-Lagrange strain tensor and C a proportionality constant depending on the rubber stiffness. Starting from the deformation gradient

$$\boldsymbol{F} = \begin{pmatrix} \lambda_1 & 0 & 0 \\ 0 & \lambda_2 & 0 \\ 0 & 0 & \lambda_3 \end{pmatrix} \tag{A.15}$$

With $\lambda_1 = \lambda_2 = \frac{r}{R}$ (r is the deformed radius of the balloon and R the undeformed one), $\lambda_3 = \frac{h}{H}$ (the same but for the thickness). By defining

$$\boldsymbol{E}^{GL} = \frac{1}{2}(\boldsymbol{F}^T\boldsymbol{F} - \boldsymbol{I}) \tag{A.16}$$

Then, using the Piola PK2 stress tensor,

$$\boldsymbol{S} = \frac{\partial W}{\partial \boldsymbol{E}^{GL}} \tag{A.17}$$

The Cauchy stress tensor can be deduced,

$$\sigma = \frac{1}{J}\boldsymbol{F}\boldsymbol{S}\boldsymbol{F}^T = \frac{4C}{\lambda_3}\left(1 - \frac{1}{\lambda^6}\right)\begin{pmatrix} 1 & 0 & 0 \\ 0 & 1 & 0 \\ 0 & 0 & 1 \end{pmatrix} \tag{A.18}$$

With $J = det(\boldsymbol{F})$. By expressing equation A.13 as a function of λ ad r,

$$p = \frac{8Ch}{\lambda_3 r}\left(1 - \frac{1}{\lambda^6}\right) = 8CH\left(\frac{1}{r} - \frac{R^6}{\lambda^7}\right) \tag{A.19}$$

Experimental results obtained by [58] is in Figure A.15, compared with the theoretical prediction.

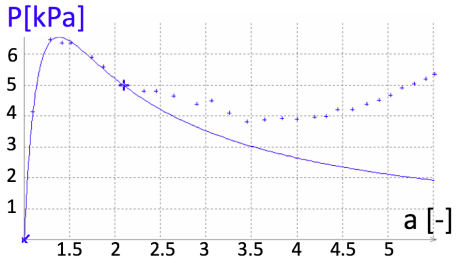

Figure A.15 – Overpressure p [kPa] inside a rubber balloon vs adimensional radius $a = r/R_{initial}$: comparison between experiment and theoretical prediction [58]

A.3.3 Setup and tools

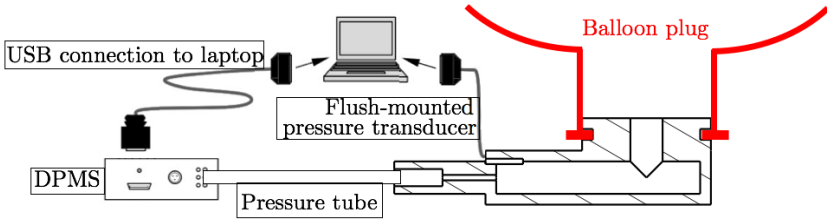

Figure A.16 – Schematic of the calibration set-up, balloon and measurement tools: design 1

Figure A.17 – Picture of the complete setup (design 2) with 3D printed support, flush mounted transducer and PVC tube inside the ballon

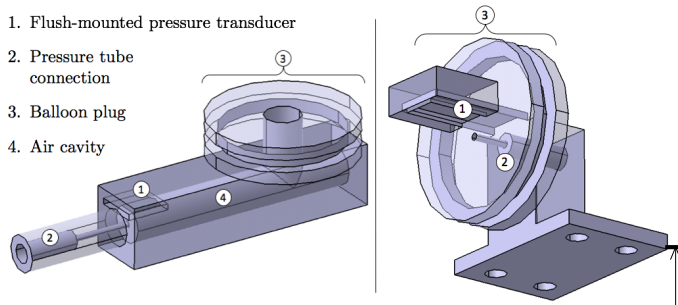

Figure A.18 – Transparent view of the calibrator cavity and the different connections, design 1 (left) and design 2 (right)

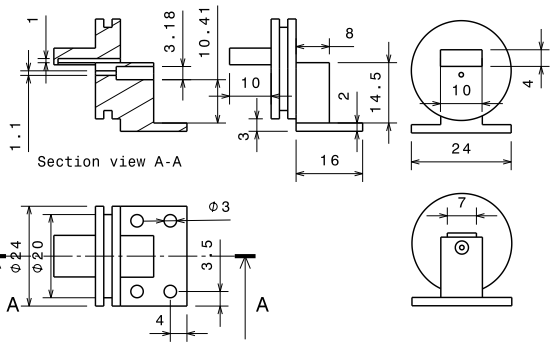

Figure A.19 – Drawing and size (in [mm]) of the 3D printed plug with scanners support (design 2)

A.4 Results

To reconstruct the reference time signal $p_{rec}(t)$ from the measured one $p_{mes}(t)$, the procedure is: inverse FFT of the ratio between FFT of p_{mes} and Transfer Function (experimental tube correction),

$$p_{rec}(t) = \mathcal{F}_f^{-1}\left[\frac{\mathcal{F}_t[p_{mes}(t)](f)}{\mathcal{F}_t^{corr}}\right] \tag{A.20}$$

With $\mathcal{F}_t^{corr} = \frac{\mathcal{F}_t[p_N(t)](f)}{\mathcal{F}_t[p_0(t)](f)}$ the Transfer Function (dynamic response, correction of the tube). Numerically, vector of $\mathcal{F}_t[p_{mes}(t)](f)$ and $\mathcal{F}_t^{corr}$ have to be of the same size. Nevertheless, $\mathcal{F}_t^{corr}$ has only discrete points (determined experimentally). A polynomial function has thus to be computed to fit data (Figure A.20).

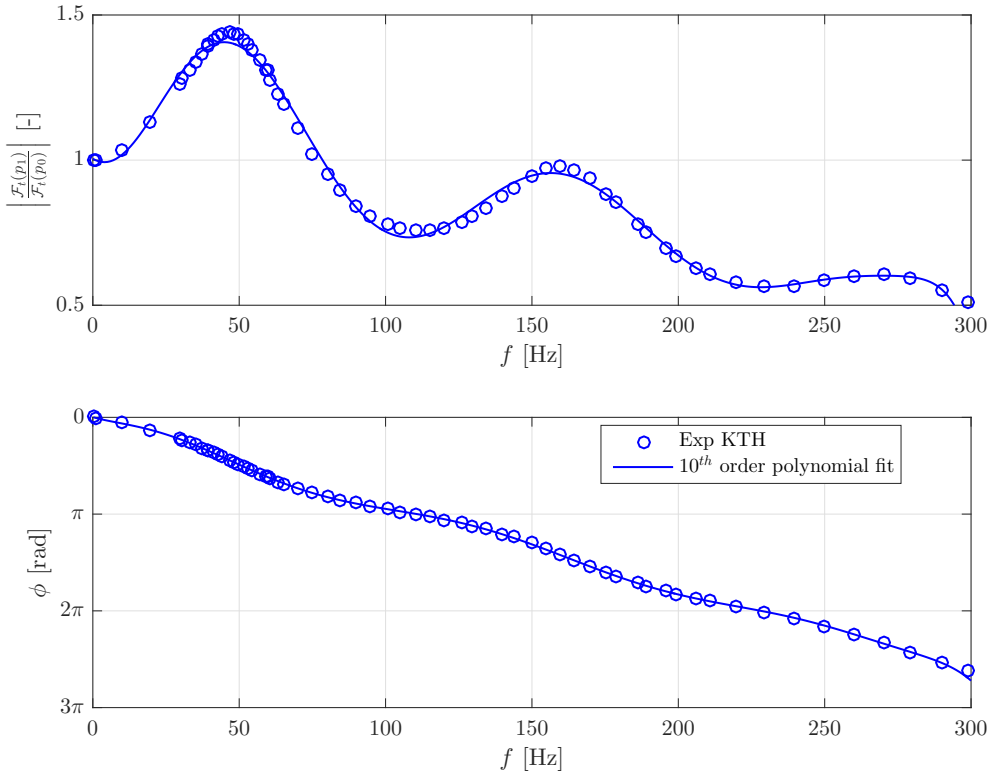

Figure A.20 – Dynamic response (case 1): experimental data and polynomial fit

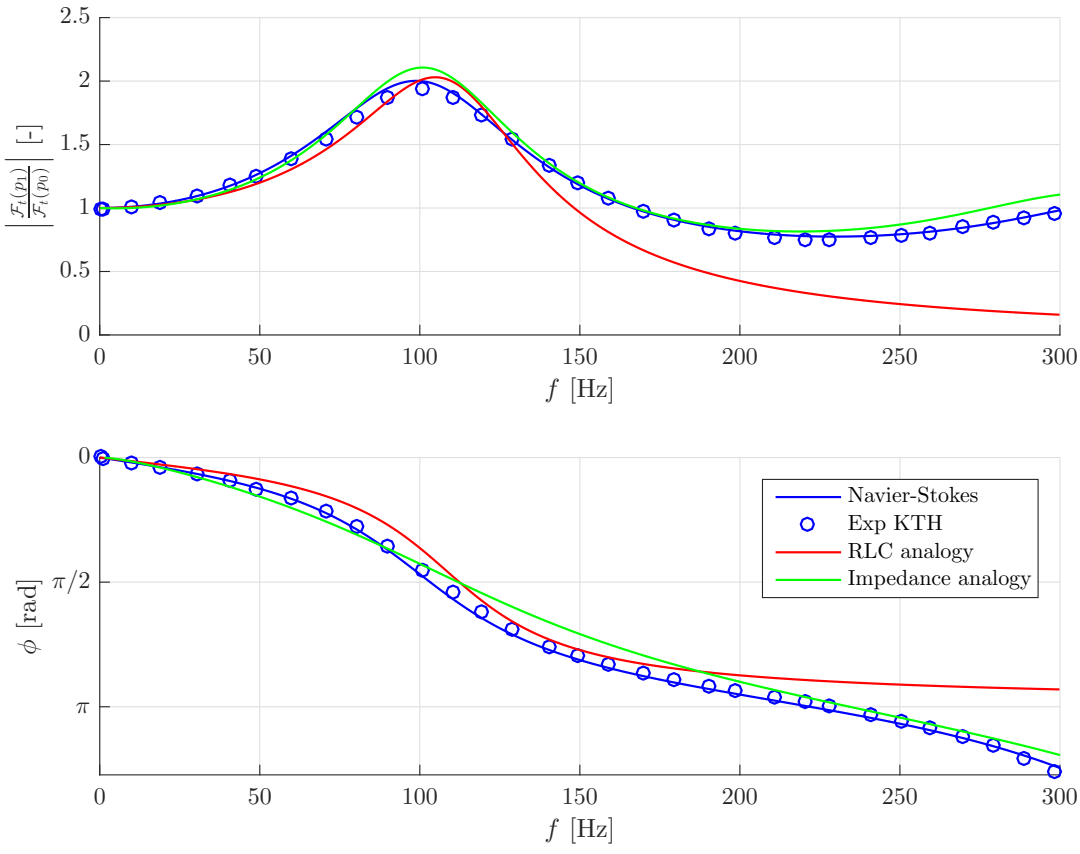

Figure A.21 – Comparison theory (3 models)-experiment (case 2: $L = 0.65$ [m], $D = 1.45$ [mm])

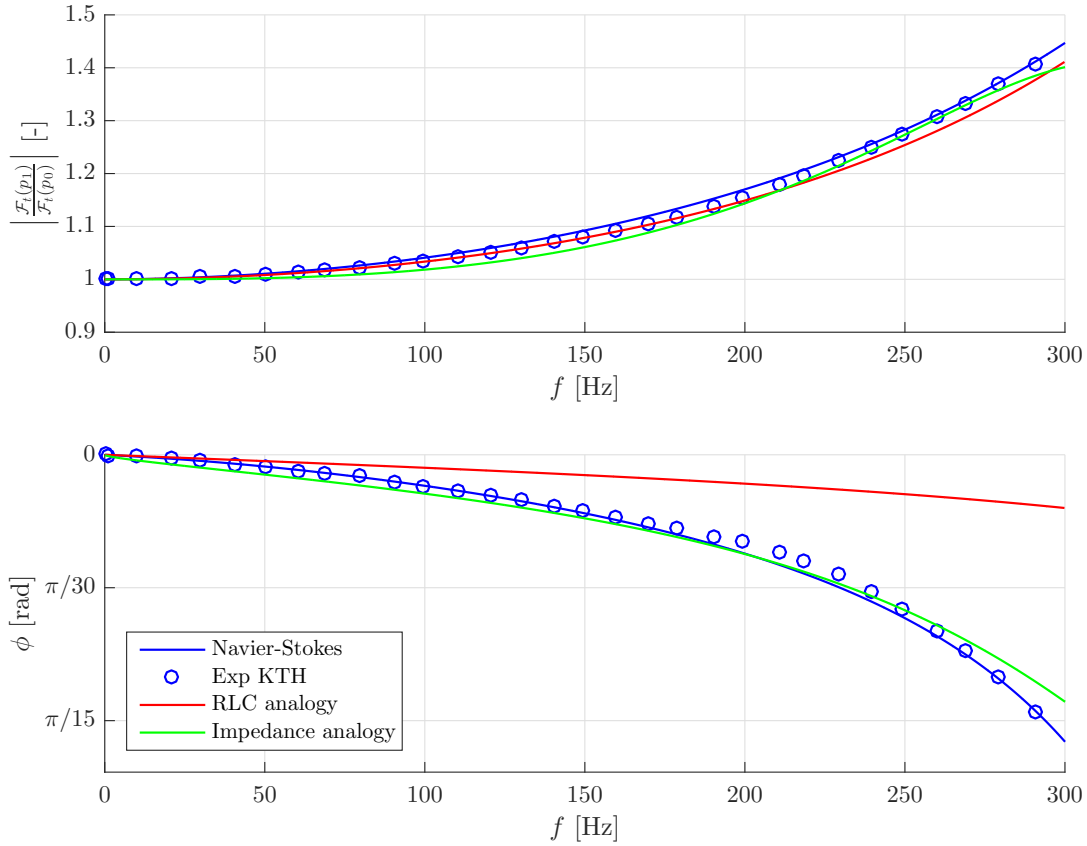

Figure A.22 – Comparison theory (3 models)-experiment (case 3: $L = 0.1$ [m], $D = 1.45$ [mm])

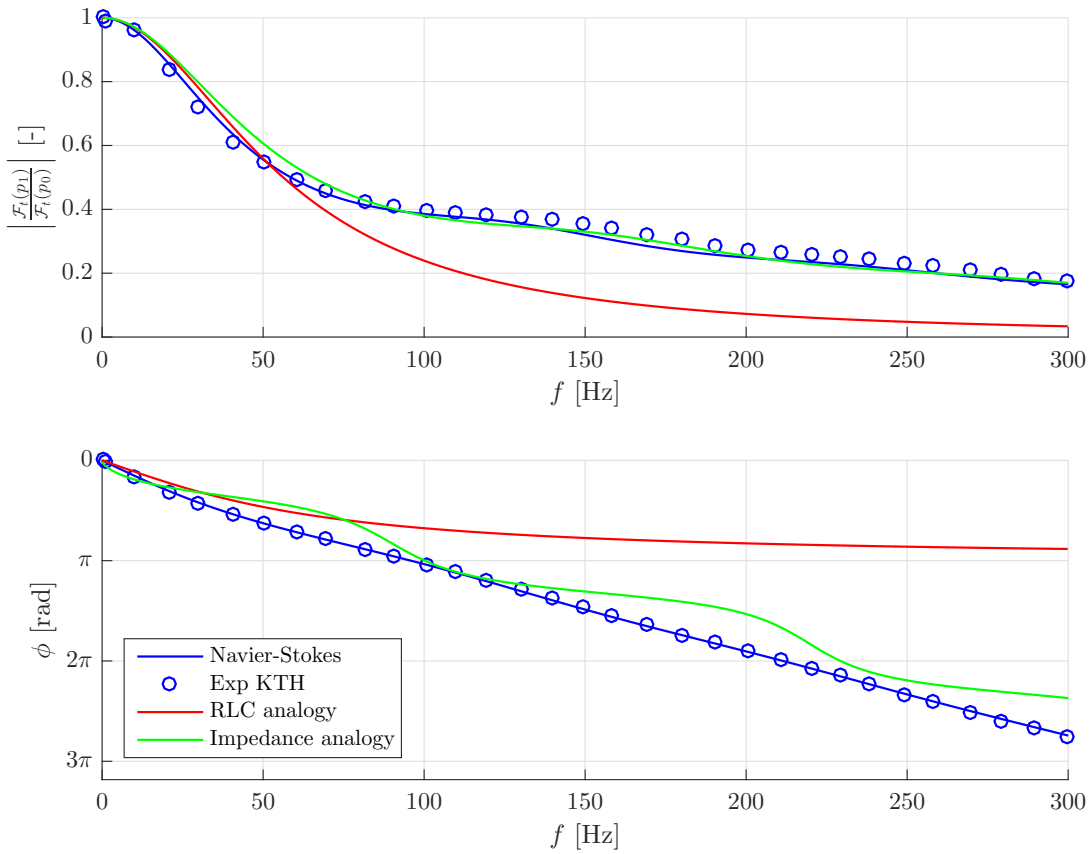

Figure A.23 – Comparison theory (3 models)-experiment (case 4: $L = 1.3$ [m], $D = 0.86$ [mm])

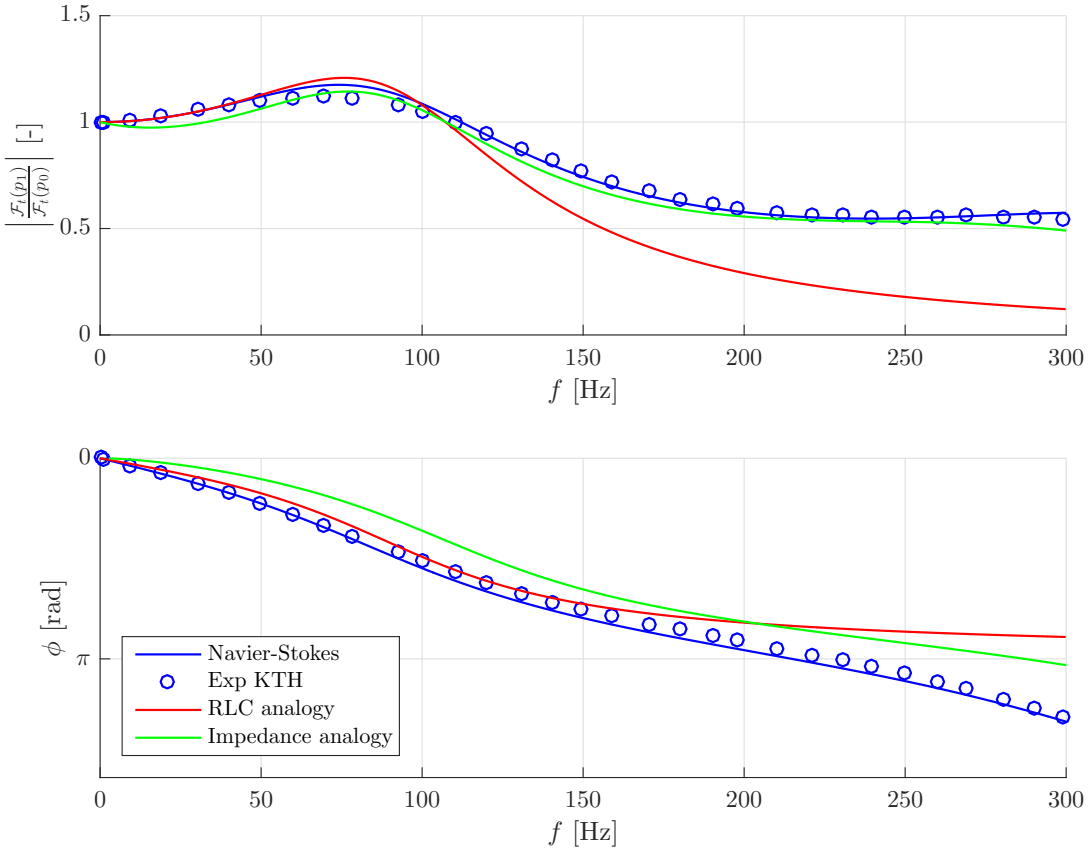

Figure A.24 – Comparison theory (3 models)-experiment (case 5: $L = 0.65$ [m], $D = 0.86$ [mm])

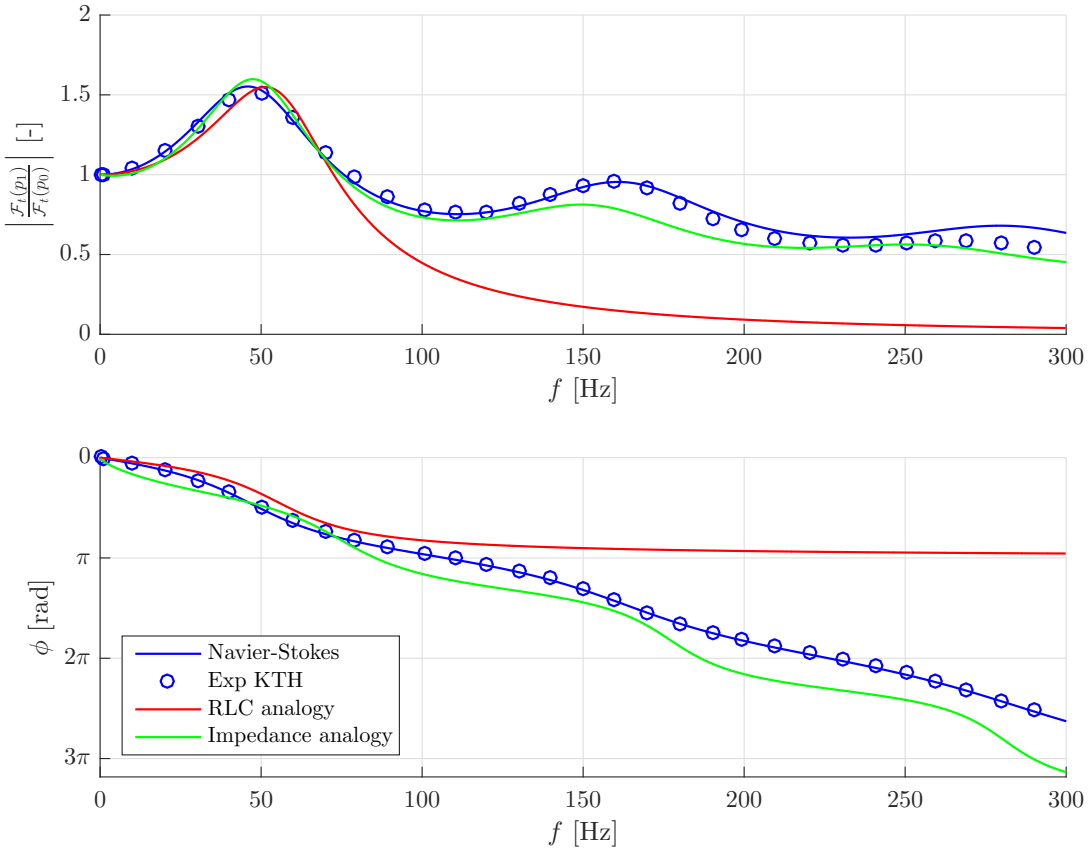

Figure A.25 – Comparison theory (3 models)-experiment (case 6: $L = 1.3$ [m], $D = 1.37$ [mm])

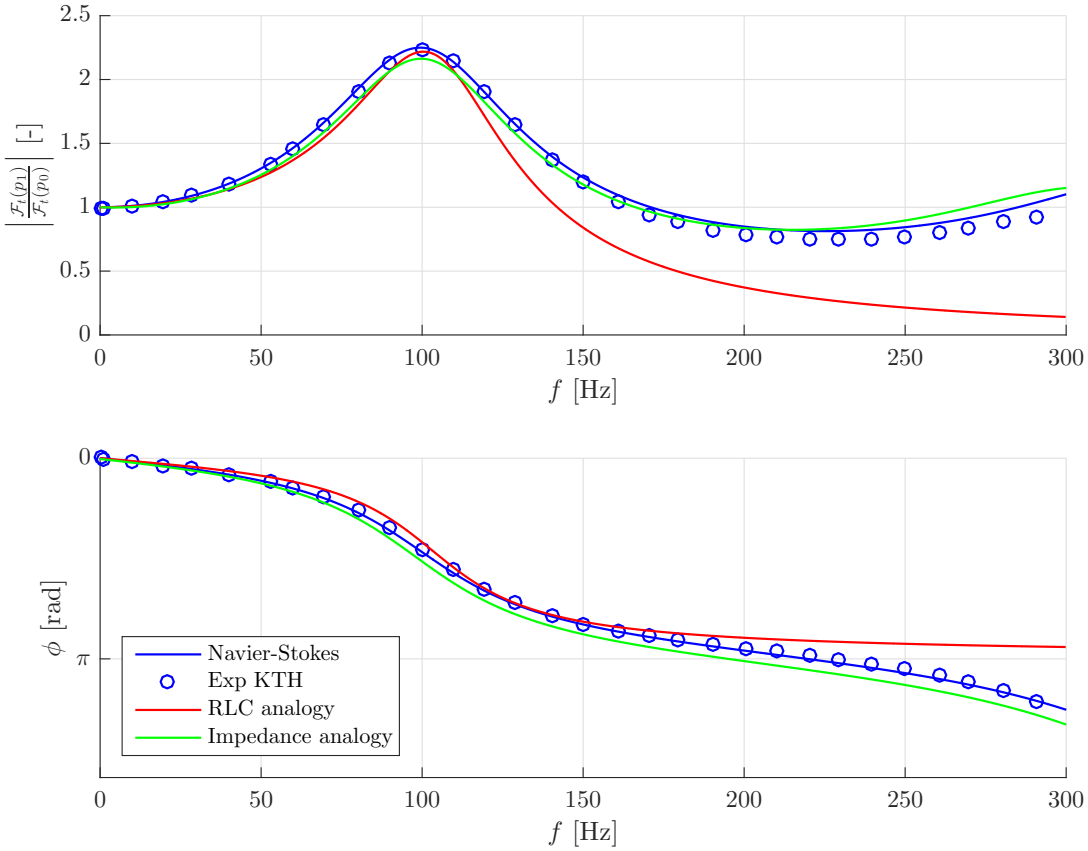

Figure A.26 – Comparison theory (3 models)-experiment (case 7: $L = 0.65$ [m], $D = 1.37$ [mm])

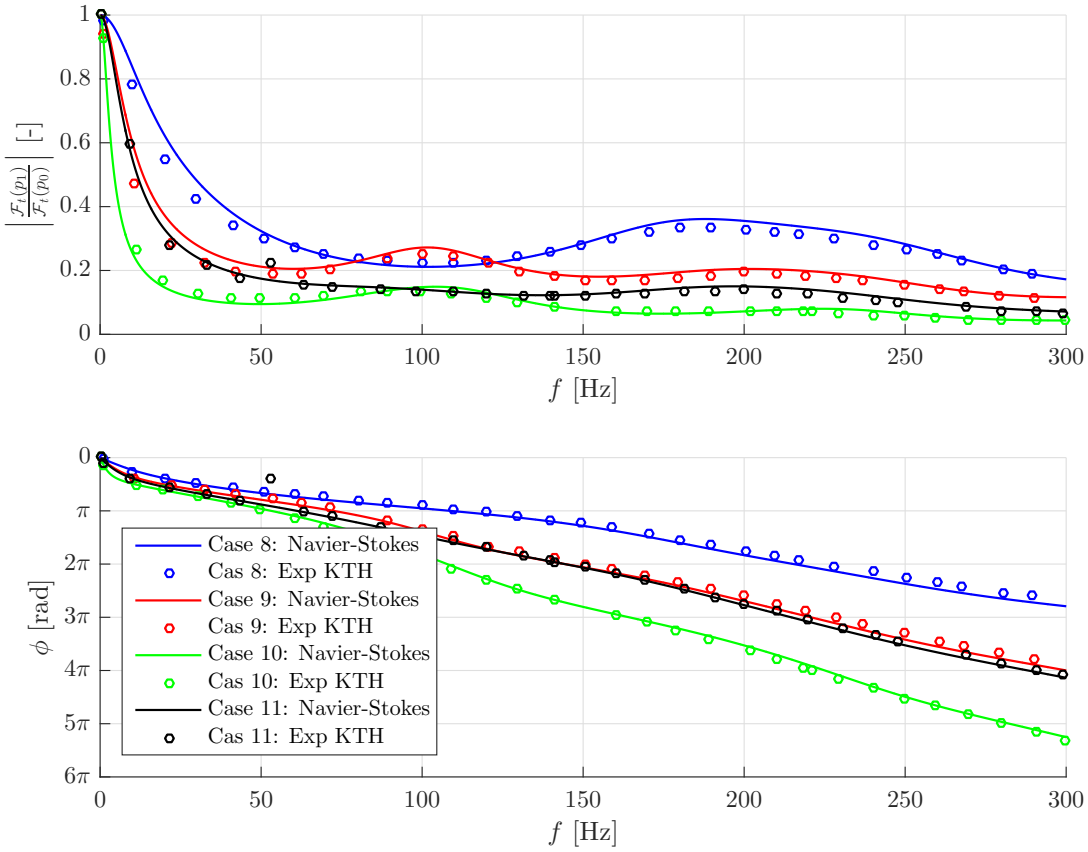

Figure A.27 – Comparison between theory (3 models) - experiment (cases 8 to 11)

Appendix B

Wind Turbine Wing

B.1 Context

Experimental error types:

- Systematic errors: Difficult to detect, since the deviation shows a constant offset compared to the real value [44]. **Example**: experiments in a wind tunnel (undesired variations of flow quantities, boundary layer growth due to wall, solid blockage,...)
- Random errors: Deviations of measures due to imperfections in the measurement system.
  - *A maximum error is introduced when even in the presence of the fluctuation of the quantity to be measured, the instrument always returns the same value*[44]
  - *A statistical error is introduced because of the intrinsic variation of the quantity to be measured. Such variation may be caused by fluctuations of the quantity.* [44] The mean μ_m and a standard deviation σ are

$$\mu_m = \frac{1}{N}\sum_{i=1}^{N}\mu_i \text{ and } \sigma = \left[\frac{1}{N}\sum_{i=1}^{N}(\mu_i - \mu_m)^2\right]^{1/2} \tag{B.1}$$

    Assuming a Gaussian distribution, values will be in the interval $[-3\sigma, +3\sigma]$. The accuracy (the inverse of the difference between measure μ_m and actual value μ) of measures increase with the number of tests N[1] $\mu_m = \mu \pm \frac{\sigma}{2\sqrt{N}}$. **Example**: Measurement instruments. They have to be calibrated to know their precision. Errors occur also for filters in Data Acquisition System, conversion from analog to digital (A/D) signals,... More generally, (white) noise is an error present in every instrument, of statistical type. Turbulence induces fluctuations present in the flow and statistical errors, even without systematic or random errors.

B.2 Theoretical models

1. **Joukowski airfoil:** Using the principle of conformal mapping, starting from a known flow around a shape in a working plane $\tilde{z}$ (a circle), the flow around another shape in the physical z plane can be known, using a transformation of the form $z = \tilde{z} + \frac{b^2}{\tilde{z}}$. The flow around a circle is easy to compute, thanks to the potential flow theory[2]. By superposing (thanks to linearity) singularities: a uniform flow, doublet and vortex, the pressure distribution and lift can be computed. Using the Joukowski transformation, characteristics of a cylinder can be extrapolated for a *Joukoswki airfoil*. Imposing the Kutta condition at the TE (the flow leaves the TE smoothly, no velocity blow-up) and using the Kutta Joukowski theorem, the 2D lift can be known. The principal problem with this theory is the limited amount of geometries that can be studied, only the maximum thickness and camber are used, not the total geometry.

[1] Valid if the quantity is directly measured. Error propagation applies if it is derived from a measure.

[2] Assumptions: Inviscid + Incompressible + Irrotational + no heat source + no heat diffusion + steady flow (constant flow velocity (no acceleration) in attached flow conditions) = potential flow

$$c_l = \frac{2\pi}{b}[(b-\varepsilon)\sin\alpha + \mu\cos\alpha] \tag{B.2}$$

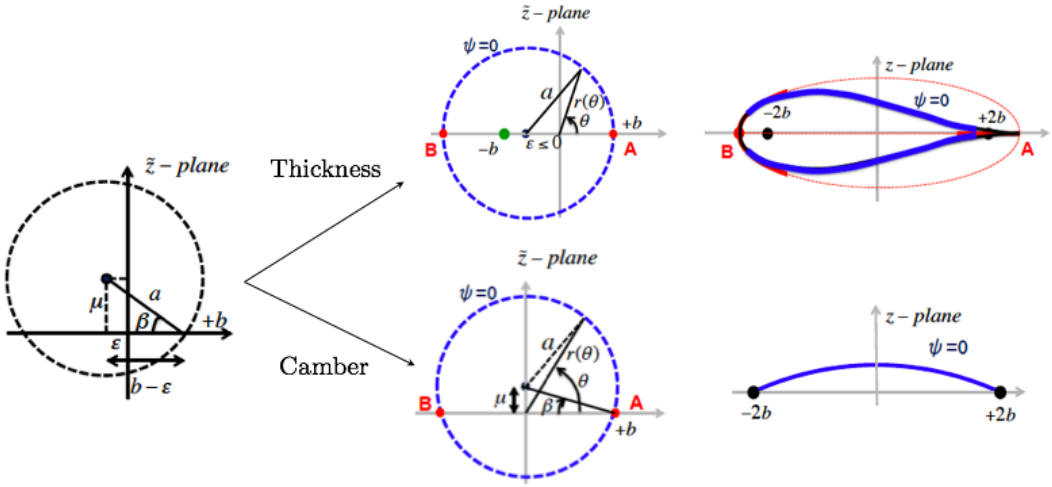

Figure B.1 – Joukowski transformation and airfoil, thickness and camber effects [63]

With $c = 2\left((b-2\varepsilon) + \frac{b^2}{b-2\varepsilon}\right) \approx 4b, \varepsilon, \mu$ in Figure B.1, computed thanks to thickness T_{max} and camber $\bar{Y}_{max}$ effects

$$\varepsilon = -\frac{c}{3\sqrt{3}}\frac{T_{max}}{c} = -0.0043 \text{ and } \mu = \frac{c}{2}\frac{\bar{Y}_{max}}{c} = 0.0016 \tag{B.3}$$

2. **Thin airfoil theory**: Specifying a body shape to compute its aerodynamic characteristics, with some approximations: thin airfoil ($Y(x) << c$, $u = U_\infty$, 2 boundary conditions on x (flow tangency condition) and small angle of attack α, $\sin\alpha \approx \alpha$, $\cos\alpha \approx 1$ (Figure B.2). The airfoil body is represented by a source (or vortices) distribution. Imposing the flow tangency and the Kutta conditions allows to compute the litf coefficient,

$$c_l = 2\pi\left(A_0 + \frac{1}{2}A_1\right) = 2\pi(\alpha + 0.0525) \text{ with } A_0 = \alpha - \frac{1}{\pi}\int_0^\pi s(\theta_0)d\theta_0 \tag{B.4}$$

$$A_1 = \frac{2}{\pi}\int_0^\pi s(\theta_0)\cos(\theta_0)d\theta_0 \ , \ x = \frac{c}{2}(1-\cos(\theta_0)) \ , \ s(\theta_0) = \frac{d\bar{Y}}{dx} \tag{B.5}$$

The exact camber is computed thanks to discrete points of the airfoil contour of upper and lower side $\bar{Y} = \frac{1}{2}(Y_u + Y_l)$. The derivative $d\bar{Y}/dx$ can be computed easily thanks to a 5 order polynomial fit (Figure B.3).

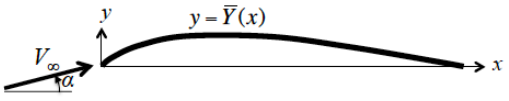

Figure B.2 – Thin airfoil at incidence, defined by its camber $\bar{Y}$

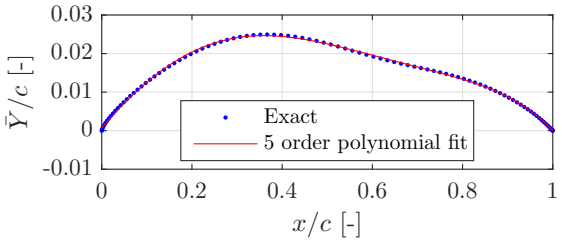

Figure B.3 – Camber $\bar{Y}$, exact and fit

3. **3D wing (Prandtl lifting line theory):** As mentioned in the introduction, real wings are finite, inducing wing-tip vortices. This results in a downward (downwash) velocity w and an effective

angle of attack α_{eff} not equal to geometric angle α because of an induced angle α_i (Figure B.4). The lift is inclined, leading to a horizontal, 3D, inviscid component: induced drag D_i (there is no d'Alembert paradox). This drag can be interpreted as a pressure imbalance created by 3D wing tip vortices (pressure drag) or as a dissipated energy (a large amount of translational and rotational kinetic energy lost downstream in the flow) [65]. The total drag is thus composed of pressure, friction and induced drag $D = D_p + D_f + D_i$, with $D_p + D_f$ being 2D quantities associated to viscosity (profile drag). Starting from Kutta-Joukowski theorem $L'(y) = \rho U_\infty \Gamma(y)$, the objective of Prandtl lifting line theory is to determine the circulation $\Gamma(y)$ (Figure B.5), with horseshoe vortex. The fundamental equation of the Prandtl's lifting line theory is

$$\alpha(y_0) = \frac{\Gamma(y_0)}{\pi U_\infty c(y_0)} + \alpha_{L0}(y_0) + \frac{1}{4\pi U_\infty} \int_{-b/2}^{b/2} \frac{d\Gamma/dy}{(y_0 - y)} dy \tag{B.6}$$

Derived using Kelvin and Helmotz theorems, computing the induced velocity by a semi$-\infty$ vortex filament (// Biot-Savart law) and using the 2D airfoil thin airfoil theory. With y_0, the location along the span (total span $= b$), c the chord and α_{L0} the lift a zero angle. An analytical solution can be found if the expression of Γ is known (for example an elliptic lift distribution). The general solution uses a Fourier sin series, $\Gamma(\theta) = 2bU_\infty \sum_{n=1}^{N} A_n \sin(n\theta)$, with the change of variable $y = -b/2 \cos\theta$. Equation B.6 becomes,

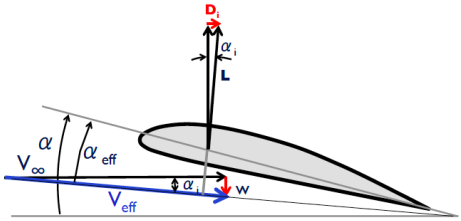

Figure B.4 – Induced angle α_i, drag D_i and downwash w due to 3D effects [65]

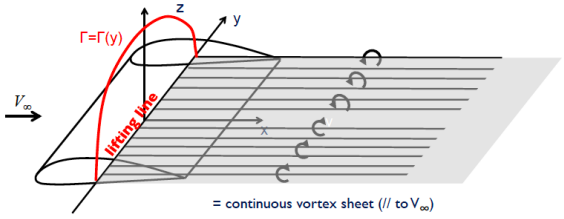

Figure B.5 – Illustration of the lifting line theory [65]

$$\alpha(\theta_0) = \frac{2b}{\pi c(\theta_0)} \sum_{n=1}^{N} A_n \sin(n\theta_0) + \alpha_{L0}(\theta_0) + \sum_{n=1}^{N} n A_n \frac{\sin(n\theta)}{\sin\theta} \tag{B.7}$$

Knowing other quantities (α, α_{L0}) on each N locations, the N unknowns A_n can be computed and the 3D lift[3]: $C_L = A_1 \pi AR$ with $AR = b^2/S$ is the aspect ratio.The induced drag is $C_{D,i} = \frac{C_L^2}{\pi AR}(1+\delta)$ with $\delta = \sum_{n=1}^{N} n(A_n/A_1)^2$. The higher the aspect ratio, the closer 3D characteristics to 2D ones. Indeed, the lift slope for a general 3D wing is (with a_0 the 2D lift slope)

$$a = \frac{a_0}{1 + \frac{a_0}{\pi AR}(1+\tau)} \text{ , with } \tau = f(A_n) \in [0.05, 0.25] \tag{B.8}$$

4. **Kutta condition:** By solving potential flow equations [4], the flow will be symmetric (Figure B.6 (a)) and the velocity will be infinite about a sharp TE. Physically, this is not observed and the flow leaves the TE smoothly and continuously so that the velocity is finite. By adding a circulation on the airfoil, the circulation on the TE is $\gamma = 0$, preventing an infinite velocity. The flow is now what is observed in reality (Figure B.6 (c)). "Reality" means that viscosity is taken into account (no-slip at airfoil wall). Thus Kutta condition is a trick to take into account viscosity effects (finite TE velocity) but using potential (inviscid) theory. The geometry of the TE has consequences: for a cusped shape (Figure B.7 left), a finite tangential velocity can exist but the normal component is 0 (not cross flow). For a finite TE angle (Figure B.7 right), normal and tangential component of the velocity must be zero (stagnation point).

[3] Usually, the 2D lift is noted in lowercase c_l and 3D in upper C_L

[4] Using sources, doublets and vortices to model the airfoil thanks to a conformal mapping (see Joukowski airfoil)

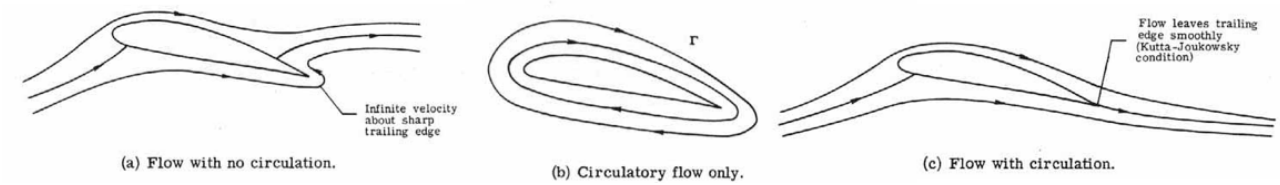

Figure B.6 – Kutta condition: No-circulatory and circulatory flows [12]

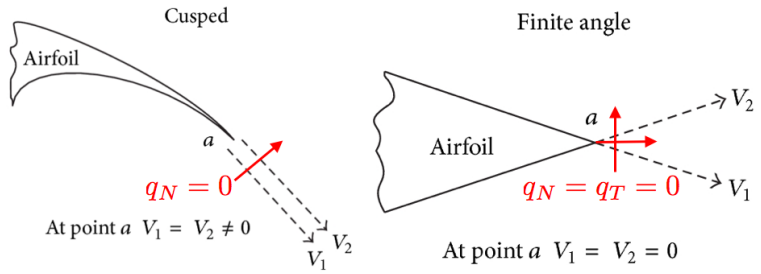

Figure B.7 – Kutta condition: cusped and finite angle TE [13]

B.3 Wind Tunnel experiment

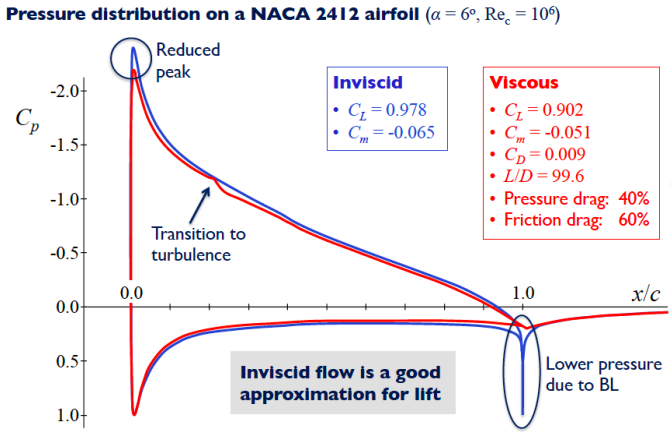

Figure B.8 – Integration of pressure around NACA 2412 airfoil [71]

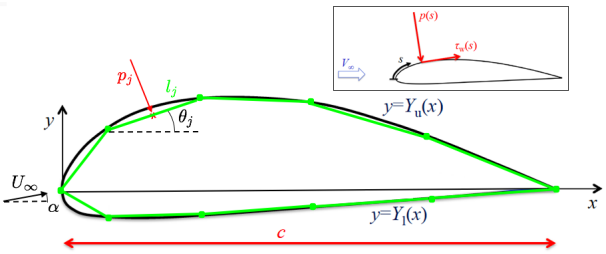

Figure B.9 – Integration of discrete pressure around airfoil [71]

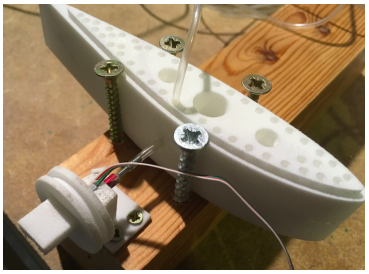

Figure B.10 – ULG calibrator: picture of the complete setup (design 2) with 3D printed support, flush mounted transducer, PVC tube inside the ballon and wing fixation

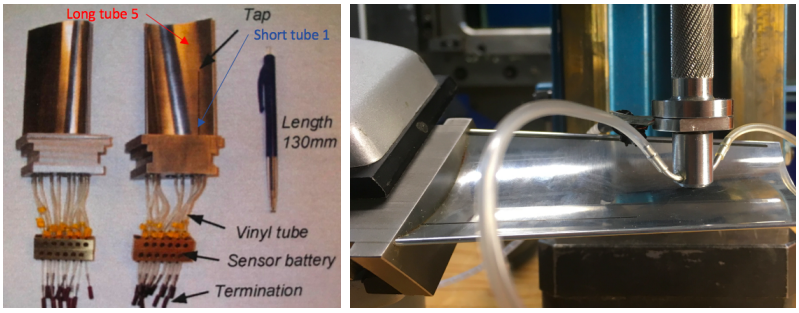

Figure B.11 – KTH calibration: test blade (short and long tubes to taps), setup and fixation

B.4 Numerical models

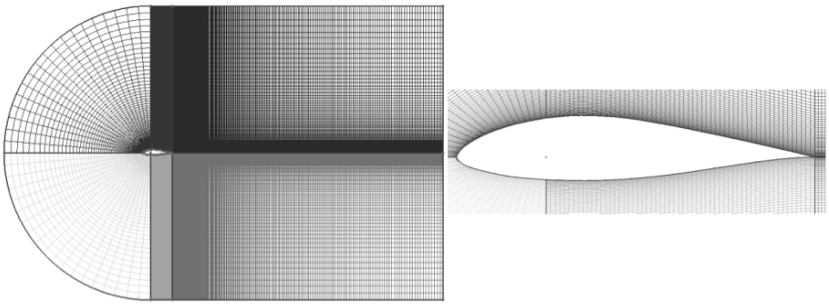

Figure B.12 – Mesh 2 used for results and comparison with experiment

B.5 Results

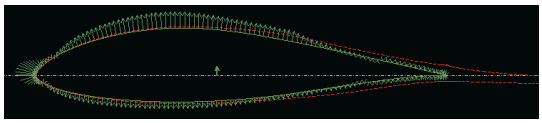

(a) `Xfoil` $Re = 0.6 \cdot 10^5$

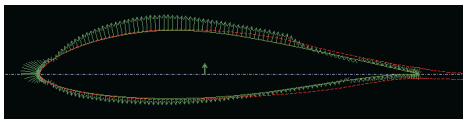

(b) `Xfoil` $Re = 1.2 \cdot 10^5$

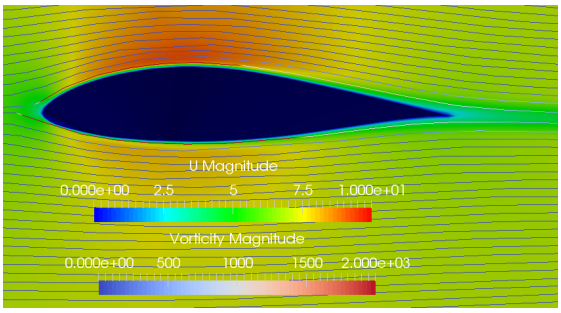

(c) CFD $Re = 0.6 \cdot 10^5$

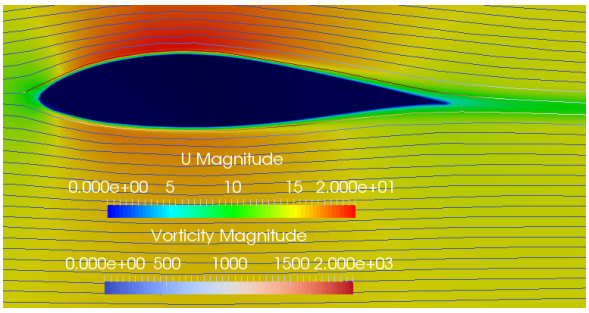

(d) CFD $Re = 1.2 \cdot 10^5$

Figure B.13 – Pressure (arrows in `Xfoil`) and velocity distribution (CFD), boundary layer (red line in `Xfoil`), streamlines with vorticity (CFD): comparison `Xfoil`-CFD at $\alpha = 0$ [°]

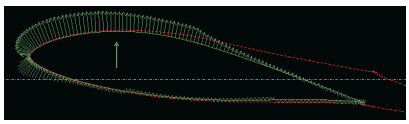

(a) `Xfoil` $Re = 0.6 \cdot 10^5$

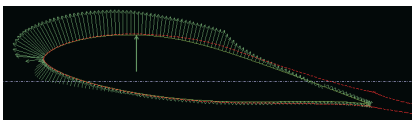

(b) `Xfoil` $Re = 1.2 \cdot 10^5$

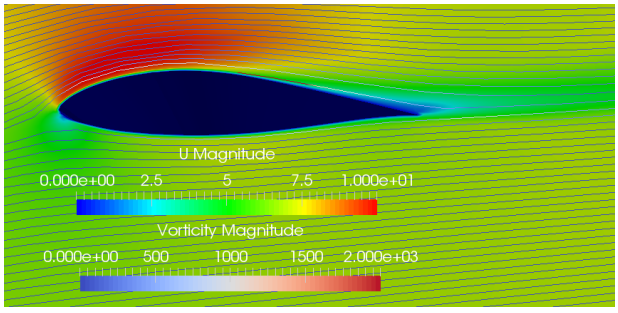

(c) CFD $Re = 0.6 \cdot 10^5$

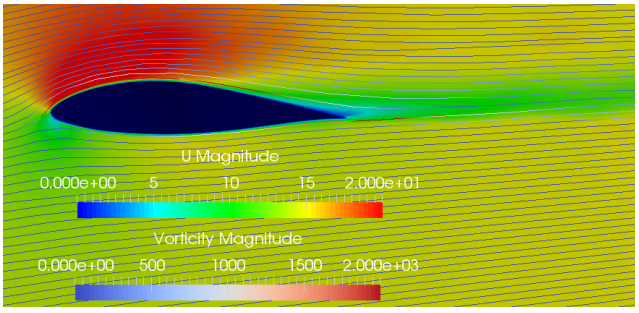

(d) CFD $Re = 1.2 \cdot 10^5$

Figure B.14 – Pressure (arrows in `Xfoil`) and velocity distribution (CFD), boundary layer (red line in `Xfoil`), streamlines with vorticity (CFD): comparison `Xfoil`-CFD at $\alpha = 8$ [°]

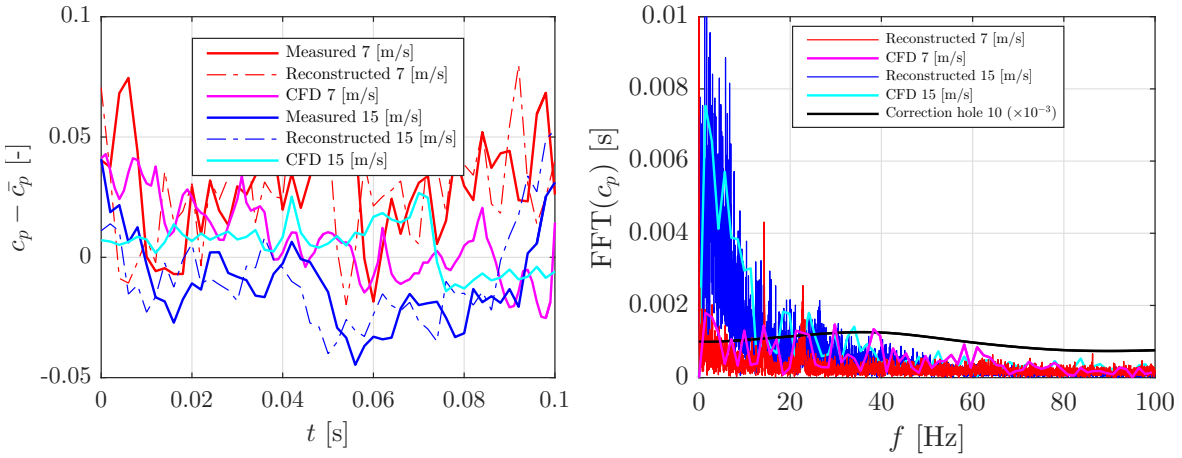

Figure B.15 – Experimental pressure coefficient fluctuation $c'_p = c_p - \bar{c}_p$ at hole 15 and $\alpha = 8$: measured and reconstructed signals for both U_∞, comparison with CFD (in time and frequency domains), dynamic response correction (pressure calibration of the profile at hole 10)

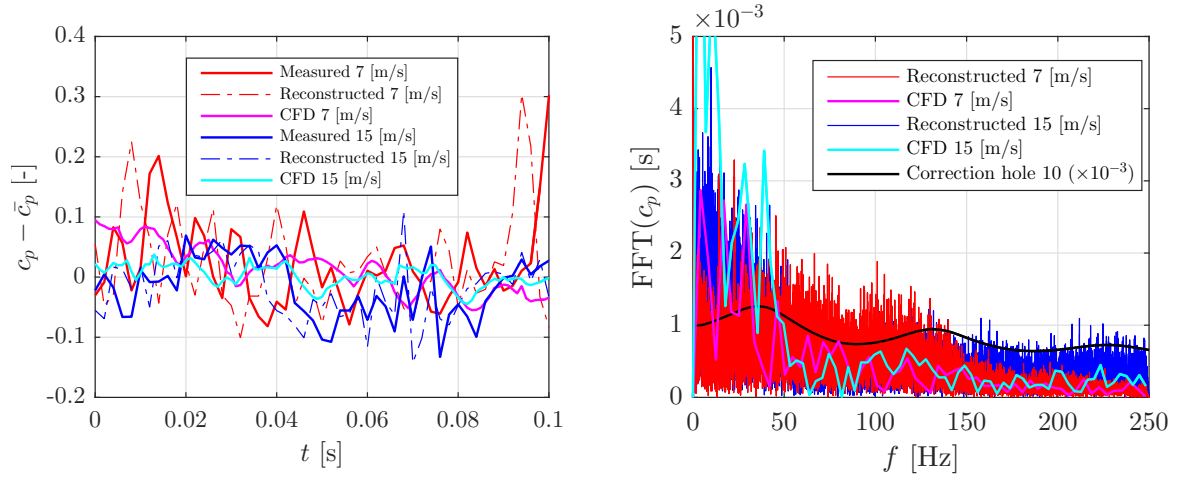

Figure B.16 – Experimental pressure coefficient fluctuation $c'_p = c_p - \bar{c}_p$ at hole 15 and $\alpha = 12$: measured and reconstructed signals for both U_∞, comparison with CFD (in time and frequency domains), dynamic response correction (pressure calibration of the profile at hole 10)

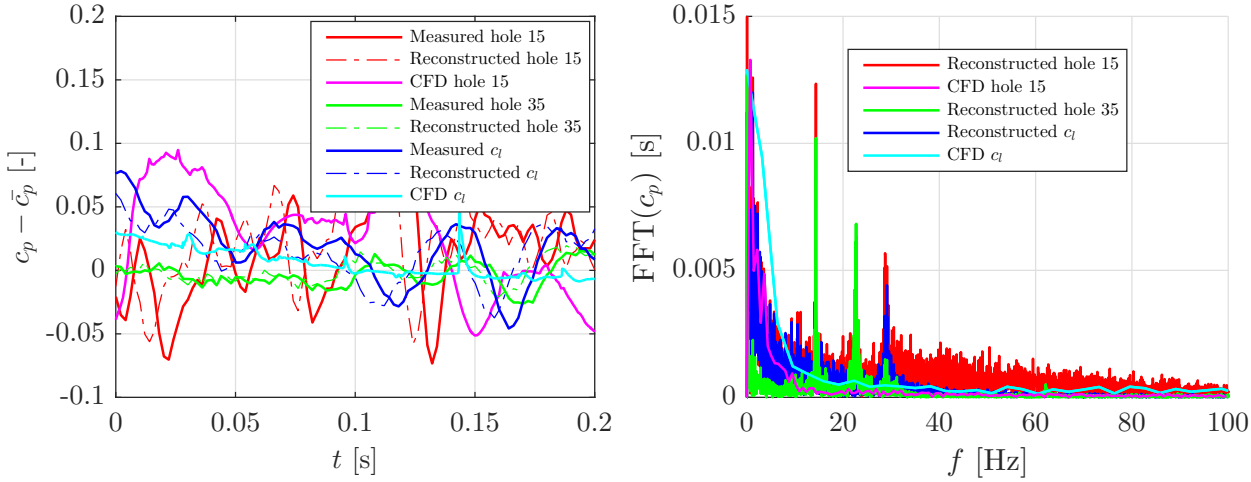

Figure B.17 – Experimental pressure and lift coefficient fluctuation $c'_p = c_p - \bar{c}_p$ at holes 15-35 and $\alpha = 20$: measured and reconstructed signals for $U_\infty = 7$, comparison with CFD (in time and frequency domains)

Appendix C

VIV grid

C.1 VIV phenomenon

Figure C.1 – Real view on site of cylinders fixation

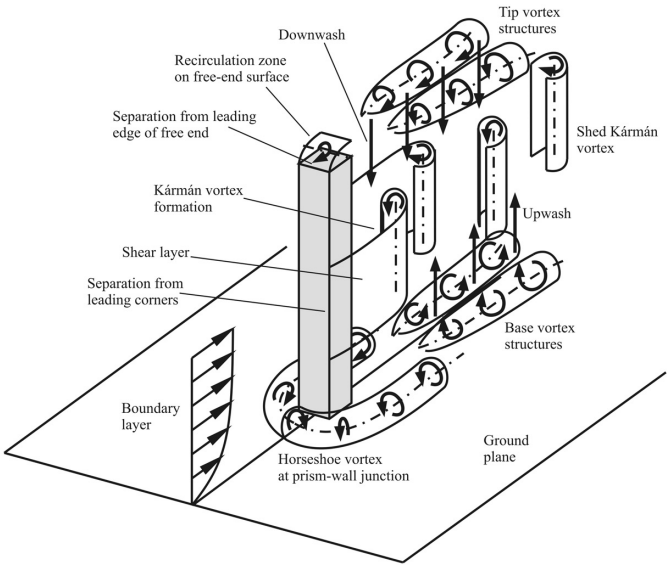

Figure C.2 – Schematic of the flow around a surface-mounted finite-height square prism partially immersed in a flat-plate boundary layer: main flow features for a prism at zero incidence angle with an aspect ratio greater than the critical aspect ratio, from [24]

C.2 Wind Tunnel Model

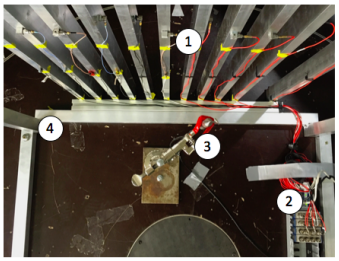

1. Accelerometers on cylinders
2. Data acquisition system
3. Cobra Probe
4. Support structure

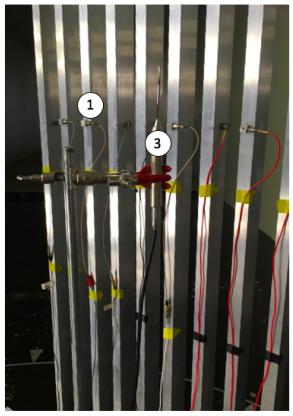

Figure C.3 – Grid model inside WT Test Section 2, instrumented with accelerometers, Cobra Probe and Hot Wire

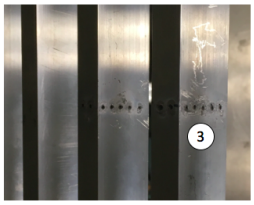

1. DPMS
2. Grid support
3. Pressure taps
4. Pitot tube
5. Turning table

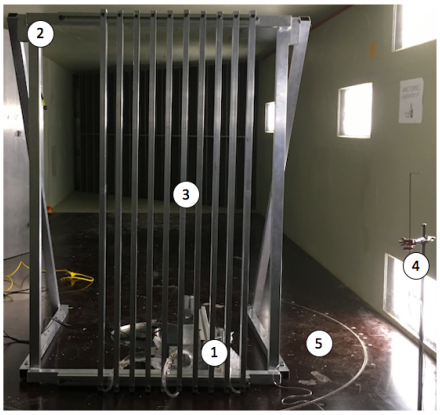

Figure C.4 – Grid model inside WT Test Section 2, instrumented with pressure tubes/taps

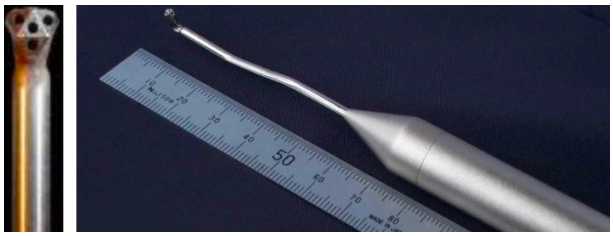

Figure C.5 – Real front and axisymmetric views of the Cobra Probe 100 series

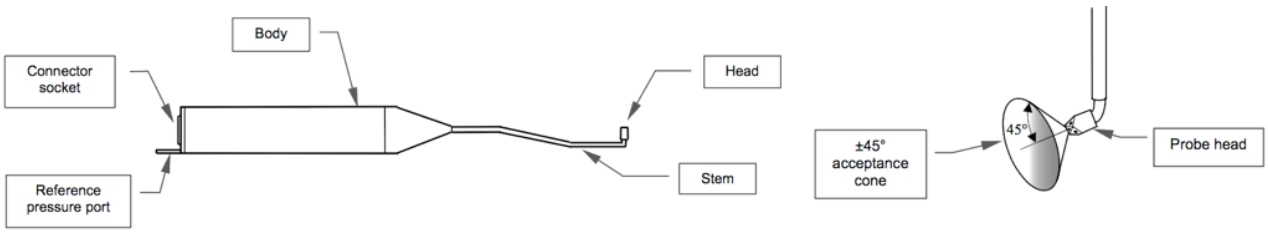

Figure C.6 – Parts of the Cobra Probe 100 series and acceptance cone

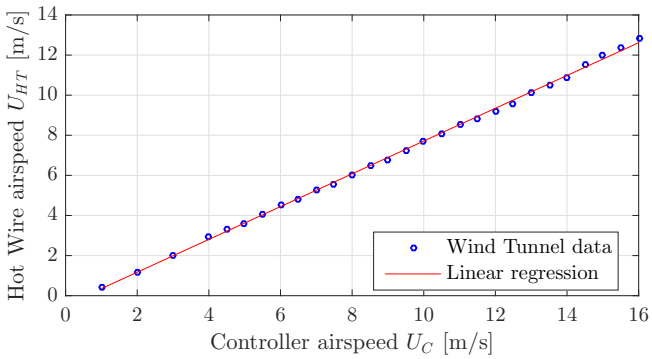

Figure C.7 – Calibration curve of airspeeds [m/s] measured by the Hot Wire (real) and demanded to the controller

C.3 Comparison

C.3.1 Pressure analysis

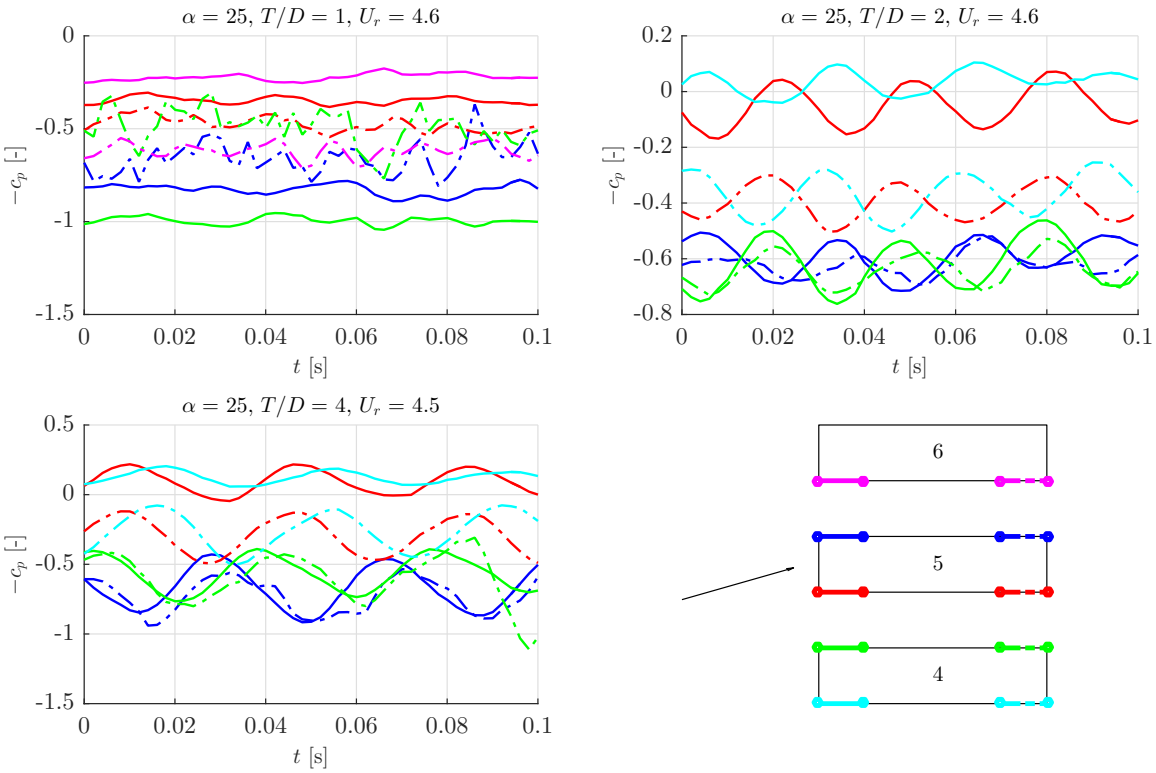

Figure C.8 – Time variation of pressure $-c_p$ at corners of cylinders 4,5,6 at $\alpha = 25$ and $T/D = 1, 2, 4$

When cylinders are at incidence (Figure C.8 at $\alpha = 25$), the synchronization is the same as the one in Figure 4.54 [1]. However, because of flow complexity for $T/D = 1$ (the air has to turn sharply from $\alpha = 25$ into a narrow channel of $T/D = 1$), vortex shedding is less "cleanly" identifiable (no smooth oscillations but more turbulent vortex ejection, turbulent BL and recirculations). In term on mean pressure, red (-) and magenta (-) are in front of the flow, the pressure is higher (or less negative) than the one on the suction side (blue (-) and green (-)). On downstream corners (-.), the flow is at the end of a channel, mean pressure for all sides (magenta, blue, red, green) is the same). For $T/D = 3$, all upper sides (or lower sides) are not synchronized with each other (blue-green not in phase, red-cyan neither) and are almost out of phase. In term of mean pressure, cyan (-) and red (-) are in front of the flow (higher pressure). However, contrary to $T/D = 1$, downstream corners (-.) on the suction side (blue, green) are at a lower pressure than those of the pressure side (red, cyan), adjacent cylinders having less influence. For $T/D = 4$, cylinders are almost independent (alternative vortex shedding on one cylinder (blue-red) but no relation between their vortex shedding blue-green and red-cyan).

[1] For $T/D = 1$: magenta-red, in opposition with blue-green. For $T/D = 3$ and 4: blue and red in opposition, green and cyan in opposition

C.3.2 Flow around the grid model: CFD results

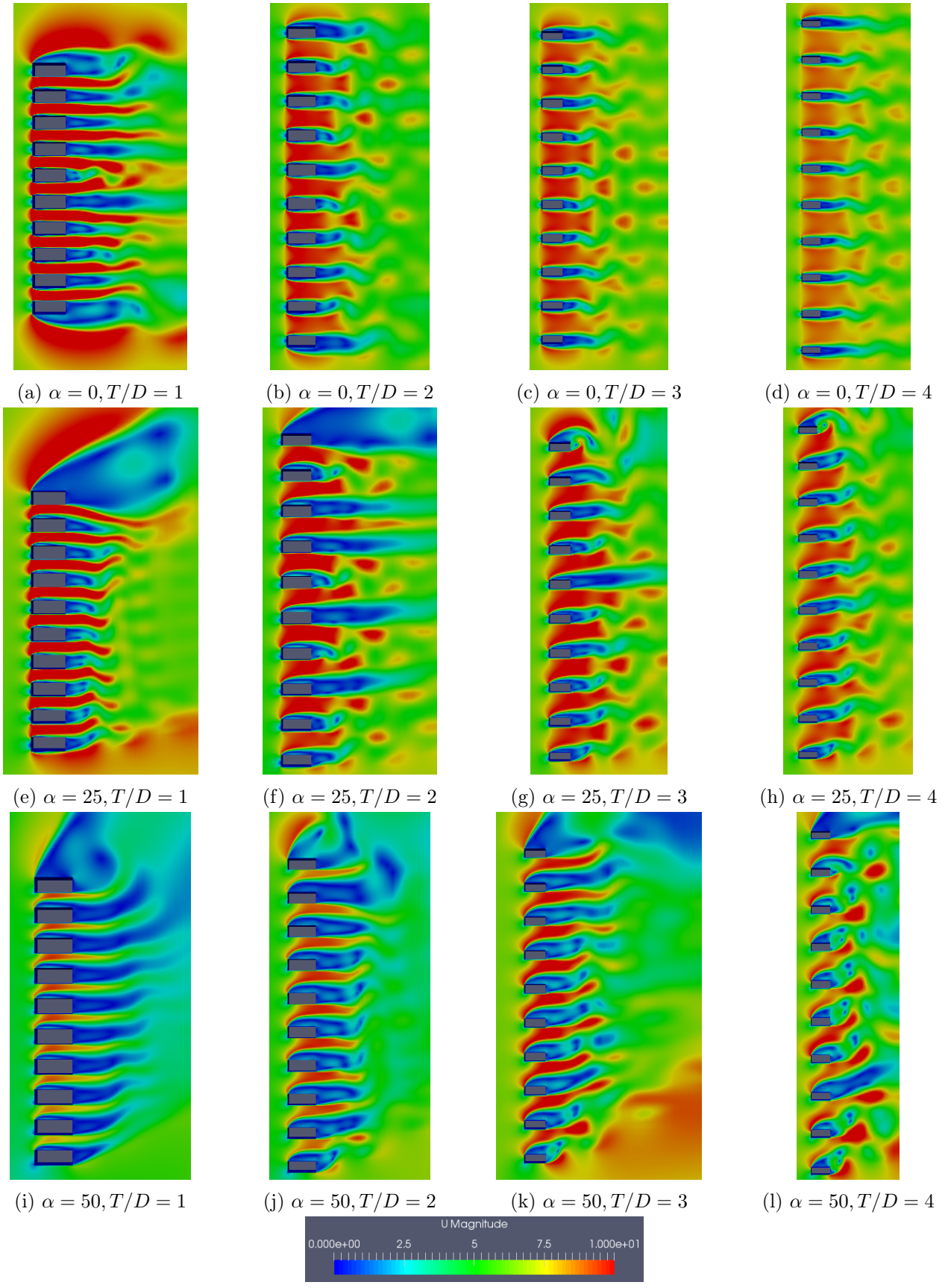

(a) $\alpha = 0, T/D = 1$ (b) $\alpha = 0, T/D = 2$ (c) $\alpha = 0, T/D = 3$ (d) $\alpha = 0, T/D = 4$

(e) $\alpha = 25, T/D = 1$ (f) $\alpha = 25, T/D = 2$ (g) $\alpha = 25, T/D = 3$ (h) $\alpha = 25, T/D = 4$

(i) $\alpha = 50, T/D = 1$ (j) $\alpha = 50, T/D = 2$ (k) $\alpha = 50, T/D = 3$ (l) $\alpha = 50, T/D = 4$

Figure C.9 – Velocity magnitude around the grid: α and T/D effect (CFD results)

Bibliography

[1] https://tonetcarlo.wordpress.com/tag/stalls/. [Online; accessed 29-April-2017].

[2] https://en.wikipedia.org/wiki/Vortex_shedding. [Online; accessed 29-April-2017].

[3] https://motherboard.vice.com/en_us/article/the-myth-of-galloping-gertie. [Online; accessed 29-April-2017].

[4] https://www.aer.mw.tum.de/en/research-groups/aerodynamics-of-buildings/. [Online; accessed 29-April-2017].

[5] http://avstop.com/ac/flighttrainghandbook/theories.html. [Online; accessed 29-April-2017].

[6] http://hep.physics.indiana.edu/~rickv/Standing_Sound_Waves.html. [Online; accessed 29-April-2017].

[7] http://www.madmadscientist.com/html/Theory.html. [Online; accessed 29-April-2017].

[8] http://mavoiescientifique.onisep.fr/quand-explosent-les-ballons-de-baudruche/. [Online; accessed 12-April-2017].

[9] http://www.mexnext.org/resultsstatus/. [Online; accessed 12-April-2017].

[10] https://www.ecn.nl/nl/nieuws/newsletter-en/2009/december-2009/aerodynamics-wind-turbines/. [Online; accessed 12-April-2017].

[11] https://www.researchgate.net/figure/224829652_fig5_Fig-9-Separation-bubble-effects-on-sucti [Online; accessed 29-April-2017].

[12] https://claesjohnsonmathscience.wordpress.com/2012/05/page/2/. [Online; accessed 29-April-2017].

[13] https://www.hindawi.com/archive/2014/676912/fig5/. [Online; accessed 29-April-2017].

[14] http://www.pcb.com. [Online; accessed 29-April-2017].

[15] https://www.dnw.aero/wind-tunnels/llf.aspx. [Online; accessed 12-April-2017].

[16] http://web.mit.edu/drela/Public/web/xfoil/xfoil_doc.txt. [Online; accessed 29-April-2017].

[17] https://geolab.larc.nasa.gov/APPS/YPlus/. [Online; accessed 29-April-2017].

[18] Iberall A. *Attenuation of oscillatory pressures in instrument lines.* Journal of research of the national bureau of standards. Vol. 45, July 1950.

[19] Okajima A. *Strouhal numbers of rectangular cylinders.* Journal of Fluid Mechanics, 1982.

[20] Vanderheyden B. *Electromagnetisme: lignes de transmission.* University of Liege, Liege, November 2014.

[21] Bowers W. Bean V. *Development of a Primary Standard for the Measurement of Dynamic Pressure and Temperature.* Metrologia, Vol. 30, 1993/94.

[22] Schnittfeld T. Bohn D. *The dynamic response of capillary tubes for use in miniature pressure probes.* In: Proc. of the 11th symposium on measuring techniques for transonic and supersonic flow in cascades and turbomachines,, Munich, Germany.

[23] Knisely C. *Strouhal numbers of rectangular cylinders at incidence: a review and new data.* Mechanical Engineering Departement, Buckell University,, Lewisburg, PA17837, USA, 1989.

[24] Dae Kun Kwon Chang Koon Choi. *Determination of the Strouhal number based on the aerodynamic behavior of rectangular cylinders.* Wind and Structures, Vol. 3, No. 3 (2000) 209-220, Department of Civil Engineering, Korea Advanced Institute of Science and Technology(KAIST), 373-1 Kusong-dong, Yusong-gu, Taejon 305-701, Korea.

[25] Funda Kurtulus D. *Experimental Aerodynamics: Unsteday Pressure Measurements.* METU Open-CourseWare, 2010.

[26] Sindre Misund Dahl. *Unsteady RANS Simulation of Flow around Rectangular Cylinders with different Aspect Ratios at High Reynolds Number.* Norwegian University of Science and Technology, Department of Marine Technology, 2014.

[27] Monteleone L. Del Prete Z. *A novel array sensor based on contact resistance variation: Metrological properties.* Review of Scientific Instruments, Vol. 72, No. 2, Gaithersburg, Maryland, USA, February 2001.

[28] Bechet E. *Computer Aided Design, Lecture 2: interpolation.* University of Liege, Liege, November 2015.

[29] Delhez E. *Mécanique des fluides.* University of Liege, Liege, March 2015.

[30] Peri M. Ferziger J. *Computational Methods for Fluid Dynamics.* ed., Springer, Berlin, 2002.

[31] Delio G. *Transient Behavior of Lumped-Constant Systems for Sensing Gas Pressures.* National Advisory Committee for Aeronautics, 1949.

[32] Dimitriadis G. *Aeroelasticity, Lecture 4: FLight Flutter Testing.* University of Liege, Liege, November 2016.

[33] Parkinson G. *The square prism as an aeroelastic non-linear oscillator.* The Quaterly Journal of Mechanics and Applied Mathematics 17: 225-239., 1964.

[34] Rixen D. Géradin M. *Mechanical Vibrations - Theory and Application to Structural Dynamics.* John Wiley & Sons, Ltd, 2015.

[35] Bergh H. and Tijdeman H. *Theoretical and experimental results for the dynamic response of pressure measuring systems.* National Aerospace Laboratory NLR, Amsterdam, March 1967.

[36] Nakaguchi H. *An experimental study on aerodynamic drag of rectangular cylinders.* Journal of Japan Aeronautics Space Science, 1968.

[37] Reichenberger H. and Naser G. Shock wave generator for generating an acoustical shock wave pulse, May 29 1990. US Patent 4,928,671.

[38] Sumer H. *Hydrodynamics around cylindrical structures.* Advanced series on ocean engineering, Vol 26, World Scientific, 2006.

[39] Taback I. *The response of pressure measuring systems to oscillating pressures.* National Advisory Committee for Aeronautics, 1949.

[40] Hjelmgren J. *Dynamic Measurement of Pressure - A Literature Survey.* SP Swedish National Testing and Research Institute, Measurement Technology, SP REPORT 2002:34, Sweden, 2002.

[41] Lally J. *Dynamic Step-Pressure Calibration", Proceedings from the NIST Workshop on the Measurement of Transient Pressure and Temperature.* Gaithersburg, Maryland, USA, April 23rd-24th, 1991.

[42] Lienhard J. *Synopsis of lift, drag, and vortex frequency - Data for rigid circular cylinders.* Technical Extension Service, Pullman, Washington, 1966.

[43] T.S. Leishman, J.G.; Beddoes. *A semi-empirical model for dynamic stall.* J. Am. Helicopter Soc., 1989.

[44] Sterenborg J. Lindeboom R. *Determination of unsteady loads on a DU96W180 airfoil with actuated flap using particle image velocimetry.* TORQUE 2010: The Science of Making Torque from Wind,, Crete, Greece, June 28-30 2010.

[45] Ong M. *Unsteady RANS Simulation of Flow Around a 5:1 Rectangular Cylinder at High Reynolds Numbers.* Volume 5: Ocean Engineering; CFD and VIV, ASME, pp. 841–846., 2012.

[46] Zdravkovich M. *Flow induced oscillations of two interfering circular cylinders.* Departement of Aeronautical and Mechanical Engineering, University of Salford, 1984.

[47] Schobeiri M.T. *Fluid Mechanics for Engineers: A Graduate Textbook.* Springer Berlin Heidelberg, 2010.

[48] Steggel N. *A Numerical Investigation of the Flow Around Rectangular Cylinders.* School of Mechanical and Materials Engineering The University of Surrey, Guildford GU2 5XH, United Kingdom, March 1998.

[49] Yoshimura T. Nakamura Y. *Flutter and vortex excitation of rectangular prisms in pure torsion in smooth and turbulent flows.* Journal of Sound and Vibration 84(3), 305–317, 1982.

[50] Léonard O. *Thermodynamique appliquée et introduction aux machines thermiques.* Université de Liège, 2015.

[51] Joris P. *Mécanique des milieux continus, TP: matériaux hyperélastiques.* University of Liege, Liege, March 2015.

[52] de Langre E. Paidoussis M., Price S. *Fluid-structure Interactions : cross-flow induced instabilities.* Cambridge University Press, 2011.

[53] Denos R. Paniagua G. *Digital compensation of pressure sensors in the time domain.* Experiments in Fluids 32, 417-424, Springer-Verlag, 2002.

[54] Pavel M. Pereira R., Schepers G. *Validation of the Beddoes-Leishman dynamic stall model for horizontal axis wind turbines using Mexico data.* Wiley Wind Energy, 2012.

[55] Binder R. *The Damping of Large Amplitude Vibrations of Fluid in a Pipe.* Jour. acous. soc. Am., vol 15, no 1, 1943.

[56] Whitford R. *Design for air combat.* jane's Publishing Inc., New York, 1987.

[57] Pope S. *Turbulent Flows.* Cambridge University Press, 2000.

[58] Blanck G. Sarazin M., Mosser S. *Que se passe -t-il lorsque l'on gonfle un ballon de baudruche ?* Olympiades de physique, Paris, 2004.

[59] Damion J. Sarraf C. *A Method for Dynamic Calibration of Pressure Transducers.* Laboratoire de Métrologie Dynamique LNE - ARTS ET METIERS ParisTech, 7th workshop on Analysis of Dynamic Measurements, Paris, October 2012.

[60] Eichberger L. Schweppe J. *Methods for the Dynamic Calibration of Pressure Transducers.* National Bureau of Standards Monograph 67, 1963.

[61] K. Shimada and T. Ishihara. *Application Of A Modified $k\breve{}\varepsilon$ Model To The Prediction Of Aerodynamic Characteristics Of Rectangular Cross-Section Cylinders.* Journal of Fluids and Structures 16(4), 465–485., 2002.

[62] ISA The Instrumentation Systems and Automation Society. *A Guide for the Dynamic Calibration of Pressure Transducers.* The American Society of Mechanical Engineers, New York, USA, 1972.

[63] Andrianne T. *Aerodynamics Lecture 3: Conformal mapping.* University of Liege, Liege, March 2016.

[64] Andrianne T. *Aerodynamics Lecture 5: panel method.* University of Liege, Liege, March 2016.

[65] Andrianne T. *Aerodynamics Lecture 6: 3D Wing.* University of Liege, Liege, March 2016.

[66] Andrianne T. *Aeroelasticity, Lecture 1: Vortex Induced Vibration.* University of Liege, Liege, November 2016.

[67] Kobota T. and Ooiwa A. *Square-wave pressure generator using a novel rotating valve.* Metrologia, Vol. 36, 1999.

[68] Magin T. *Aerothermodynamics of High Speed Flows, Lecture 2: Flow with discontinuities.* University of Liege, Von Karman Institue, March 2017.

[69] Momma T. and Lichtarowicz A. *A new calibration method for dynamically loaded transducers.* Proceedings of the 1994 ASME Fluids Engineering Division Summer Meeting, Nevada, USA, June 19th-23rd, 1994.

[70] Santosham T. *Force measurements on bluff body cylinders and aeroelastic galloping of a rectangular cylinder.* University of British Columbia, Glasgow, 1966.

[71] Andrianne T. Terrapon V. *Aerodynamics Lecture 1: introduction.* University of Liege, Liege, March 2016.

[72] Terrapon V. *Aerodynamics Lecture 9: Boundary layer III.* University of Liege, Liege, March 2016.

[73] Terrapon V. *Computational Fluid Dynamics.* University of Liege, Liege, November 2016.

[74] van Rooij R. Design of airfoils for wind turbine blades. https://gcep.stanford.edu/pdfs/energy_workshops_04_04/wind_van_rooij.pdf, 2004. [Online; accessed 12-April-2017].

[75] Fransson T. Vogt D. *A technique for using recessed-mounted pressure transducers to measure unsteady pressure.* In: Proc. of the 17th symposium on measuring techniques for transonic and supersonic flow in cascades and turbomachines,, Stockholm, Sweden, 2004.

[76] Chapin W. *Dynamic-Pressure Measurements Using an Electronically Scanned Pressure Module.* NASA Technical Memorandum 84650, Langley Research Center Hampton, Virginia, 1983.

[77] Nakamura Y. and Mizota T. *Torsional flutter of rectangular prisms.* Journal of the engineering mechanics division, ASCE 101(EM2): 125-142, 1975.

[78] Kurita T. Yoshida A., Tamura Y. *Effects of bends in a tubing system for pressure measurement.* Journal of Wind Engineering and Industrial Aerodynamics 89 (2001) 1701–1716, Department of Architectural Engineering, Tokyo Institute of Polytechnics,1583 Ilyama Atsugi-si, Kanagawa 243-0297, Japan, 2001.

[79] Wroobel K. Zakrzewski J. *Dynamic Calibration of Low Range Silicon Pressure Sensors.* Instrumentation and Measurement Technology Conference, Budapest, Hungary, May 21st- 23rd, 2001.